

THE UNIVERSITY OF HULL

Human Movement Energy Harvesting:
A Nonlinear Electromagnetic Approach

being a Thesis submitted for the Degree of
Doctor of Philosophy
in the University of Hull

by

Chun Keat Yew, BEng (Hons)

January 2015

.. To My Parents

Abstract

Energy harvesting is one of the methods that currently engage actively in energy “recycling”. Of the many energy sources that carry the potential to have energy harvested and recycled, humans are seen as a potential source of energy. High amounts of energy are wasted from daily activities that humans do, if only a portion of the wasted energy can be harvested and reused with the aim of improving the quality of life of the user.

To do that, the accelerations of selected movements are recorded from sensors attached to four different locations of the body. Human movements operate on a low and wide frequency scale, nonlinear energy harvesting techniques is seen as a suitable technique to be applied. Nonlinear energy harvesting techniques are expected to increase the bandwidth of operation of the energy harvester. The electromagnetic method of transduction is also selected (using two opposing magnets) to be paired with the nonlinear energy harvesting techniques to evaluate the potential of energy harvesting from human movements. The pick-up coil to be used will be placed at a novel location within the energy harvester prototype.

Through simulations and experiments, frequency responses obtained did show an increase in bandwidth which agrees with literature from nonlinear energy harvesting techniques. Phase portraits are also used to provide a more in depth understanding on the movements from the cantilever under linear and nonlinear dynamics. Result comparisons were made between the simulation model and the experimental prototype to verify the agreement between the two.

Additionally, results obtained also showed that the resonant frequency of the system was reduced when operating under the nonlinear regime. These attribute favour energy harvesting through human movements.

Finally, the novel placement of the pick-up coil within the nonlinear electromagnetic energy harvester had the desired effect. Similar power outputs were achieved even though the separation distances between the two opposing magnets were varied.

Acknowledgements

First and foremost, I am ever grateful and deeply indebted to Professor James Gilbert. Without his constant support, guidance and care, none of this would have been possible. The amount of time and patience spent revising the draft, along with the countless impromptu meetings is very much appreciated. I consider myself extremely lucky to have the opportunity to work under his supervision.

Special thanks go to Dr Jay Wadhawan, Dr Igor Itskevich and Dr Antony Wilkinson for providing insights, motivation, inspiration and friendship along this journey. I would also like to thank secretarial staff as well as the technicians within the School of Engineering for helping me with countless requests, big or small.

The guys in the lab, Dr Beng Lee Ooi, Jie Bai, Dr Farouk Balouchi, Dr Lam Aun Cheah and Roberto Rodrigues, thank you for your company and friendship. The times spent discussing random topics will be missed. You guys make the long days in the lab an enjoyable one.

I would also like to thank Dr Septavera Sharvia, Dr Kuan Yoow Chan, Zhao Yong Ho and Dr Qiang Chen for their friendship, company, advice, encouragements and good food!

Special mention also goes to my better half, Shu Zeng, for her unwavering love, encouragements, kindness and understanding.

Finally, my deepest gratitude goes to my parents and my brothers. I cannot possibly write enough to describe everything you all have done for me. To provide me with unconditional sacrifice, love and support which I, undeservedly, take for granted. I am very proud of you all.

Thank you.

Table of Contents

Abstract	3
Acknowledgements	4
1.0 Introduction	15
1.1. Research Aims.....	16
1.2. Organisation of the Thesis.....	16
2.0 Overview of Energy Harvesting.....	18
2.1 Power from Ambient Sources	19
2.2 Human Power	22
2.2.1 Summary of Human Power	24
2.2.2 Potential Applications of Human Energy Harvesting.....	25
2.2.2.1. Applications of Energy Harvesting Outside the Body or Wearable Body Sensor Networks.....	26
2.2.2.2. Telemetry Systems.....	27
2.2.3. Summary of human power	29
2.3. Vibrational Energy Harvesting.....	29
2.3.1. Model of a Vibration to Electric Transducer	30
2.4. Comparison of Different Methods of Vibration to Electric Transduction	34
2.4.1. Electromagnetic Transduction	34
2.4.2. Piezoelectric Transduction.....	35
2.4.3. Magnetostrictive Transduction.....	36
2.4.4. Summary of transduction methods	37
2.5. The Electromagnetic Energy Harvester.....	39
2.5.1. Existing Electromagnetic Harvesters in Micro/Wafer Scale Implementations.....	41
2.5.2. Existing Electromagnetic Harvesters in Macro-Scale Implementations...	42
2.5.3. Summary of electromagnetic energy harvesters	44
2.6. Nonlinear Energy Harvesting	45

3.0	Generation and Capture of Human Movement Accelerations	51
3.1.	Measurement Systems	53
3.2.	Measurement Results	57
3.3.	Further Discussions of Results Obtained	62
3.3.1.	Total Accelerations for a Single Placement of the Sensor with Different Body Movements	63
3.4.	Summary	66
4.0	Nonlinear Energy Harvester Set Up.....	67
4.1.	Prototype Design	68
4.2.	Modelling the Nonlinear Prototype	71
4.2.1.	Magnets	71
4.2.2.	Modelling of the Magnets	72
4.2.3.	Measuring the Magnetic Flux Density of the Magnets	76
4.2.4.	Comparison of Modelling and Experimental Results of magnets.....	77
4.3.	Modelling the Forces Between the Two Magnets.....	79
4.4.	Modelling the Cantilever.....	80
4.5.	Matlab Simulink Model of Complete Nonlinear Cantilever Prototype	87
4.6	Human Movement and Nonlinear Energy Harvesting	90
4.7	Frequency Response of the Nonlinear Cantilever Model	94
4.8	Phase Plane Plots.....	99
4.9	Summary	111
5.0	Verification of Simulation Results.....	112
5.1	Calibration of the Vibrator and Vibration Generation for the Prototype	112
5.2	Experimental Comparison with Simulation Results	114
5.3	Experimental Phase Plane Plots	122
5.4	Summary	135
6.0	Power Generation from the Experimental Cantilever System.....	136
6.1.	Coils Used in the Prototype.....	136

6.2. Location of Optimum Resistive Load for Power Generation for Prototype System.....	139
6.3. Peak to Peak Voltage Output from the Bar Coil	141
6.4. RMS Output Voltage.....	143
6.5. Maximum Power and bandwidth from the Prototype	147
6.6. Summary	150
7.0 Further Discussions, Conclusions and Future Work.....	151
7.1. Further Discussions Regarding Nonlinear Model and Prototype.....	151
7.2. Recommendations for Future Work	154
8.0 References	156
Appendix A: Source Code Used For Importing Accelerometer Measurements into Matlab Workspace and Analysis.....	162
Appendix B: Frequency Sweep of Calibrated Vibrator	164
Appendix C: Voltage Outputs from Cylindrical Coil	168
Appendix D: Source Code for Modelling Nonlinear Forces Generated by Dipoles.	170
Appendix E: Source Code for Frequency Response from Simulink model of Nonlinear Cantilever	171
Appendix F: Frequency Responses for All Separation Distances under All Accelerations from Simulation	172
Appendix G: Frequency Responses for All Separation Distances under All Accelerations from Experimental Prototype.....	175
Appendix H: Additional Info on Human Movement Measurements.....	181
Sensor Location Acceleration Comparisons	181
Channel by Channel Acceleration Comparisons	185
Movement by Movement Acceleration Comparisons	188

List of Figures

Figure 1: Potentially harvestable energy from selected human motions. Total power for each action is included in the parenthesis. [9].....	23
Figure 2: An example architecture of wireless health monitoring system. [20]	27
Figure 3: Schematic diagram of the transducer.....	30
Figure 4: Frequency spectrum of power generated around resonance frequency with different damping factors. [26]	33
Figure 5: (a) Prototype of the magnetostrictive transducer by Wang, (b) Metglas 2065SC and laminate. [29].....	36
Figure 6: Silicon electromagnetic generator by Beeby [35].	42
Figure 7: (Left) First prototype; (Right) Second Prototype by Glynne-Jones. [41]	43
Figure 8: Micro cantilever generator from Beeby.....	44
Figure 9: Experimental apparatus by Cottone, Vocca and Gammaitoni [43]	46
Figure 10: Schematic diagram of a piezoelectric energy harvester by Stanton and colleagues. [44]	47
Figure 11: Left: Experimental setup by Ferrari with dimensions of piezoelectric material used. Right: Open-circuit output voltage response with varying distance between the two magnets. [45].....	48
Figure 12: Left: Schematic diagram of the magnetic levitation system with coils wrapped around both the top and bottom sections of the device. Right: Complete experimental set up used by Mann and Sims. [46]	49
Figure 13: Black Box: Mechanical Spring design. Red Box: Magnetic-Spring design. Green box: Prototype of magnetic-spring produced. [47]	50
Figure 14: An illustration of the static High Knees movement (left) and the static Jogging movement (right) [48].	52
Figure 15: Location and orientations of the sensors placed on the body.	53
Figure 16: Floor plan of the laboratory that was used to conduct movement measurements. (Blue colour indicates tables/objects, Light Brown indicates doorways.)	54
Figure 17: Schematic of the Sensor Board. (Input of the LM3940 comes from the output of the 7805 Voltage Regulator).....	55
Figure 18: Schematic of the Sensor Base Board.....	56
Figure 19: Block diagram of the vibration capture process.	57
Figure 20: Orientation of the accelerometer that was attached to the foot.	57
Figure 21: Left foot walking raw data, all channels.....	58

Figure 22: Left foot walking in frequency domain in Channel X.....	59
Figure 23: Left foot walking in frequency domain in Channel Y.....	60
Figure 24: Left foot walking in frequency domain in Channel Z.	60
Figure 25: Total acceleration comparisons of different body placement of the sensor and with different movement (Walking – average of both sets of measurements).	62
Figure 26: Left Foot Walk.....	64
Figure 27: Left Foot Jog.....	65
Figure 28: Left Foot High Knees	65
Figure 29: Schematic of proposed nonlinear energy harvesting device.	67
Figure 30: Construction and dimensions of the fork which is attached to the cantilever.	68
Figure 31: Cantilever prototype design with magnets attached shown in green.....	69
Figure 32: Cantilever prototype design with magnets attached shown in green from another angle.	69
Figure 33: The constructed prototype mounted on top of the shaker.	70
Figure 34: Block diagram of nonlinear cantilever prototype.	71
Figure 35: Tablet/Button magnet and Bar magnet that is being used.	72
Figure 36: Block diagram of magnet interaction modelling process	72
Figure 37: Dipole model movement assumption.	73
Figure 38: Diagram showing the orientation of the dipole modelled.	73
Figure 39: Diagram explaining dipole's radial and normal direction.....	74
Figure 40: Direction of forces which act upon the dipole model during the modelling process.....	75
Figure 41: Dipole measurement direction.....	76
Figure 42: Comparison of both measured magnets' magnetic flux density.	77
Figure 43: Modelled magnetic density for the tablet magnet compared with measured values from experiment.....	78
Figure 44: Modelled magnetic density for the bar magnet compared with measured values from experiment.....	78
Figure 45: Block diagram of the modelling process of forces of the dipoles.	79
Figure 46: Force generated from dipole model with varying distances.....	79
Figure 47: Comparison of peak forces measured from 5mm up towards 18mm dipole distance separation.	80
Figure 48: Red dot showing the centre of gravity for the fork and magnet attachment as tip mass of the cantilever.....	82

Figure 49: Spring constant experiment set up. A and B (Yellow and Red dots) are locations where Force was applied.	82
Figure 50: Result from the experiment of determining Spring Constant of the spring cantilever system.	83
Figure 51: Drawing showing the cantilever's slope angle and maximum deflection.	84
Figure 52: Logarithmic Decrement.	85
Figure 53: Damping Coefficient Experiment.	86
Figure 54: Simulink prototype used to simulate the cantilever.	87
Figure 55: Simulated output compared with measured experimental results.	89
Figure 56: Dipole forces simulated with spring constant.	89
Figure 57: Displacement outputs when $k=6.7\text{N/m}$ at 0.5g acceleration.	91
Figure 58: Displacement outputs when $k=6.7\text{N/m}$ at 2g acceleration.	92
Figure 59: Displacement outputs when $k=6.7\text{N/m}$ at 3g acceleration.	93
Figure 60: Bandwidth from the models at 0.5g, 2g and 3g acceleration.	93
Figure 61: Frequency response simulated for a selected set of separation distances at 0.5g acceleration.	95
Figure 62: Simulated frequency response at an external acceleration of 1g.	96
Figure 63: Simulated output at an external excitation of 2g.	97
Figure 64: Comparisons of the maximum displacements achieved by the modelled cantilever.	97
Figure 65: (Right): Experimental phase plane plot at 18mm separation distance (Left) Simulated phase plot.	100
Figure 66: Phase plane plots for 5mm separation distance of magnets (unscaled).	102
Figure 67: Phase plane plots for 5mm separation distance of magnets (scaled).	103
Figure 68: Phase plane plots for the separation distance of the magnets at 7mm (unscaled).	105
Figure 69: Phase plane plots for the separation distance of the magnets at 7mm (Scaled).	106
Figure 70: Phase plane plots for the separation distance of the magnets at 18mm (Unscaled).	108
Figure 71: Phase plane plots for the separation distance of the magnets at 18mm (Scaled).	109
Figure 72: Block diagram for vibration generation.	112
Figure 73: Block diagram for the calibration process of the vibrator.	113

Figure 74: Calibrated outputs across 0.5g to 2g acceleration during frequency sweep from 8Hz to 50Hz with cantilever harvester attached.....	114
Figure 75: A section of the frequency sweep experiment showing an example of the rapid increase of displacement (Red Rings) before settling (Green Ring) during the "OFF" to "ON" phase.....	115
Figure 76: Bandwidth, average and peak displacement comparison across all separation distances at 0.5g acceleration.....	116
Figure 77: Bandwidth, average and peak displacement comparison across all separation distances at 1g acceleration.....	117
Figure 78: Bandwidth, average and peak displacement comparison across all separation distances at 2g acceleration.....	118
Figure 79: Frequency of which the peak displacements were recorded for all separation distances from 0.5g, 1g and 2g accelerations.....	120
Figure 80: Phase plane plots of selected separation distances at selected frequencies.	124
Figure 81: Phase plane plots of 3mm, 5mm and 6mm separation distances of the experimental cantilever at 1g acceleration.....	126
Figure 82: Phase plane plots of 7mm, 12mm and 18mm of the experimental cantilever at 1g acceleration.....	128
Figure 83: Phase plane plots from 3mm, 4mm and 5mm separation distance at 2g accelerations.....	130
Figure 84: Phase plane plots from 6mm and 7mm separation distance at 2g accelerations.....	132
Figure 85: Phase plane plots from 12mm and 18mm separation distance at 2g accelerations.....	134
Figure 86: Placement of the bar coil within the prototype during the experiments.....	138
Figure 87: Resistive Load Calibration.	139
Figure 88: Power output curve across different resistive loads attached to the prototype system.....	140
Figure 89: Peak to peak voltage output of the bar coil under 0.5g acceleration across various frequencies.....	141
Figure 90: Peak to peak voltage output of the bar coil under 1g acceleration across various frequencies.....	142
Figure 91: Peak to peak voltage output of the bar coil under 2g acceleration across various frequencies.....	142
Figure 92: Dimensions of the coil and cantilever magnet and actual prototype.....	143

Figure 93: RMS voltage from all separation distances under 0.5g acceleration.....	144
Figure 94: RMS voltage from all separation distances under 1g acceleration.....	144
Figure 95: RMS voltage from all separation distances under 2g acceleration.....	145
Figure 96: Power output and bandwidth comparison for prototype under 0.5g acceleration.	147
Figure 97: Power output and bandwidth comparison for prototype under 1g acceleration.	148
Figure 98: Power output and bandwidth comparison for prototype under 2g acceleration.	149
Figure 99: Copy of Figure 79.....	152
Figure 100: Potential cantilever design.....	155
Figure 101: Voltage outputs of the cylindrical coil at 0.5g acceleration.	168
Figure 102: Voltage outputs of the cylindrical coil at 1g acceleration.	169
Figure 103: Voltage outputs of the cylindrical coil at 2g acceleration.	169
Figure 104: Frequency response of simulated cantilever at 0.5g acceleration from 3mm to 10mm separation.	172
Figure 105: Frequency response of simulated cantilever at 0.5g acceleration from 11mm to 18mm separation.	172
Figure 106: Frequency response of simulated cantilever at 1g acceleration from 3mm to 10mm separation.	173
Figure 107: Frequency response of simulated cantilever at 1g acceleration from 11mm to 18mm separation.	173
Figure 108: Frequency response of simulated cantilever at 2g acceleration from 3mm to 10mm separation.	174
Figure 109: Frequency response of simulated cantilever at 2g acceleration from 11mm to 18mm separation.	174
Figure 110: Frequency response of experimental prototype at 0.5g acceleration from 1mm to 5mm separation.....	175
Figure 111: Frequency response of experimental prototype at 0.5g acceleration from 6mm to 10mm separation.....	175
Figure 112: Frequency response of experimental prototype at 0.5g acceleration from 11mm to 15mm separation.....	176
Figure 113: Frequency response of experimental prototype at 0.5g acceleration from 15mm to 18.5mm separation.....	176

Figure 114: Frequency response of experimental prototype at 1g acceleration from 1mm to 5mm separation.	177
Figure 115: Frequency response of experimental prototype at 1g acceleration from 6mm to 10mm separation.	177
Figure 116: Frequency response of experimental prototype at 1g acceleration from 11mm to 15mm separation.	178
Figure 117: Frequency response of experimental prototype at 1g acceleration from 15mm to 18.5mm separation.	178
Figure 118: Frequency response of experimental prototype at 2g acceleration from 1mm to 5mm separation.	179
Figure 119: Frequency response of experimental prototype at 2g acceleration from 6mm to 10mm separation.	179
Figure 120: Frequency response of experimental prototype at 2g acceleration from 11mm to 15mm separation.	180
Figure 121: Frequency response of experimental prototype at 2g acceleration from 15mm to 18.5mm separation.	180
Figure 122: Acceleration Readings of Left Foot Sensor Placement.	181
Figure 123: "kick out" motion used from the walking movement.	182
Figure 124: Orientation of the accelerometer placed on the chest.	182
Figure 125: Acceleration Readings of Chest Sensor Placement.	183
Figure 126: Orientation of the accelerometer placed on the hand.	183
Figure 127: Acceleration Readings of Right Hand Sensor Placement.	184
Figure 128: Orientation of the accelerometer when placed on the ankle.	184
Figure 129: Acceleration Readings of Right Ankle Sensor Placement.	185
Figure 130: Acceleration readings based on channels for Left Foot movement.	186
Figure 131: Acceleration readings based on channels for Chest movement.	187
Figure 132: Acceleration readings based on channels for Right Hand movement.	187
Figure 133: Acceleration readings based on channels for Right Ankle movement.	188
Figure 134: Side by side comparison of acceleration values from different placement of the sensor from walking movement.	189
Figure 135: Side by side comparison of acceleration values from different placement of the sensor from jogging movement.	190
Figure 136: Side by side comparison of acceleration values from different placement of the sensor from high knees movement.	191

List of Tables

Table 1: Comparison of selected potential power sources. [4]	20
Table 2: Vibrational readings from various sources. [8]	22
Table 3: Human energy consumption for everyday activities. Derived from [9].	23
Table 4: Power consumption for selected medical sensors. [18] [19]	26
Table 5: Summary of commercially available sensor network nodes. [21]	28
Table 6: Two models of implantable medical transceivers from Microsemi.....	28
Table 7: Piezoelectric materials and corresponding properties.....	35
Table 8: Summary of comparison of different vibrational types of harvesting methods. [29]	38
Table 9: Output voltage with varying distances between magnets. [45]	48
Table 10: Max acceleration (g) with frequency for specific body movements at selected body parts.	61
Table 11: Variables and values used within the modelling process.....	87
Table 12: Parameters / variables used for the nonlinear cantilever model.	88
Table 13: Experimental results on "New" equilibrium points for selected distances of separation of magnets.....	90
Table 14: Behaviour observed from the simulations results.....	111
Table 15: Design specifications of the coils.	137

1.0 Introduction

The world is currently obsessed with “Energy” with the fear that one day; the earth might run out of fuel. This is true yet also untrue. The world might one day run out of fossil fuels, but it will not run out of energy as energy is indestructible; it cannot be created nor destroyed. It can only be converted from one type of energy to another. Hence so long as humans continue to find efficient methods to convert one type of energy to another, the energy crisis may just be held off slightly longer.

Many types of energy are available, as well as many sources of ambient energy available for “harvest” or “conversion”. Human power just so happens to be one of the sources available for “harvest”. Humans are huge storehouses of energy with huge amounts of energy being used daily even while resting from which a significant amount is wasted. Some devices have also been invented to actively or passively harvest a portion of this wasted energy [1] [2] to be reused.

With low powered electronics prevalent in current times, the ability to recycle energy efficiently and as conveniently as possible has arrived [3]. Daily movements that humans do such as walking, jogging and jumping do possess wasted energy. In an ideal situation, if a portion of the energy is recovered and used for something that would be able to improve the quality of life of the user. This is the main research motivation for using human movements as a source of energy for harvesting.

Along with all movements, along with vibrations, there will be accelerations and decelerations. These changes in accelerations can be harvested off or converted using a technique called Vibrational Energy Harvesting which has several methods that enables the process of harvesting energy through the process of energy conversion. One of which is through electromagnetic transduction where it uses magnets and coils to create electrical power, just like a simple dynamo!

In addition to that, nonlinear energy harvesting is an additional branch off the vibrational energy harvesting’s book. It provides more flexibility to the operational window of harvesting energy but is more complex compared to conventional / linear methods.

As human movements have no fixed frequency nor predetermined pattern, nonlinear energy harvesting seemed like a perfect fit along with the electromagnetic method of converting vibrational accelerations into electrical energy. In conclusion, this

research aims to verify this theory through theoretical simulations and experimental methods.

1.1. Research Aims

The aim of this research is, to evaluate the potential of a nonlinear electromagnetic energy harvester powered by human movements through a novel placement of the pick-up coil within the harvester.

To achieve this aim, the following research objectives were defined:

1. To determine the potential of “human movements” available in everyday motion for energy harvesting.
2. To investigate if nonlinear energy harvesting is a suitable technique (wider bandwidth) to be used for energy harvesting from human movements.
3. To investigate the potential of a novel placement of a pick-up coil within the nonlinear electromagnetic energy harvester.

1.2. Organisation of the Thesis

As the thesis contains multiple sections, the structure of the thesis is as follows.

Section 2 contain introduction and discussions regarding previous studies of energies available for harvesting as well as the technologies available for harvesting it. These sections provided an introduction to the research which along the way formulated goals for the project to achieve. Sections 3, 4, 5 and 6 contain the developments of the research which includes results obtained as well as discussions of each section. Section 7 summarizes the entire work and provides a conclusion but also poses ideas and questions for further work. The details of the sections 2 to 7 are presented below.

Section 2 introduces potential sources of energy that are available for harvesting with a special focus on human power. More details regarding human power are provided as well as currently available applications which are powered by human power. The section ends with an introduction to possible energy storage options for potential energy harvesting devices. Additionally, Section 2 introduces the theory of vibrational energy harvesting for which the energy harvester to be built will be based on. The section also introduces and compares the different technologies of conversion

which are available and selects the Electromagnetic method of conversion to be the choice of method of conversion. Continuing on, Section 2 also explores further theory regarding the chosen Electromagnetic energy harvesting technology. Existing devices which use such technology are also introduced. Finally, Section 2 concludes with the introduction of Nonlinear Energy Harvesting technology and work done by other authors.

Section 3 follows the introduction of human power from Section 2 and presents an experiment to determine the amount of accelerations available within normal daily human movements from four different locations on the body. The results obtained from the experiment are presented and discussed.

Section 4 investigates nonlinear energy harvesting which is an important element of the proposed research. The section then progresses towards the design and build of the nonlinear energy harvester prototype as well as the modelling requirements, parameters and process of it. The section concludes with simulation results and discussions from the model.

Section 5 verifies the simulation results obtained from the previous section. The prototype is subjected to the similar experimental process which was simulated in the previous section. This section also includes the calibration process of the vibrational shaker used to provide external accelerations to the prototype.

Section 6 proceeds further with the investigation of the power generation ability of the prototype energy harvester. It also includes the process of obtaining optimum power from the prototype system through an optimum selection of load attached to the prototype.

Section 7 summarizes and presents discussions that round up the entire work. The section also provides additional ideas and questions for further work as well as an overall conclusion to the whole research.

2.0 Overview of Energy Harvesting

This section explores the potential of Energy Harvesting while looking at sources that are available to harvest, especially the human body. This is due to one of the main objectives of this research being to look at the ability to harvest energy from human movements and applying the harvested energy to one if not several applications for example, powering medical sensors and telemetry systems.

That said, this research is mainly focussed on utilizing human energy as a potential source of power but an introduction of power from different ambient sources will be discussed and compared. Human power will be discussed more extensively in Section 2.2. These include possible energy sources within the human body as well as an introduction about the current applications using human powered energy harvesting devices.

A simple motivation to harvest energy from human movements is the desire to capitalise on the wasted and excess energy that humans spend on “moving” from location A to B. The “movements” are not limited or defined by only getting a person from A to B, for example: walking and running. The “movements” include all general movements by the human limbs, be it handshaking or the waving of hands. This provide challenges as everyone moves differently, additionally how will this technique harvest excess energy from the movement as efficiently and as unobtrusively as possible. Thus, a generic list of requirements for any potential human movement energy harvesting applications should typically contain these:

- To be able to work with the power harvested though human motions.
- To be able to be integrated with other electronics and possibly telemetry systems (Example: medical sensors or medical telemetry systems).
- To be able to run on very-low power configurations.
- Requires little to no maintenance.
- Safe for the person who are using the system.
- Dimensions and weight considerations of the energy harvesting system.

The list is neither exhaustive nor limited to the above and can be adapted to suit any applications that are being considered for potential use along with the ability of energy harvesting from human movements.

2.1 Power from Ambient Sources

Energy is defined as “the ability to do work” and the law of conservation of energy states that energy cannot be created or destroyed. It can only change its form from one to another, for example the change of chemical energy into potential energy and into kinetic energy. It also states that the total amount of energy in an isolated system cannot change. Hence, the world is a place full of energy and the trick is how to maximize the efficiency of this energy conversion process and recycle as much power as possible.

Table 1 shows power sources that are currently commercially available such as batteries as well as power from ambient sources such as air flow and temperature gradients. As with the vast size and power consumption reduction from sensors and all other kinds of electronics from earlier generations until current times, these power sources are tabulated with regards to its energy or power density to offer a better perspective on how much energy is available on any given size.

Power Source	P/cm ³ (μ W/cm ³)	E/cm ³ (J/cm ³)	P/cm ³ /yr (μ W/cm ³ /yr)	Secondary Storage Needed	Voltage Regulation	Off The Shelf
Non-Rechargeable Battery	-	2880	90	No	No	Yes
Rechargeable Battery	-	1080	34	-	No	Yes
Micro-Fuel Cell	-	3500	110	Maybe	Maybe	No
Heat Engine	-	3346	106	Yes	Yes	No
Radioactive (⁶³ Ni)	0.52	1640	0.52	Yes	Yes	No
Solar (Outside)	15000*	-	-	Usually	Maybe	Yes
Solar (Inside)	10*	-	-	Usually	Maybe	Yes
Temperature	40**	-	-	Usually	Maybe	Soon
Human Power	330	-	-	Yes	Yes	No
Air Flow	380***	-	-	Yes	Yes	No
Vibrations	200	-	-	Yes	Yes	No

*Denotes sources whose fundamental metric is power per **square** centimetre rather than power per **cubic** centimetre.

**Demonstrated from a 5 °C temperature differential

***Assumes air velocity of 5m/s and 5% conversion efficiency.

Table 1: Comparison of selected potential power sources. [4]

Non-rechargeable batteries are usually manufactured from battery chemistries such as Alkaline, Lithium or even Zinc-Air. Primary batteries usually possess a higher energy density (2880 J/cm^3) compared to secondary batteries and have relatively stable voltage output hence are widely used to power electronics. However, due to the relatively short life span and single use capacity, a replacement is needed once the power generating chemistry in the battery runs out. This proves to be a problem environmentally in how to dispose of the batteries as the chemicals from many batteries are toxic. Secondary batteries do not eliminate this issue completely but help alleviate it by being able to be recharged after running out of power. Common rechargeable battery chemistries are Nickel-cadmium (Ni/Cd), Nickel-metal Hydride (Ni/MH) and Lithium-ion. The power density of these batteries is lower (1080 J/cm^3) than of primary batteries but they will last a lot longer in the long run. Secondary batteries generally have higher up-front costs than of primary batteries but are more cost effective in the long term.

The Micro-Fuel Cell, the heat engine and also a radioactive power source is not something that can be purchased commercially. Micro-fuel cells are generally specially made for certain applications (power campervans or yachts) by using different types of battery chemistry and technology. Capacities and lifetime of use can differ from one manufacturer to another as well as what materials and technology are used to manufacture them. Larger types of fuel cells however have been used as power sources for a certain period of time but micro-fuel cells are starting to slowly emerge onto the market now [5]. The heat engine and any type of radioactive power source are types of power sources that are neither easily manageable nor maintained. These possess high energy densities but at a small scale, the heat engine is not an efficient method.

Solar cells on the other hand are very common nowadays with power harvested from the sun used for many applications. Solar cells even used on a mass scale as a method of reducing reliance on non-renewable energy sources or even used as a stand-alone power source. On a sunny day, power density from solar radiation on the earth's surface is around 100 to 150 mW/cm^2 and modern solar cells offer efficiencies ranging from about 15% to 20% [6]. Furthermore, if used indoors the power measured or obtained will decrease significantly even though the light source maybe only a few inches away from the solar cells.

Temperature gradients can be used naturally as a source of energy but conversion efficiency is limited to the Carnot efficiency which is given as:

$$\eta = \frac{T_{high} - T_{low}}{T_{high}} \quad \text{Equation 2.1}$$

Where T_{high} is the absolute higher temperature on one side of the harvesting device and T_{low} is the absolute lower temperature on the other side. The greater the temperature difference, the higher the efficiency will be for the energy conversion.

Wind power has also been commonly used on a large scale since the days of windmills and is not commonly used on a small scale. The available power from moving air can be described as:

$$P = \frac{1}{2} \rho A v^3 \quad \text{Equation 2.2}$$

Where P is the power, ρ is the density of air, A is the cross sectional area of the wind turbine blade swept area and v is the air velocity. Current technologies allow large scale windmills to operate at around 40% efficiency and no more than 59% [7] but efficiency is dependent on wind velocity. They are typically designed to run at maximum efficiency at wind speeds of around 18mph and tend to show an average efficiency of around 20% [4].

Lastly, ambient vibrations are present in many types of environment. The ability to convert this into use depends on its amplitude and frequency. Ooi [8] compiled a list of vibrating objects with the respective acceleration amplitudes and frequency of the vibration source.

Vibrating Source	Acceleration (m/s ²)	Fundamental Frequency F _{re} (Hz)
Car engine compartment	12	200
Second floor of busy office	0.2	100
Windows next to busy road	0.7	120
Bread maker	1.03	121

Washing machine	0.5	109
Blender casing	6.4	121
Clothes dryer	3.5	121
Small microwave oven	2.5	121
HVAC vents	0.2-1.5	60
Desktop computer casing (Top of casing)	0.5	120
Desktop computer casing (with CD Rom running)	0.54	120
Fan heater	1.5	34
Mobile phone vibration	12.3	170
Domestic freezer	0.1	50

Table 2: Vibrational readings from various sources. [8]

Ooi's compilation shows the frequencies recorded ranged from 34Hz up to 200Hz and acceleration amplitudes go from 0.1 to 12.3 m/s² from the different sources. It also has to be noted that all vibrations do not only happen at a single frequency but are made up from a number of fundamental frequencies as well as their harmonic frequencies. In essence, a vibrational energy harvester that is tuned to accept these frequencies will be able to harvest and "recycle" a portion of the available power that is available from the vibration source.

2.2 Human Power

As this research is focussed on trying to harvest power through the accelerations (vibrations) generated by human movement. The human body is actually a storehouse filled with tremendous energy. The energy in a gram of fat represents 9 dietary Calories which equals to 9000 calories or 37,700J per gram of fat [9]. So an average person of about 68kg and with 25% of body fat will have about 641MJ available.

Activity	Kilocal/hr	Watts
Sleeping	70	81
Lying Quietly	80	93
Sitting	100	116
Standing At Ease	110	128
Conversation	110	128
Eating Meal	110	128
Strolling	140	163
Driving Car	140	163

Playing Violin or Piano	140	163
Housekeeping	150	175
Carpentry	230	268
Hiking at 4mph	350	407
Swimming	500	582
Mountain Climbing	600	698
Long Distance Run	900	1048
Sprinting	1400	1630

Table 3: Human energy consumption for everyday activities. Derived from [9].

From Table 3, while the power consumption from each of the everyday activities seems high, the harvestable energy from those motions is much lower if compared to the expended energy.

Figure 1 shows the potentially available power for harvesting through certain activities [9] with elaborations on selected sections.

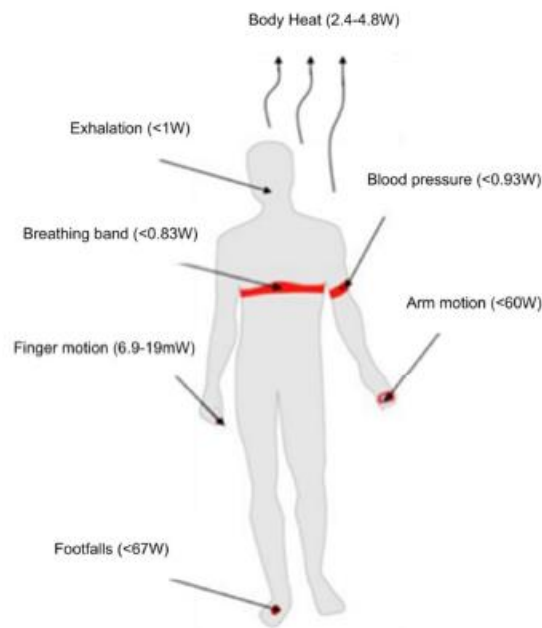


Figure 1: Potentially harvestable energy from selected human motions. Total power for each action is included in the parenthesis. [9]

Firstly, breathing is an action that humans perform involuntarily. It enables oxygen to be transported to vital organs of the body to enable proper functionality. Even plants need to “breathe” to maintain their daily functions. Assuming a normal person has an approximate air intake of about 30 litres per minute [10], findings from Paradiso et al [9] shows that there is a potential available power of 1W, however using breathing figures published from the University of Notre Dame [11] brings the available power down to 0.24W. Other authors have also shown only 3uW was harvested off using changes of breath pressure from a user wearing a respirator mask [12].

Human body heat has also been looked at as an area of potential energy source. However, the efficiency of this method of heat recovery is extremely low and it puts a limit on how well it can be recovered. Carnot efficiency defines that limit [13]. The higher the difference of temperature between the body and its environment, the higher the efficiency is. Assuming ambient temperature of 20°C would provide 7W of power. It should also be noted that the timing of extracting of the user's body heat is very important. If the user is undergoing strenuous activities which results in the rise of core body temperature, then it is an ideal situation to be trying to harvest the excess body heat and also cool them at the same time. But if the situation is reversed and the user's body is barely generating enough heat to keep them warm, trying to harvest the user's body heat is not ideal and will result in the user feeling cold or in extreme cases, falling into hypothermia (body temperature falling below 35°C) or even leading to fatality.

Walking is another movement that humans do that are seen as a potential source for energy harvesting. Each step from a walk is typically broken down into a "heel strike" and a "toe lift off". A heel strike motion is understood to typically have a 5cm fall in vertical distance of a heel in the human gait [14]. So a person of 68kg walking at two steps a second would have 67W of power available from each heel. However, utilizing the full 5cm stroke would result in significant load and discomfort on the user. In order to be realistic, the compression of the shoe heel should be similar to that found in normal footwear. A heel compression of 1cm is comparable to a padded running shoe [15] [16].

2.2.1 Summary of Human Power

The human body does indeed have a lot of potential to have energy harvested from to be converted into electrical energy for various applications. However, great care must be exercised during the design phase of these systems to ensure that the benefits outweigh its disadvantages and be able to fulfil its potential.

Harvesting energy from insides of a person will inevitably be more complex than trying to harvest energy externally from a person (examples: arm and leg movement and also body heat). However, it may potentially be more efficient owing to the systems being implanted or embedded into the user's body, eliminating external variations. The reverse could be said for external harvesting of human energy. Detachable systems that fit onto a person's skin harvesting off arm or leg motion or

even body heat will be a little less tricky but may pose a problem to the user's convenience depending on its application as well as the efficiency of the whole energy harvesting system. It all depends on how the application is applied to the situation.

However due to ethical issues related to the implantation of devices within the human body, this research will only focus on harvesting energy externally from movements such as walking, jogging and high-knees. The next section discusses about the currently available applications that are powered by human energy harvesting, mainly within the health and medical context.

2.2.2 Potential Applications of Human Energy Harvesting

With the availability of many types of human powered energy harvesting methods, the combination of applying the right applications to pair with the right locations of human energy sources is equally as important as the method of harvesting energy itself. As the power source is the human body, any power harvested would be logical to be used for improving quality of life. Hence this section looks at applications within the health and medical sector which helps aid the user through pervasive health monitoring.

Applications for Human Energy Harvesting are commonly split into two sections [17]: Energy Harvesting inside the body or Implantable devices and Energy Harvesting outside the body or referred to as On Body Monitoring or even called Body Sensor Networks. Both sections present different challenges but share a common goal in improving pervasive health monitoring and quality of life. Both types of application also share a common theme of data transfer method, wireless data transfer technology. However, this research only focusses on external application of energy harvesting.

The need for wireless data transfer for implantable devices is clear as it is medically unsatisfactory and unsafe to have physical wires pass through under the skin. The wires could potentially cause medical complications to the patient and in severe cases, lead to fatalities. A second argument is the convenience that wireless data transfer brings into the application. Hence, an ideal situation that human energy harvesting brings is an application that enables health monitoring in a fit-and-forget package.

2.2.2.1. Applications of Energy Harvesting Outside the Body or Wearable Body Sensor Networks

From the title of this subsection, it is opposite to implantable devices where as these devices can be worn or attached to patients to monitor vital signs or other indicators. The Body Sensor Networks are an advanced version with similar overlap which are commonly used by first responders. They collect data from vital signs and are wireless and intelligently processed to provide a view of the patient’s health at any particular point. This could enable remote health monitoring or even intervention in certain cases and could be particularly helpful to patients who are suffering from chronic diseases such as diabetes, asthma and heart attacks.

It is hoped that these devices would enable:

- Point of care diagnostics
- Remote Telemonitoring
- Chronic disease self-management
- Delivery of personalised care and treatment
- New insights into disease progression
- Post-operative recovery monitoring away from hospital

However, general medical sensors or devices are not designed for wireless use and in many cases are not optimised for low power requirements. Table 4 presents power consumption requirements for selected commonly used medical sensors. Note that commercial health sensors generally have a much higher power consumption as they commonly rely on batteries as a main power source.

Device	Power Requirements
Wearable Electrocardiogram (EEG)*	0.5-1 mW
Pulse oximeter (SpO2 sensor)*	62-90 μ W
Hearing aid*	1 mW
Electrocardiogram (ECG)**	200-300 mW
Blood Pressure**	3.75W (Pump Running); 200-300 mW (Nominal)
Oximetry with pulse monitoring**	20-60 mW
Temperature**	50-75 mW

Table 4: Power consumption for selected medical sensors. [18] [19]

** Commercial medical sensors that are not specifically designed for use as wearable health sensors. * Power consumption depending on sample rate.

2.2.2.2. Telemetry Systems

Sensors are used to sense and read a patient's data in selected categories but if the data cannot be transmitted to be processed then the data is useless. Telemetry systems are designed and used to provide a platform for the data collected by the sensors from the patient to be sent out into a system as securely as possible as well as accurately whilst using minimal power. Ideally, such systems would be wireless.

Wireless based medical sensors network are the current trend in trying to acquire patient data within an enclosed area such as a hospital. However, putting sensors and telemetry systems on a moving patient without addressing the power requirements of the electronics involved will defeat the purpose of such systems. While batteries are used in all kinds of mobile electronics, replacements are needed when power is depleted. Thus a sensor and telemetry system that is maintenance free would be ideal.

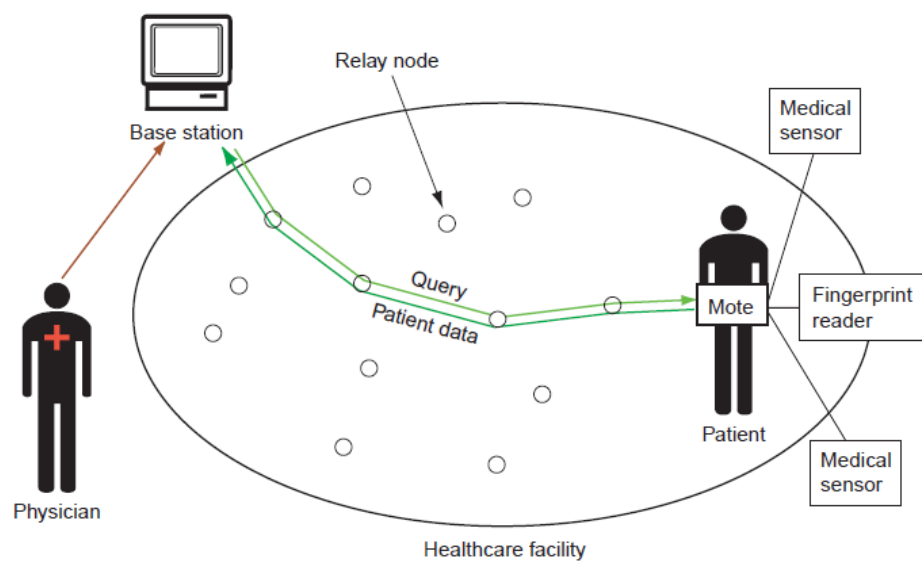


Figure 2: An example architecture of wireless health monitoring system. [20]

Figure 2 shows an example of how wireless medical sensors systems would work. Additionally, a mesh of medical sensors can be placed within the telemetry system which can be implemented along the applications that are shown in Section 2.0, even fingerprint recognition devices may be implanted in this system as well. The data from the mesh of sensors can then be transmitted to a base station/mainframe where this

could potentially improve the quality and use of the information available to health professionals. In this example, a mote is a low powered computing device with a radio [20] that will send data over to the main system which will be monitored by healthcare professionals within the hospital. These systems should be secure, with the ability to verify the authenticity of the patient data while also being able to run on power harvested from human motion. In extreme cases, the systems should have a power back-up system to ensure that 100% up-time of these important systems. Table 5 presents a summary of a selection of commercially available sensor network nodes by Gilbert and Balouchi under certain operating conditions. [21] The average power value is given by 1% TX and RX transmission time, 10% processing time and ‘sleep’ for the remaining time.

	Crossbow MICAz ^[27]	Intel IMote2 ^[28]	Jennic JN5139 ^[29]
Radio standard	IEEE 802.15.4/ZigBee	IEEE 802.15.4	IEEE 802.15.4/ZigBee
Typical range	100 m (outdoor), 30 m (indoor)	30 m	1 km
Data rate (kbps)	250 kbps	250 kbps	250 kbps
Sleep mode (deep sleep)	15 μ A	390 μ A	2.8 μ A (1.6 μ A)
Processor only	8 mA active mode	31–53 mA*	2.7+0.325 mA/MHz
RX	19.7 mA	44 mA	34 mA
TX	17.4 mA (+0dbm)	44 mA	34 mA (+3 dBm)
Supply voltage (minimum)	2.7 V	3.2 V	2.7 V
Average	2.8 mW	12 mW	3 mW

*Consumption depends on clock speed selected between 13–104 MHz

Table 5: Summary of commercially available sensor network nodes. [21]

Furthermore, two types of implantable medical transceivers available from Microsemi that can be used for surgical procedures that requires wireless data transmission within the human body. These are presented in Table 6.

Model Number	Use	Power Consumption
LX1802 [22]	Implantable Cardiac Defib	<2 mA
ZL70102 [23]	<ul style="list-style-type: none"> • Cardiac Rhythm Management • Neurostimulators • Drug delivery, sensors and diagnostics • Body Area Network using 433MHz ISM Band 	5 mA for continuous TX/RX 1 mA idle

Table 6: Two models of implantable medical transceivers from Microsemi.

This show that to have a complete “application” that enables health and medical monitoring with energy harvested from human power, consideration needs to be placed in not only the sensing section of the application, but also the ability to transfer the

collected data from the patient or wearer onto an external or main system as data analysis of that information is as important as the sensing section. Power consumptions of various different transceivers need to be taken into account during the application design phase to enable a 'complete' package from the application.

2.2.3. Summary of human power

As presented throughout the section, mankind has been trying to recycle and reuse Energy through various mediums and methods. There are many ambient sources of energy available for harvesting or scavenging but human power is chosen within this research with an aim of hoping to improve the quality of life with applications that use the power that is harvested. By taking the harvested power and applying it within the health and medical sector, the technique and the speed of how new information or knowledge are discovered can be improved and shortened which, in turn, improves the quality of lives of many.

To achieve the goal of successfully harvesting off human power, many components are needed. A source or location that is suitable, the method or technology of harvest, the processing and analysis of the information available, the power storage and telemetry options of the harvester and all other mechanical and electronic components that make the harvester a complete system. All components have to in the right order to be able to successfully harvest power from a human to be used for applications that will improve the quality of life of many. And by looking at the applications that are currently available, mankind are taking small steps in achieving that goal.

2.3. Vibrational Energy Harvesting

To be able to effectively understand and utilize human movement energy harvesting, factors that will affect the efficiency of how the system converts human movements into electrical energy has to be introduced and understood. This section presents the basic model of vibration to electric transduction as well as different types of transduction techniques and will discuss available devices further along the section.

There are several types of transduction methods that are suitable for the conversion of vibration to electric model. The transduction methods will be compared with the advantages and disadvantages of each method discussed briefly.

2.3.1. Model of a Vibration to Electric Transducer

This section describes a generic model proposed by Williams and Yates [24] that converts kinetic energy of a vibrating seismic mass into electrical energy. The model shown in Figure 3 consists of a seismic mass, m , mounted on a spring with stiffness, k . When the transducer is vibrated at a displacement of $y(t)$, the seismic mass moves out of phase with the transducer housing, hence there is a net movement, $x(t)$, between the mass and housing.

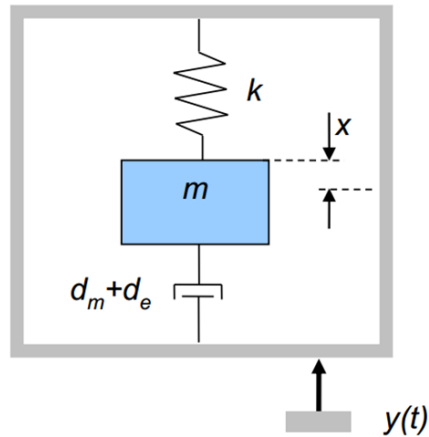


Figure 3: Schematic diagram of the transducer.

The mechanical energy conversion process from mechanical energy to electrical energy can be expressed by d_m , which damps the mass while d_e , expressed as the electrically induced damping from the electro-mechanical conversion process. This transducer is also an inertial device which means it only needs one point of attachment to a vibration source.

Williams and Yates also made an assumption which the seismic mass of the transducer is negligible when compared to the seismic mass of the vibrational source. Additional assumptions include the vibrational source energy is infinite and will not be affected by the transducer's movement. As mentioned previously, if the transducer is vibrated with a displacement of $y(t)$, the differential equation of the motion is described as:

$$m\ddot{x}(t) + (d_m + d_e)\dot{x}(t) + kx(t) = -m\ddot{y}(t) \quad \text{Equation 2.3}$$

where m is the seismic mass of the transducer, d_m and d_e is the damping constant and k is the spring constant. The force on the mass is also equal to the transducer (mass-spring-damper) system and with a sinusoidal amplitude vibration is:

$$f(t) = -m\ddot{y} = Y \sin(\omega t) \quad \text{Equation 2.4}$$

The steady-state solution for $x(t)$ in Equation 2.4 can be written as:

$$x(t) = \frac{\omega^2}{\sqrt{\left(\frac{k}{m} - \omega^2\right)^2 + \left(\frac{(d_e + d_m)\omega^2}{m}\right)^2}} Y \sin(\omega t) \quad \text{Equation 2.5}$$

The instantaneous kinetic power transfer to the mass, $p(t)$ is the product of the force on the mass and its velocity:

$$p(t) = -m\dot{y}(t)[\dot{y}(t) + \dot{x}(t)] \quad \text{Equation 2.6}$$

For a sinusoidal excitation vibration as defined in Equation 2.4, the total power dissipated at the damping elements can be expressed as:

$$P_{diss} = \frac{m\xi_T Y^2 \left(\frac{\omega}{\omega_n}\right)^3 \omega^3}{\left[1 - \left(\frac{\omega}{\omega_n}\right)^2\right]^2 + \left[2\xi_T \left(\frac{\omega}{\omega_n}\right)\right]^2} \quad \text{Equation 2.7}$$

where ξ_T is the total damping ratio:

$$\xi_T = (\xi_e + \xi_m) = \frac{d_T}{2m\omega_n} \quad \text{Equation 2.8}$$

where $d_T = d_m + d_e$ which is the total damping coefficient and ω_n which is the resonant frequency of the system. If the excitation frequency is tuned to the resonant frequency of the transducer, maximum energy can be harvested. The resonant frequency is given by:

$$\omega_n = \sqrt{\frac{k}{m}} \quad \text{Equation 2.9}$$

Hence, when $\omega = \omega_n$, maximum power can be described as:

$$P_{diss} = \frac{mY^2\omega_n^3}{4\xi_T} \quad \text{Equation 2.10}$$

Equation 2.10 can be rewritten when displacement Y is substituted with acceleration A , $A=Y\omega^2$. This yields Equation 2.11.

$$P_{diss} = \frac{mA^2}{4\omega_n\xi_T} \quad \text{Equation 2.11}$$

In Equation 2.11, maximum power at resonant frequency is inversely proportional to the damping ratio, the lower the damping ratio, the higher the power at resonant frequency. In an ideal case, zero damping would be desired as that would provide infinite power. That however is not possible in reality. Hence maximum amount of power that can be generated is finite and is down to its designs governed by the size and geometry of the transducer.

In order to reduce the transducer's damping ratio $\xi_T = (\xi_e + \xi_m)$ to as low as possible, wasted damping or also known as parasitic damping ξ_m caused from friction or air resistance during the energy conversion process has to be as low as possible. ξ_e is defined electrical damping and when $\xi_e = \xi_m$, the equation can be rewritten as:

$$P_{damp} = \frac{m\xi_e A^2}{4\omega_n(\xi_m + \xi_e)^2} \quad \text{Equation 2.12}$$

Additionally, Roundy [25] also proved that power is maximized when $\xi_m = \xi_e$. However, Roundy also proved the generator shows weak results or has a large penalty when $\xi_m > \xi_e$ while if the condition is reversed into $\xi_m < \xi_e$, there is only a small

penalty for the power available. Therefore, a high electrically damped system will only show slightly lower output compared to a light electrically damped system.

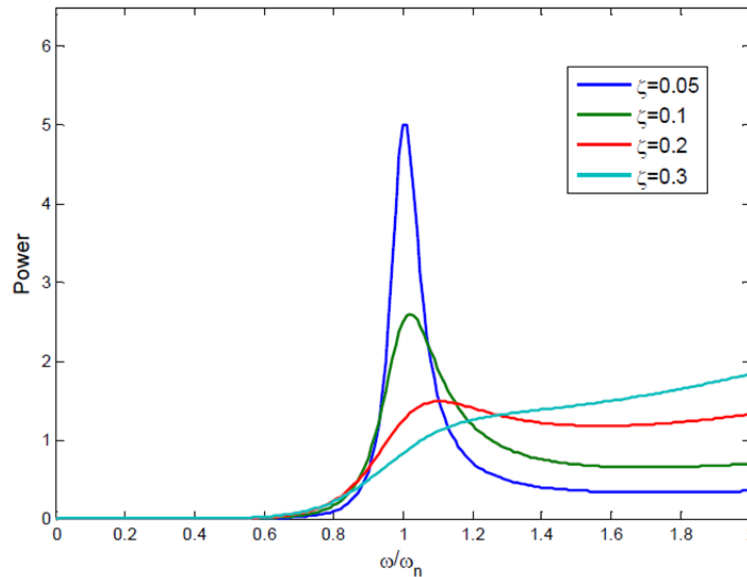


Figure 4: Frequency spectrum of power generated around resonance frequency with different damping factors. [26]

Figure 4 shows the power output for the different damping factors that was used around resonance frequency for the model described. It is clearly shown that when the total damping factor is increased, the output power of the system is greatly decreased while increasing the bandwidth response. While a system with lower total damping factor will have the potential for a higher power output, the output power also drops off very quickly as it moves away from its resonance frequency, limiting bandwidth. In certain configurations, it also showed when a system is off its resonance frequency by about 20%, power output drops about 80%. This highlights the importance of matching the design of the generator system to have a frequency response that matches its resonance frequency fairly easily whilst the source is a sinusoidal vibrating source. Lastly, Williams and Yates also note that this model is likely to produce more power in applications where the source vibration frequency is high compared to poor performance in low frequency applications. [24]

2.4. Comparison of Different Methods of Vibration to Electric Transduction

Here we are comparing three types of transduction models for converting vibrational kinetic energy to electrical energy. The three methods are:

- Electromagnetic
- Piezoelectric
- Magnetorestrictive

and each method have individual advantages and disadvantages that will be described to provide a better understanding of how each method can be best suited to certain applications.

2.4.1. Electromagnetic Transduction

In a sentence, an electromagnetic transducer for a vibrational energy harvester has a magnet attached to the mass of the transducer or generator and will be able to produce a voltage with a coil attached to the system as the magnet moves.

This method has several advantages as it does not need the use of any smart material, for example a piezoelectric film that will be able to produce electrical power when it is compressed. Secondly, this system does not need any type of external voltage source or excitation voltage to enable the system to work. As long as the arrangement of the magnet and coil is suitable, the system will work. Thirdly, if designed carefully, this type of system will be able to work without any mechanical contact or friction between the parts that are required for this system to function properly. This will in turn increase reliability as well as prolong its “shelf-life” and also decrease the all important factor of its mechanical damping to an absolute minimum with no mechanical moving parts.

However, there are certain limitations to this method of transduction too. This method of transduction usually involves a substantial dimension or size when compared to other method of transduction as each system will have to accommodate the inclusion of the magnets and the pick-up coil. This is limited to how the electromagnetic harvesters are designed as well as fabrication technology too. William and Yates’s design of the microgenerator of a size of 5mm x 5mm x 1mm is predicted to produce 0.1mW at 330Hz [24]. Another design with a volume of 0.15cm³ producing 46μW at 52Hz was achieved by Beeby and his colleagues [27]. Another disadvantage of this method of transduction is its difficulty in integrating itself with microsystems primarily

of the Micro-electro-mechanical systems (MEMS) group due to cost and size issues. For example, micro magnets are hard to manufacture and costly, additionally these systems usually need a large mass displacement on the system to achieve sufficient power generation.

But the output from these systems can be increased when a stronger magnetic field is provided as more current will flow through the coil during the movement of the magnets around the coil. Output will also be increased if coil conductivity is improved as it lowers the internal resistance of the system and in turn also lower its power losses for a more efficient system.

2.4.2. Piezoelectric Transduction

Piezoelectric transducers are pretty straight forward, they do not require any form of external voltage source as the piezoelectric material that is used will convert the mechanical strain into electrical power. It can also be packaged into pretty compact footprints or small dimensions which is suitable for use with MEMS. Also, there is generally fewer or no mechanical parts on a piezoelectric transducer thus generating a very low mechanical damping.

On the contrary, a piezoelectric transducer with thin film piezoelectric have relatively low electromechanical coupling coefficient and large loads impedances are usually required to enable the system to be working in an optimum state.

There are piezoelectric materials that are being used quite commonly currently and two of the materials are mentioned by Kim, Tadesse and Priya [28] that possesses high energy density are the PVDF piezoelectric polymer and the relaxor piezoelectric single crystals, PZN-7%PT. The piezoelectric properties of the two materials are listed in Table 7.

Material	d_{33} (pC/N)	ϵ_{33}/ϵ_0	g_{33} (m ² /C)
PVDF	33	13	286.7×10^{-3}
PZN-7%PT	2500	6700	42.1×10^{-3}

Table 7: Piezoelectric materials and corresponding properties.

Table 7 shows that the PVDF piezoelectric polymer possesses the highest piezoelectric constant g_{33} of 286.7×10^{-3} m²/C while the relaxor based piezoelectric single crystals have the highest product of (d_{33}, g_{33}) of 1.0525×10^{-10} m²/N. However,

due to the high costs and the difficulty in synthesizing the single crystals and polymers, current mass applications are focussed on improving the properties of polycrystalline ceramics.

2.4.3. Magnetostrictive Transduction

Magnetostrictive energy harvesters are relatively new compared to the other types of energy harvesters or transducers. It basically is a process of magnetization that causes the material to change its shape or dimension. During this change, the material's magnetic flux density changes which, in turn generate an induced voltage.

There are two commonly used magnetostrictive materials (MsM) namely a crystalline alloy Terfenol-D and also an amorphous metallic glass Metglas 2605SC. Wang [29] evaluated the Metglas 2605SC and was able to list several advantages of this method of transduction. Firstly, it was stated that the Metglas material was capable of being annealed under a strong transverse magnetic field in its width direction hence improving the magnetomechanical coupling coefficient to > 0.9 as well as the ability to reduce the footprint of this transducer in this situation.

However, several challenges of this method of transduction were also noted. As a coil is needed within the transducer system, it complicates things when trying to integrate with MEMS and certain types of magnetostrictive materials may need bias magnets within their system too.

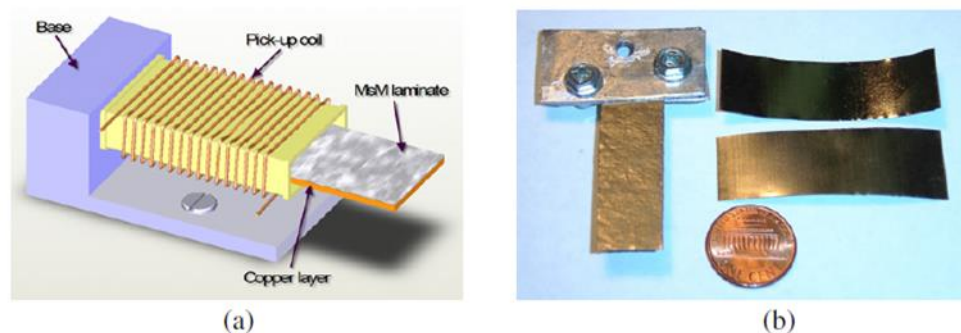


Figure 5: (a) Prototype of the magnetostrictive transducer by Wang, (b) Metglas 2065SC and laminate. [29]

There have also been findings of researchers combining piezoelectric materials and magnetostrictive materials together in a single transducer to evaluate if it is a better option. Dai [30], evaluated a vibration energy harvester that combined magnetostrictive material with piezoelectric material in a Terfenol-D/PZT/Terfenol-D sandwich and the

prototype achieved a load power of 1.055mW at 51Hz. Lafont [31] on the other hand combined two sheets of PZT-5 piezoelectric material with a sheet of Terfenol-D magnetostrictive material. Using a magnetic field that rises to 0.3T, causing the magnetostrictive material to change its shape and in turn, channel that change onto the piezoelectric material which produced a maximum of 214V and generated 95 μ J of energy. This shows by smartly combining piezoelectric materials which require mechanical strain to generate electrical power with magnetostrictive materials, the designs of the energy harvesters could be improved to eliminate the need for a pick up coil in pure magnetostrictive transducers.

2.4.4. Summary of transduction methods

The above discussion presents all three types of vibration to electric transduction methods. The primary purpose of performing this comparison is to be clear about what type of methods may be suitable for narrowing the range of design possibilities before performing detailed design, performance analysis and further optimization.

Primary advantages and disadvantages of each type of transduction method have been laid out in Table 8. This table shows that the piezoelectric method of transduction exhibits similar as the electromagnetic method of transduction whilst being able to provide higher output voltages. On the contrary, the materials and characteristic behaviours from the electromagnetic method of transduction are suited to this research's potential frequency range as well as the size of the prototype to be built which will be discussed further in later sections. This led to the decision to select electromagnetic as the method of transduction for the energy harvester that will be tested. The electromagnetic method of transduction will also be designed to operate in a nonlinear fashion which will be introduced and discussed in subsequent sections.

Type	Advantages	Disadvantages
Electromagnetic	<ul style="list-style-type: none"> - No smart materials required - No external voltage source 	<ul style="list-style-type: none"> - Bulky size: magnets and pick-up coils - Difficult to integrate with MEMS
Piezoelectric	<ul style="list-style-type: none"> - No external voltage source - High voltages: 2-10V - Compact configurations 	<ul style="list-style-type: none"> - Depolarization - Brittleness in bulk piezolayer - Poor coupling in piezo-film

	- Compatible with MEMS	(PVDF)
	- High coupling in single crystals	- Charge leakage - High output impedance
Magnetostrictive	- Ultra-high coupling coefficient >0.9	- Nonlinear effect
	- No depolarization problem	- Pick-up coil
	- High flexibility	- May need bias magnets
	- Suited to high frequency vibration	- Difficult to integrate with MEMS

Table 8: Summary of comparison of different vibrational types of harvesting methods. [29]

Lastly, although different methods of vibration to electric transduction have been introduced in this section, only the electromagnetic method will be considered and discussed further in detail in following sections.

2.5. The Electromagnetic Energy Harvester

In Section 2.4.1, the electromagnetic method of transduction from vibrational energy to electrical energy was introduced. As the electromagnetic method of transduction was chosen, this section will discuss in greater detail from a theoretical standpoint of the method of transduction and will also about currently available electromagnetic energy harvesters.

Electromotive force (emf) is produced when a conductor is moved through or exposed to varying levels of magnetic fields (flux). This phenomenon is called the electromagnetic induction named after Michael Faraday as Faraday's Law of electromagnetic induction and it is proportional to the time rate of change of the magnetic flux within the circuit. This law applies to either the changes in magnetic flux itself or the movement of the conducting material and can be described as:

$$V = -\frac{d\Phi_B}{dt} \quad \text{Equation 2.13}$$

Where Φ_B is the magnetic flux flowing through the circuit and the electromotive force (emf) is displayed with the unit Volts(V). The direction of the emf is given by Lenz's law.

For a coil to be moving through a perpendicular constant magnetic field, the maximum open circuit voltage across the coil can be expressed as:

$$V = NBl \frac{dx}{dt} \quad \text{Equation 2.14}$$

Where N is the number of turns in the coil, B is the strength of the magnetic field, l is the length of the winding of the coil and x is the relative distance or displacement between the coil and magnet.

In most situations, the motion between the coil and magnet is only on one axis. It can also be said that emf is proportional to the moving velocity when the coil is moving

through the magnetic field. Hence, by increasing the length and also number of turns on the coil will result in an increase of emf. However, the interaction between the induced current and the magnetic field generates an electromagnetic force, F_{em} to which by acting against it enables the mechanical energy to be transformed into electrical energy. The electromagnetic force can be described as:

$$F_{em} = D_{em} \frac{dx}{dt} \quad \text{Equation 2.15}$$

Where D_{em} is the electromagnetic damping and should be maximised in the design of the generator to extract maximum power coming from R_L which is the load resistance connected from the coil. Instantaneous power is obtained by the product of Equation 2.15 and velocity shown in Equation 2.16

$$P_e = F_{em}(t)dx(t)/dt \quad \text{Equation 2.16}$$

Power is dissipated in the coil and load impedance and equating the power dissipation from the electromagnetic force gives:

$$F_{em} \frac{dx}{dt} = \frac{V^2}{R_L + R_c + j\omega L_c} \quad \text{Equation 2.17}$$

Where R_L and R_c are the load and coil resistances and L_c is the coil inductance. Using Equation 2.13 and Equation 2.15 and substituting into Equation 2.17 to obtain the expression for electromagnetic damping which can then be expressed in Voltage as:

$$D_{em} = \frac{1}{R_L + R_c + j\omega L_c} \left(\frac{d\Phi}{dx} \right)^2 \quad \text{Equation 2.18}$$

From Equation 2.18, it is clear that to increase the output, the magnetic field (flux) around the coil has to be higher or the coil impedance has to be lowered. The change of magnetic field is dependent on the magnets that are used as well as the

arrangement, the size and also the location of the coil. Coil impedances are influenced by the number of turns in them as well as coil material such as wire winding and micro-fabrication.

2.5.1. Existing Electromagnetic Harvesters in Micro/Wafer Scale Implementations

As the electromagnetic transduction method has been widely used in recent years, many variations and types of electromagnetic harvesters have been designed and tested by researchers. A typical principle is when the generator or transducer is subjected to external vibrations, the mass within the generator moves vertically out of phase with the generator itself producing a net movement between the coil and the magnet. This behaviour produces electrical energy.

Williams and Yates's design produced a microgenerator of 5mm x 5mm x 1mm dimensions and was capable of producing $1\mu\text{W}$ at 70Hz with its mass displacement at $\pm 50\mu\text{m}$. The design was also capable of producing $100\mu\text{W}$ at 330Hz [24]. The model exhibited a behaviour called hard-spring effect. It effectively raises its resonant frequency when excitation amplitude is increased. It was showed that a low damping factor was required to improve and maximize power generation.

Another design based on the same model by Huang was presented and showed to generate $0.16\mu\text{W}$ from a 'finger tap' excitation. The system presented aimed at obtaining power from human motion. Resonant frequency of Huang's system was 100Hz but with an excitation input amplitude of $50\mu\text{m}$, the output could be ramped up to $1.4\mu\text{W}$ [32].

A group from University of Barcelona was also able to produce a system based on electromagnetic method of transduction. They had a Neodymium Iron Boron magnet bonded to polyimide membrane to form a spring-mass system producing $1.44\mu\text{W}$ with an excitation displacement of $10\mu\text{m}$ while having a resonant frequency of 400Hz. However, the maximum output was not possible due to poor assembly and thus introducing a much higher parasitic damping compared to the electromagnetic damping to the system [33]. A later update was provided by the group [34], this time using a Kapton membrane in the spring-mass element provided an improved power output of $55\mu\text{W}$ at 380Hz from $5\mu\text{m}$ of excitation amplitude. However, the updated design did not completely eradicate the problems faced by the initial design. The updated design

still demonstrates stress stiffening as well as potential creep and fatigue failure from the use of polymer membranes.

One of the main limitations of microscale or wafer electromagnetic generators is the limited number of coil turns physically possible with integrated circuit technology. To get round this limitation, Beeby [35] attempted to integrate a traditionally wound coil within a micro-machined silicon structure. The device created included using four Neodymium Iron Boron (NdFeB) magnets, a silicon cantilever beam supporting a ‘paddle’ which houses the 600 turn coil and sandwiched between two Perspex chips as shown in Figure 6. The device managed to generate 21nW of electrical power from an acceleration level of 1.92 m/s^2 with a resonant frequency of 9.5 kHz.

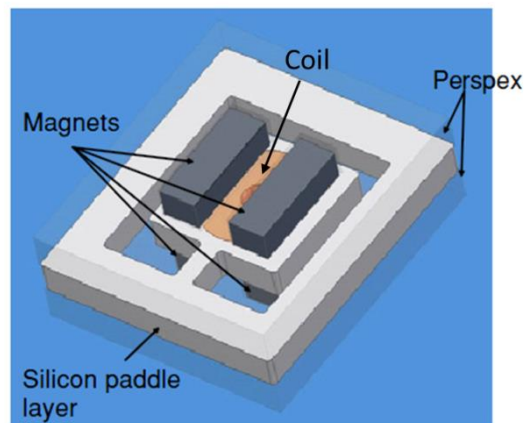


Figure 6: Silicon electromagnetic generator by Beeby [35].

Another device described by Sari [36] which has a dimension of 14mm x 12.5mm x 8mm with an array of 40 cantilevers of varying length to enable widening of the bandwidth due to varying resonance frequencies from the cantilevers. The cantilevers are all arranged around a central square permanent magnet and each have a 10 turn coil. The device was able to produce $0.5\mu\text{W}$ over frequencies of 3.3 – 3.6 kHz but have low voltage output as not all the cantilevers were resonating at a selected frequency at any single time.

A more comprehensive list of devices can be found with all parameters listed from each generator or device can be found in [37] [38] and [39].

2.5.2. Existing Electromagnetic Harvesters in Macro-Scale Implementations

Macro-scale devices are categorised in this group when the devices have sizes that ranges from 150mm^3 to above 30cm^3 . However, if they have similar sizes to micro or wafer scale devices then they also fall into this category if their manufacturing

processes are not micro-machined or using MEMS processes or just from using discrete components [39].

El-Hami [40] carried out simulation, modelling and fabrication of an electromagnetic transducer. The device occupies a space of 240mm^3 which also includes the space needed for maximum deflection of the device. The device operates on a principle that is based on the relative movement of a permanent magnet with respect to a coil. 0.53mW was achieved when having an excitation input vibration of $25\mu\text{m}$ at 322 Hz .

Following the work, Glynne-Jones [41] assessed two types of prototypes based on different configurations of magnets and coil structure. The first prototype has a moving coil between two fixed magnets; the second prototype was a moving four-magnet generator with a fixed coil with the aim of improving output voltage by improving the magnetic coupling between the magnets and the coil. Figure 7 shows both prototypes that were assessed. The first prototype generated $180\mu\text{W}$ with a displacement of 0.85mm whilst the second prototype generated more than four times higher instantaneous power compared to the first prototype.

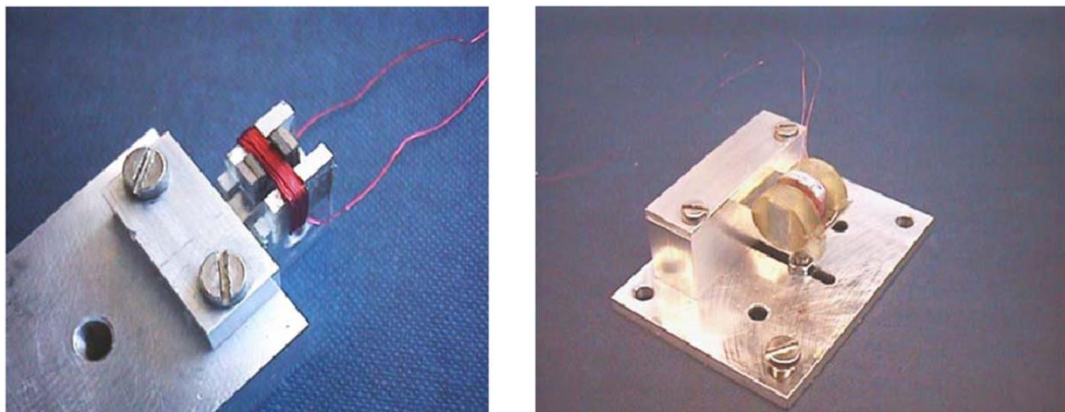


Figure 7: (Left) First prototype; (Right) Second Prototype by Glynne-Jones. [41]

Another device with a volume of 150mm^3 from Beeby [27] which uses conventionally wound coils, discrete magnets and machined components. By using a coil wound from enamelled copper which is as thin as $12\mu\text{m}$, an output of $46\mu\text{W}$ was achieved at 52 Hz from an excitation amplitude of $5.5\mu\text{m}$. The device is shown in

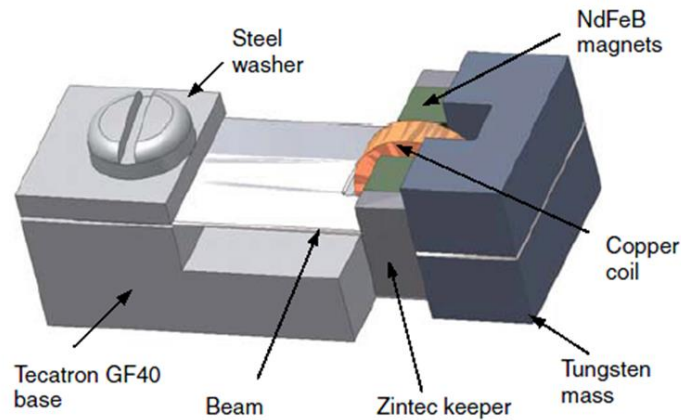


Figure 8: Micro cantilever generator from Beeby.

A more comprehensive list of devices can be found with all parameters listed from each generator or device can be found in [37] [38] and [39].

2.5.3. Summary of electromagnetic energy harvesters

In summary, based on the designs that have been reviewed including coil and magnet arrangements, the electromagnetic method of transduction was chosen and this section presented the theory behind the method of transduction and also the works of other authors. The sizes and dimensions of the electromagnetic harvesters from other authors vary widely as well as the power produced by the systems. As described earlier in the section, many contributing factors such as the number of turns in the windings on the coils used, the size and dimensions of the coil and the harvester, the magnetic field and the location of the coil within the field and so on are directly related to the output power of the system.

However, the electromagnetic harvesters reviewed from Section 2.5 and Section 2.5.2 have something in common. The harvesters presented are linear electromagnetic harvesters. The linear electromagnetic harvesters behave in a way where it produces peak outputs when it is operating at resonance frequency. However, the harvesters suffer a high amount of power loss away from the resonance frequency.

As human movements do not conform to a fixed frequency, the decision to introduce and apply nonlinear dynamics towards the electromagnetic harvester design within the research was taken and the next section will introduce and discuss nonlinear energy harvesting.

2.6. Nonlinear Energy Harvesting

Following earlier sections of introducing various components of the technologies and methodologies that encompasses energy harvesting, nonlinear energy harvesting is introduced in this section as it is a main research component within this research to justify the compatibility of nonlinear energy harvesting with human movements as a harvesting source.

Experiments from the author as well as Godfrey and colleagues show that human movements tend to be in the low frequency range (0.6Hz to 5.0Hz) and do not have a fixed frequency [42]. Whilst linear energy harvesters have the ability to provide high power output at resonance frequency, literature from Section 2.3 shows that linear energy harvesters lose 80% of power whenever it is away from the resonance frequency by 20%. Hence, conventional energy harvesters do not operate over the wide bandwidth which would cater to the demand for use with human movement energy harvesting which nonlinear energy harvesting systems provide.

There has been a large focus placed on vibrational energy harvesters using linear electromechanical devices which provide high output power upon resonance frequency excitation. In realistic ambient environments vibrations do not only occur at a set specific frequency but can be more accurately described as stochastic, multi-frequency, time varying or some combination of some or all of these components. Hence, using a linear system which only provides high power on a narrow frequency band is not an effective method under these conditions. On the other hand, nonlinear energy harvesting systems are capable of responding over a broader range of frequencies; thus suggesting better compatibility with applications from ambient environment vibration sources.

In this section, a novel nonlinear energy harvesting system is considered. This is a bistable driven oscillator which comprises two permanent magnets which are aligned in a way that the magnets have similar polarities opposing each other. One of the magnets is attached to a cantilever (as cantilever tip mass) while the other is mounted on a platform where the distance between both magnets can be controlled precisely (pushed towards each other or withdrawn from each other). This distance of separation is what controls the nonlinearity of the system. When the two magnets are separated by a large distance, the system behaves like a conventional linear oscillator. However if the distance between the magnets is very low, the restoring force of the cantilever is overcome by the magnetic repulsion force, forcing the cantilever to deflect into one of

1. A large distance between the two magnets resulting in the system behaving similarly to a linear system which the inverted pendulum has a resonance frequency of 6.67Hz.
2. A very small distance between the magnets resulting in the pendulum swing confined almost exclusively to one of the two potential wells. Hence the behaviour is also similar to a linear system.
3. At distances in between the first and second regime but one where the pendulum is highly nonlinear where the cantilever swing reaches maximum amplitude when it jumps between the two potential wells assisted by the excitation vibrations.

It is regime 3 where the system showed a potential gain for power harvesting between 400% and 600% compared to standard linear systems from an excitation of 0.3 to 1.2 mN excitation force on their prototype system.

Stanton, McGehee and Mann [44] have also devised a system where the nonlinear energy harvesting concept was evaluated where a piezoelectric system was used but mounted horizontally. The cantilever beam was made from a bimorph piezoelectric (V22BL, Mide Corporation) and similarly used two magnets which were similarly poled to oppose each other to create the nonlinear dynamics. Figure 10 presents the schematics which Stanton used for his nonlinear energy harvesting system.

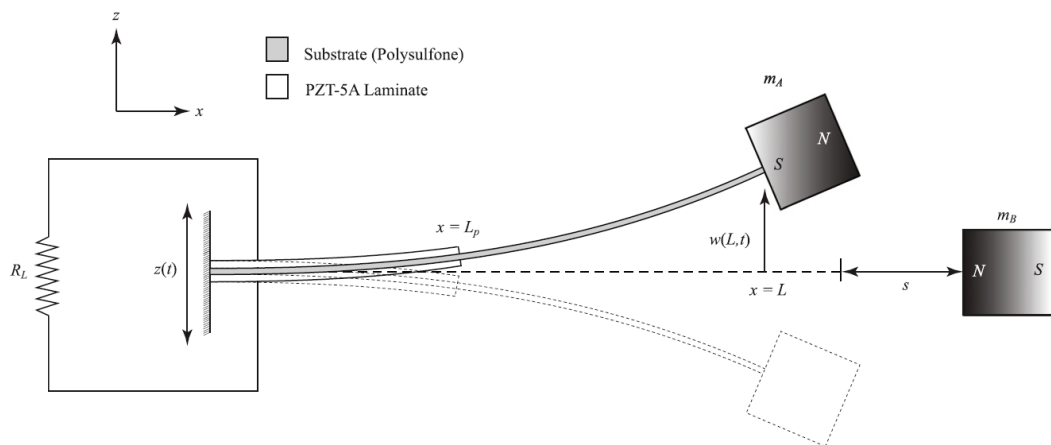


Figure 10: Schematic diagram of a piezoelectric energy harvester by Stanton and colleagues. [44]

Through frequency sweep experiments, Stanton also notes that in a situation that is similar to Cottone's Regime 3, the system displays complex hopping behaviour between the two extreme potential wells as well as hopping inside the potential wells.

Stanton also notes that these hopping behaviours are capable of enhancing power output and is especially clear at higher frequencies above 15Hz. However the broadband energy harvesting enabling factor is particularly profound at frequencies less than 15Hz but requires more sophisticated power management circuitry to optimize power transduction. [44]

Comparisons have been made to Stanton’s approach by Ferrari [45] by having a similar setup. Figure 11 shows the set up used by Ferrari. The distance between the two magnets was controlled by a micrometer and an open circuit output voltage was measured with varying excitation frequency at 1g acceleration. Table 9 shows the output voltages obtained and at a separation distance of 10.5mm for both magnets, the output voltage significantly increases as the system becomes bistable and switching occurs between the two potential wells. This behaviour is similarly to that described by Cottone’s Regime 3 and the output voltage waveform is presented in the right figure of Figure 11.

Distance Between Magnets	25.0mm	12.0mm	10.5mm
Open-Circuit Output Voltage	0.78V	1.68V	3.33V

Table 9: Output voltage with varying distances between magnets. [45]

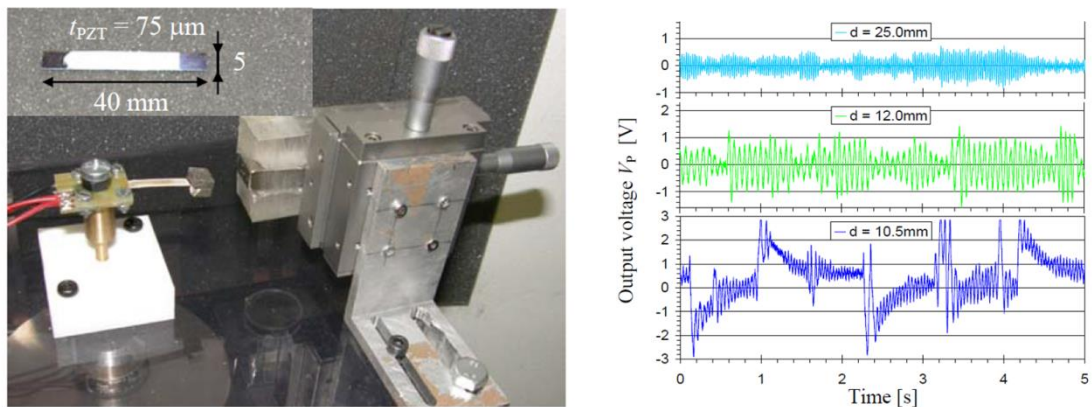


Figure 11: Left: Experimental setup by Ferrari with dimensions of piezoelectric material used. Right: Open-circuit output voltage response with varying distance between the two magnets. [45]

Another interesting concept from Mann and Sims [46] uses magnetic levitation from three different magnets where two fixed outer magnets are aligned so that it opposes the polarity of a movable central magnet, thus suspending the central magnet with a nonlinear restoring force. Figure 12 shows the magnetic levitation device created which is then surrounded with coils at both the top and bottom to produce an electromagnetic energy harvester. Agreements were made that nonlinear systems

provide an additional option with the ability to harvest energy at a wider range of frequencies unlike linear devices where one needs to be operating at resonance frequency to be able to obtain maximum power.

However, Mann and Sims noted that the harvester design's maximum power output has not been explored. This is due to the nonlinear response of the system being heavily dependent on the damping levels that is applied. A very large input excitation would be required due to the large mechanical damping within the system. Improvements have been suggested to rectify this issue to improve power output in the future.

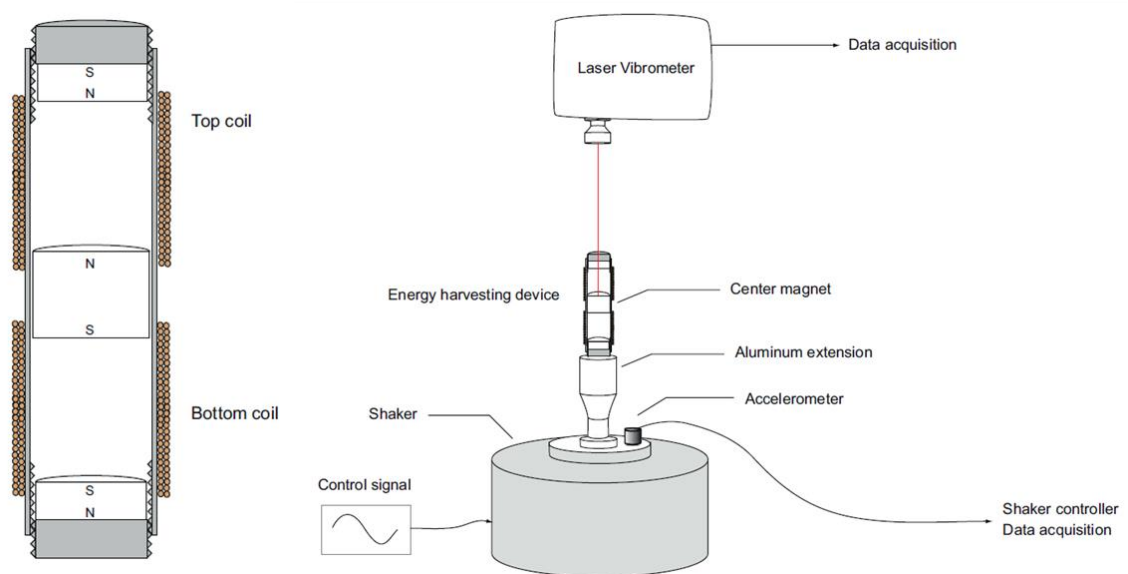


Figure 12: Left: Schematic diagram of the magnetic levitation system with coils wrapped around both the top and bottom sections of the device. Right: Complete experimental set up used by Mann and Sims. [46]

With a slightly similar set-up to Mann and Sims' design, Huang [47] designed a mechanical spring electromagnetic generator with a resonant frequency of 3.45Hz and two magnetic-spring electromagnetic generator (resonant frequencies of 4.15Hz and 4.42Hz) which allowed a displacement of $\pm 25\text{mm}$ of the central moving magnet (Figure 13). The mechanical spring generator was wrapped in 5 sets of coil whereas the magnetic-spring generator was wrapped around with 7 sets of coil with each coil wound at 2000 turns/coil. The placement of the coils was aligned in a way that the induced voltage does not cancel each other out when the magnetic field cuts through the coils.

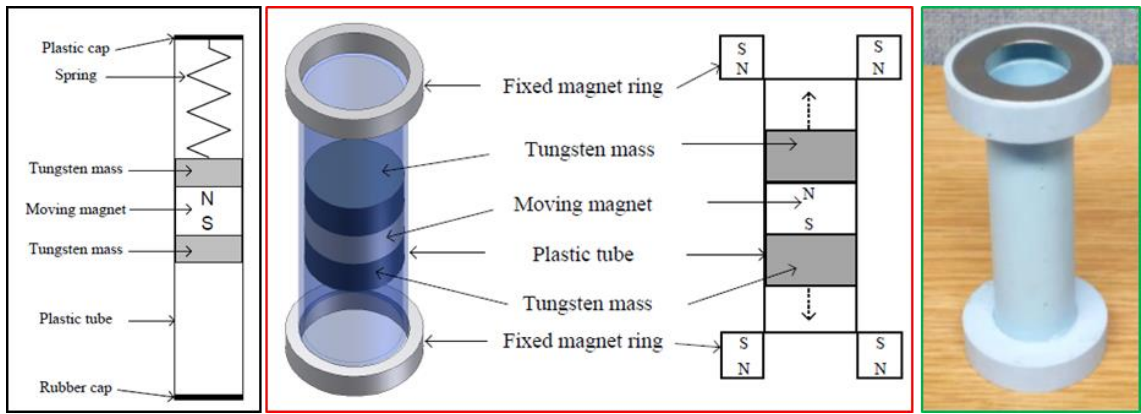


Figure 13: Black Box: Mechanical Spring design. Red Box: Magnetic-Spring design. Green box: Prototype of magnetic-spring produced. [47]

It was also noted that the magnetic spring design was able to produce four times higher power output under the same operating conditions compared to the mechanical spring design. This is due to a higher number of coils wrapped around it and also due to the higher flux density in the magnetic spring design.

3.0 Generation and Capture of Human Movement Accelerations

To prove that human movements have the potential as a power source, this section presents the method of measurements and capture of the accelerations which are present during human movement. The accelerometer is placed on selected body parts (chest, hands, ankle and foot) as shown in Figure 15 with measurements being taken during a selected repetitive set of movements (walking, jog & high knees*).

The measurement of the accelerations from different parts of the body is done to aid the process of determining the optimum location to place an energy harvester on the human body depending on the motion / gesture that was used. Literature reviewed in Section 2.2 did not specify what type of movements that were done; only the available power was mentioned. The amount of acceleration from all three axis of the accelerometer will be measured and used to determine which axis and location would be the most suitable for an energy harvester placement.

Finally, the sensor is placed on the hands and feet because they are the most outer limbs that are used most frequently for most movements or gestures. Gestures are mostly done with the hands such as pointing or making shapes. The movement of hands during physical motion also help supports the body in keeping balance and maintaining body position. The feet are generally used to transport ourselves from one place to another. Movements of the feet that are considered in this research are walking, jogging and high knees. Finally, placing the sensor on the chest also allow for measurements to be taken from a central point of the body without any moving limbs.

*High Knees (Figure 14): Typically combine running movements with exaggerated knee lifts, usually trying to get the knees as close as possible to chest position. High Knees can be done in a static location or as a running motion.

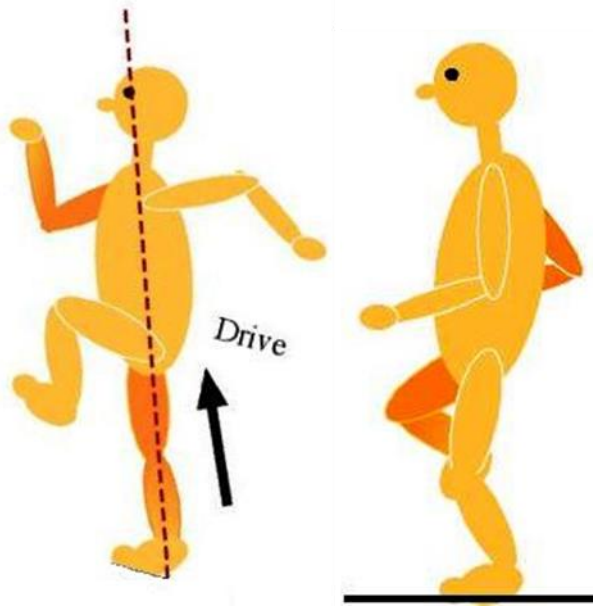


Figure 14: An illustration of the static High Knees movement (left) and the static Jogging movement (right) [48].

3.1. Measurement Systems

Assumptions of the experiment that should be taken into account are:

- The test subject is a young male with no health issues.
- All movements are done under lab conditions with it replicating as close as possible to actual normal daily movements.
- Subject is wearing shoes and had the sensor attached on top of the shoe in a similar position as shown on Figure 15 to simulate real life conditions.
- Due to the limited space in the lab, the ‘jogging’ and ‘high knees’ movements are done on the spot / static (Figure 14).
- “Walking” movements are done as shown on the map on Figure 16. After reaching the end of the lab, the subject then turned around and continues walking in the other direction until measurement was complete to simulate real life walking conditions with turns.
- The sensor is “attached” to the subject via tape directly onto the skin (image shown with clothing on) as tightly as possible to the selected body parts to eliminate any potential loss of acceleration or vibration.

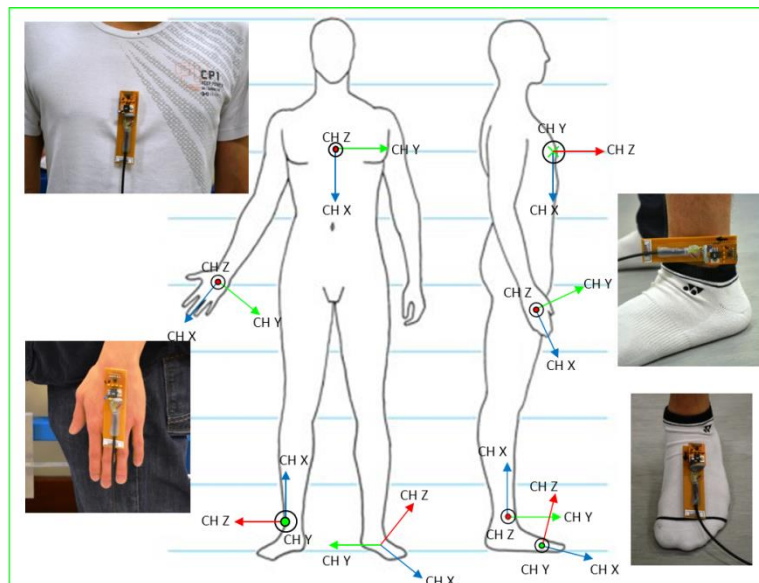
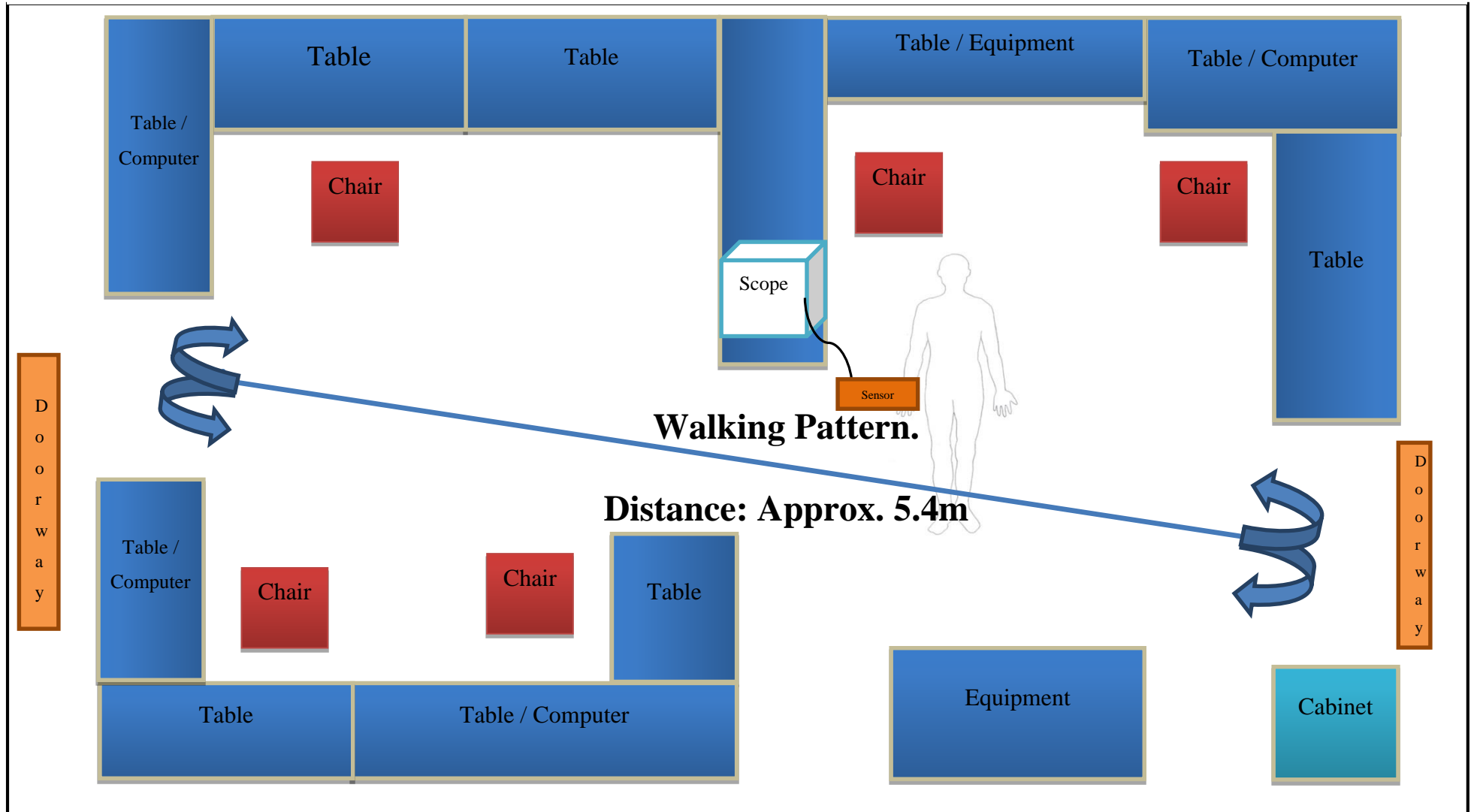


Figure 15: Location and orientations of the sensors placed on the body.

Figure 16: Floor plan of the laboratory that was used to conduct movement measurements. (Blue colour indicates tables/objects, Light Brown indicates doorways.)



A base board PCB was also produced to be used as a medium to relay the output from the sensors to the oscilloscope (Agilent MSO-6054A). The base board is separated into three channels to accommodate the output from the sensors and each channel is also fitted with a coupling capacitor to ground to limit noise in the output produced. Probes from the oscilloscope are then connected to the base board and measurements being fed into oscilloscope. Figure 18 shows the schematic of the base board.

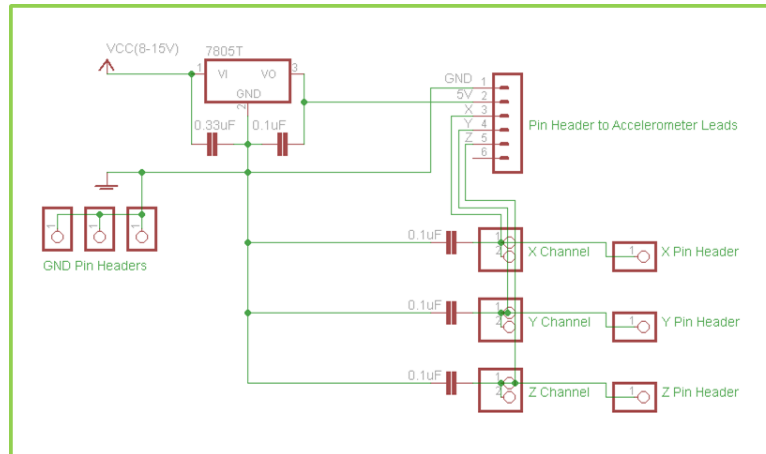


Figure 18: Schematic of the Sensor Base Board.

Measurements obtained are then stored onto a memory stick which is connected to the oscilloscope in binary format and transferred onto the Matlab workspace through a function file provided by Agilent Technologies. The outputs from the graphs are then normalized and Fast Fourier Transformed (FFT) applied to show the measurements in the frequency domain. The Matlab source code is attached in 0for reference. A block diagram of the whole capturing process is shown on Figure 19.

The oscilloscope is set up at:

- Sampling rate of: 10000 samples per second
- Duration: 10 seconds
- X-axis range: 1s/div
- Y-axis range for all 3 channels: 200mV/div

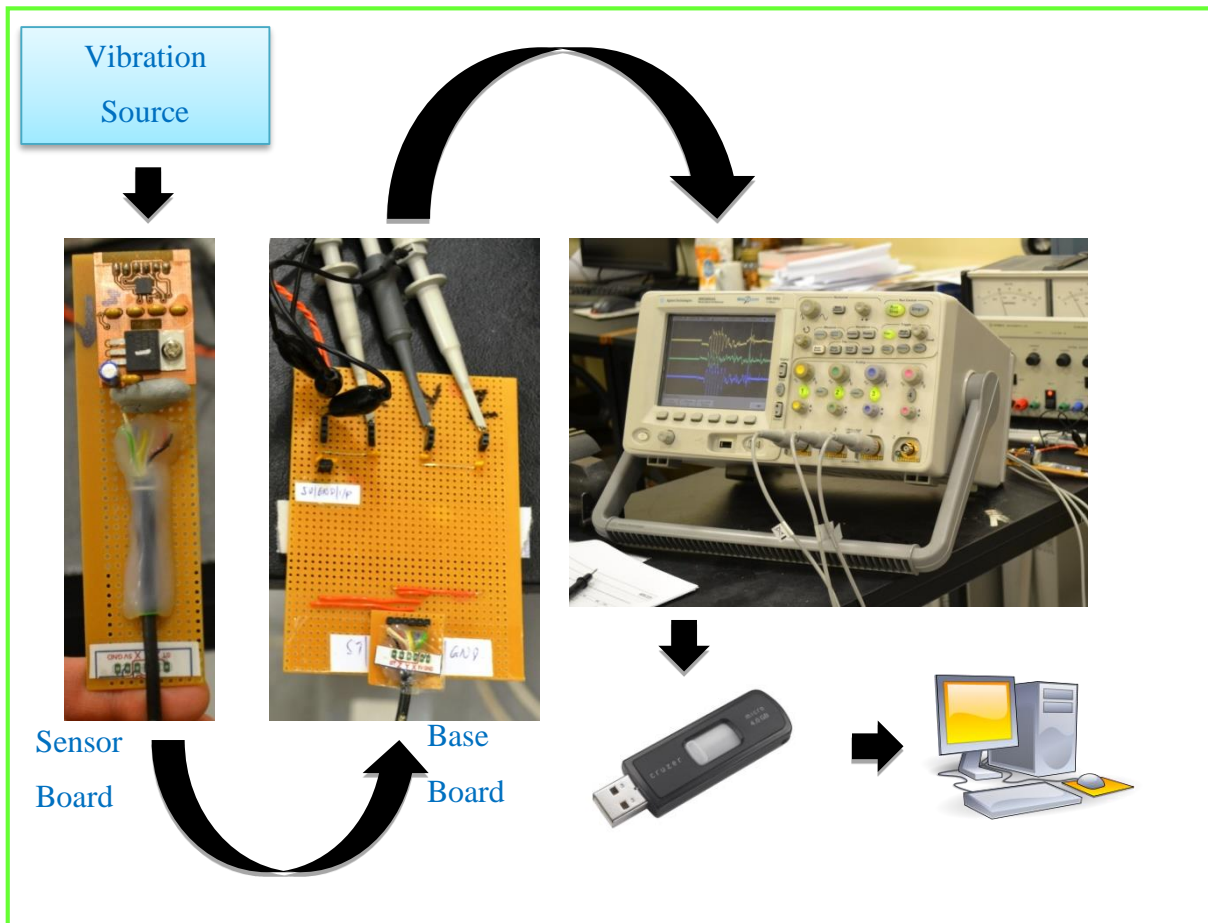


Figure 19: Block diagram of the vibration capture process.

3.2. Measurement Results

An example of the data obtained from the sensor placed on the foot while walking is attached: Figure 21 shows all three channels of the collected measurement from the oscilloscope. Channel Z is recorded at +1g due to the orientation of the accelerometer. Figure 20 shows the orientation of the accelerometer.

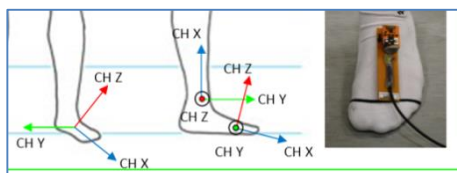


Figure 20: Orientation of the accelerometer that was attached to the foot.

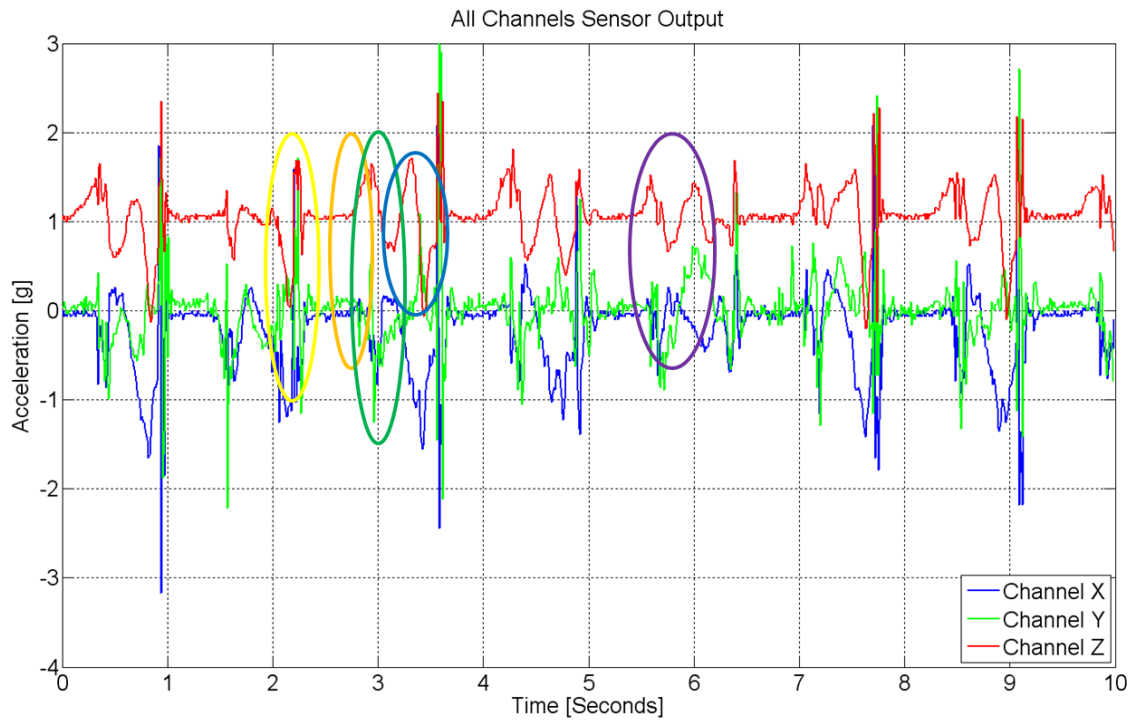


Figure 21: Left foot walking raw data, all channels.

To further break down the movements, coloured rings are placed on Figure 21 as well as individual figures to show which position the foot is in.

- Yellow coloured rings: Foot lowering down to “heel strike” position.
- Orange coloured rings: Complete foot is on the ground. (Metatarsals of the foot have landed on the ground)
- Green coloured rings: Toe lift off.
- Blue coloured rings: Foot kicking out / in motion swinging forward.
- Purple coloured rings: Turned around after reaching the end of the lab.

The graphs also show that each single step took about 1.3 seconds, which is also 0.7 steps per second on a single foot. It took about 4 steps from each foot (8 steps in total on both sides) to arrive at the end of the lab before requiring a turn to go in the opposite direction. From this, the step length is calculated at 67.5cm/step ($5.4\text{m} / 8 \text{ steps} = 67.5\text{cm/step}$).

Figure 22, Figure 23 and Figure 24 show the output of the individual channels X, Y and Z after Fast Fourier Transform (FFT) was performed. This is to present the results in a frequency domain rather than a time domain. Channel X is shown to have a

peak acceleration of 0.17g at 1.47Hz while Channel Y has shown that it has a peak acceleration of 0.10g at 0.78Hz. Channel Z exhibits a peak of 0.12g at 2.83Hz.

All 3 channels displayed different peak acceleration at different frequencies but this was expected as normal human walk is said to be within a region of 1 to 3Hz [42]. Only the highest acceleration value was chosen from the whole range of frequencies even though some of the amplitudes' of the harmonic frequencies are fairly close to the highest values.

Channel Z has its peak acceleration at about twice the frequency of Channel X is because it accounts for both the footfall as well as the liftoff of the foot. Whereas Channel X's peak acceleration only comes from the foot liftoff and kicking out towards the next step at every cycle. Channel Y is shows the lowest peak at the lowest frequency as it is measuring the horizontal axis of the foot movement.

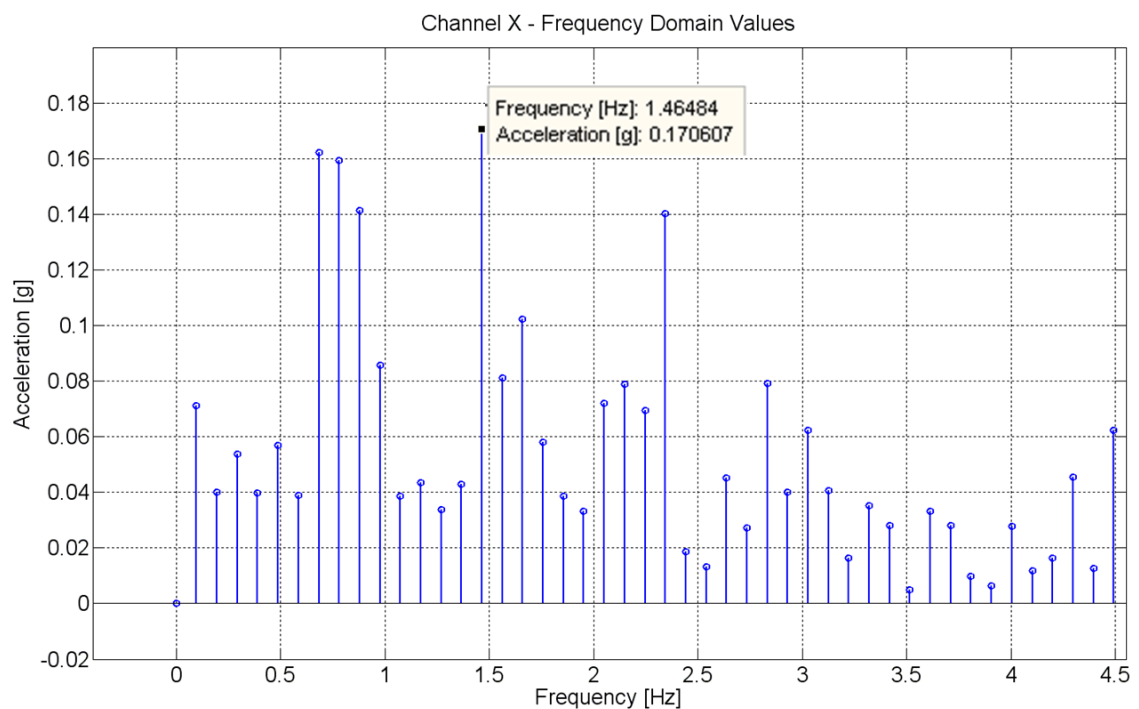


Figure 22: Left foot walking in frequency domain in Channel X.

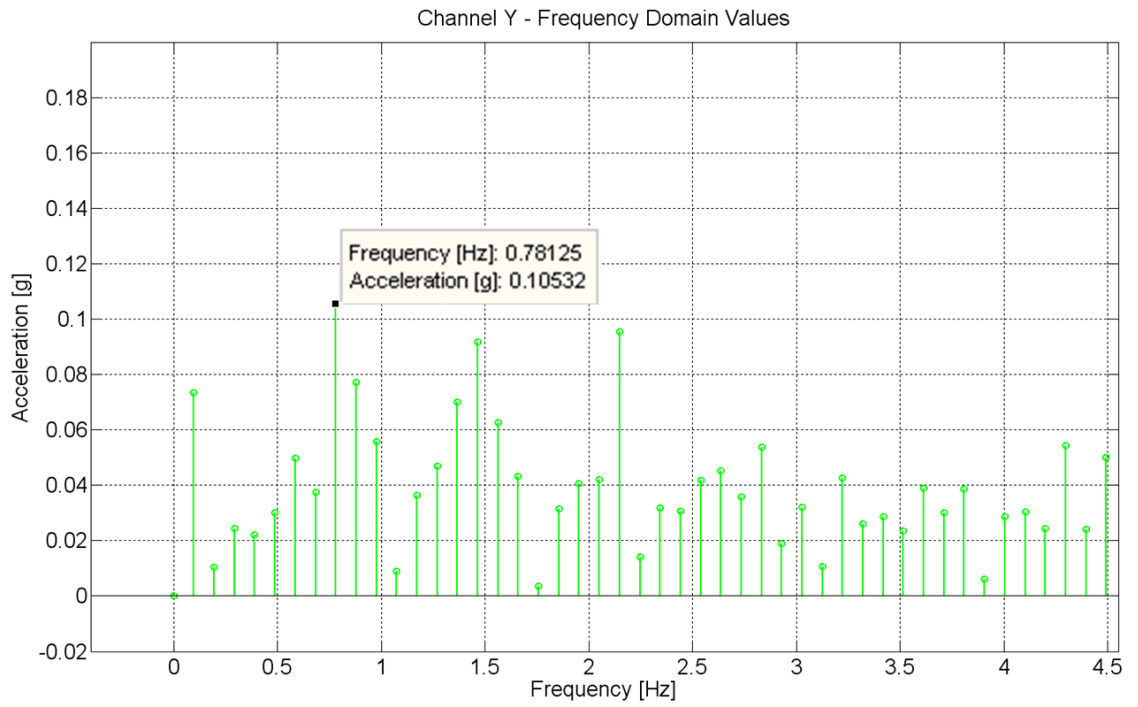


Figure 23: Left foot walking in frequency domain in Channel Y.

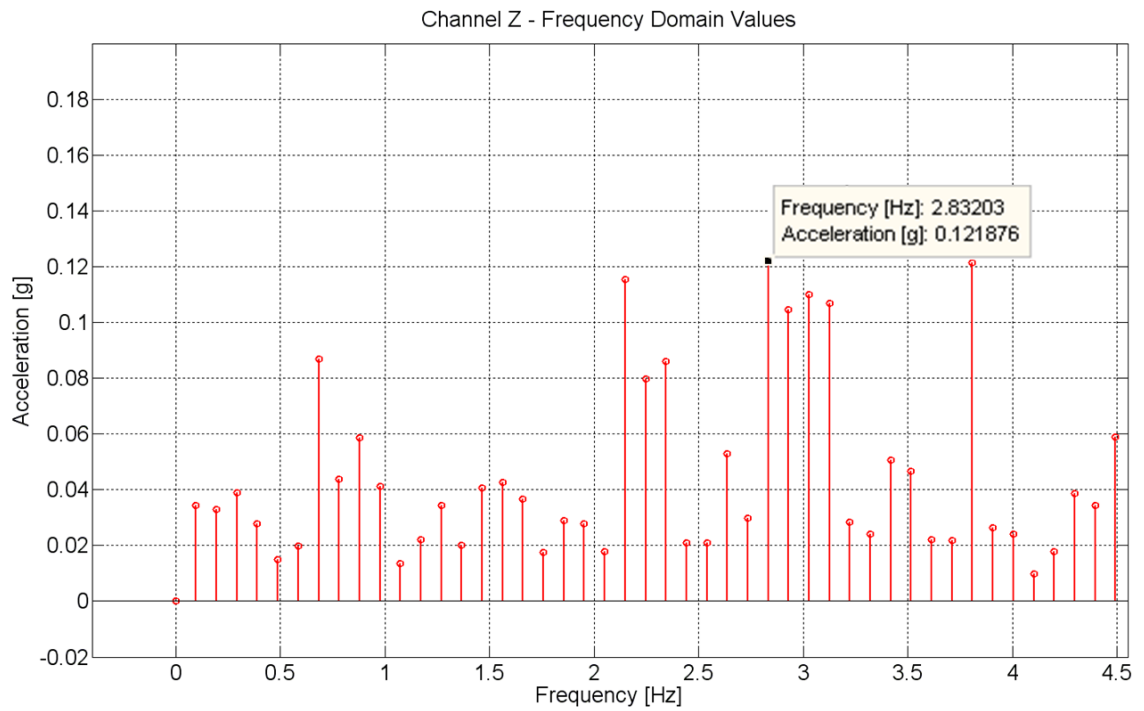


Figure 24: Left foot walking in frequency domain in Channel Z.

Max Acceleration with Frequency recorded towards specific body movement at selected body parts					
Movement	Body Part	Channel X (g)	Channel Y (g)	Channel Z (g)	Total Acceleration (g)
Walking 1	Chest	0.12 at 1.66Hz	0.13 at 0.78Hz	0.08 at 1.66Hz	0.15 at 1.66Hz
Walking 2	Chest	0.16 at 1.66Hz	0.10 at 0.78Hz	0.07 at 1.66Hz	0.17 at 1.66Hz
Jog	Chest	0.97 at 2.93Hz	0.26 at 1.49Hz	0.06 at 2.93Hz	0.97 at 2.93Hz
High Knees	Chest	1.75 at 3.61Hz	0.25 at 3.61Hz	0.21 at 3.61Hz	1.78 at 3.61Hz
Walking 1	Right Hand	0.15 at 1.66Hz	0.19 at 0.88Hz	0.08 at 0.59Hz	0.20 at 0.88Hz
Walking 2	Right Hand	0.20 at 1.56Hz	0.19 at 0.78Hz	0.08 at 0.98Hz	0.22 at 0.78Hz
Jog	Right Hand	0.64 at 1.56Hz	1.01 at 3.13Hz	0.30 at 3.13Hz	1.13 at 3.13Hz
High Knees	Right Hand	1.08 at 3.42Hz	1.50 at 1.76Hz	0.28 at 3.42Hz	1.59 at 1.76Hz
Walking 1	Right Ankle	0.23 at 1.56Hz	0.11 at 1.56Hz	0.12 at 0.78Hz	0.27 at 1.56Hz
Walking 2	Right Ankle	0.31 at 1.56Hz	0.16 at 1.56Hz	0.11 at 0.78Hz	0.35 at 1.56Hz
Jog	Right Ankle	0.48 at 1.56Hz	0.23 at 1.56Hz	0.16 at 1.56Hz	0.56 at 1.56Hz
High Knees	Right Ankle	2.06 at 1.76Hz	1.05 at 1.76Hz	0.83 at 1.76Hz	2.45 at 1.75Hz
Walking	Left Foot	0.17 at 1.47Hz	0.10 at 0.78Hz	0.12 at 2.83Hz	0.20 at 1.46Hz
Jog	Left Foot	0.22 at 2.93Hz	0.11 at 3.03Hz	0.43 at 1.47Hz	0.45 at 1.46Hz
High Knees	Left Foot	1.04 at 3.22Hz	0.37 at 3.22Hz	1.40 at 1.56Hz	1.44 at 1.56Hz

Table 10: Max acceleration (g) with frequency for specific body movements at selected body parts.

3.3. Further Discussions of Results Obtained

This section presents and discusses the results recorded. Firstly, the results are discussed in terms of the total accelerations that were recorded from the movements (Section 3.3.1). Additional methods of presenting the recorded data are attached in Appendix H.

From Section 3.2, it was clear that many measurements were taken from the four different positions that the sensor was placed on the body which all went through similar types of movements. This coupled with the measurements from the three different axes of the accelerometer from each position for each movement equates to a substantial amount of data and graphs. Thus in this subsection, comparisons will be taken from selected parts from each movement pattern as well as each axis' acceleration or total acceleration achieved.

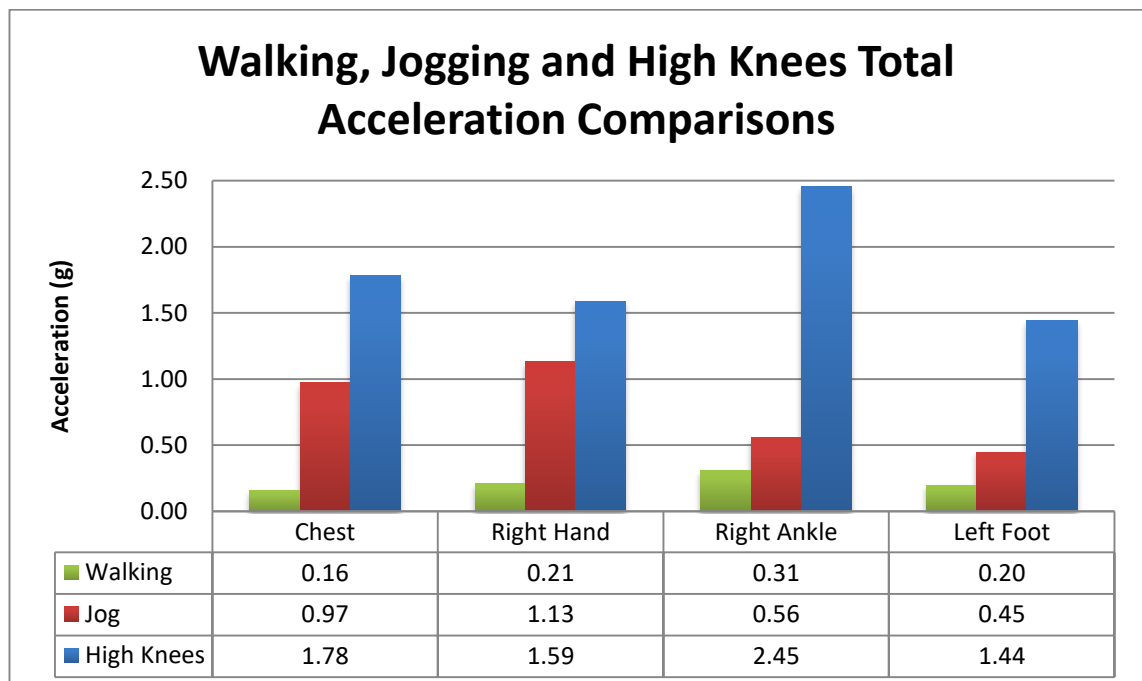


Figure 25: Total acceleration comparisons of different body placement of the sensor and with different movement (Walking – average of both sets of measurements).

Figure 25 is a summary of the data presented in Table 10. It shows the total acceleration values of different movements with sensors placed on different parts of the body. The right ankle placement shows the highest total values of all three movements added together whereas the left foot placement has the lowest value.

The walking movement measurements that are presented in Figure 25 are an average of both sets of walking movement data obtained during measurement (Walking 1 & Walking 2).

3.3.1. Total Accelerations for a Single Placement of the Sensor with Different Body Movements

As the total number of measurements was high, only the total accelerations of the Left Foot sensor placement will be compared. All 3 movements (walk, jog and high knees) will be compared with their total accelerations.

From Figure 26 to Figure 28, it was apparent that there is a slight shift of frequency at max acceleration from a lower frequency of 1.46Hz to a maximum frequency of 1.56Hz. Figure 26 shows there is a max acceleration of 0.20g at 1.46Hz. Human walking is defined at 1-3Hz [49] and this measurement falls between the ranges that was defined. In section 3.2, it was shown that the walking frequency was recorded at 0.75steps/second on one single foot.

The sensor was only placed on the left foot thus only measuring the footfall of the left foot. An assumption was made that the right foot should be able to follow in the same pattern that was showed by the left foot. Figure 26 shows that the maximum acceleration for the walking movement was recorded at 0.20g at 1.46Hz. Figure 27 shows the max acceleration of the left foot during the jogging movement to be 0.45g at 1.46Hz. There was an increase of 0.25g of acceleration at the same frequency of 1.46Hz over the walking movement. But the maximum acceleration value of the walking movement of 1.46Hz could have been a harmonic frequency at the maximum acceleration as the measured frequency steps was only 0.75steps/second. Furthermore, the acceleration at 0.78Hz was 0.20g too.

The increased acceleration values of the jogging movement are due to the increased frequency of steps of the left foot during the jogging movement. The additional energy that goes through the body system also contributes to a higher acceleration measurement. It should also be noted that the measured acceleration values will differ from one person to another and that might be down to how the measured subject walks or runs. One person might walk with a harder heel strike compared to someone who has a softer heel strike during the jogging movement.

Figure 28 presents high knees movement and it has the highest value of accelerations compared to the Walking and Jogging movement. It shows a value of acceleration at 1.44g at 1.56Hz. This showed the trend of the increased frequency at maximum measured acceleration. This is in line with projected measurements as the high knees movement involves the most rapid leg movements as it is almost a standing sprint action. Thus the maximum acceleration values also represent a big increase compared to the walking and jogging movement. The pounding heel strike and toe lift off action of the high knees also contributed to higher acceleration values across its harmonic frequencies.

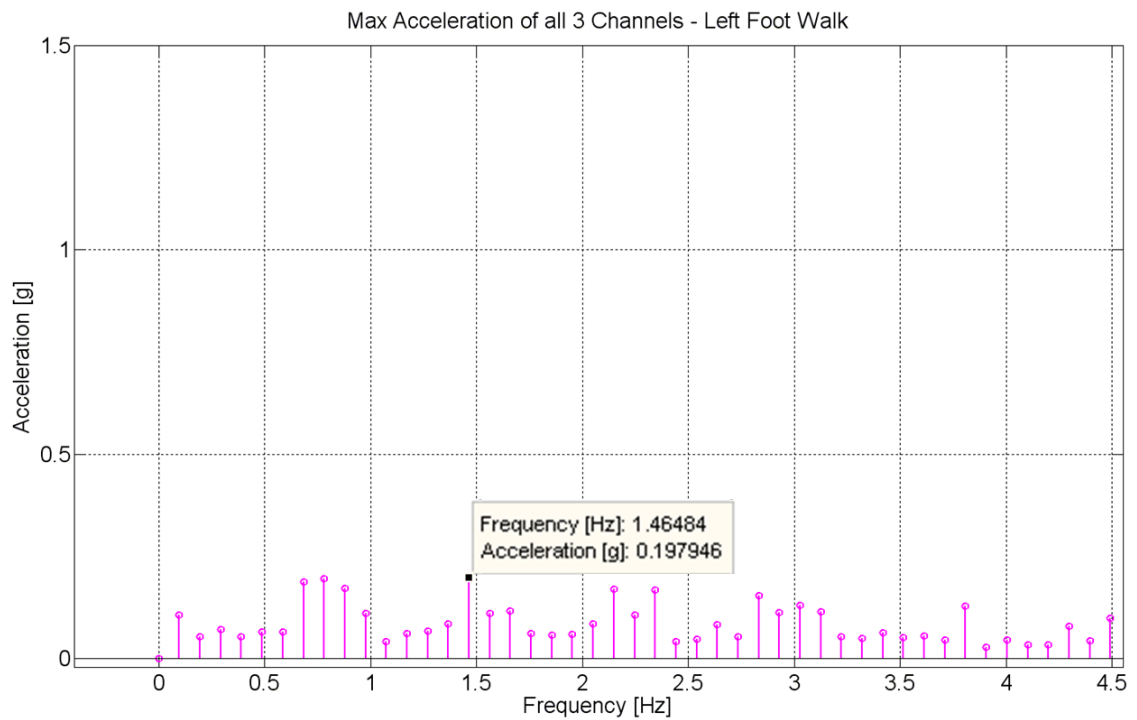


Figure 26: Left Foot Walk

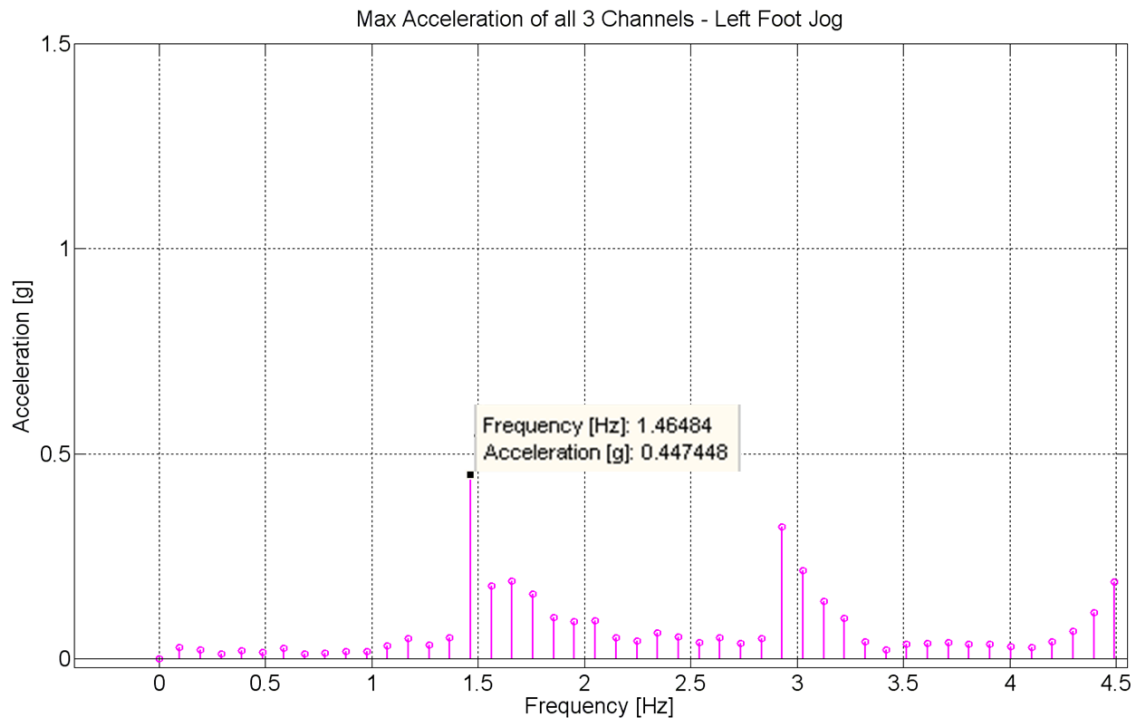


Figure 27: Left Foot Jog

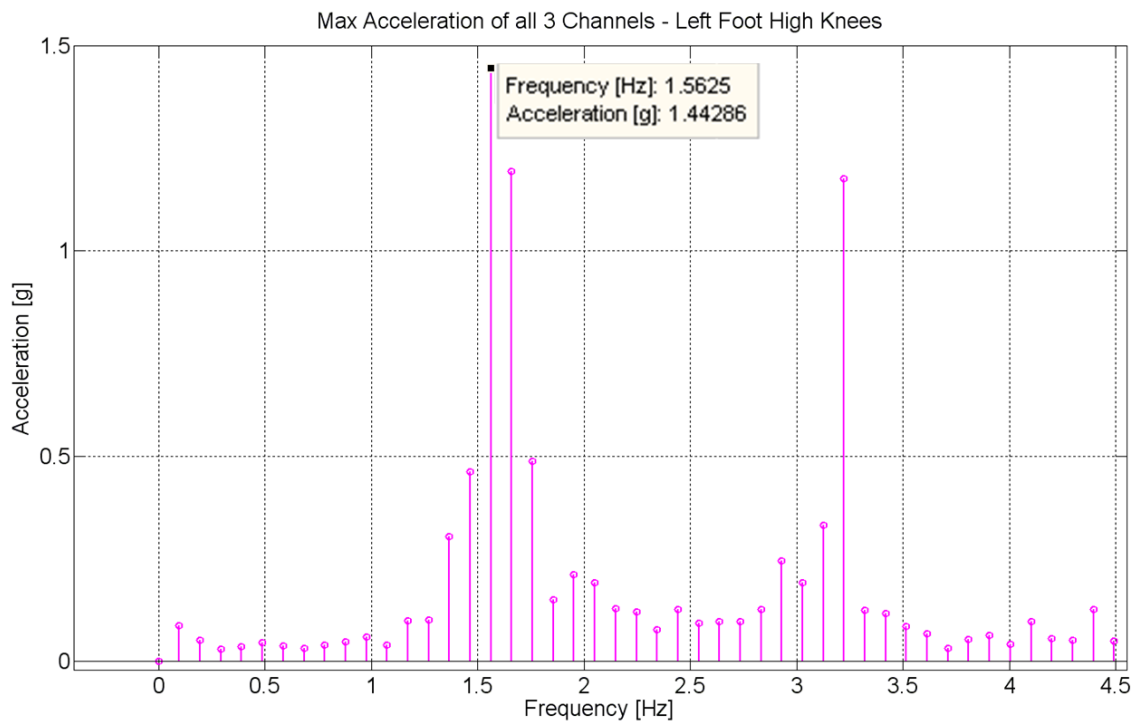


Figure 28: Left Foot High Knees

The other sets of measurements (Chest, Right Ankle and Right Hand) were obtained using a very similar testing procedure with the only difference being the placement of the sensor.

3.4. Summary

In conclusion, the experiment was successful in determining which body part would undergo the most acceleration during a certain type of movement. The three movements that were chosen were designed to cover most basic activities from walking to an activity that requires a little bit of athleticism (high knees). These give a slightly more realistic approach and a good gauge on how much acceleration is available to be harnessed if an energy harvester is attached to one of the body parts.

The experiment also revealed that the vertical component provides the highest acceleration values, where total acceleration values of all three components usually are quite similar to the highest vertical component value. This provides good information on where and which axis to place a single degree of freedom energy harvester.

Another insight is how the results obtained here could be used. For example, a person who is an office worker who walks 80% of the day, 10% jogging and 10% high knees (exercise time).

In a different situation, for an athlete who spends 40% of the total movement time walking, 40% jogging and the remainder 20% doing high knees, it would be beneficial to have the harvester attached to the ankle or hand as opposed to the foot. This is because the ankle or hand does not provide as much acceleration as the foot during the walking movement but it provides much more acceleration during jogging and high knees movements. Knowing the weightage of each individual's movements before attaching a harvester to suit their movement patterns would be ideal situation before tuning them to the optimum axis.

4.0 Nonlinear Energy Harvester Set Up

A number of authors have studied nonlinear systems with two opposing magnets fitted to the system, one on the cantilever and another usually on a platform where the distance between the magnets can be easily controlled. Almost all reviewed systems within the literature have used piezoelectric materials attached to the cantilever as a method of vibration to electrical conversion, thus leaving the space between the two opposing magnets unused. A decision was made to investigate the use of a coil within the gap that was available between the two opposing magnets which produces the nonlinear dynamics from the nonlinear energy harvesters as an electromagnetic harvester. Additionally, the voltage outputs from the coil would also be expected to be slightly higher with two opposing magnets compared to a one magnet configuration as the two opposing magnets will provide a stronger magnetic field to the coil which results in a higher voltage output. Figure 29 shows a drawing of the proposed nonlinear device. Another reason for doing so is trying to maximize electrical generation and output from a single system. If a system could utilize a larger percentage of its size for generating power from one or more sources whilst retaining the original size, it should be explored.

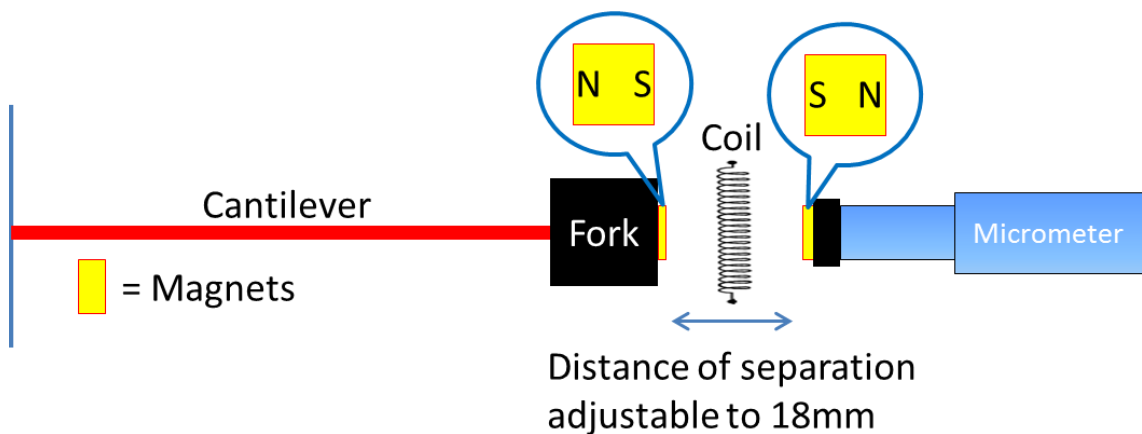


Figure 29: Schematic of proposed nonlinear energy harvesting device.

Additionally as no similar literature has been produced from having a coil generating power from the gap in between the magnets of the nonlinear dynamics generating magnetic fields; it is a good idea to explore such a concept. Lastly, piezoelectric materials could then be added to the cantilever of the nonlinear system created to enhance the power generation even further in the future.

4.1. Prototype Design

To evaluate the performance of the proposed energy harvester, a prototype nonlinear energy harvesting system has been constructed. A 304 Stainless steel spring cantilever beam with a free length of 65mm and a width of 19mm as well as a thickness of 0.9mm was clamped at one end and coupled with a fork attached to the free end. The fork is made of steel and measures equally on all three sides with dimensions of 25mm length, 20mm width and 1mm in thickness across each side. The fork also contributes as a tip mass of 11.7g. Figure 30 presents the construction of the fork which is attached to the cantilever (refer to Figure 29, Figure 31 and Figure 32).

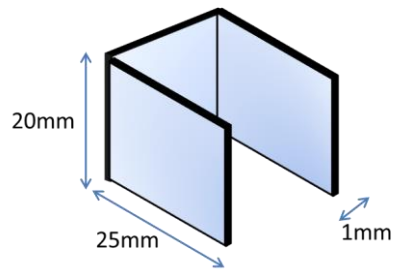


Figure 30: Construction and dimensions of the fork which is attached to the cantilever.

A Neodymium Iron Boron bar magnet is attached to the end of the fork which acts as one half of the pair of nonlinear dynamics generating magnet, it has dimensions of 25mm length, 10mm width and a 3mm thickness and weighs 5.625g which makes the total cantilever tip mass, 17.325g.

The remaining (button) magnet from the pair of magnets is attached to a micrometer which enables the distance between the magnets to be controlled easily and accurately. The maximum distance of separation between the magnets is 18mm. The prototype is then mounted on a shaker (LDS-V406/8) which has a power amplifier (LDS-PA100E) to amplify the source signal. Figure 31 and Figure 32 shows the CAD models of prototype cantilever design. Figure 33 shows the cantilever prototype mounted on top of the vibrational shaker. Besides the micrometer, cantilever, fork and magnets, all other components are made from aluminium. The prototype design will be modelled and simulated to allow comparison with the actual prototype. The model of the prototype system will be split into two major components:

- The magnetic interaction which produces the nonlinear dynamics of the system.
- The cantilever which will be modelled as a linear lumped spring-mass system.

The magnetic system behaviour will be considered first.

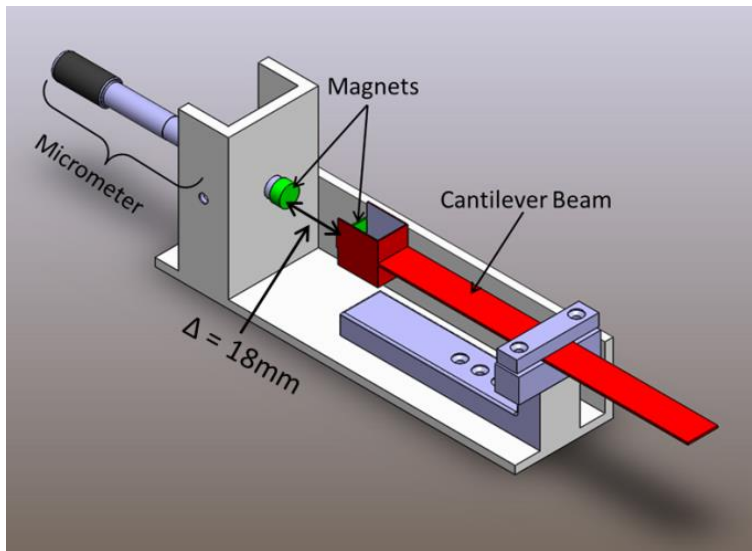


Figure 31: Cantilever prototype design with magnets attached shown in green.

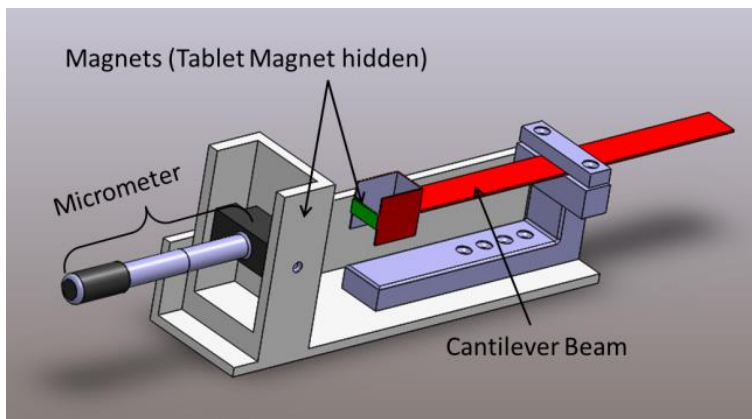


Figure 32: Cantilever prototype design with magnets attached shown in green from another angle.

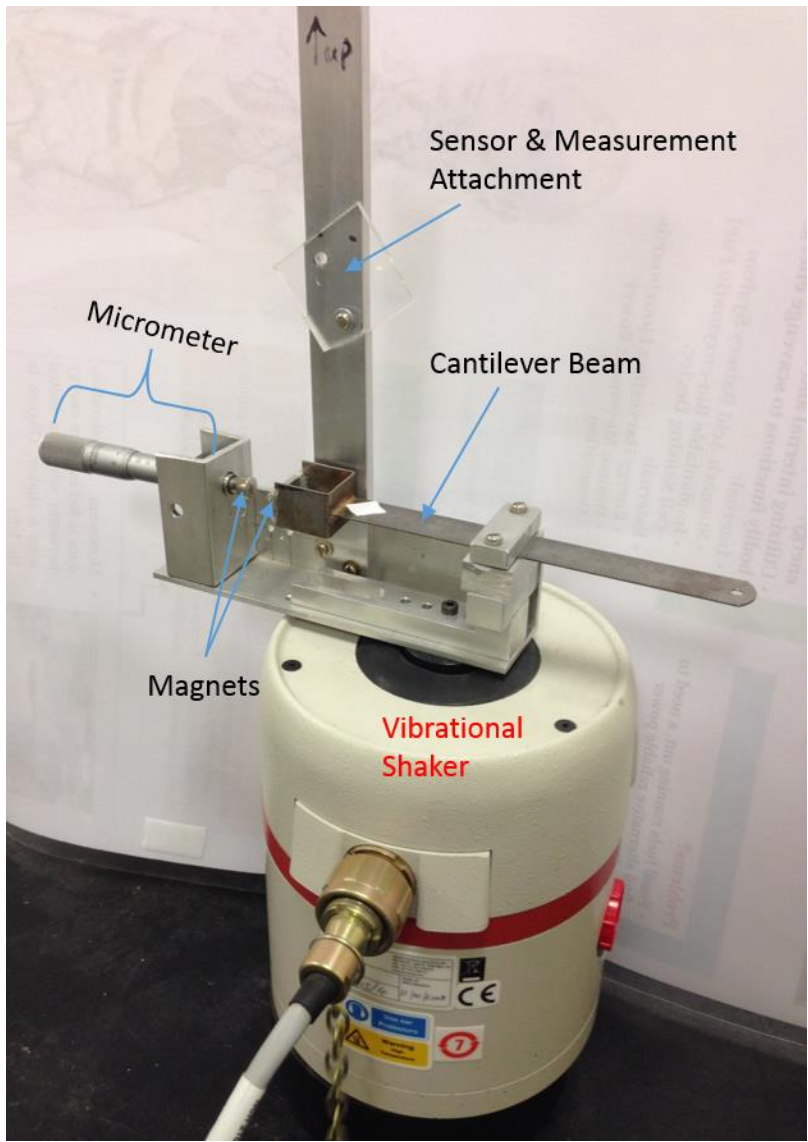


Figure 33: The constructed prototype mounted on top of the shaker.

4.2. Modelling the Nonlinear Prototype

This section covers the complete process of modelling the proposed nonlinear cantilever prototype. Figure 34 shows a simplified block diagram of the nonlinear cantilever system that is to be modelled which comprises of two main sections. The cantilever model system which requires the cantilever composition itself, for example the spring constant, damping coefficient, dimensions and so on. The second main section covers the magnets which are attached to the cantilever as well as the micrometer to create the opposing force to generate the nonlinear dynamics. Both sections has to be modelled as accurately as possible as both sections rely on each other.

Firstly, the magnetics surrounding the prototype will be modelled. This then proceeds to experiments that validate the magnetic modelling process. Only after that, the composition of the parameters of the cantilever will be discussed. The completed model is then compared against measurable results from the constructed prototype before ending the section with phase plane plots which look very closely at the movements of the cantilever to be able to simulate and predict cantilever response.

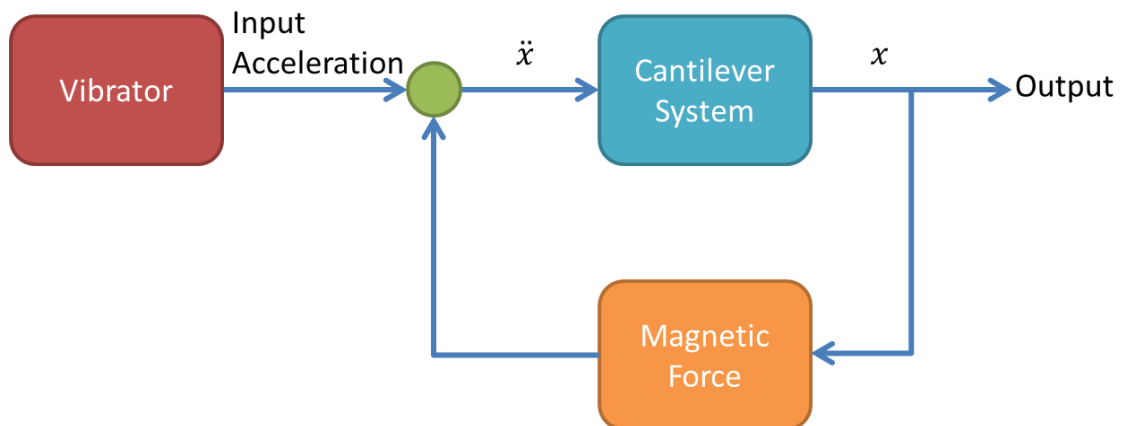


Figure 34: Block diagram of nonlinear cantilever prototype.

4.2.1. Magnets

This section explains more about the 2 magnets that are used. The first magnet is a button/tablet magnet which has a 10mm diameter and a thickness of 5mm as shown in Figure 35. The second magnet used is a bar magnet which has a dimensions of 25mm in length, 10mm in width and 3mm in thickness. Both magnets are N35 Neodymium magnets which provides about 800-900 kA/m in Coercivity.

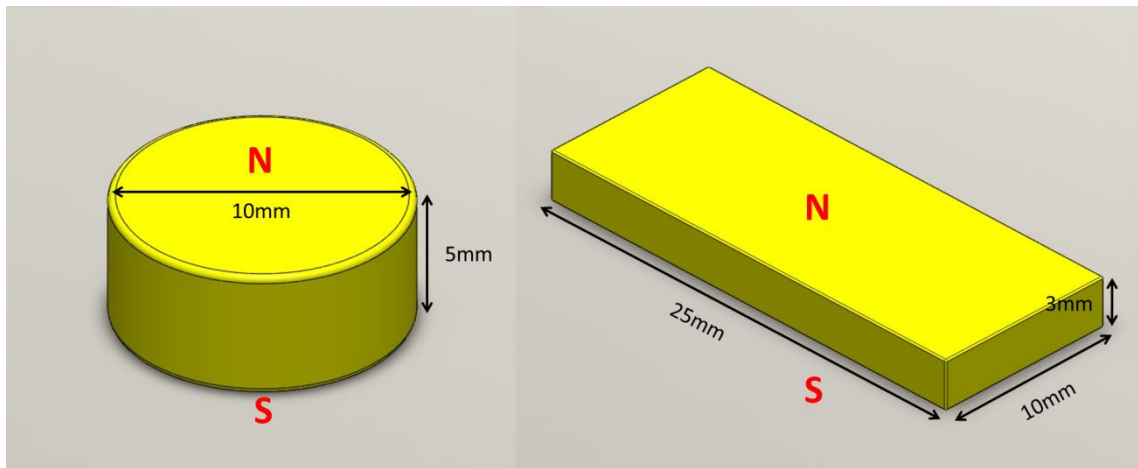


Figure 35: Tablet/Button magnet and Bar magnet that is being used.

4.2.2. Modelling of the Magnets

In order to simplify the modelling process, the magnets are treated as dipoles. The position of the dipole is then determined along with the angle for the dipole. The effective magnetic moment is then added into model to complete it. A simple block diagram (Figure 36) is attached below to illustrate the process.



Figure 36: Block diagram of magnet interaction modelling process

The aim of modelling the magnetic interaction is to determine the component of the force which causes the cantilever to deflect upwards or downwards. The assumption for the model is made that the tip of the cantilever only moves vertically with no bending or change of angle of the dipole/magnets (which the reason is explained further in Section 4.4).

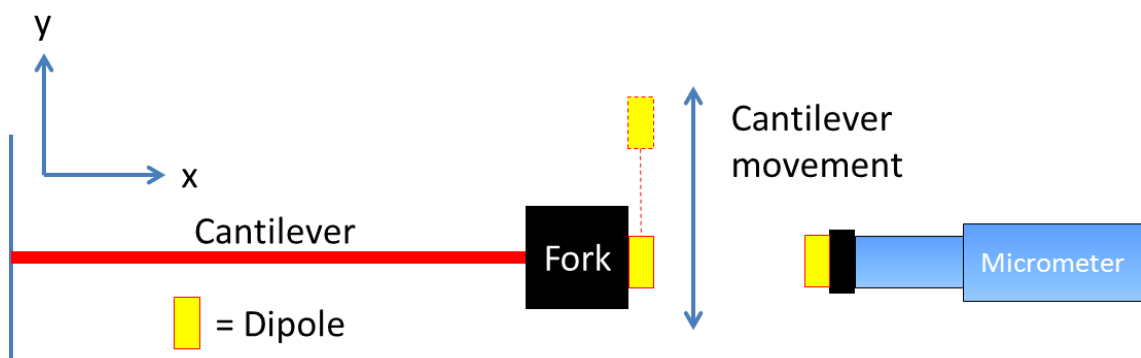


Figure 37: Dipole model movement assumption.

To start modelling the dipoles, the angular face of the corresponding magnet has to be calculated. This is done through equations:

$$\theta = \tan^{-1} (x - x_0, y - y_0) \quad \text{Equation 4.1}$$

Where x and y are the locational points for the modelling calculation
 x_0 and y_0 are the dipole positions

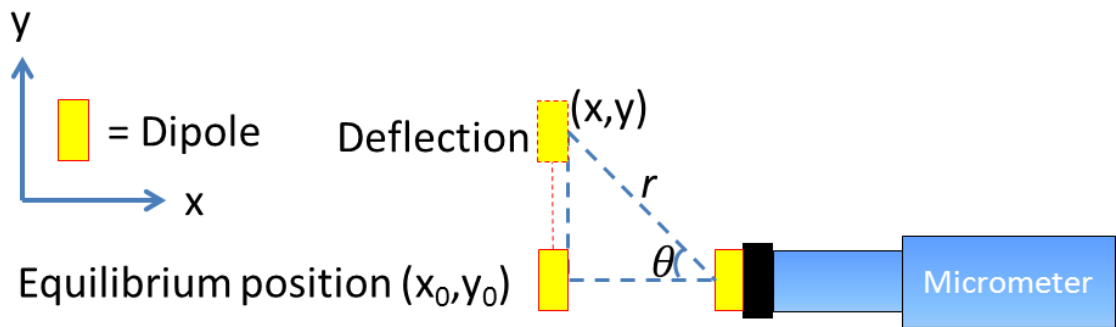


Figure 38: Diagram showing the orientation of the dipole modelled.

The *atan2* function from Equation 4.1 is to ensure that all 4 quadrants are calculated instead of only 2. The next step is then to determine the radius of the magnet model by using Equation 4.2.

$$r = \sqrt{(x - x_0)^2 + (y - y_0)^2} \quad \text{Equation 4.2}$$

Where r is used to calculate the radius of the dipole model.

For a magnetic dipole, the magnetic field in the radial direction can be expressed as Equation 4.3 and in normal direction is given by Equation 4.4 (Figure 39):

$$Hr = \frac{M_{eff} \times 2 \times \cos(\theta)}{4 \times \pi \times \mu_0 \times r^3} \quad \text{Equation 4.3}$$

And

$$H\theta = \frac{M_{eff} \times \sin(\theta)}{4 \times \pi \times \mu_0 \times r^3} \quad \text{Equation 4.4}$$

Where M_{eff} is the effective magnetic moment of the magnet
 μ_0 is a constant which is also known as the permeability of free space

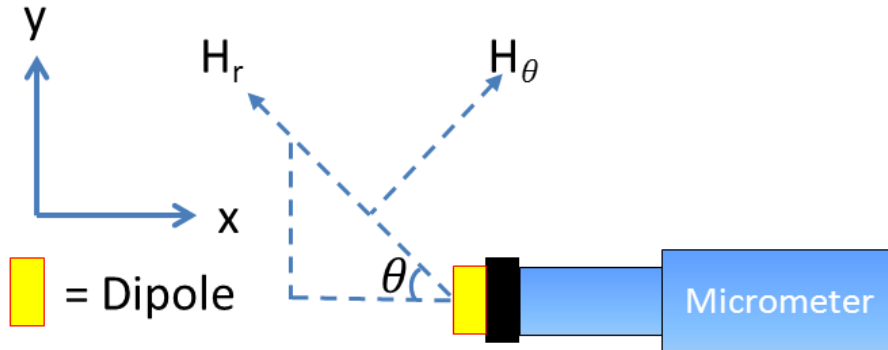


Figure 39: Diagram explaining dipole's radial and normal direction.

After obtaining the magnetic field strength of both θ and r (Equation 4.3 and Equation 4.4), the magnetic field strength for the x and y axis of the magnetic model can be obtained using:

$$H_x = H_r \times \sin(\theta) + H_\theta \times \cos(\theta) \quad \text{Equation 4.5}$$

And

$$H_y = H_r \times \cos(\theta) - H_\theta \times \sin(\theta) \quad \text{Equation 4.6}$$

Combining Equation 4.5 and Equation 4.6 will come to Equation 4.7 providing the magnetic field profile for the magnet that is being modelled.

$$H = \sqrt{H_x^2 + H_y^2} \quad \text{Equation 4.7}$$

Effectively, both magnets can be modelled using the same method.

Additionally, the Y-axis forces (Figure 40) between the dipoles can then be calculated using Equation 4.8 [50].

$$\vec{F}_{(r,m1,m2)} = \frac{3\mu_0}{4\pi r^5} \left[(\vec{m}_1 \cdot \hat{r})\vec{m}_2 + (\vec{m}_2 \cdot \hat{r})\vec{m}_1 + (\vec{m}_1 \cdot \vec{m}_2)\hat{r} - \frac{5(\vec{m}_1 \cdot \hat{r})(\vec{m}_2 \cdot \hat{r})}{\hat{r}^2} \right] \quad \text{Equation 4.8}$$

Where r is the distance between the two dipoles. m_1 and m_2 are the dipole moment (magnetic moment) of the two dipoles that are being calculated.

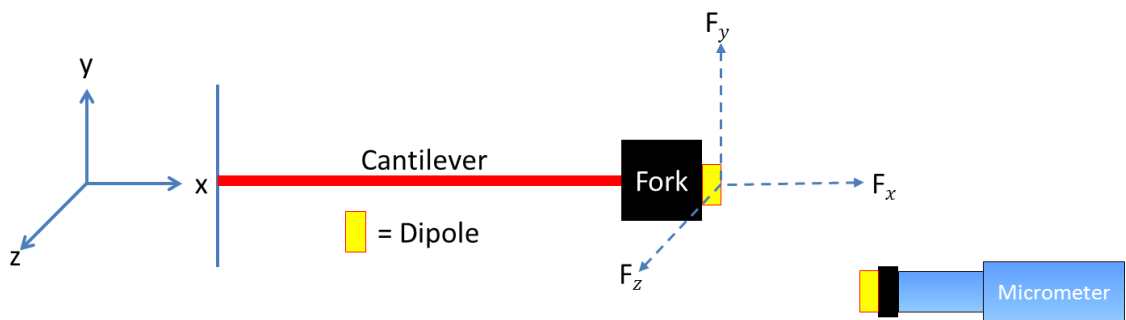


Figure 40: Direction of forces which act upon the dipole model during the modelling process.

As the magnetic moment values were not supplied with the purchase of the magnets, in order to determine appropriate values of m_1 and m_2 in Equation 4.8, an experiment was done to compare the measurements of the magnetic field strength of the model at different distances along the x-axis as well as the magnets so that these values can be used in the model.

Measurements are obtained from the experiment by measuring at the edge of the dipole moving away from the dipole on the horizontal axis. This is shown in Figure 41. Measurement starting position for each dipole measurement is different as both magnets have different thickness. The initial measurement distance of the magnet is the distance from the centre of the dipole which is taken from the thickness of the physical magnets (half thickness of tablet magnet is 2.5mm and 1.5mm was half the thickness of the bar magnet). Once the measurements were obtained, the values are then input into the model to verify the dipole model behaviour.

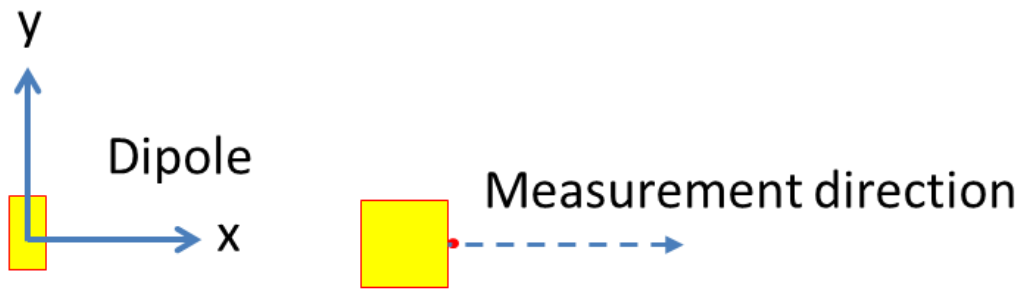


Figure 41: Dipole measurement direction.

4.2.3. Measuring the Magnetic Flux Density of the Magnets

A Gaussmeter was used to measure the magnetic flux density of the magnets. A few of assumptions were in place:

- The Hall probe sensor was positioned along the central axis of the magnet measured.
- The starting position of the hall probe sensor was as close as possible (touching) the magnet surface and moving away 1mm horizontally for each measurement.
- Measurements were taken until there was no reading (below 0.000T) on the Gaussmeter.

After obtaining the measured values of both magnets' magnetic flux density, a comparison was done between the modelled dipole measurements and the experimental measured magnetic flux density.

Figure 42 shows a comparison of the measured magnetic flux density for both magnets and that the bar had a slightly different profile compared to the button magnet. This is due to the volume and shape of the magnets. The bar magnet has a volume of $7.5 \times 10^{-7} \text{ m}^3$ while the button magnet is smaller and has a volume of $3.93 \times 10^{-7} \text{ m}^3$. The bar magnet has a lower peak flux density but this decreases more slowly than the button magnet.

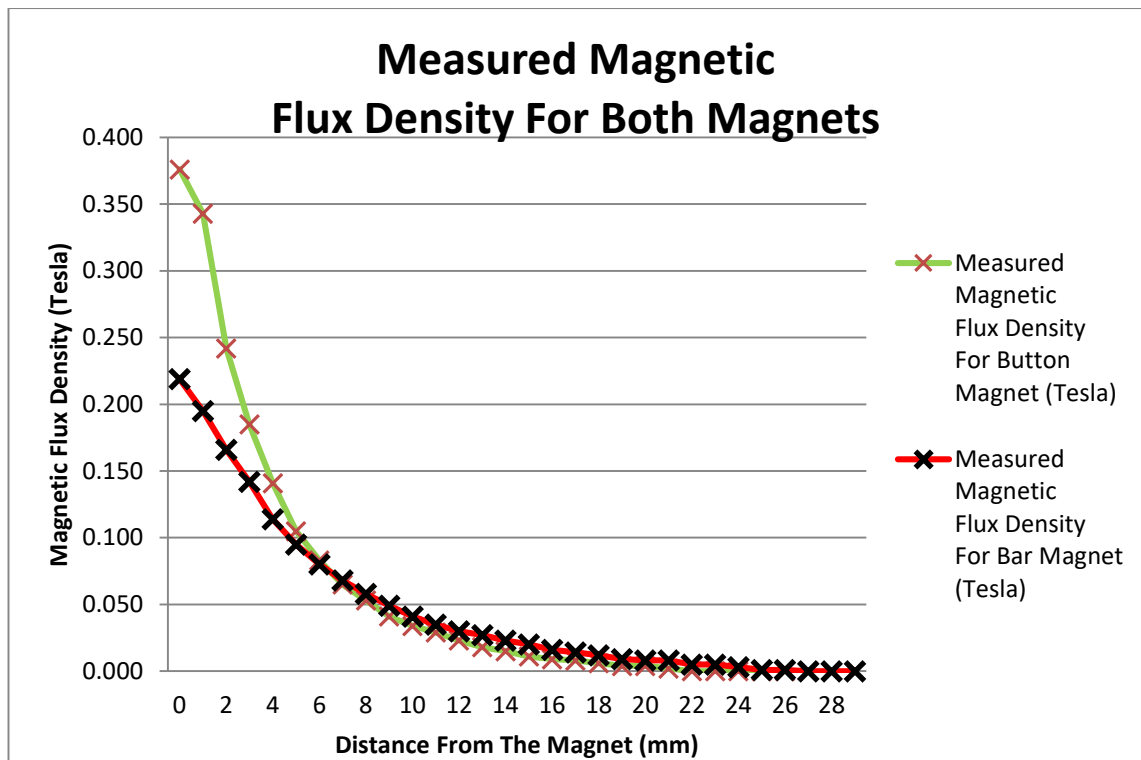


Figure 42: Comparison of both measured magnets' magnetic flux density.

4.2.4. Comparison of Modelling and Experimental Results of magnets

Figure 43 shows the results of the model of the tablet magnet against the results obtained from the experiment and Figure 44 shows similar results for the bar magnet. Both sets of experimental results show a similar trend and also displayed magnetic flux density values which are similar to the results from the models from about 10mm away from the magnets. Both these trends continued throughout the remainder of the experiment with good agreement between measured data points and the modelled values. Similar discussion could be said for the results obtained from the initial phase of the model. The results from the model of the magnet from its initial distance up towards distances before 5mm are much higher than what was measured from the experiment conducted. This is due to the dipole model breaking down at lower distances (approx. $5\text{mm} \pm 2\text{mm}$). In comparison to the experiment, the model's results were plotted in an ideal situation whereas the experiment results had to take many factors into consideration such as the tolerances and discrepancies of the experiment equipment.

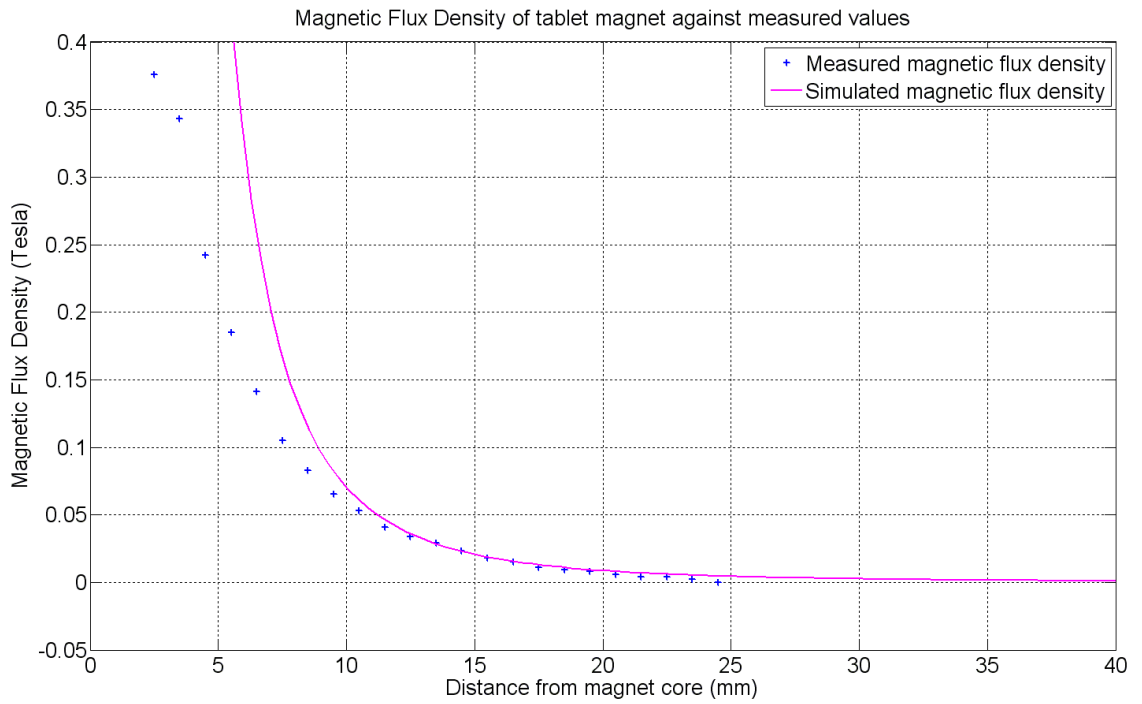


Figure 43: Modelled magnetic density for the tablet magnet compared with measured values from experiment.

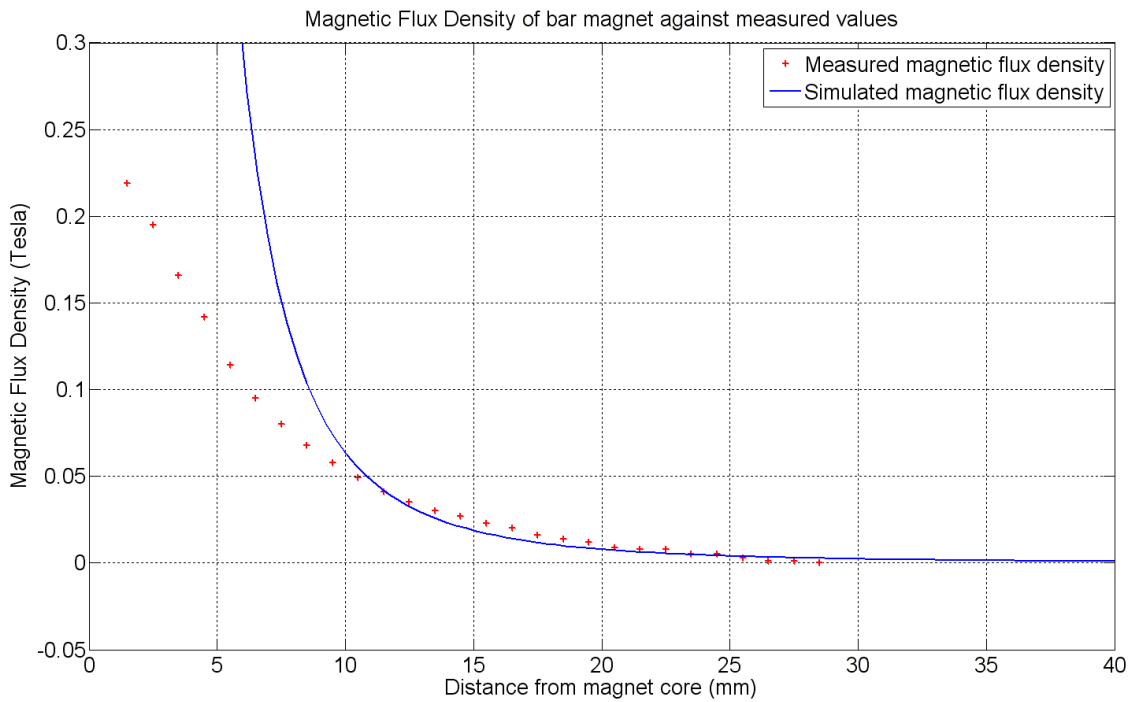


Figure 44: Modelled magnetic density for the bar magnet compared with measured values from experiment.

In conclusion, both sets of modelled magnets show the same trend upon comparison with the results obtained from the experiment.

4.3. Modelling the Forces Between the Two Magnets

This section models the forces (Equation 4.8) that are acting on the magnets which are attached to the cantilever prototype system. Figure 45 shows a block diagram of the process of modelling the forces that is acting upon the magnets and ultimately the whole cantilever prototype system. Matlab source code for this section is attached in 0



Figure 45: Block diagram of the modelling process of forces of the dipoles.

Figure 46 presents the output forces when the dipoles are simulated for similar distances which the prototype design is capable of. The force is modelled at each distance of separation from 5mm up to 18mm with the direction of deflection of the cantilever being in both positive and negative deflection. As the prototype is designed as an electromagnetic energy harvesting device; there is a need to leave a gap between the magnets for the coil. Hence the 5mm starting position was chosen to reflect that.

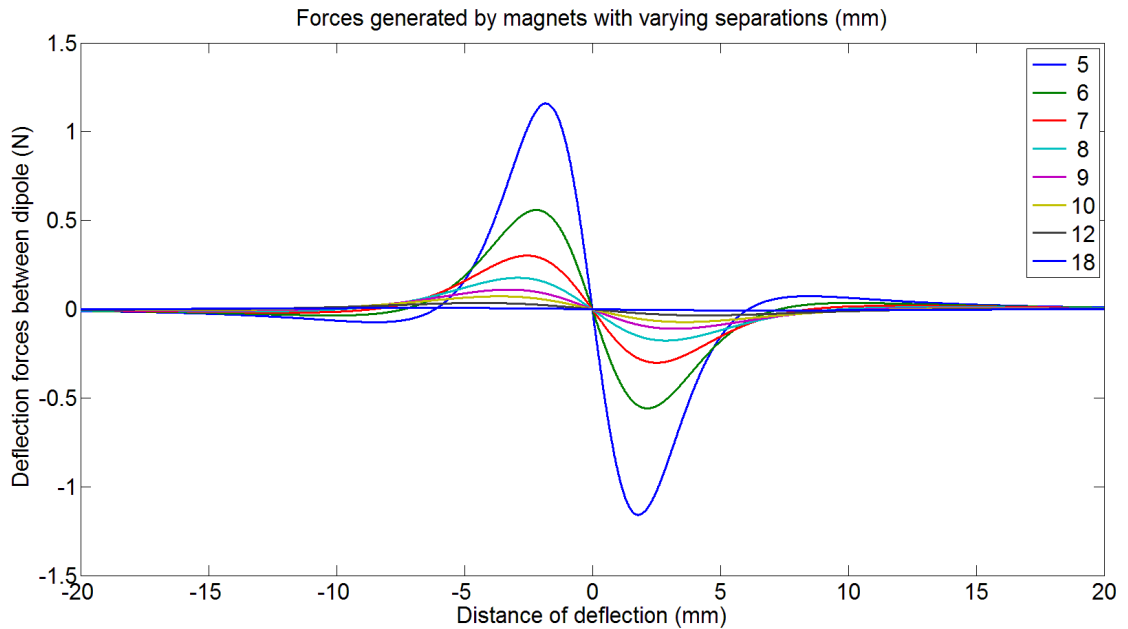


Figure 46: Force generated from dipole model with varying distances.

As expected, the deflection force at zero deflection is zero but then increases in magnitude for a deflection of around 2mm before returning to zero for a large deflection. The peak forces for different distance of separations are shown in Figure 47.

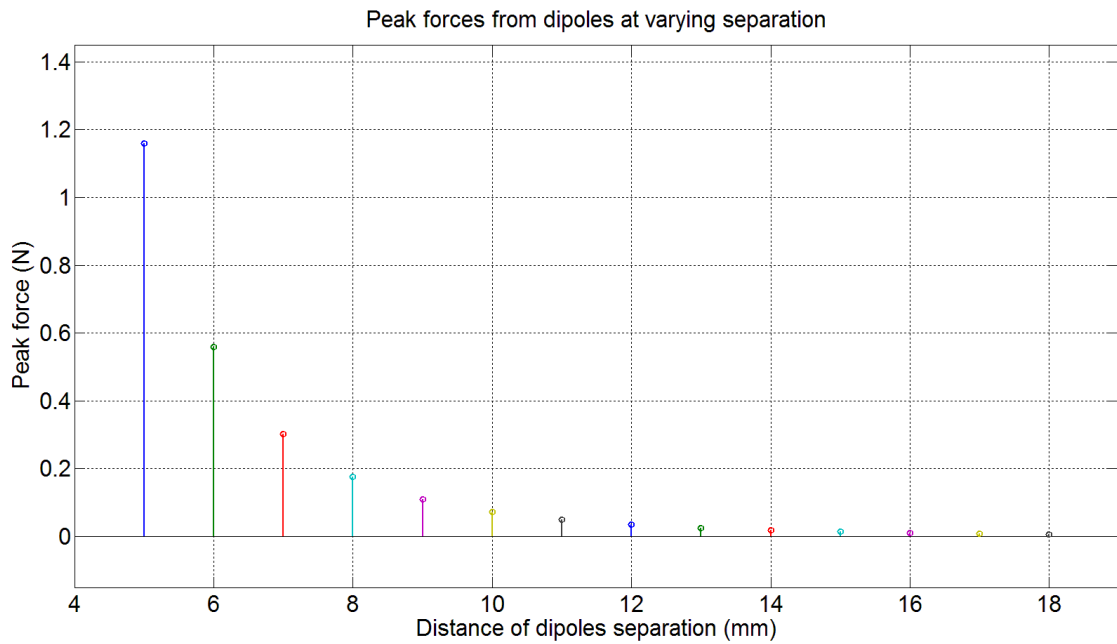


Figure 47: Comparison of peak forces measured from 5mm up towards 18mm dipole distance separation.

The data plotted in Figure 46 is included in a look up table and combined with the cantilever model in Matlab Simulink as shown in Figure 54 when used to model the complete system.

4.4. Modelling the Cantilever

This section discusses the process of modelling the cantilever that is used within the prototype constructed. In order to be able to have accurate modelling of the cantilever system, a few parameters should be set to replicate the actual system. These parameters can be determined from physical measurements but also require experimental validation. They are:

- The total mass of the cantilever system including the tip mass.
- The spring constant of the cantilever.
- The damping ratio and damping coefficient.
- The resonant frequency of the actual prototype.

The mass of the spring steel cantilever which has a volume of 65mm x 19mm x 0.9mm is multiplied by the material density which contributes to a total of 8.8g. The weight of the tip mass is then added into Equation 4.9 [51] [52] producing a total effective mass of 19.4g.

$$m_{eff} = 0.23m_{beam} + m_{tip} \quad \text{Equation 4.9}$$

The spring constant of a simple cantilever can be determined using Equation 4.10 [51].

$$k = \frac{3EI}{L^3} \quad \text{Equation 4.10}$$

Where L is the length of the cantilever and E is the Young's modulus of the beam material (Young's modulus for 304 Stainless Steel which is the material of the cantilever is 200GPa) and I is moment of inertia of the beam cross-section shown in Equation 4.11 for a rectangular cross section.

$$I = \frac{bh^3}{12} \quad \text{Equation 4.11}$$

Where b is the width of the beam and h is the depth/height of the beam. Completing Equation 4.10 provides a value of 2522N/m. The prototype structure is more complex than the simple cantilever model; the total length of the complete cantilever is approx. 93mm with the addition of the fork which houses the magnet and not 65mm which is only the cantilever spring. Additionally, the fork and magnet do not flex whereas the spring does. If L of Equation 4.10 is taken as 93mm, k would only be 861N/m which differs greatly compared to the original value of 2522N/m. Hence, more consideration needs to be taken into account for a more accurate spring constant reading of the whole spring cantilever system.

Back in section 4.1, it was mentioned that the fork that is attached to the end of the spring has three equal faces and weighs 11.7g. The magnet which weighs 5.6g is attached to the open end of the fork. Putting equal amount of weight on each side of the fork makes it 3.9g/side of the fork. The weight distribution of the fork and magnet is calculated to be leaning towards the magnet by 1.53mm from the centre of the whole attachment. Figure 48 shows a simple drawing with the important dimensions of the whole attachment with the red dot showing the true balance point of the fork and magnet attachment.

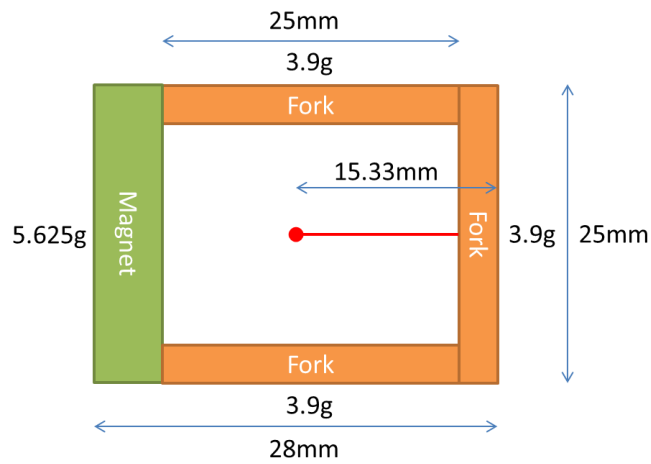


Figure 48: Red dot showing the centre of gravity for the fork and magnet attachment as tip mass of the cantilever.

Taking 15.33mm as the centre of gravity of the fork and magnet attachment, the new L from Equation 4.10 is taken as 80mm which ultimately provides 1336N/m as the representative value of k for the whole cantilever spring system.

To verify the appropriate value of spring constant, an experiment was carried out where a laser displacement sensor was placed on the blue pad (Figure 49) at the end of the spring shown in Figure 49 and a force was applied on positions A and B which are represented by a yellow and red dot respectively. The displacement of the spring was recorded and compared.

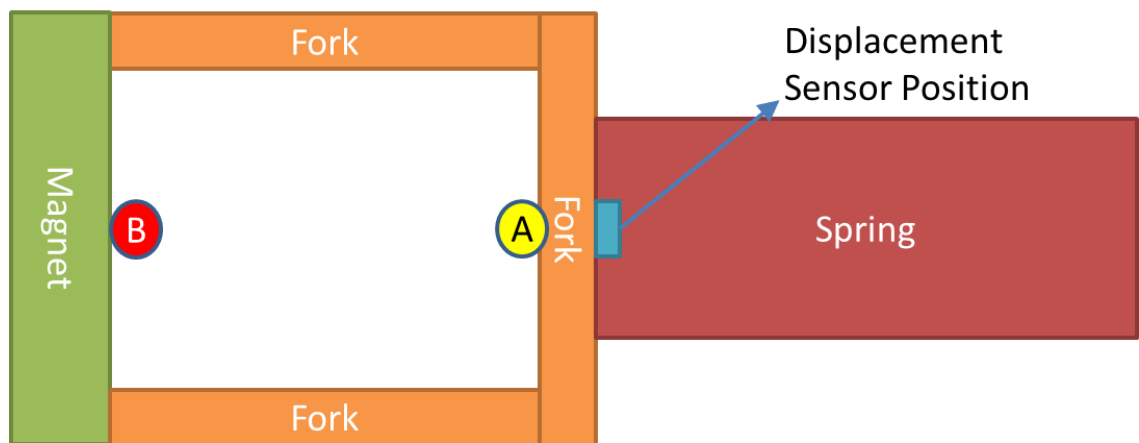


Figure 49: Spring constant experiment set up. A and B (Yellow and Red dots) are locations where Force was applied.

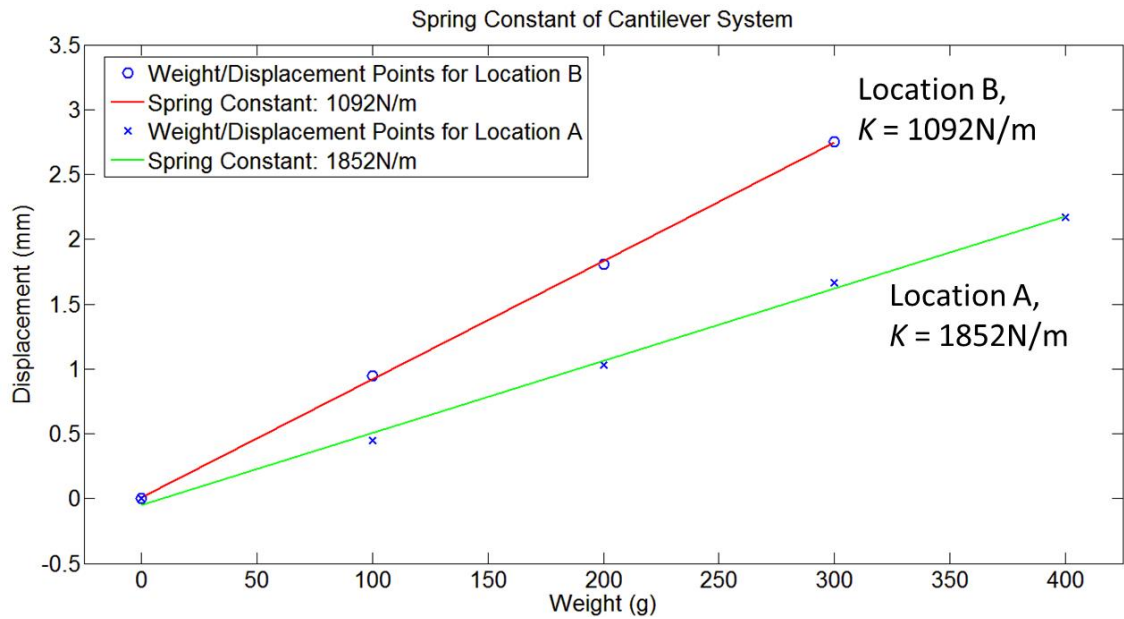


Figure 50: Result from the experiment of determining Spring Constant of the spring cantilever system.

Figure 50 shows the results obtained from the experiment. It also proved that the calculations based on Equation 4.10 were accurate as the overall value for k for location B to be close to the theoretical value of 861N/m. The values recorded for location A was also reasonable even though the overall value differs by 669N/m. However, looking closer at 100g, the measured spring constant value was approx. 2200N/m, differing by about 13% to the 2522N/m calculated. As the displacement was measured in mm and force was applied in grams, even a small tolerance within the experiment system will result in a fairly large difference in result. So it would seem that taking a representative value of approx. 1300N/m as the cantilever spring constant during the modelling process is within the design limits.

The next stage after obtaining the spring constant, k and the effective mass of the system, m_{eff} would be obtaining the resonant frequency of the system. Using k and m_{eff} that has been obtained and replacing them into Equation 2.9, $\omega_n = \sqrt{\frac{k}{m}}$ will provide us with a resonant frequency of 41.7Hz.

With the ability to measure accurately the prototype system's actual resonant frequency with a signal generator, a frequency sweep was done to confirm the prototype's resonant frequency. The resonant frequency measured turned out to be 33.7Hz which differs from the 41.7Hz which was calculated previously.

Using the resonant frequency measured from the prototype, reversing Equation 2.9 provided k with a value of 868N/m. This value differs greatly compared to the 1336N/m value for k but is almost identical to the 861N/m value which was obtained when L of Equation 4.10 was set as 93mm which was the full length of the cantilever even with only 65mm of it was the spring element. Based on the experimental resonance frequency, the ultimate representative value for k which is to be used within the model will be set to 867.6N/m for k for all simulations.

Additionally, the cantilever is being modelled where there is a free end load or tip mass, P . The cantilever's (Figure 51) slope θ and maximum deflection δ_{max} of a cantilever are then governed by Equation 4.12 and Equation 4.13 [53] [54].

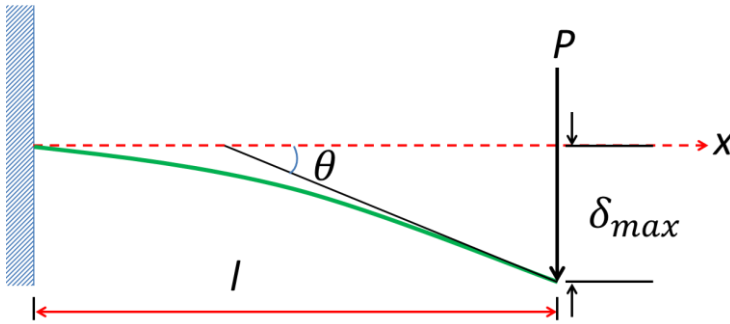


Figure 51: Drawing showing the cantilever's slope angle and maximum deflection.

$$\theta = \frac{Pl^2}{2EI} \quad \text{Equation 4.12}$$

$$\delta_{max} = \frac{Pl^3}{3EI} \quad \text{Equation 4.13}$$

Taking the maximum deflection on one side of the cantilever (fork and spring) at 20mm will result in maximum force, δ_{max} , pushing upon the cantilever to be at 17.15N which then corresponds to the maximum slope θ , of 18.5 degrees. Furthermore, the interaction between both magnets to generate nonlinear response is at the lowest point at maximum deflection of the cantilever. Based on the forces generated by the magnets simulation (Figure 46), there is no significant amount of interaction between the magnets after the 10mm deflection mark. Hence it could be said that at 10mm or less of deflection, the cantilever will experience a maximum of 9.2 degrees slope or less which

is negligible. So an assumption was made to treat the system as a lumped spring-mass system.

Another experiment was conducted to determine the damping ratio ξ of the system. A downward force was applied onto one end of the cantilever when the cantilever is at its furthest separation distance at 18mm. It is then released and the cantilever displacement was measured using a laser displacement sensor from the time at which it was released until it reached equilibrium. Using the “logarithmic decrement” method, the damping coefficient of the system can be found which in turn will reveal the damping ratio of the system.

Logarithmic decrement shows the rate of decrease of amplitude of free vibration with damping. It is based on the natural logarithm of the ratio of two successive amplitudes within a system [55]. Based on Figure 52, the damping coefficient can be obtained through Equation 4.14.

$$\delta = \ln \frac{X_1}{X_2} = \xi \omega_n T_d \quad \text{Equation 4.14}$$

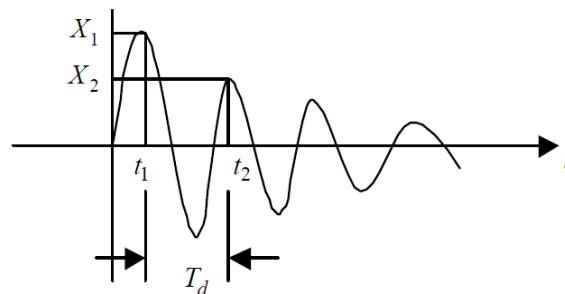


Figure 52: Logarithmic Decrement

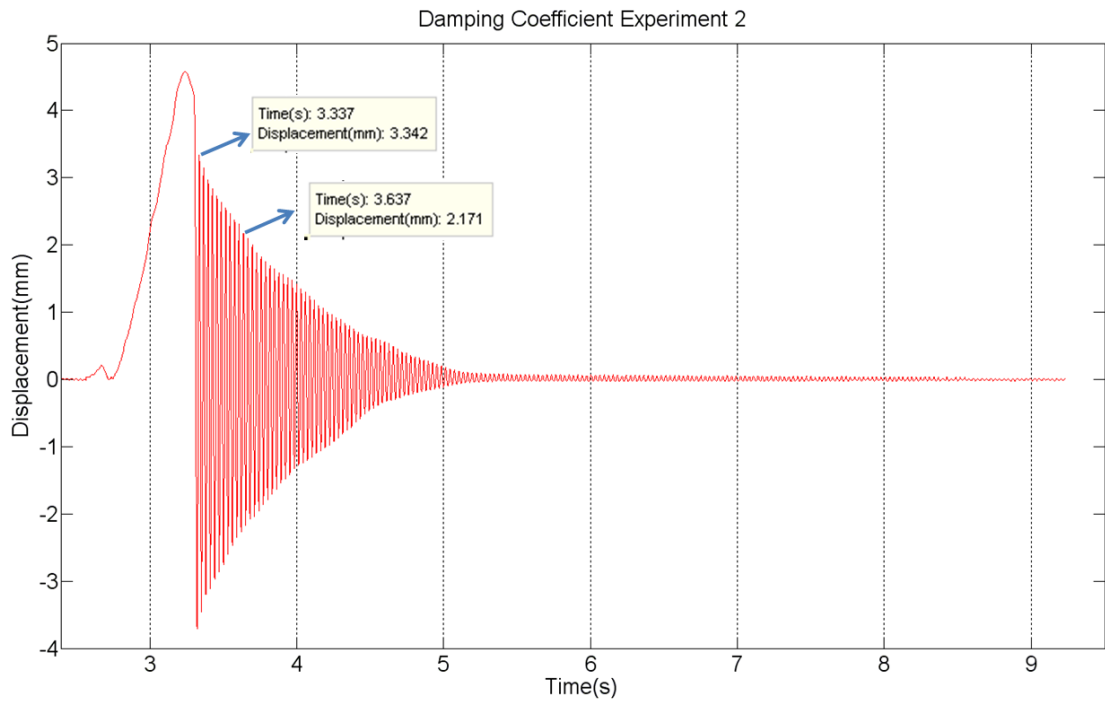


Figure 53: Damping Coefficient Experiment.

Based on the experiment data obtained from Figure 53 and Equation 4.14, δ can be determined as 0.0617 and $\xi = 0.010$. This is taken from the first two peaks of the measurements obtained. This is due to the system possesses the highest amount of damping whilst it still has the highest potential energy / displacement. The amount of damping decreases along with the available potential energy /displacement left in the system until it reaches equilibrium position. Hence, a value of 0.01 will be selected for use in the simulation as the damping ratio.

Additionally, the frequency of the cantilever obtained from the experiment for the damping measurements was 33.33Hz. These were taken from the measured values and averaged over 10 cycles to obtain a more accurate frequency. Additionally, this result is also very similar to the representative value of 33.7Hz which was measured previously through the spring constant experiment hence is within the acceptable limits.

With the values of the mass of the cantilever system, m_{eff} , the spring constant, k and the damping ratio of the system, ξ , the system can be modelled to behave similarly to the prototype. Figure 54 shows the model of the system is input with the values which are obtained and shown in Table 11.

Description	Symbol	Chosen Value
Spring Constant	K	868N/m

Damping Ratio	ξ	0.01
Effective Mass of Cantilever	m_{eff}	19.3g

Table 11: Variables and values used within the modelling process.

4.5. Matlab Simulink Model of Complete Nonlinear Cantilever Prototype

This section combines the earlier findings of section 4.2, 4.3 and 4.4 into a complete model which represents the nonlinear prototype system. To help with the modelling process of the nonlinear prototype, a model was built in Simulink to reflect Equation 2.3 with the addition of the nonlinear forces generated by the 2 opposing magnets to enhance accuracy of the model. Matlab source code for this section is attached in Appendix D and Appendix E.

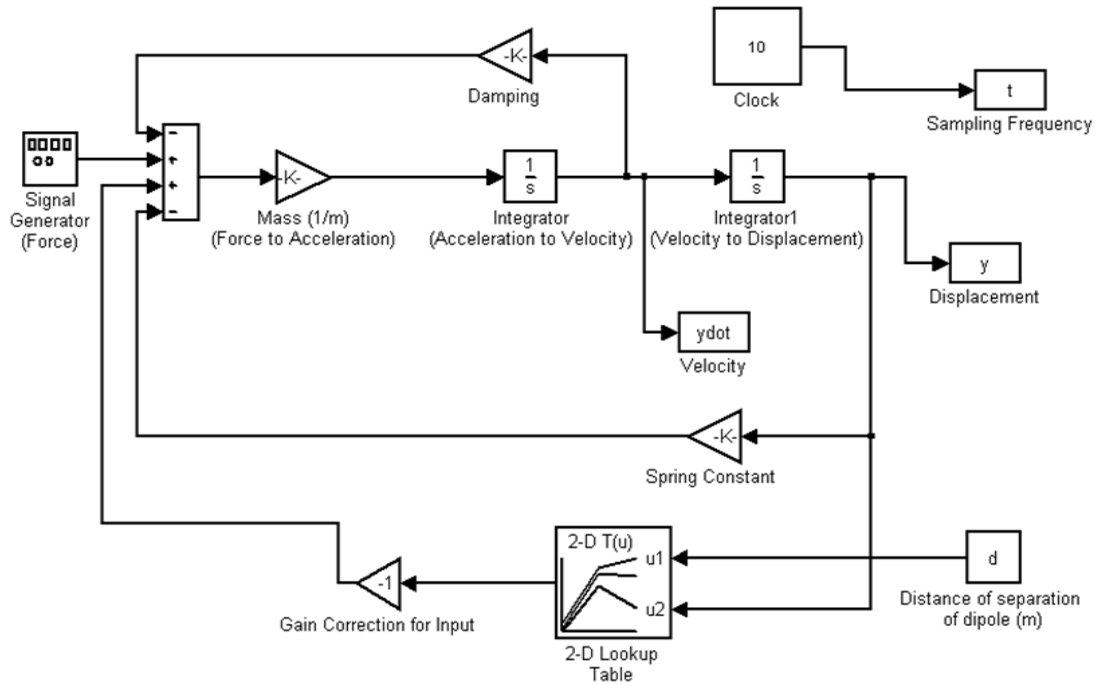


Figure 54: Simulink prototype used to simulate the cantilever.

$$m\ddot{x}(t) = -(d_m + d_e)\dot{x}(t) - kx(t) - fx_{nl}(t) + f_{source}(t) \quad \text{Equation 4.15}$$

Figure 54 corresponds to Equation 4.15 which is the nonlinear function within the feedback channel where fx_{nl} is the nonlinear force that is generated by the two opposing dipoles in this model. Calculation of the nonlinear forces of fx_{nl} stems from Equation 4.8 which requires the displacement of the dipoles at any given time as well as the magnetic

moment of the magnets which the outputs are stored in the lookup table within the model. Table 12 provide the values that were used to model the nonlinear cantilever.

Description	Symbol	Chosen Value
Spring Constant	K	868N/m
Damping Ratio	ξ	0.01
Effective Mass of Cantilever	m_{eff}	19.3g
Forces of Excitation Acceleration	F	0.5g, 1.0g and 2.0g
Simulation Frequency	ω	7.16Hz to 55.71Hz
Distance of Separation	d	5mm to 18mm
Maximum Deflection	yy	-20mm to 20mm
Sampling Frequency	t	10000Hz

Table 12: Parameters / variables used for the nonlinear cantilever model.

After having input the values into the model, a simulation was run to check if the simulated model would produce the same levels of output as the prototype. The waveform from the Damping Coefficient Experiment (Figure 53) is compared to the model produced in Figure 55. This proves the accuracy of the model when provided the same levels of initial displacement. The frequency obtained from the simulation was 33.7Hz which is extremely close to the experimental value of 33.33Hz which is acceptable. This confirms that the model is an accurate representation of the cantilever prototype along with the magnetic model which was discussed in previous sections.

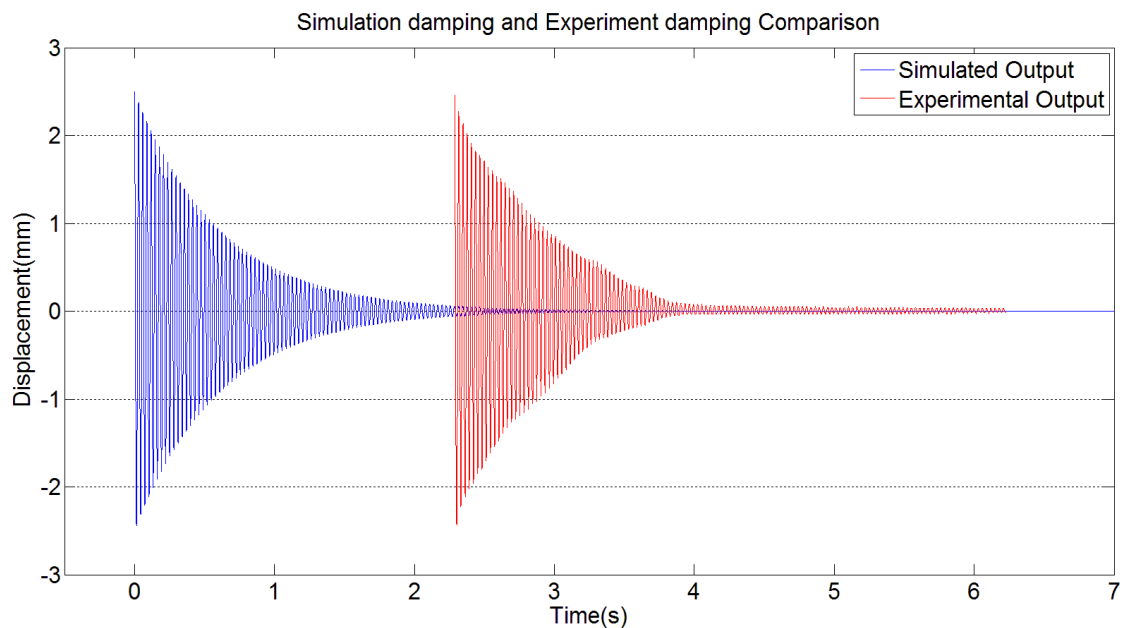


Figure 55: Simulated output compared with measured experimental results.

The model (Figure 54) takes the dipole force calculations (Section 4.3) and stores it as a 2-D look-up table which is continuously referred to during the modelling process. This is also added into the model along with the input acceleration to calculate how much deflection or displacement has occurred on the cantilever model.

Additionally as it is a nonlinear system with opposing magnets attached to each other, there will be a situation where at low distance of separation between the two magnets, the repulsion force of the magnet has the ability to “push” the cantilever away from its natural equilibrium point to a new equilibrium point. To verify this, taking the spring constant obtained previously and compared with the forces generated by the dipole models, a graph is plotted across the forces generated and intersection points would be able to tell where the “new” equilibrium points are within the cantilever system at the selected distance of separation of the magnets. Figure 56 presents the dipole forces that are “intersected” with the spring constant of the cantilever. Note that only the 5mm distance of separation are intersected by the spring constant which will show a + or - 1.16mm deflection as the new equilibrium and the rest of the distances are unaffected.

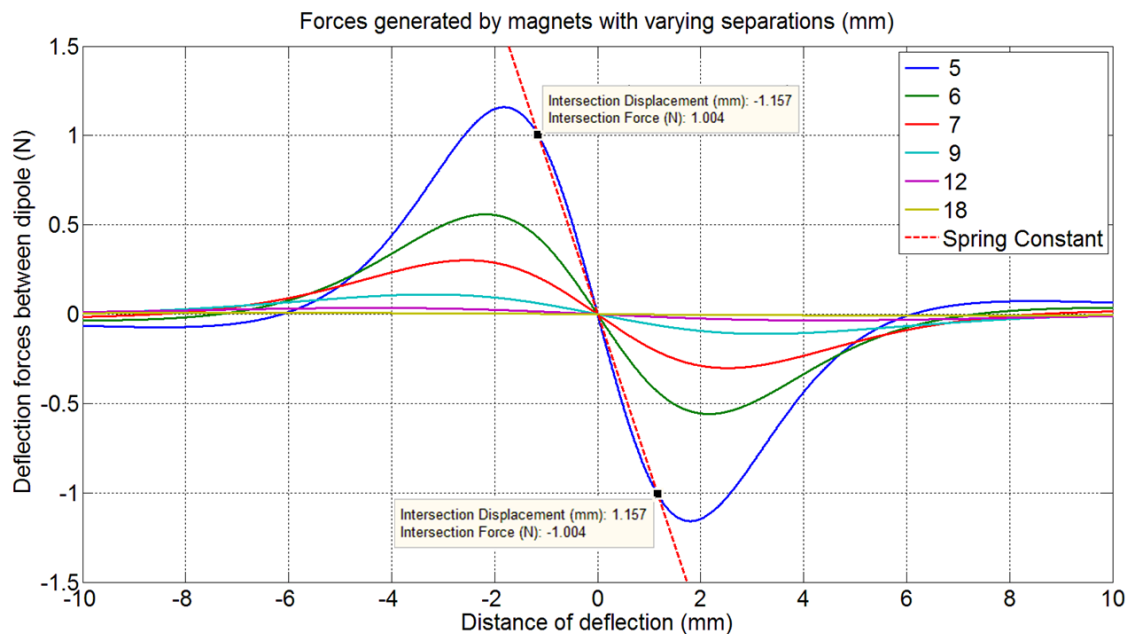


Figure 56: Dipole forces simulated with spring constant.

An experiment was conducted to measure and validate the simulated “new” equilibrium points on the constructed prototype and is shown in Table 13. Table 13 also

shows that all selected measurement points showed an upward movement of the cantilever equilibrium position except the 18mm distance of separation.

Distance of separation of magnets	Deflection of cantilever
5mm	+1.905mm
6mm	+1.444mm
7mm	+1.058mm
12mm	+0.125mm
18mm	0.000mm

Table 13: Experimental results on "New" equilibrium points for selected distances of separation of magnets.

In comparison to the simulated result, the experimental results showed a slower rate of decay of opposing magnetic forces which resulted in the cantilever being shifted up into a “new” equilibrium position for all measurement points except the 18mm position. This is due to the modelling process which treated the magnets as dipoles of a similar size whereas in the prototype, both magnets are of different size and shape which is reacting in a slightly different way compared to the model.

However, the measured result of +1.905mm shift from the original equilibrium position at 5mm distance of separation differs by 0.748mm, which is a negligible amount of difference as this is less than 4% discrepancy compared to the total displacement. Hence, the model is deemed acceptable.

4.6 Human Movement and Nonlinear Energy Harvesting

From Section 3.0, the human movements were defined as everyday movements which covered “walking”, “jogging” and “high-knees”. It was designed to cover typical everyday movements which are extremely normal like walking to something slightly athletic like high-knees.

In an ideal situation, the prototype harvester itself would be used directly to test in real time with the human movements generated if it was capable of producing the power achieved on the shaker. However, it has been clearly shown that the prototype has a resonant frequency of around 34Hz which is about ten times higher in frequency than the highest recorded movement frequency shown in Table 10 in Section 3.2. This is limited by the spring constant and mass of the cantilever. Having an extremely low

resonant frequency (3Hz) would require either a much larger mass and/or a much lower spring constant, both of which would cause considerable inconvenience to the user.

Hence if the resonant frequency of the new prototype system is set to 3Hz and the effective mass of the cantilever would stay the same, the spring constant that is required of the cantilever would be 6.7N/m (ie: polymer foams). On the other hand, if the original spring constant is kept and the mass needed to be changed to achieve 3Hz resonant frequency, a mass of over 400g would be required. This would be inconvenient to the user.

However, constructing a prototype with the new specifications and testing it in a systematic manner with the shaker would not be possible because the shaker is not able to produce sufficiently large displacements at 3Hz. For this reason, the simulation model will be adjusted to investigate the kind of behaviour which might be expected for a cantilever designed for lower frequency. The model may be used to simulate the output of the harvester if the cantilever spring constant was adjusted to 6.7N/m whilst keeping the same effective mass to achieve 3Hz resonant frequency. It has to be noted that only the spring constant of the cantilever is changed in the model to reflect the change of resonant frequency required. The frequency sweep is then set to run from 0.8Hz to 4.8Hz (5 rad/s to 30 rad/s). Additionally, there are no limitations on the maximum displacement achievable from the model.

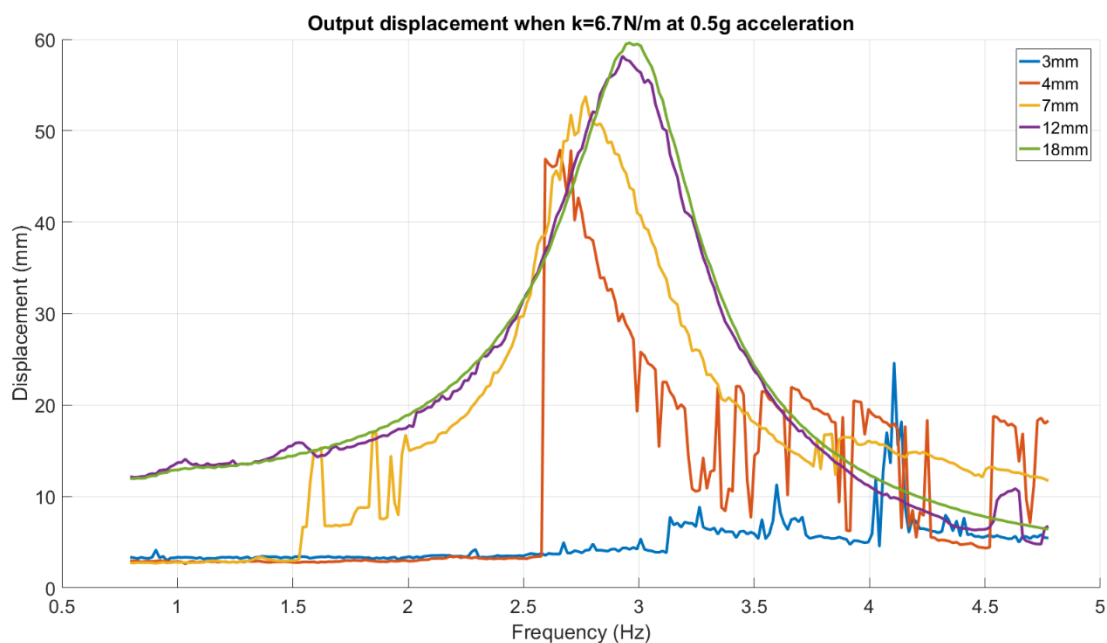


Figure 57: Displacement outputs when $k=6.7\text{N/m}$ at 0.5g acceleration.

Figure 57 shows the displacement output from the model after the change of the spring constant to 6.7N/m to achieve a resonant frequency of 3Hz (18.8 rad/s). It is clearly shown that only the 18mm separation distance has its resonant frequency at 3Hz and the lower the separation distance, the lower the resonant frequency is with the 3mm separation having a resonant frequency after 4Hz frequency. This model indicates again that the nonlinear dynamics are able to change the resonant frequency of the system whilst operating within the nonlinear region.

Subsequent models were running at 2g and 3g accelerations even though producing 3g acceleration from daily human movements might be uncommon and unpleasant but it is to verify if higher accelerations are sufficient to overcome the opposing forces which is holding back the lower separations model.

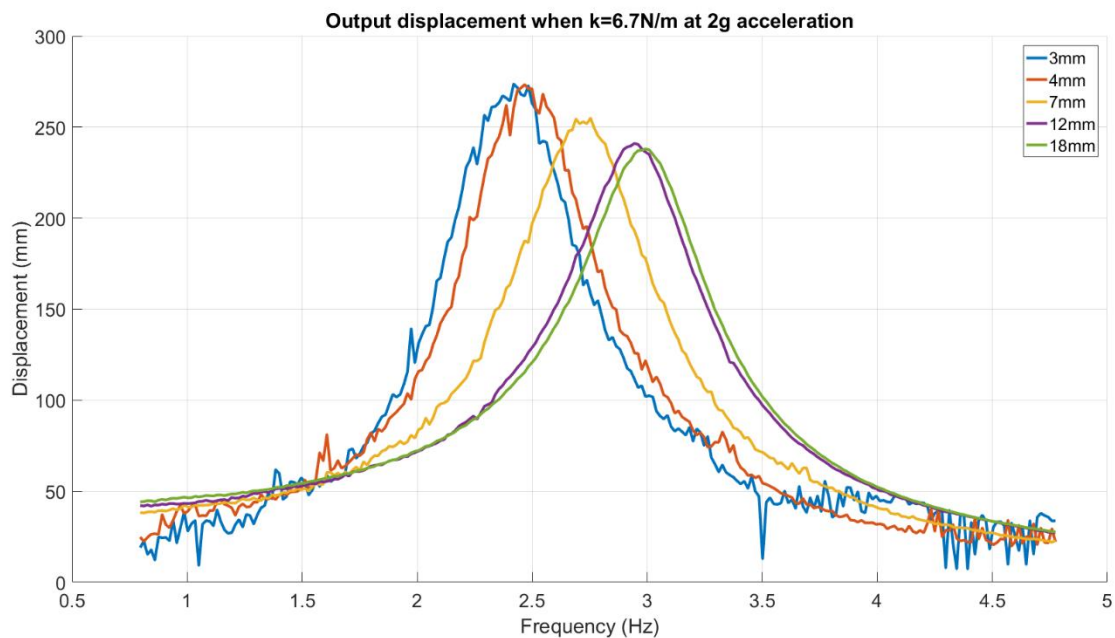


Figure 58: Displacement outputs when $k=6.7\text{N/m}$ at 2g acceleration.

Figure 58 and Figure 59 shows the model displacement outputs when run at accelerations of 2g and 3g. Here, both models showed higher response compared to the linear region (18mm) as well as wider bandwidth too. Bandwidth measurements are set at Full Width Half Max (FWHM) from the output displacements and are shown in Figure 60.

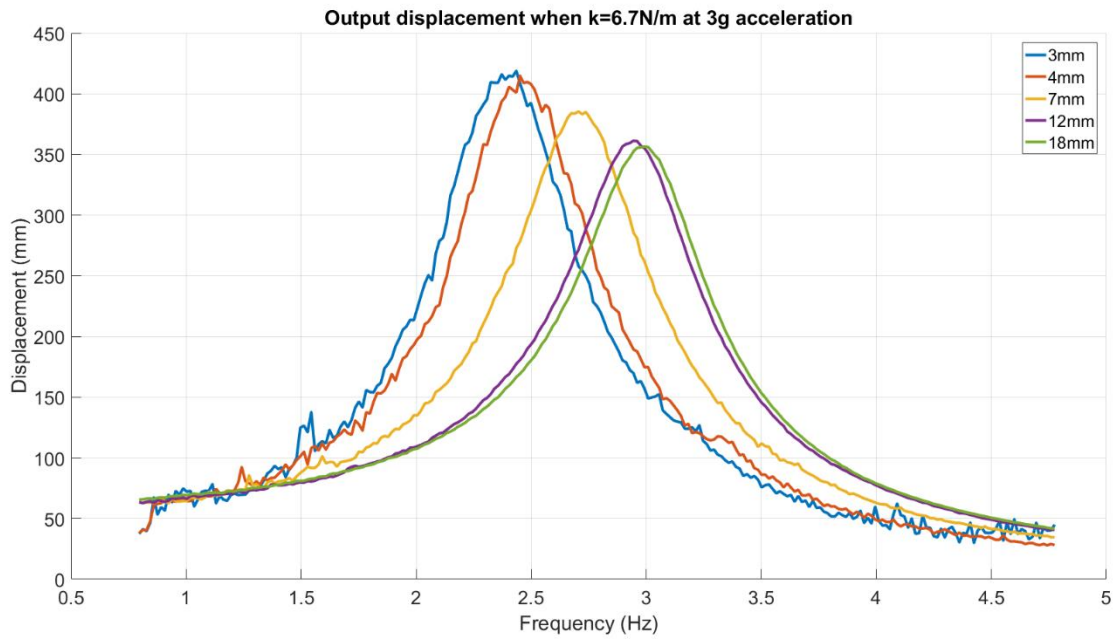


Figure 59: Displacement outputs when $k=6.7\text{N/m}$ at 3g acceleration.

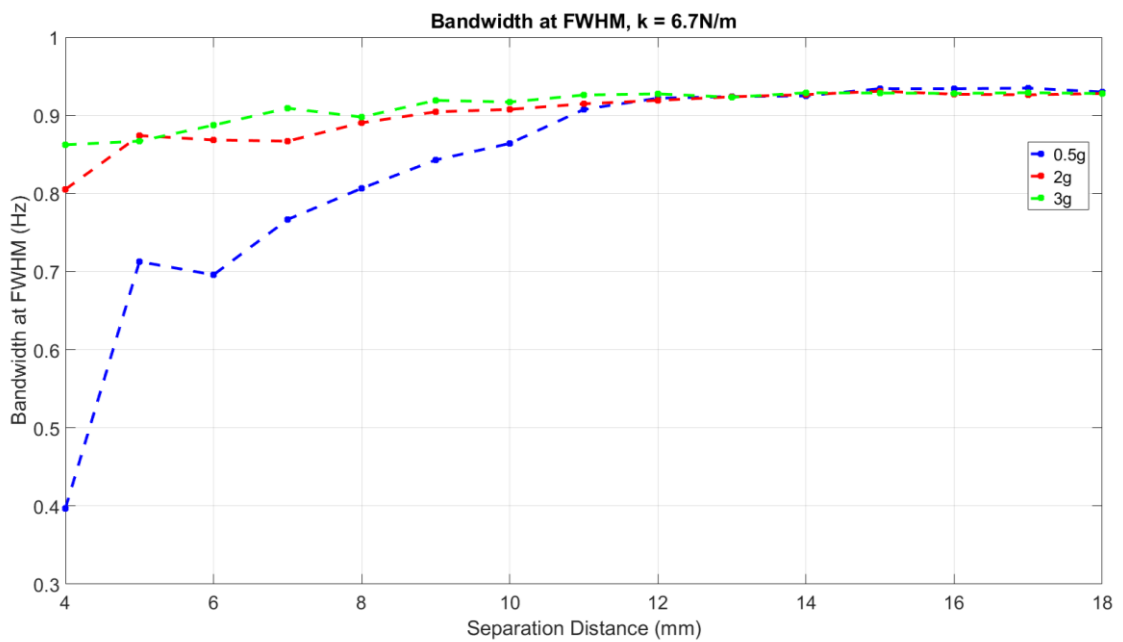


Figure 60: Bandwidth from the models at 0.5g, 2g and 3g acceleration.

By using the results obtained from the model, it is clear that the nonlinear region is the preferred region as it provides a higher peak displacement. The nonlinear dynamics acting upon the cantilever system also shifted and reduced the resonant frequency which helps with lower frequency human movements such as walking.

From the bandwidth measurements, it is shown that the cantilever was not able to vibrate freely at very low separation distances at low accelerations thus contributing to bandwidths as low as 0.4Hz at 4mm separation under 0.5g acceleration. This problem however was not seen in similar models under 2g and 3g accelerations where the bandwidth measurements were almost constant at around 0.9Hz throughout all separation distances. It also has to be noted that the models achieved in excess of 400mm displacement under the 3g acceleration model and this is not possible from the prototype. Hence, further modelling work as well as experimental work would be based around the prototype's resonance frequency (ie: +/- 20Hz from resonance frequency).

4.7 Frequency Response of the Nonlinear Cantilever Model

This section discusses about the frequency response obtained from the Nonlinear cantilever model (Figure 54) The modelling process is repeated for different amplitudes of acceleration excitation on the system as well as each change towards the distance of separation of the two dipoles (magnets).

A frequency response ranging from 8 to 50Hz was simulated under an excitation force of 0.5g, 1.0g and 2.0g acceleration. Distances of separation of the magnets which are too close such as 1mm to 4mm are not considered because the values obtained from the simulation are not realistic representations in the actual prototype because it assumes a dipole model of the magnets (the frequency response simulation ran at 1mm separation returned displacements upwards of 20m!).

The displacements of the modelled cantilever are measured and displayed instead of the velocity of the cantilever (which determines output voltage for the whole system eventually). This is due to the difficulty measuring the velocity of the cantilever in experiments. Whilst measuring the displacements of the cantilever experimentally would not pose a problem with a laser displacement sensor at high frequencies.

Also, due to the number of separation points between the magnets that were simulated, it is impossible to show every single result or output obtained. Hence a few distances of separation between the magnets were chosen and the frequency responses for the selected distances of separation are presented in Figure 61. All frequency responses from all separation distances from all 3 accelerations are placed in Appendix F for references.

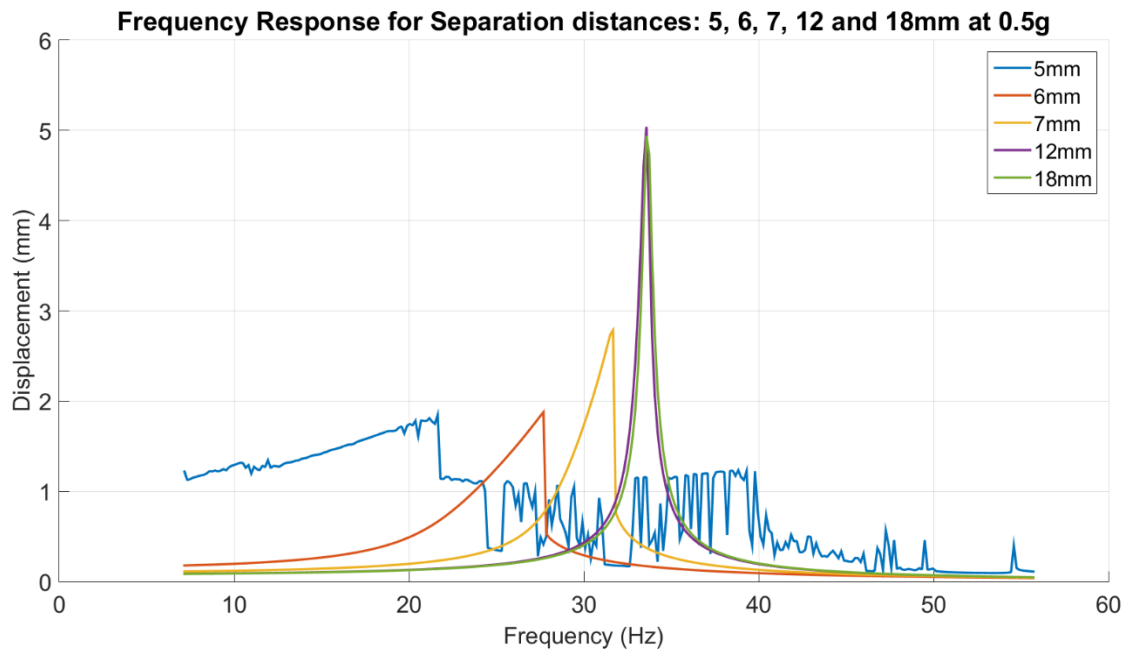


Figure 61: Frequency response simulated for a selected set of separation distances at 0.5g acceleration.

From Figure 61, there is a clear trend of that the peak displacement of the cantilever simulation increases as the separation distance between the magnets gets wider up until the latter section of the separation distances (12mm and 18mm) where the peak displacement was achieved at 33.6Hz. The simulated cantilever exhibits nonlinear behaviour when the separation distance between the two magnets are very small (5mm, 6mm and 7mm) even up to 12mm where there is still a small amount of nonlinear behaviour during the drop off phase from the peak displacement, coming down from the resonance frequency. However, when the distance between the two magnets is sufficiently large, the simulated cantilever behaves like a typical linear cantilever system.

A closer look when the 5mm distance of separation of magnets show that there is a lot of complex movements from the simulated results as the displacements from the cantilever can have a fairly large jump in amplitude from one frequency to another. This could be caused by the cantilever moving into one of the two extreme potential wells, oscillating (smaller displacement) within the well and coming back out of the extreme potential well in a similar situation to Cottone's Regime 3 in Section 1.0. The cantilever may also potentially return into the equilibrium / normal plane from the extreme potential wells during another frequency. A study of the phase plane plots will reveal if the cantilever is actually doing so. This will be discussed further in Section 4.8. Another reason for the chaotic behaviour of the simulated displacements during the frequency

response might be due to the fairly low external acceleration (0.5g). In a situation where the cantilever has moved into an extreme potential well and is oscillating in within, it will require a fairly large amount of acceleration to allow it to oscillate within the extreme potential well. Hence, larger excitation acceleration might be needed to “smoothen” out the frequency response at very low distance between the two magnets.

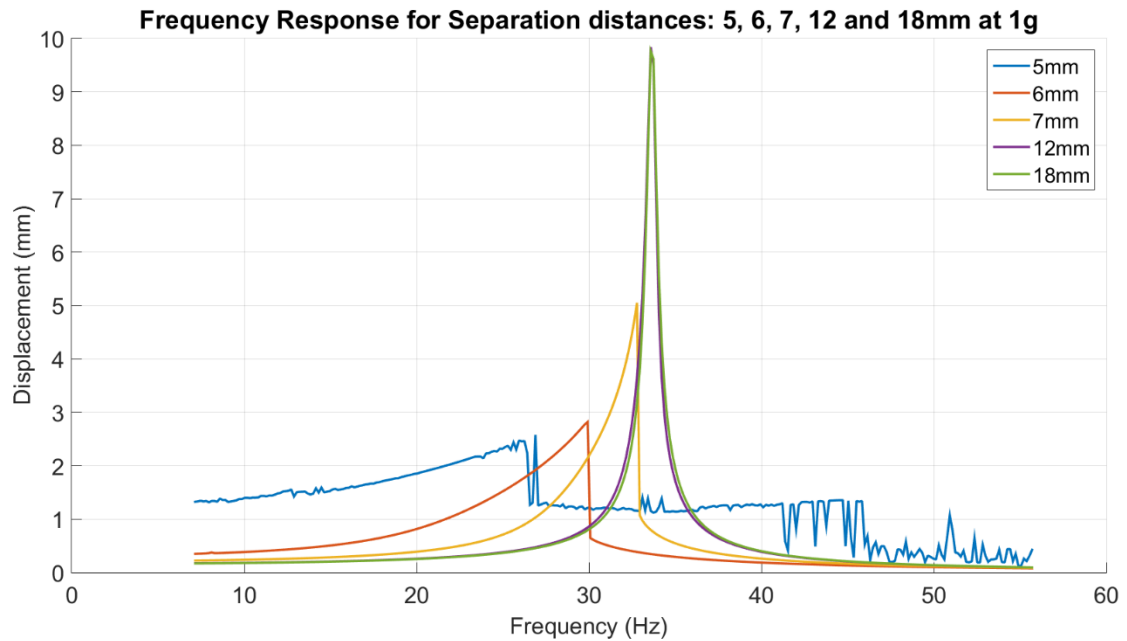


Figure 62: Simulated frequency response at an external acceleration of 1g.

Figure 62 was simulated at 1g excitation vibrational force and it indeed did “smoothen” the frequency response from the 5mm separation distance of the magnets as the cantilever now has more acceleration forces to help it oscillate within the extreme potential wells and back out again. It was observed that at the smaller distances the peak displacements happen at higher frequency notably for 5, 6 and 7mm separations with much higher displacements too compared to the 0.5g simulation.

Continuing on to push the external excitation to 2g acceleration resulted in a slightly different scenario in Figure 63. It did continue the trend seen with the 1g simulation and pushed the frequency of peak displacements from the selected distance of separations, closer to the resonance frequency of the system. It was also found that at 7mm separation, the system almost behaved like a linear system when it was building displacement towards its peak displacement at resonance frequency. But it behaved nonlinearly after achieving peak displacement resulting in a very steep drop-off after resonance frequency.

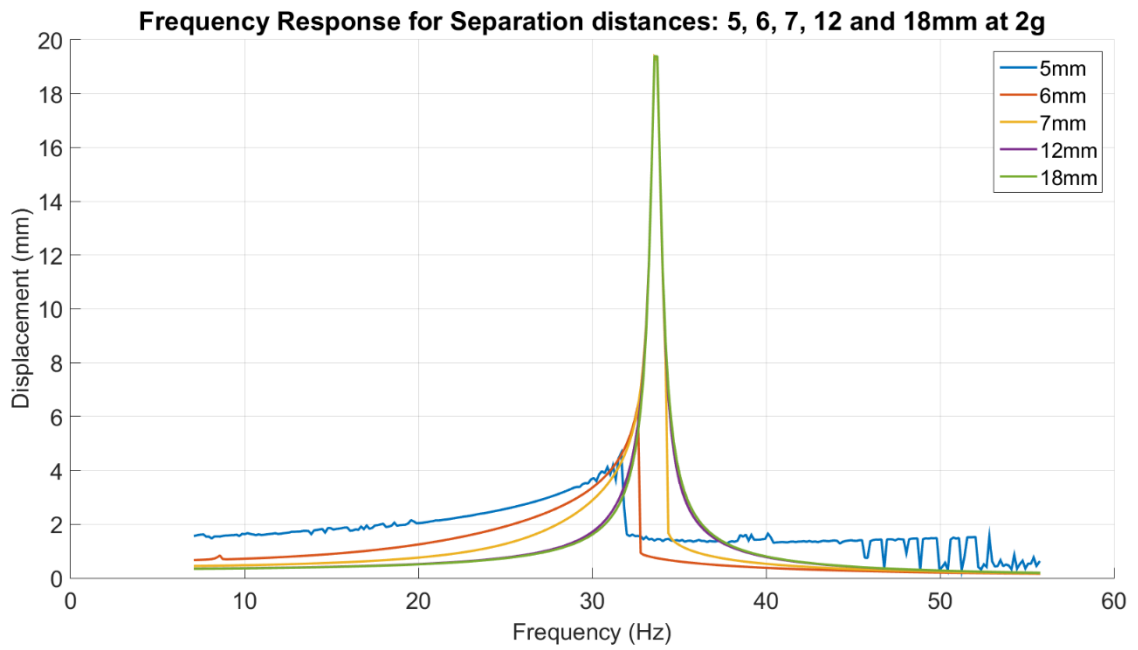


Figure 63: Simulated output at an external excitation of 2g.

Figure 64 also further provides a simple comparison between all the presented data.

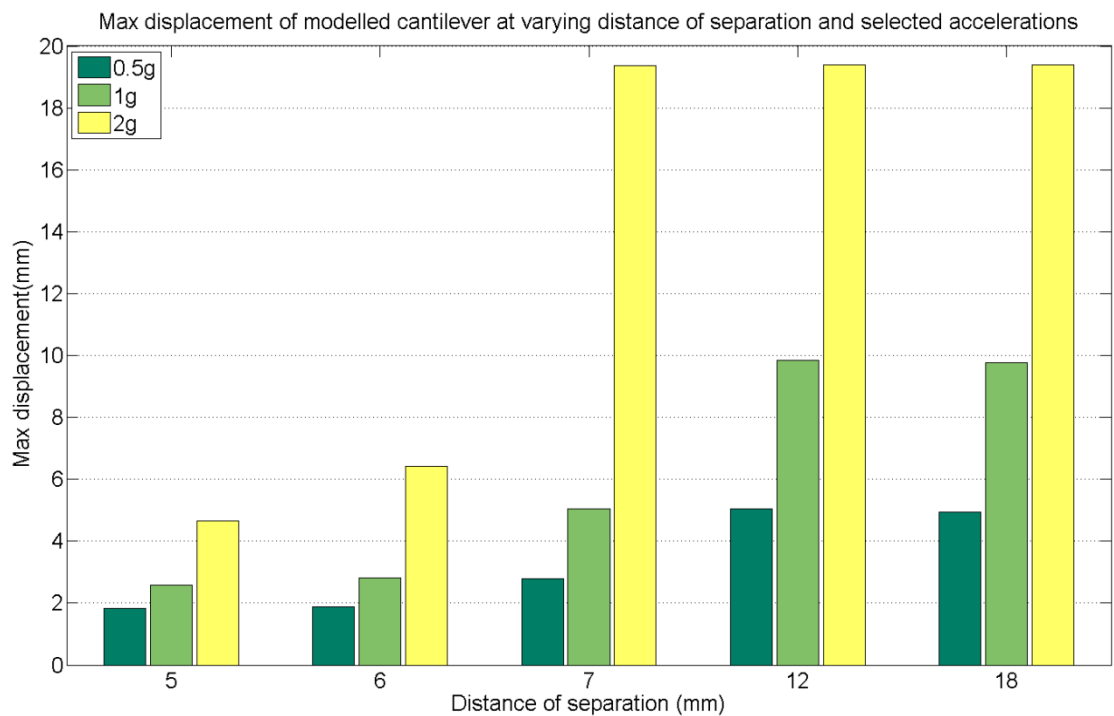


Figure 64: Comparisons of the maximum displacements achieved by the modelled cantilever.

Simulating at 0.5g, 1g and 2g accelerations took reference from the recorded accelerations from earlier experiments from the author's movement measurements. Vertical components from the measurements show that during the "jogging" and "high knees" movement, results showed recordings of around 1g and 2g accelerations. "Walking" movement showed recordings of around 0.25g. But as the value could easily double with another test subject, a decision was taken to use 0.5g as a representative value for simulations.

However, as this system is designed to be "powered" by human movement. It would be almost an impossible task to sustain 2g accelerations for long periods of time, not to mention the effort levels and also being uncomfortable too.

4.8 Phase Plane Plots

In reference to the simulation results that were presented in the previous section, these only provide the displacements of the cantilever from the frequency responses do not do the system's complexity justice. The complexity of the system comes in where the nonlinear cantilever system is judged to have the ability of move into one of the two potential wells outside its original equilibrium state.

By showing the phase plane plots of the system under simulation, one can further understand how the system works and this can be used to further enhance the understanding of the current nonlinear model. Simulation is very useful for a system with such complexity as it can be easily repeated and is not affected by noise or other unwanted components. Hence it is able to provide a better platform for understanding the behaviour of the whole system.

A sample of comparison of the phase plane plots obtained while undergoing the prototype's damping coefficient experiment is (with reference to Figure 55) shown in Figure 65. Note that both phase plane plots exhibit the same trend with the plots going in decreasing clockwise motion until it arrives at its equilibrium points in the centre of the plot at 0 at both X (position) and Y (velocity) axis. Also, note that in the experimental phase plot, the plot is not as smooth (straight line sections) as the simulated phase plot. This is due to the limitation of the maximum sampling frequency of the laser displacement sensor that was used to measure the displacement of the cantilever. The laser displacement sensor was only able to record up to 750Hz whilst the simulation was run at 10000Hz.

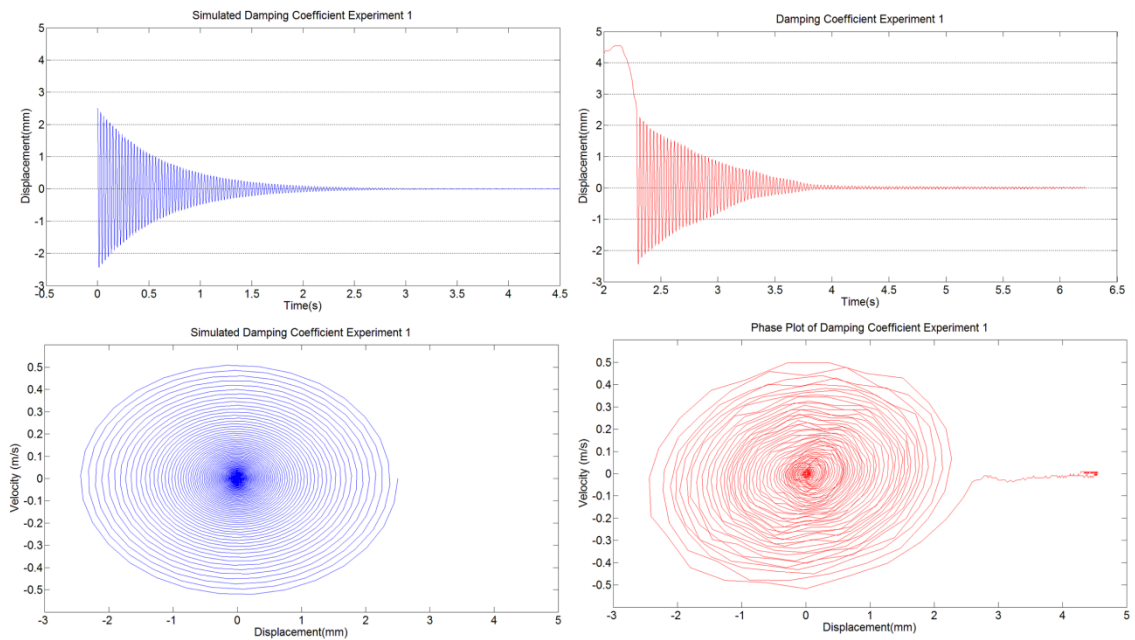


Figure 65: (Right): Experimental phase plane plot at 18mm separation distance (Left) Simulated phase plot.

In this section, the phase plots for separation of distances 5mm, 7mm and 18mm will be considered. These are chosen because, from the simulated frequency response, 5mm distance seems to exhibit the most nonlinear behaviour in comparison to the other two distances. The 7mm distance on the other hand provided a higher peak displacement compared to the 5mm separation, but it shows a wider bandwidth compared to the 18mm model in the build up to peak displacement and also a nonlinear drop off after that. Finally the 18mm distance is shown to be very similar to a linear model where the peak displacement of the model is only found at the resonance frequency. Phase plane plots simulations are done at 0.5g

The phase plots are shown in both scaled and unscaled version. This puts the movements of the simulated cantilever results in a new light and shows another perspective of the movements that has been observed in a closer and more detailed manner. The unscaled version shows the actual size comparison between different frequencies within the same distance of separation. It also shows the change of size of displacement in each frequency as well as the velocity too resulting in presenting different “shapes” of phase plots. Whereas the scaled version show the detail within each phase plot at any given frequency at any distance of separation.

Description of the plots will be given after each set of plots which provide more information on the often complex plots. Comparisons will be made wherever relevant to the plots. Each phase plot was simulated for a duration of 10 seconds to ensure that the

simulated cantilever response has enough time to settle into its stable movement pattern and rhythm.

The phase plane plots for the separation distance of 5mm are shown in Figure 66 (unscaled) whilst the scaled phase plots are shown in Figure 67, followed by the separation distance of 7mm and lastly 18mm.

The number of phase plots available through the simulation at the different separation distance through the frequency sweeps is very high and each plot can show a different type of behaviour. To illustrate the novelty of the behaviour exhibited, only the phase plots that are especially unique at the selected separation distance and at the selected frequency are presented.

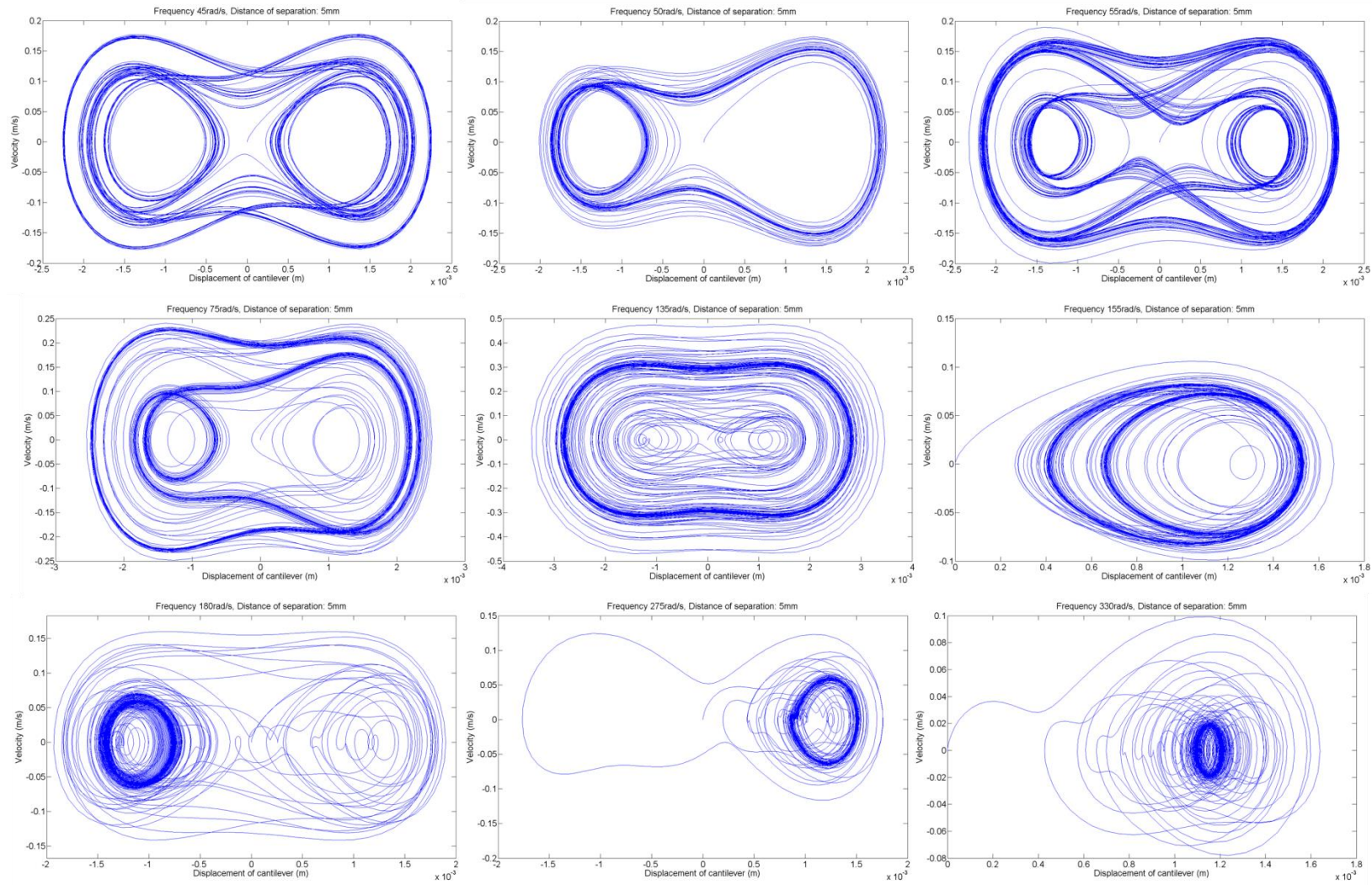


Figure 66: Phase plane plots for 5mm separation distance of magnets (unscaled).

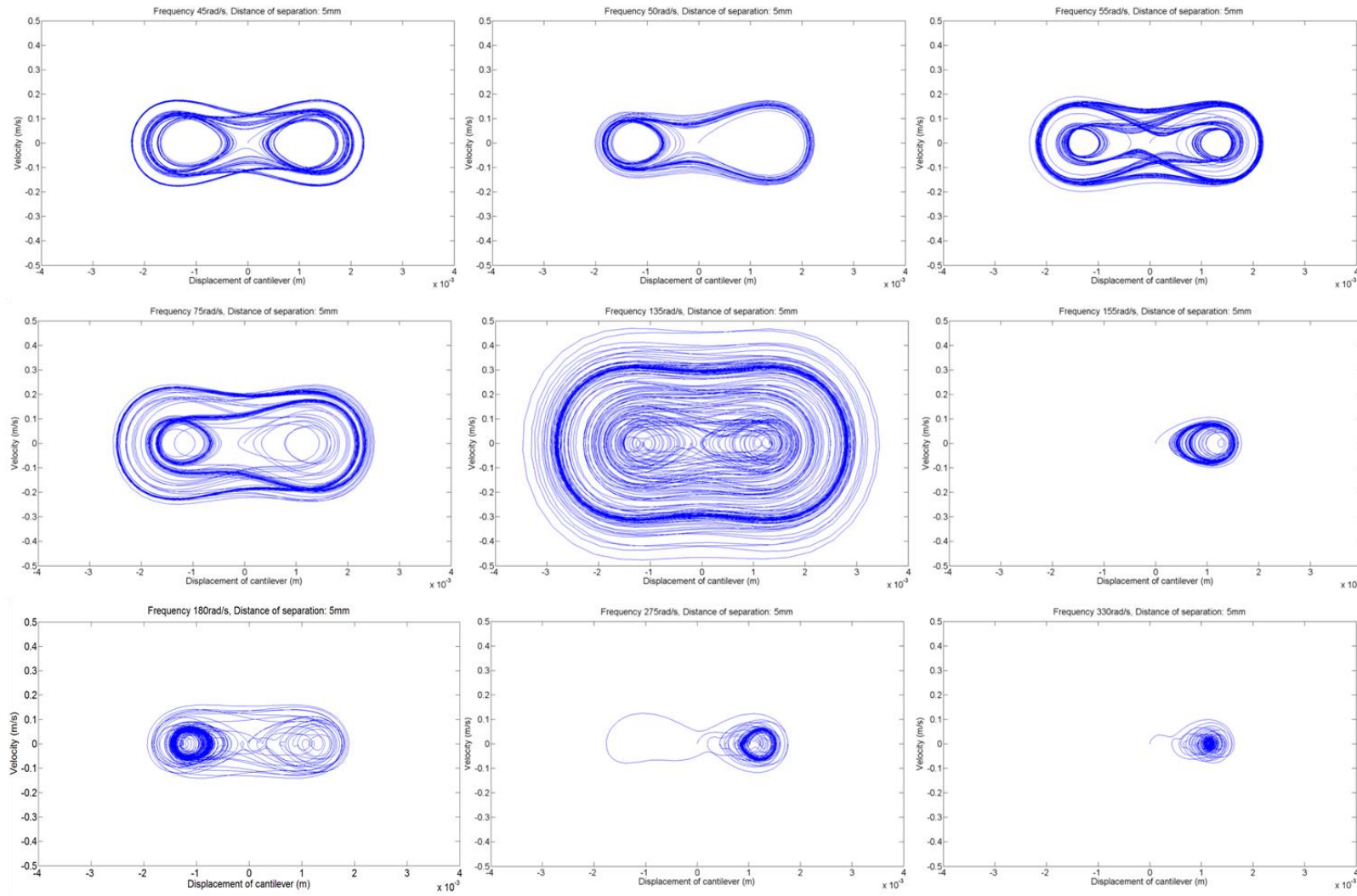


Figure 67: Phase plane plots for 5mm separation distance of magnets (scaled).

Figure 66 and Figure 67 show the different simulated behaviours of the cantilever under different excitation frequencies. Descriptions of the individual phase plots at 5mm separation are:

- 45 rad/s – The cantilever is oscillating around both equilibrium points. Starting with a smaller displacement on the positive side leading to a larger displacement on the negative side and repeating this process again and vice versa as well.
- 50 rad/s – A larger oscillation is observed in the positive displacement region, however the negative region has a smaller displacement but carrying more oscillations.
- 55 rad/s – A combination of both the behaviours observed from 45 rad/s and 50 rad/s where the oscillations of the cantilever switches from a smaller region to a bigger region on the opposite end and vice versa.
- 75 rad/s – A simpler version of behaviour observed with the 55 rad/s phase plot. Only the negative region of the oscillation behaves in a similar way to the 55 rad/s phase plot.
- 135 rad/s – Peak displacement is very close to this frequency and the cantilever oscillates in both regions very heavily at very close to peak displacements.
- 155 rad/s – The cantilever is observed to be oscillating in only the positive region (one of the two extreme potential wells) within the system and does not oscillate in the negative region at all.
- 180 rad/s – Only infrequent oscillations are observed in the positive region (initial stages) and heavy oscillations are observed in the negative region (settled stage).
- 275 rad/s – Almost identical to the 155 rad/s phase plot except where the cantilever has one oscillation into the negative region (during initial stage) and returned back into the positive region until the end of the simulation.
- 330 rad/s – Another extension of the 155 rad/s phase plot where the cantilever only oscillates in the positive region and does not enter the negative region at all, albeit with a slightly less stable oscillation compared to the 155 rad/s cantilever behaviour.

A different set of results was observed when the distance of the two magnets is set to 7mm. They are shown in Figure 68 (unscaled) and Figure 69 (scaled).

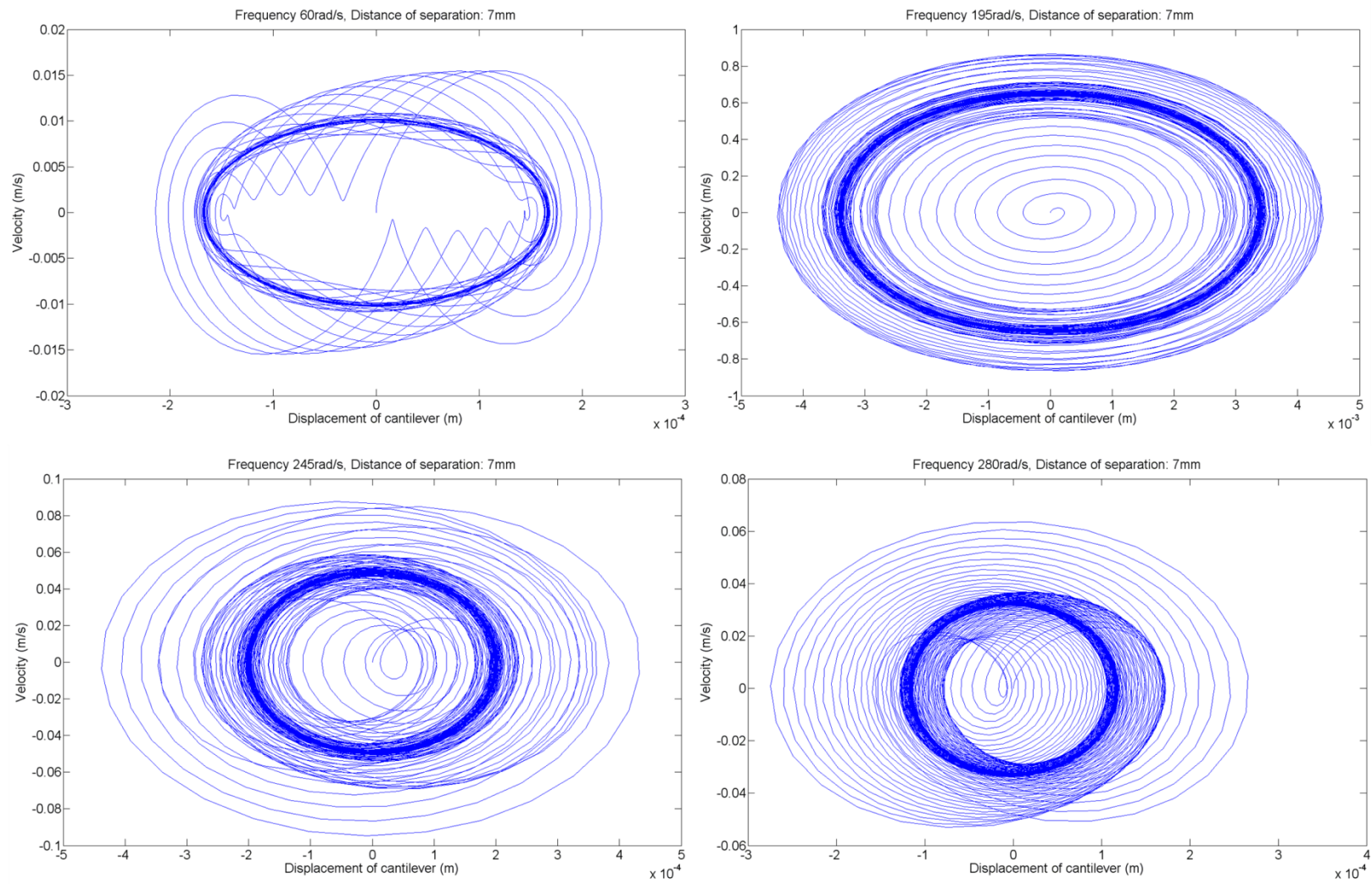


Figure 68: Phase plane plots for the separation distance of the magnets at 7mm (unscaled).

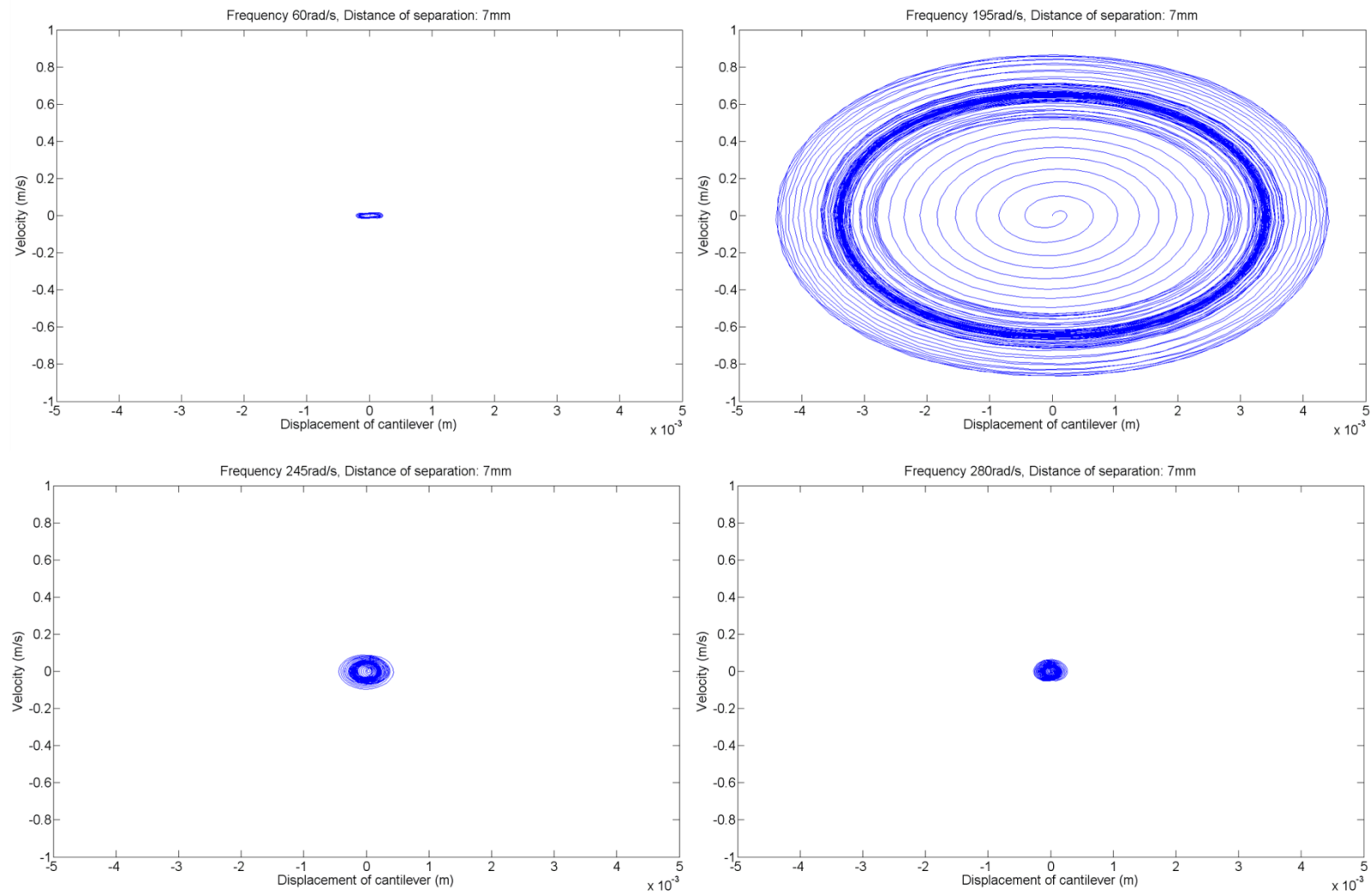


Figure 69: Phase plane plots for the separation distance of the magnets at 7mm (Scaled).

At 7mm separation distance of the two magnets:

- 60 rad/s – Starting out with higher displacement oscillation before settling down into a rhythm and oscillating at a slightly smaller but stable trajectory.
- 195 rad/s – Very close to the peak displacement frequency and similar to the behaviour observed at 60 rad/s, started from initial equilibrium point and steadily growing in displacement up until max displacement before shrinking slightly to settle on a fixed amplitude trajectory.
- 245 rad/s – A slightly more complex behaviour compared to the previous two with occasional detours of oscillation which sometimes achieves maximum displacement for the frequency but tend to settle at a smaller displacement of oscillation.
- 280 rad/s – Similar to the 245 rad/s behaviour except that starting with a small oscillation in the positive region before swinging into max displacement in the negative region. Returning to the equilibrium point and repeating the process again whilst losing displacement with every cycle until it settles on an oscillation that covers both positive and negative region. Note the displacements achieved at this frequency are smaller compared to the 195 rad/s and 245 rad/s phase plots.

Finally the phase plots for the distance of separation of 18mm will be presented in Figure 70 (unscaled) and Figure 71 (scaled).

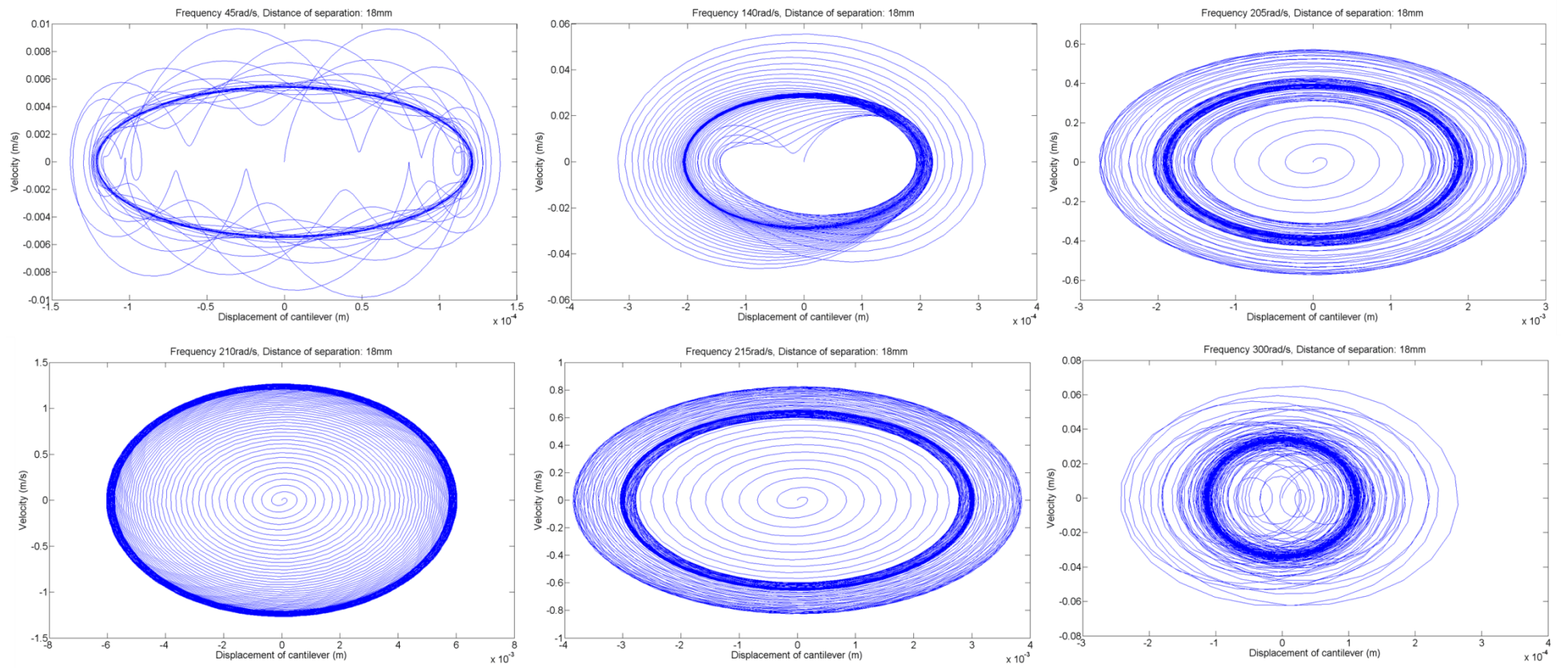


Figure 70: Phase plane plots for the separation distance of the magnets at 18mm (Unscaled).

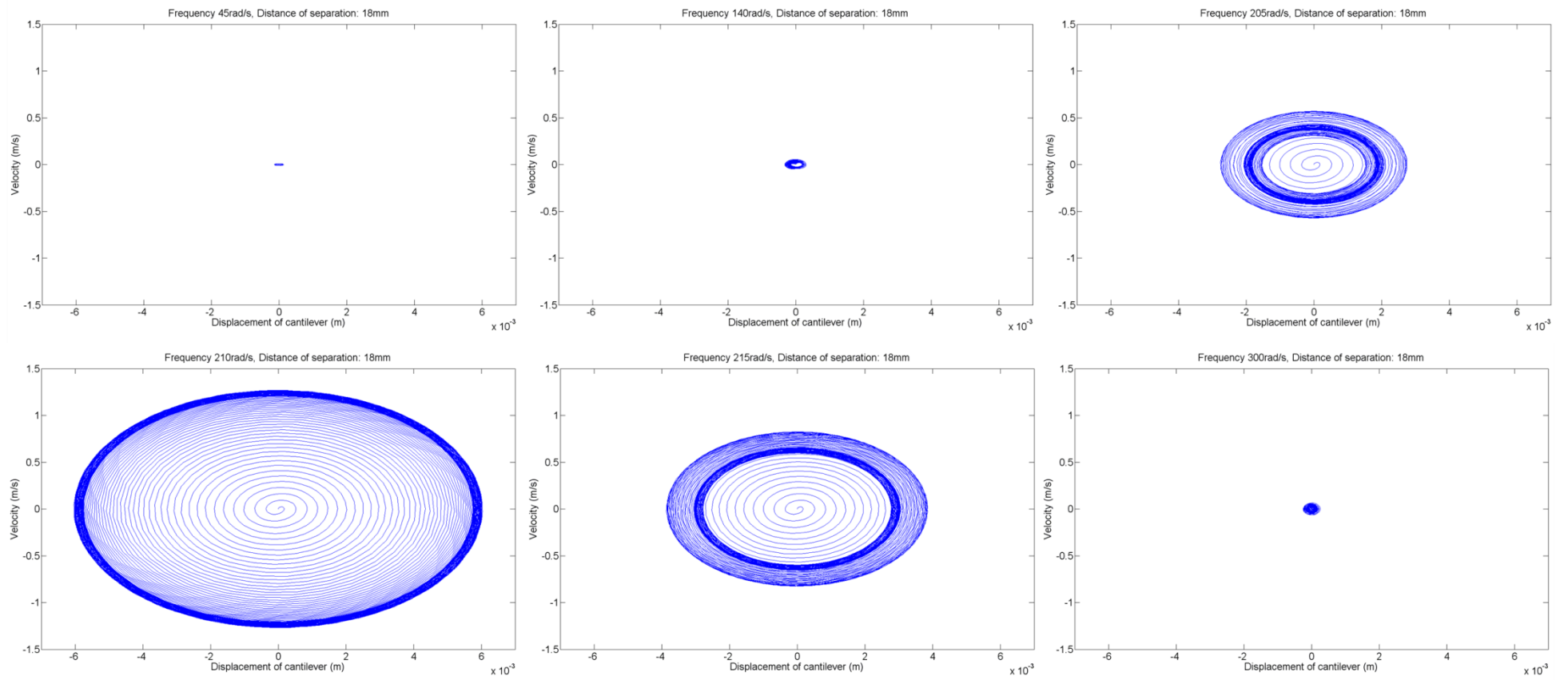


Figure 71: Phase plane plots for the separation distance of the magnets at 18mm (Scaled).

At 18mm separation, the cantilever behaves similarly to a linear model which has peak displacements at resonance frequency and drops off rapidly away from it.

- 45 rad/s – Quite far away from resonance frequency and oscillating in both the positive and negative region in a stable manner after settling down from the initial oscillations which achieved a higher displacement compared to the displacement which it has settled at.

- 145 rad/s – A similar behaviour to what was observed during a frequency of 280 rad/s at 7mm separation of magnets. Although at 18mm separation, this behaviour happened at almost half the frequency at what was observed at 7mm separation.

- 205 rad/s – Close to resonance frequency and hence a pretty stable phase plot which initially the cantilever oscillates at max displacements before settling into a slightly lower displacement.

- 210 rad/s – 1 rad/s of frequency away from resonance frequency and it can still be seen that the cantilever is oscillating at max displacement at all times after building up from its initial starting point.

- 215 rad/s – A similar situation to what was observed at 205 rad/s where once the system is out of its resonance frequency, the displacements (outputs) of the cantilever drops off rapidly.

- 300 rad/s – At a frequency higher, away from its resonance frequency and is oscillating and operating similarly to what was observed in 45 rad/s where the occasional detour of oscillation from one region to another whilst achieving max displacement before settling on a lower but stable trajectory.

With these phase plane plots, a better understanding with greater detail of what actually happens during the oscillations at different separation distances.

4.9 Summary

The modelling process of a nonlinear energy harvester is very complex and requires many components to be accurately “described” within the model process to enable an accurate representation of the physical model which then enables good understanding between the simulation and the prototype built. Certain assumptions were made through the modelling process in order to aid the already very complex modelling process.

This section has described the modelling process as well as the build of the prototype of the proposed nonlinear energy harvester. The results obtained from the simulations were very encouraging and within prediction. A summary of the results of the modelling process showed that within the separation distances that showed very strong nonlinear dynamics (low separation distance) the frequency response showed a higher bandwidth compared to the bandwidth for larger separation distances where the behaviour is essentially linear (high separation distance). Table 14 shows the summarized behaviour observed from simulation results.

Separation Distance	Regime	Peak Displacement Output	Bandwidth
Low	Strongly influenced by nonlinear dynamics	Lowest	High
Medium	Slightly influenced by nonlinear dynamics	Moderate to high	Low
High	Linear	Highest	Lowest

Table 14: Behaviour observed from the simulations results.

This has confirmed the behaviours seen from literature that has been reviewed earlier in the section. The next section will present and discuss experimental results from the prototype. The results obtained from the experiments will be compared to the simulation results from this section to verify the modelling process.

5.0 Verification of Simulation Results

This section aims to verify the findings of Section 4.3 by using the prototype that has been modelled and constructed. Experiments are run similarly to Section 4.4 starting with a frequency sweep across all the settings (frequency and acceleration) of the prototype obtaining the output displacements before presenting the phase plane plots of the prototype. Discussions will be presented within its respective sections.

5.1 Calibration of the Vibrator and Vibration Generation for the Prototype

In Section 4.1, the prototype model was introduced and the construction described to experimentally verify its behaviour. The prototype model was attached on top of a vibrator (LDS-V406/8) which in turn was connected to a power amplifier (LDS-PA100E) that amplifies the input signal coming from a signal generator (PicoScope 3404A). The signal generator is connected to the computer and is programmed within the Matlab environment to enable accurate and precise control of its output in terms of frequency and amplitude. A simple block diagram of the process is shown in Figure 72.



Figure 72: Block diagram for vibration generation.

It is understood that the vibrator (LDS-V406/8) used has its own frequency response. Hence a calibration has to be done to allow it to produce a consistent amount of acceleration across the frequency range that will be tested. In order to achieve this, an accelerometer (ADXL 325) was attached to the vibrator with the cantilever harvester on to accurately measure the output accelerations of the vibrator during the calibration process. The measured output acceleration was then fed back into the system, which is then used to scale the input voltage to the correct levels so that consistent output acceleration is achieved. Calibration was done from 8Hz to 50Hz across 0.5g, 1g and 2g accelerations. A block diagram of the process of calibration is shown in Figure 73.

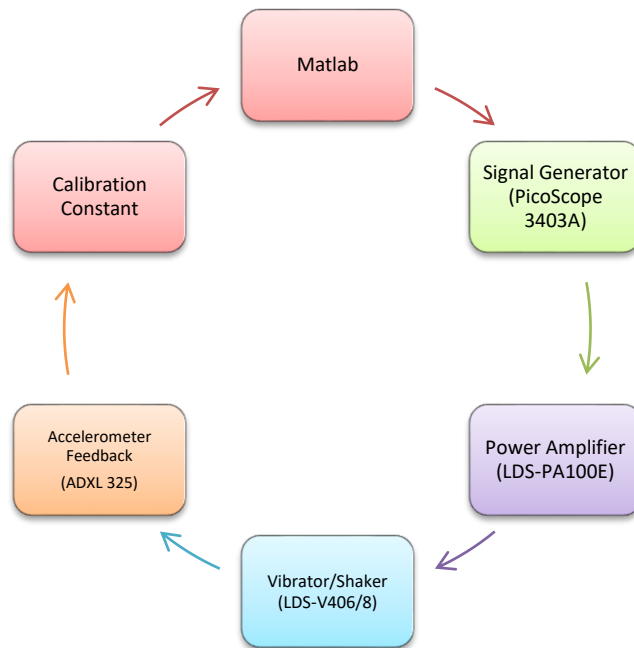


Figure 73: Block diagram for the calibration process of the vibrator.

A script was written to allow the vibrator to perform a frequency sweep in upwards or downwards frequency steps automatically whilst maintaining a consistent acceleration output at the vibrator throughout the sweeping frequencies. The codes for these Matlab Scripts are attached in Appendix B (Frequency Sweep Function).

Figure 74 shows the calibrated acceleration outputs measured by the accelerometer over the frequency sweep of 8Hz to 50Hz across all 3 accelerations with the energy harvester attached to the vibrator. At no point that the vibrator acceleration across all frequencies were above or below the target acceleration by 10% during the frequency sweep. This is key to ensuring the cantilever is stimulated by a consistent level of acceleration across the frequencies tested.

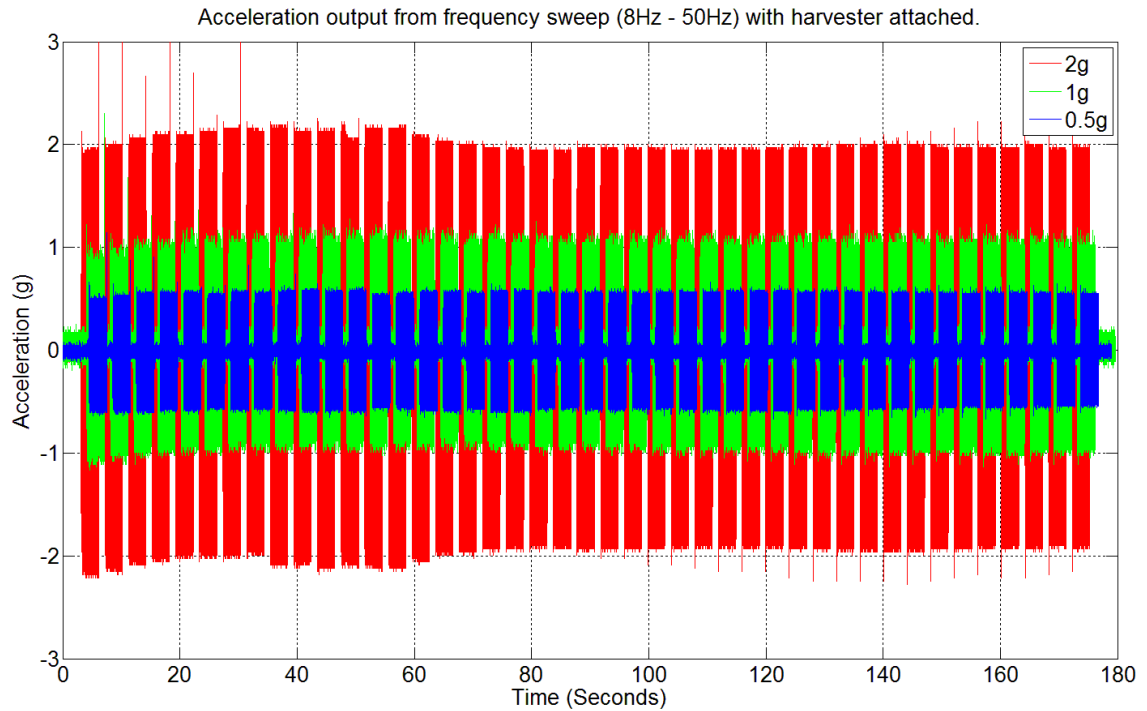


Figure 74: Calibrated outputs across 0.5g to 2g acceleration during frequency sweep from 8Hz to 50Hz with cantilever harvester attached.

5.2 Experimental Comparison with Simulation Results

This section looks at the results obtained from the experiments that were run after the calibration of the vibrator system. The experiment involves a frequency sweep upwards from 8Hz to 50Hz. This was applied for similar distances between the magnets comparable to the simulations previously. The described experiments were repeated for all distances and all accelerations used. The displacements of the cantilever are measured using a laser displacement sensor (Micro-Epsilon optoNCDT 1302-50mm) at 750Hz and transferred into the Matlab environment for further processing and analysis. The frequency sweep had an “ON” frequency time of 3 seconds and “OFF” time of 1 second before the next frequency was applied and this procedure was repeated until the end of the frequency sweep.

During the experiment, it was found that the prototype cantilever’s displacement will increase greatly whilst going from the “OFF” phase into the “ON” phase of the subsequent frequency (Figure 75 – Red Rings). The cantilever will then settle into a stable pattern of displacement (Figure 75 – Green Ring). To avoid the effect of the initial transient behaviour, the displacement measurements of the experimental results

do not take into account the initial rapid increase of the displacement of the cantilever but only the stabilised displacement (Green Ring section).

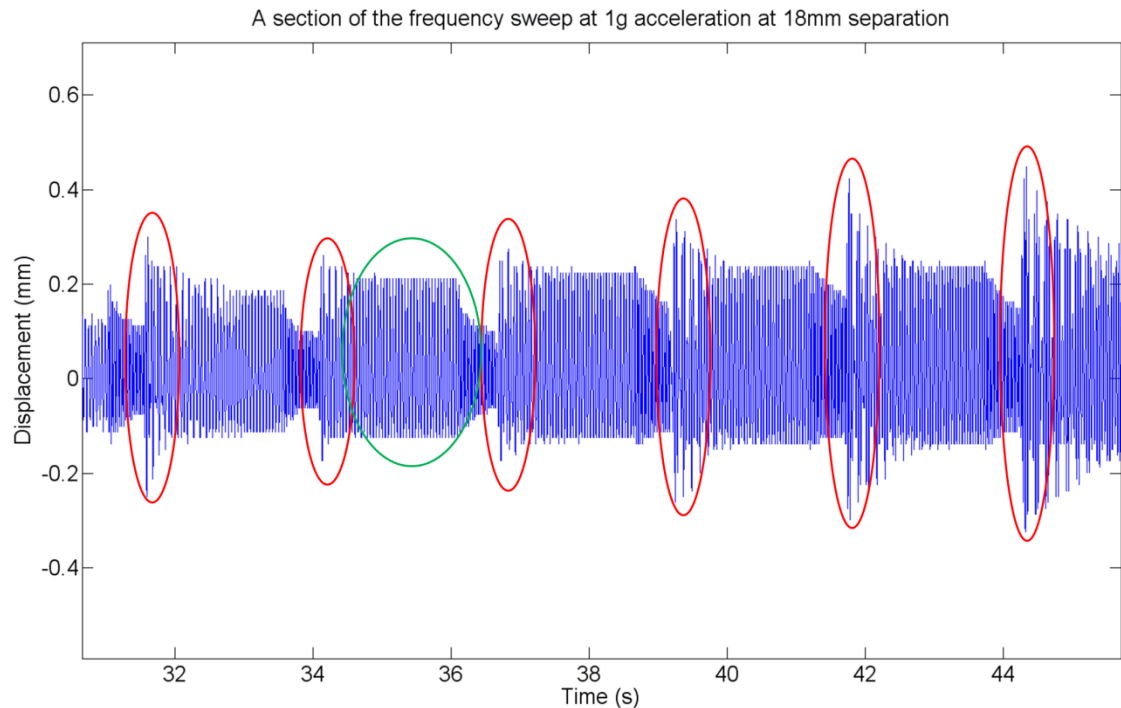


Figure 75: A section of the frequency sweep experiment showing an example of the rapid increase of displacement (Red Rings) before settling (Green Ring) during the "OFF" to "ON" phase.

The results, presented in RMS values will be comparing simulation and experimental results from all 3 accelerations across different separation distances. The decision to use RMS values in comparison to raw outputs are due to RMS values provide a more accurate representation of the data collected. The results will compare the bandwidth of each frequency response defined at Full Width Half Max (FWHM) of each separation distance across all accelerations, the average displacement as well as the peak displacement obtained and finally the frequency of each of the peak displacements recorded across all accelerations. These parameters allow the results to be assessed quantitatively even though it will not reveal if the prototype harvester displayed any nonlinear behaviour. Phase plane plots will provide a clearer analysis of the corresponding behaviour and validation of the nonlinear behaviour will be determined later in the section.

Additionally, results from the simulations are added into the output graphs for comparison purposes. These are added after the 3mm separation distance as the simulation results for the first 2 millimetres of separation returned unrealistic values of up to 1m in displacement as it was operating in an ideal mode.

Lastly, the frequency responses from all simulation and experimental set ups are attached in the Appendix F and Appendix G for reference.

0.5g acceleration

This section presents the results obtained from the prototype harvester being externally excited by the shaker at 0.5g acceleration.

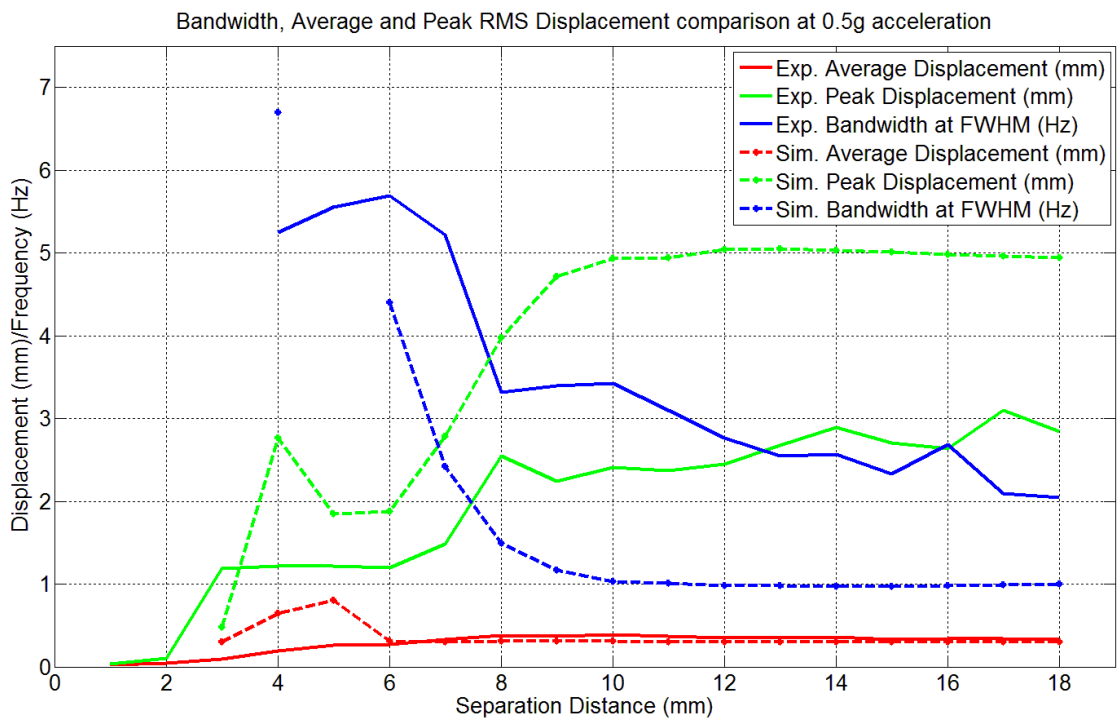


Figure 76: Bandwidth, average and peak displacement comparison across all separation distances at 0.5g acceleration.

From Figure 76, the bandwidth achieved by the experimental set up across all separation distances are mostly higher with a similar trend pattern when compared to the simulated values. From the missing data points on both 3mm and 5mm, this is due to the lowest displacement value recorded is higher than half of its peak displacement value, hence it is impossible to record any value at FWHM which is defined for this bandwidth calculation. At peak bandwidth, the experimental set up recorded a bandwidth of 5.69Hz at 6mm separation distance which has a 22% increase in the bandwidth recorded from the simulated set up. However, the biggest difference in bandwidth measurements occurred at the separation distance of 10mm where the experimental set up produced an output, which is 3 times higher than the simulated output.

However, peak displacement outputs from the experimental set up are lower in comparison to simulated outputs even though both outputs share the same general trend. Highest displacement was produced at a separation distance of 17mm on the experimental set up with an output of 3.1mm, which in comparison to the simulated output of just under 5mm shows a difference of almost 2mm in output. This 2mm gap of output is true for the ‘linear’ region of the cantilever which has a higher separation distance of 10mm and above. The difference of peak displacements between simulated and experimental outputs are lower than 2mm for separation distances below 10mm. Finally, average displacements outputs are very similar for both set-ups with no output exceeding 1mm.

1g acceleration

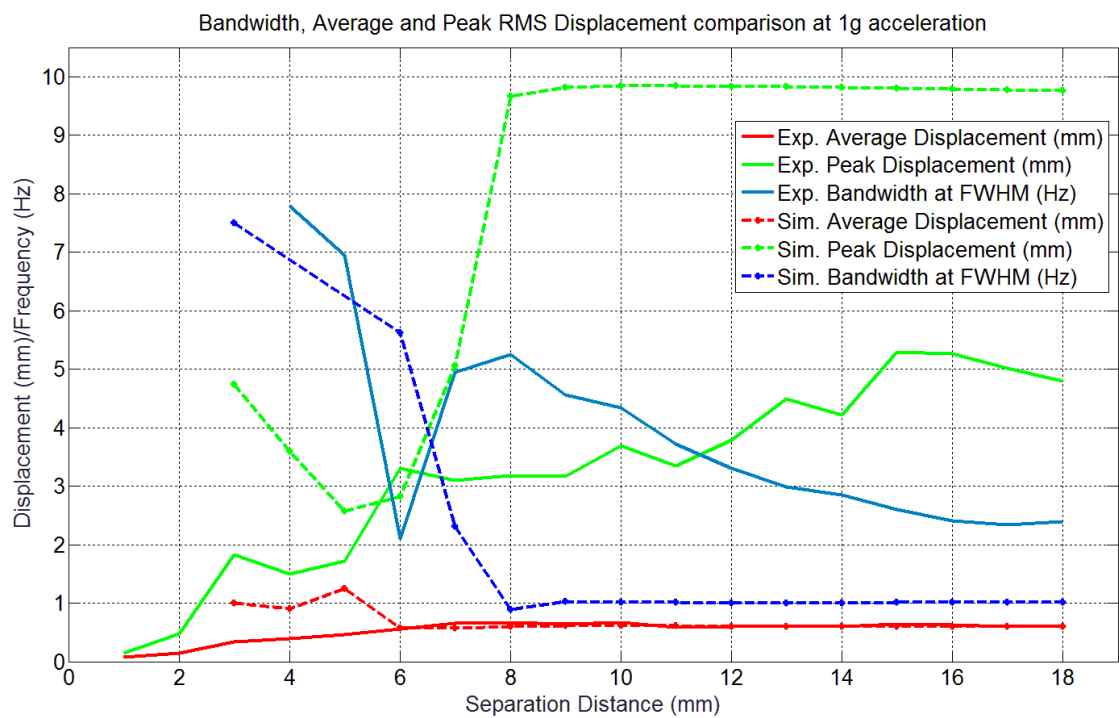


Figure 77: Bandwidth, average and peak displacement comparison across all separation distances at 1g acceleration.

Figure 77 presents the comparison of the bandwidth, average and peak displacements achieved by both the experimental and simulated set up at 1g external acceleration. Peak displacement comparisons between the experimental set up and the simulations show that there is a different trend in outputs. The experimental set up climbs steadily unlike the simulated results where the displacements recorded has plateaued after the 8mm separation distance for the remaining 10mm. Furthermore

during the plateau period, the peak displacement outputs of the simulation were double if not more in comparison to the experimental output.

However, the bandwidth outputs show a different trend where the simulated results are lower at every single separation distance except the 6mm separation distance. Both experimental and simulated results show that at the lower separation distances within the nonlinear region, the bandwidth of the set up increases. The biggest difference between the two set ups come from the 8mm separation distance where the experimental output has a 5.25Hz bandwidth and the simulated output below 1Hz. This set of result also confirms that the bandwidth within the linear region (>10mm separation distance) is indeed lower compared to the nonlinear region.

Finally, the average displacement of the two set ups was similar with the only exception happening at the 5mm simulated separation distance that was above 1mm in average output.

2g acceleration

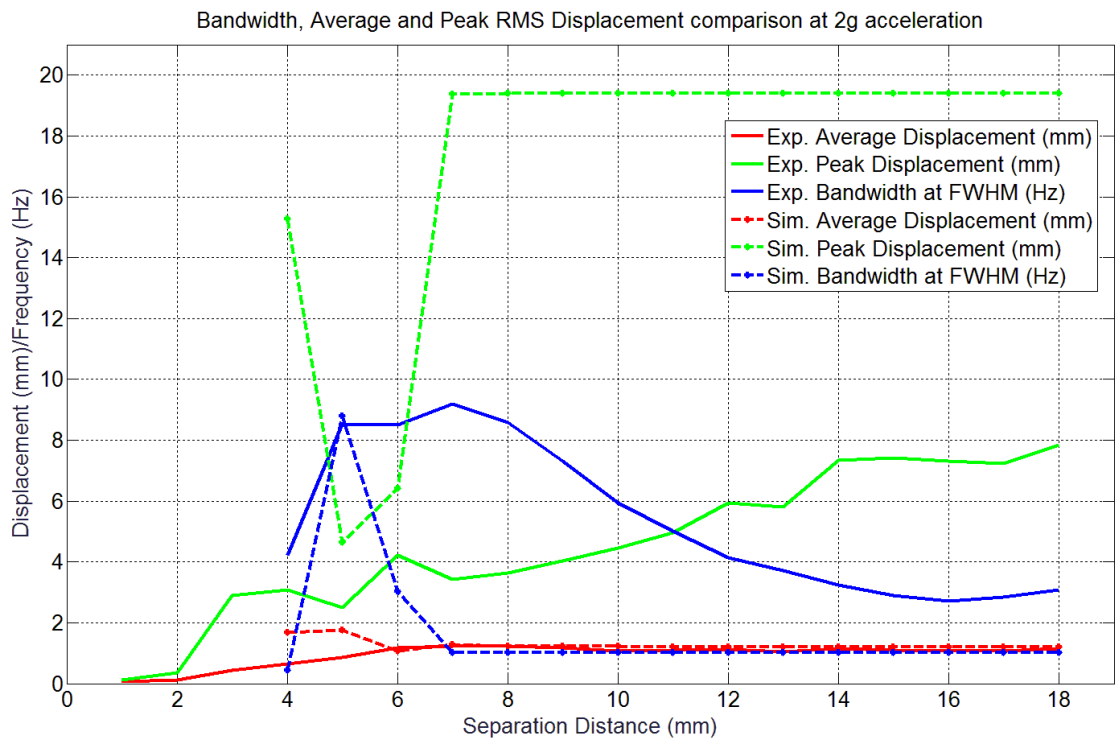


Figure 78: Bandwidth, average and peak displacement comparison across all separation distances at 2g acceleration.

Figure 78 shows the comparison between all three parameters from all separation distances for 2g acceleration. The peak displacement from the simulation showed the model achieving a high peak displacement from 3mm separation and

subsequently dropping to under 5mm peak displacement at 5mm separation distance before registering a constant peak displacement output from 7mm separation onwards to 18mm separation. On the other hand, the experimental set showed RMS outputs, which are significantly lower, compared to the simulated results but are higher and in line with growth when compared to the 0.5g and 1g acceleration outputs. The biggest difference in both set up in terms of peak displacements achieved came from the 7mm separation distance with a difference of just under 16mm of displacement. However, observations during the frequency sweep of the experimental set up at 7mm separation noted that the cantilever prototype was very clearly showing nonlinear behaviour resulting in a higher bandwidth in comparison to the simulated output. Bandwidth from the simulated results have been consistent at 1.01Hz from 7mm separation up until 18mm separation. The simulated outputs showed the cantilever responded in a linear fashion, whereas nonlinear behaviour was observed in the experiment set up during the frequency sweep process across 3mm to 7mm separation distance. The nonlinear behaviour resulted in higher bandwidths as the cantilever was able to produce sustained resonant outputs across more frequencies compared to the linear behaviour during high separation distances. The nonlinear behaviour will be presented and explained in detail in the next section, Phase Plane Plots.

Discussion of the Experimental Results in Comparison with Simulated Results

From the results presented for both simulation and experimental set up, it is clear that the results only provided measurements in terms of displacements and not frequencies. One of the hypothesis behind placing the two opposing magnets with the cantilever set up is the opposing forces from the magnets will alter the natural resonant frequency of the cantilever based on the separation distances.

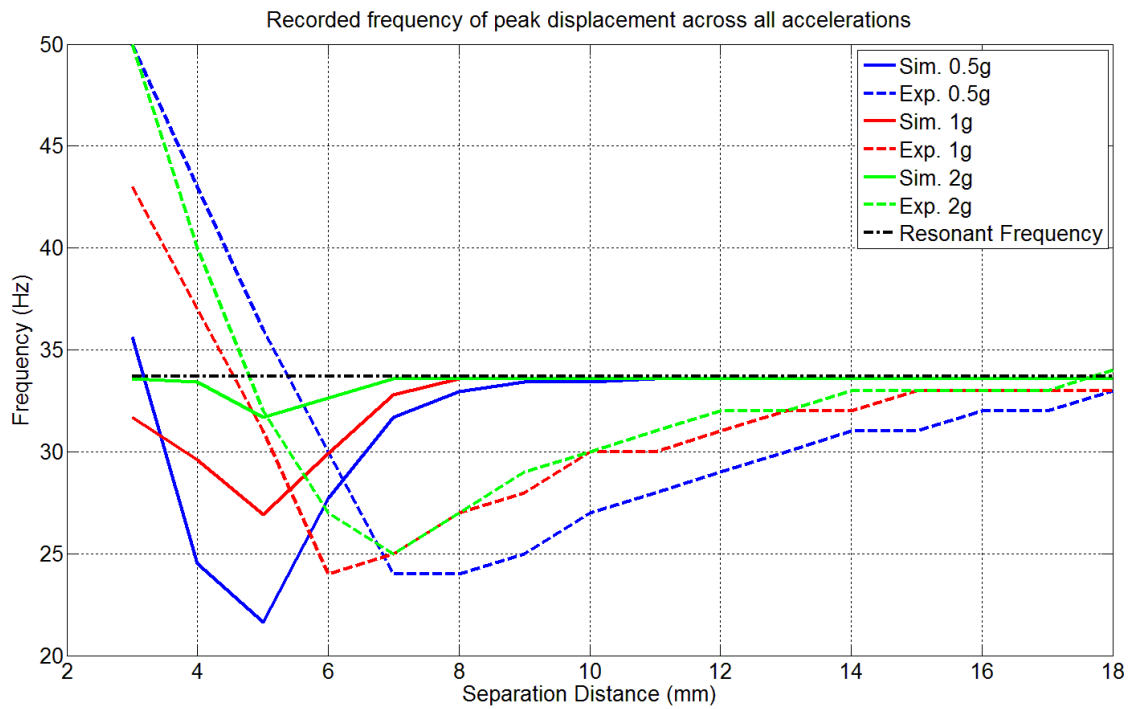


Figure 79: Frequency of which the peak displacements were recorded for all separation distances from 0.5g, 1g and 2g accelerations.

Figure 79 shows the frequencies that were recorded when peak displacements were achieved under all separation distances from all 3 accelerations. In simulation at low separation distances (<5mm separation), it is shown that the frequency of which the peak displacements are recorded differ widely to the natural resonant frequency of the cantilever. This behaviour reduces when the simulated set up is close the linear behaviour region (high separation distance, >12mm separation). However, this was not exactly the case from the experimental set up. When the separation distance between the 2 opposing magnets were low, the frequency of which the peak displacements were recorded were higher than the resonant frequency. Inversely when the separation distance between the magnets was within the nonlinear region (medium separation distance, 6-10mm), the cantilever seems to produce its peak displacements at frequencies lower than the resonant frequency before gradually returning to its resonant frequency at higher separation displacements.

This proves that with the set-up of the 2 opposing magnets which produces this nonlinear behaviour, one has the ability to control the production of the peak displacement outputs by adjusting the separation distance between the 2 opposing magnets. This behaviour can be maximized to suit specific applications where the setup is adjusted to obtain the highest output possible under specific circumstances.

Additionally, as shown from the experimental results, high peak displacements obtained during the linear phase (high separation distances) of the set up will result in a low bandwidth output. However, under situations where the system is within the nonlinear “sweetspot” region (medium separation distance), the system will have a lower peak displacement compared to the linear region but significantly higher bandwidth at the same time (ie: experimental set up, 2g acceleration, 6-8mm separation distance). This increase of bandwidth stems from the ability to sustain displacements across a larger amount of frequencies resulting in higher outputs as proven by the experimental results (shown in Appendix). This increase of bandwidth has also agreed with the hypothesis behind the 2-opposing magnet set up as a method to increase output from the cantilever system. A limitation from this set up also has to be noted, if the separation of the two opposing magnets are very low, the opposing forces of the cantilever would be far too great and will require significant external acceleration/forces to overcome this to generate any useful displacement from the cantilever.

5.3 Experimental Phase Plane Plots

This section will be dedicated to present and analyse the behaviours of which the cantilever exhibited during the experimental process. Similarly, to the presentation of the simulation results, phase plane plots will be used to describe the cantilever's complex and unique behaviour during the frequency sweep experiments across all 3 accelerations with selected separation distances covered as there are too many data points to present.

The results will start with the behaviours seen on the 0.5g external acceleration and followed by the 1g acceleration and finally with the 2g acceleration's cantilever behaviour outputs. At each acceleration, labels of "(a), (b), etc.." will be attached to the figure and description for ease of identification. Additionally, for 1g and 2g acceleration, there will be multiple figures presenting various phase plane plots at certain selection points, as there are too many to fit within a single figure.

0.5g Acceleration

Figure 80 shows the phase plane plots for several selected frequencies across the separated distances of 5mm, 6mm, 7mm, 12mm and 18mm. The frequency response showed by the graphs are the raw output achieved from the cantilever that is required to show the behaviour of the cantilever.

Starting with the 5mm separation distance of the blue line on the graphs (a), the phase plane plot during 36Hz excitation frequency at 0.5g shows that the cantilever is producing peak displacement of slightly over 3.5mm. However, the balance of displacement achieved is not split equally among both the positive and negative region with the positive region (right side) having a stabilised displacement of about 2mm and the negative region (left side) having only 1.5mm, thus have an 'avocado' shape phase plane plot. This is due to the opposing forces of the two opposing magnets forcing the cantilever to bend in one direction during the resting stage.

The 6mm phase plane plot (b) also showed a very similar 'avocado' response but with very slight change in the velocity of the cantilever at a different frequency of 30Hz. At 8mm separation at 12Hz (c), there is a very slight nonlinear response from the cantilever which results in an 'infinity' shape where the cantilever oscillates between both positive and negative regions including oscillations within a specific region (positive / negative) without switching regions. This provided a slightly higher displacement output in comparison to frequencies immediately next to it. (d) shows a

slightly different nonlinear response where the positive region shows a smaller oscillation in comparison to the negative region during stabilized oscillation.

(e) shows the behaviour of the cantilever which behaves linearly during resonant frequency at the selected separation distance of 12mm. The cantilever's displacement grows and shows a larger displacement before settling in a stabilized displacement output without any complex behaviour and is echoed by (g) at 18mm separation distance too. The only slight difference in (g) compared to (e) is the phase plane plot at (g) shows the cantilever stabilizing at the highest displacement achieved rather than shrinking slightly in (e). Finally, (f) shows that there is a big difference in cantilever output and behaviour at just 4Hz away from (g) with a behaviour that is similar to (d).

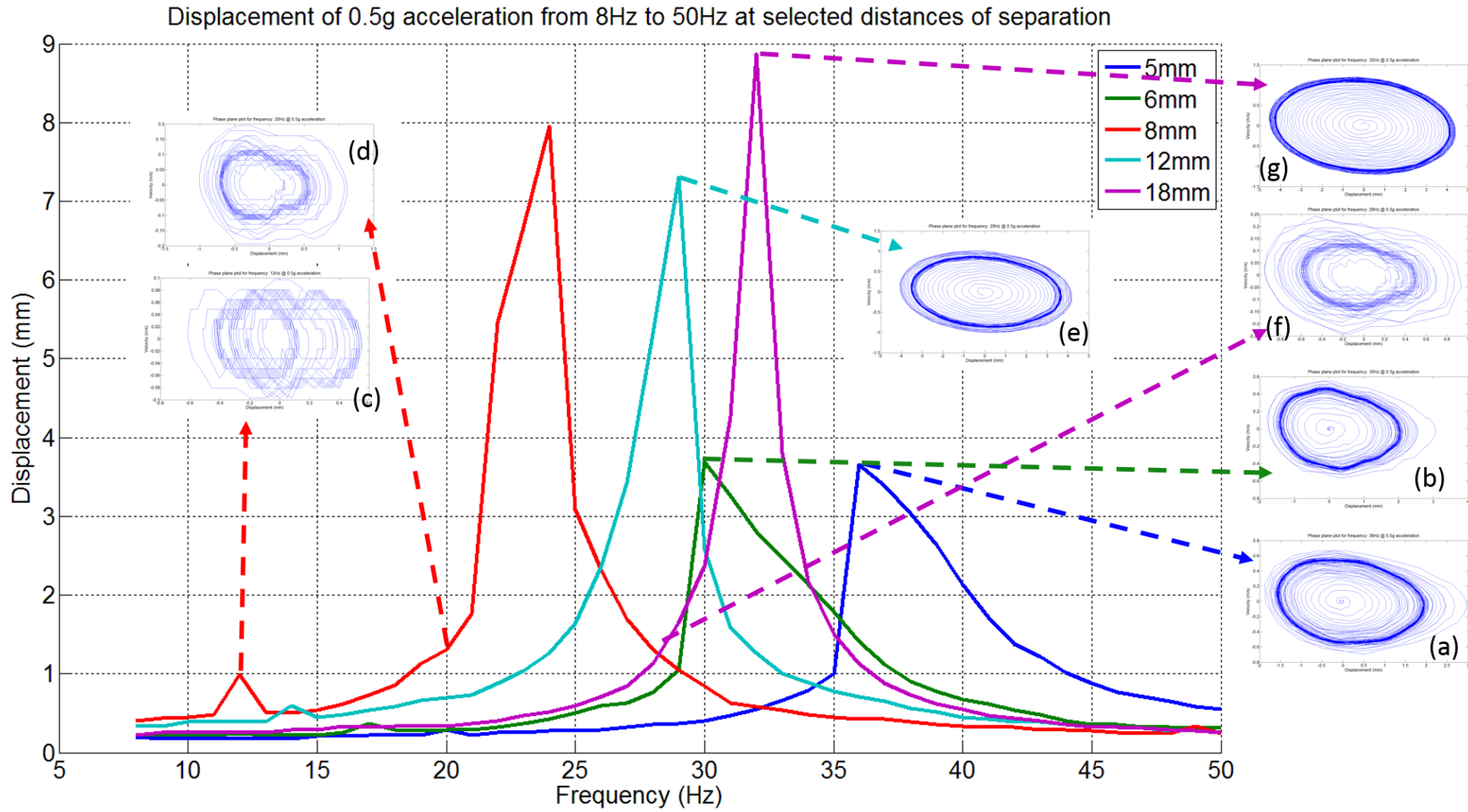


Figure 80: Phase plane plots of selected separation distances at selected frequencies.

1g Acceleration

This section presents the phase plane plots from the outputs of the cantilever from a 1g acceleration through the selected separation distances of 3mm, 5mm, 6mm, 7mm, 12mm and 18mm. The figures are split into two with Figure 81 presenting phase plane plots from 3mm, 5mm and 6mm separations and Figure 82 showing 7mm, 12mm and 18mm of separation distance.

Starting with (a) at 43Hz in Figure 81 during the frequency sweep at 3mm separation, the phase plane plot showed that the cantilever demonstrated nonlinear behaviour for two oscillations producing close to 10mm displacement in an instant towards the positive region before settling into oscillations with a radius of about 2.5mm between both positive and negative regions. This showed that the initial response of the cantilever towards the applied 1g acceleration at 43Hz frequency prompted the nonlinear behaviour. However, as the opposing force of the magnets at 3mm separation proved too strong for the cantilever to overcome, it stayed oscillating at a much smaller displacement after stabilising.

(b) at 15Hz and (e) at 18Hz showed that the cantilever behaved very similarly even though the cantilever was on different separation distances, which the cantilever had a small oscillation starting from the neutral point before continuing onto the larger, full oscillation for each cycle resulting in a larger displacement output in comparison to immediate frequencies next to it. (c) on the other hand showed a slightly unstable oscillation at 23Hz of which the displacement obtained was less than 1mm in total when the separation distance was at 5mm. At the same separation distance, (d) showed the cantilever's phase plane plot during its resonant frequency at 31Hz where the same 'avocado' response where the cantilever has a much higher displacement on the positive region compared to the negative region.

Finally, (f) and (g) from the 6mm separation distance shows the difference of outputs between the change of a single Hz frequency with (f) showing the phase plane plot for 23Hz and (g) 24Hz. The cantilever response from (f) is similar to (c) but with a slightly higher output at about 1.5mm displacement but (g) is showing the behaviour of the cantilever at resonant frequency where the cantilever grew in displacement until settling on an oscillation that is 70% on the positive region. This behaviour is also part of the nonlinear response of the cantilever which the opposing magnetic forces contribute to.

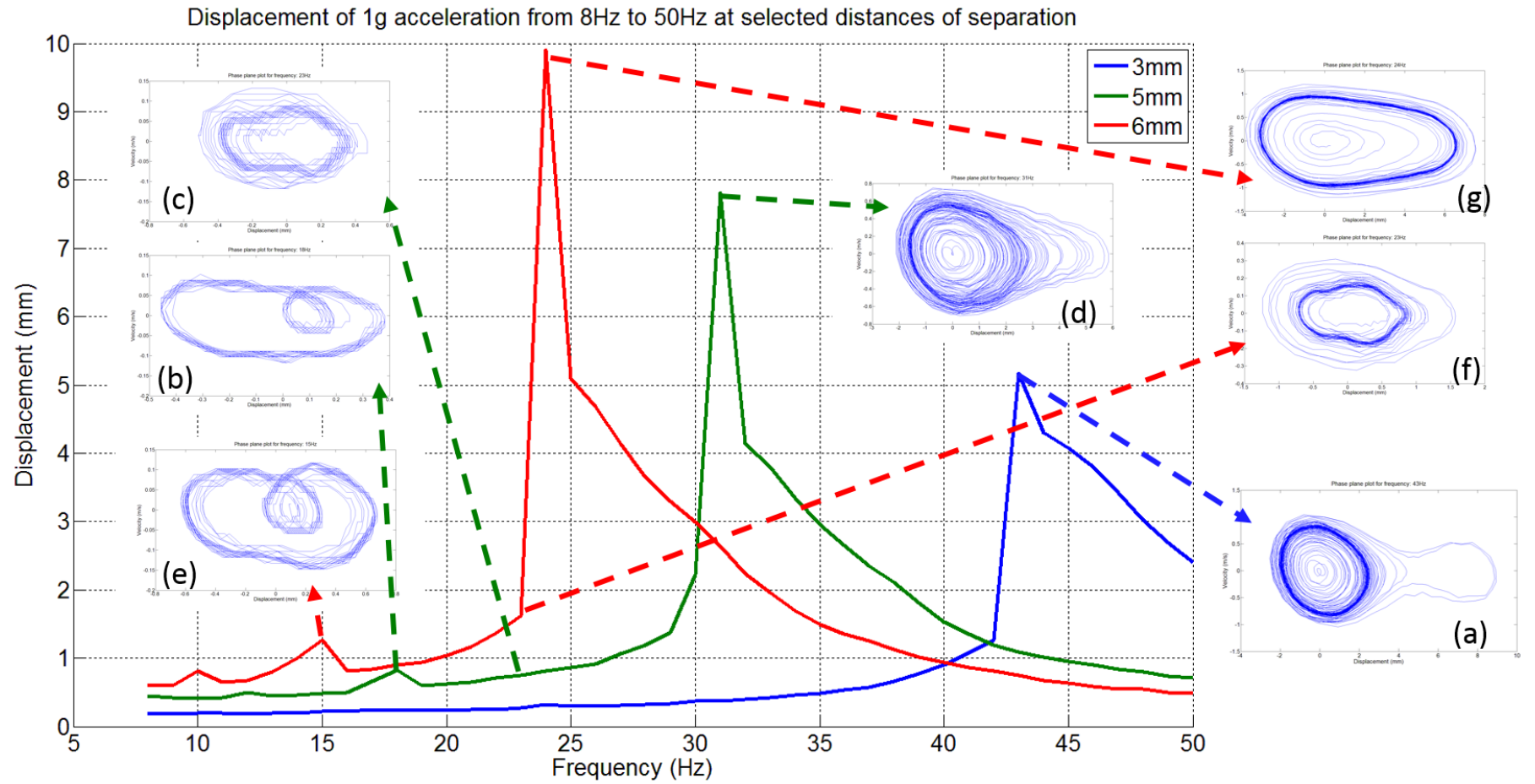


Figure 81: Phase plane plots of 3mm, 5mm and 6mm separation distances of the experimental cantilever at 1g acceleration.

Figure 82 follows the previous figure and continues to show the unique behaviour observed from the cantilever during the experimental phase for separation distances of 7mm, 12mm and 18mm. From (i) and (l), the cantilever is behaving in a similar pattern to (b) and (e) from Figure 81 whereas (m) is similar (f) and (j) is similar to (g). Thus, its clear that at frequencies below 20Hz, the cantilever undergoes a nonlinear behaviour where it completes a smaller oscillation before completing the full oscillation every cycle. However, (h) from 7mm separation distance does show a slightly more chaotic behaviour where the cantilever seemed unable to settle on a movement pattern and is alternating between smaller and larger oscillations. This behaviour of (h) is due to it being a harmonic frequency of the resonant frequency of the cantilever at that separation distance. Additionally, at 50hz from the same separation (k), the cantilever was oscillating with a small displacement before suddenly showing an increase in displacement and settling with a much larger displacement even though the oscillation between positive and negative regions was not entirely smooth.

Finally, (n) and (o) showed that when the cantilever is far apart (>10mm separation), the cantilever is behaving in a linear fashion with minimal or no opposing magnetic force acting upon the cantilever. Both phase plane plots showed equal amounts of displacement achieved on both positive and negative regions during the peak outputs at 31Hz and 33Hz respectively albeit at different separation distances.

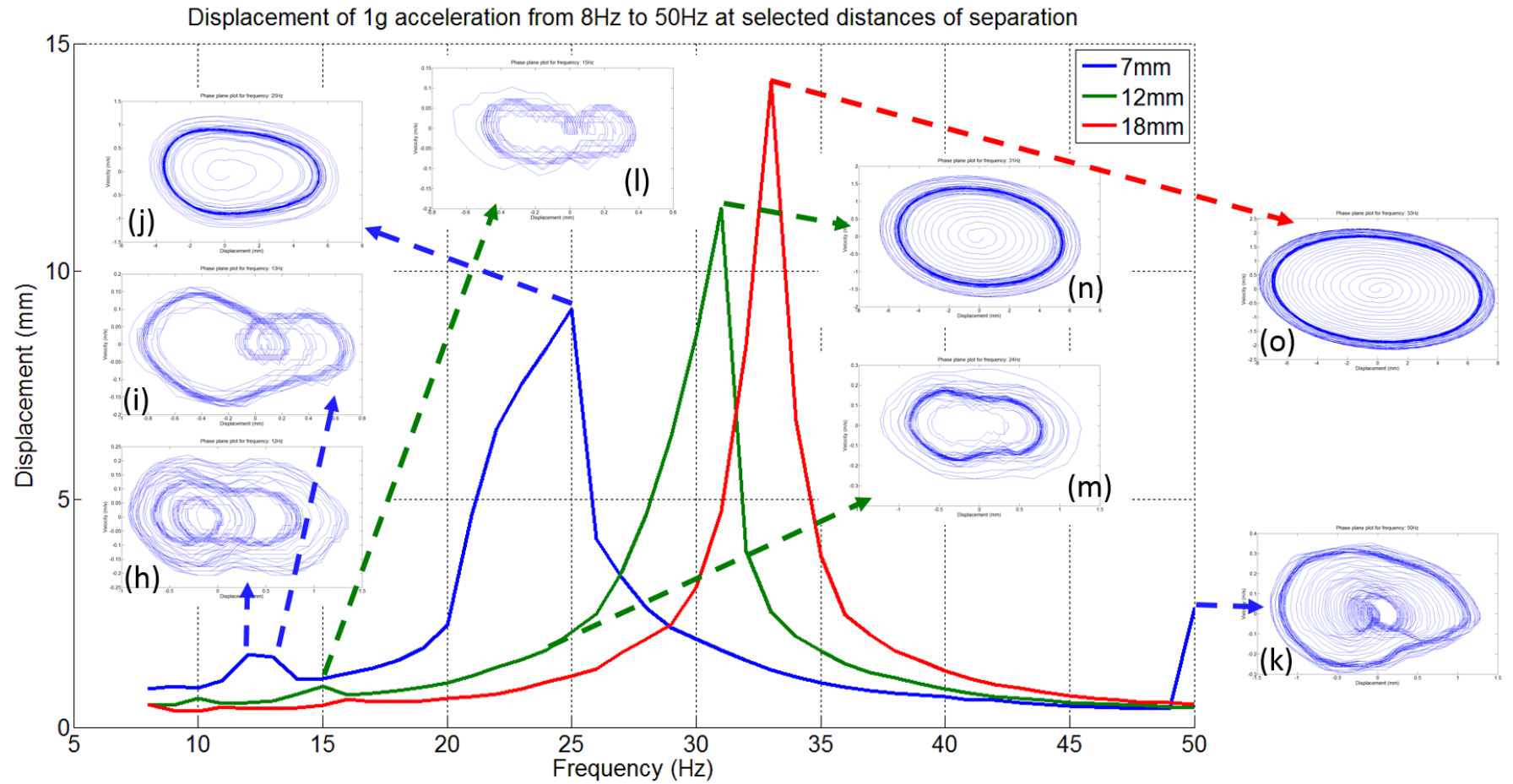


Figure 82: Phase plane plots of 7mm, 12mm and 18mm of the experimental cantilever at 1g acceleration.

2g Acceleration

Phase plane plots from 2g accelerations has to be split into 3 figures (Figure 83 to Figure 85) as there were far too many phase plane plots to be displayed without compromising the clarity of the plots. As the 2g acceleration experimental set up produced the most nonlinear behaviour, Figure 83 shows the phase plane plots from 3mm, 4mm and 5mm separation distances while Figure 84 presents the 6mm and 7mm separation's phase plane plots and finally the 12mm and 18mm separation's phase plane plots showed in Figure 85.

Starting with 3mm separation, clear nonlinear behaviour was observed when the cantilever suddenly achieved a high displacement output from an excitation of 46Hz at 2g acceleration (a) with the cantilever displaying independent oscillations within the positive and negative regions with occasional switching within both regions. Additionally, from (a), (b) towards (c), there is a clear trend that the cantilever's stabilised region is shifting from the negative region towards the positive region whilst still increasing in displacement.

(d) also showed similar nonlinear behaviour where the cantilever oscillated independently within both regions at a lower frequency of 40Hz whilst (e) did not manage to oscillate independently within the positive region but only the negative region even though the cantilever did travel significantly into the positive region.

(f), (g) and (h) were also displaying nonlinear behaviour from the 5mm separation distance, again at an even lower frequency compared to the 3mm and 4mm's nonlinear output. The cantilever did travel significantly into the positive region but was not able to oscillate independently within that region similarly to (a) to (d), however it did show that at 5mm separation, the cantilever response did have a much better bandwidth at Full Width Half Max (FWHM) compared to the former two separations.

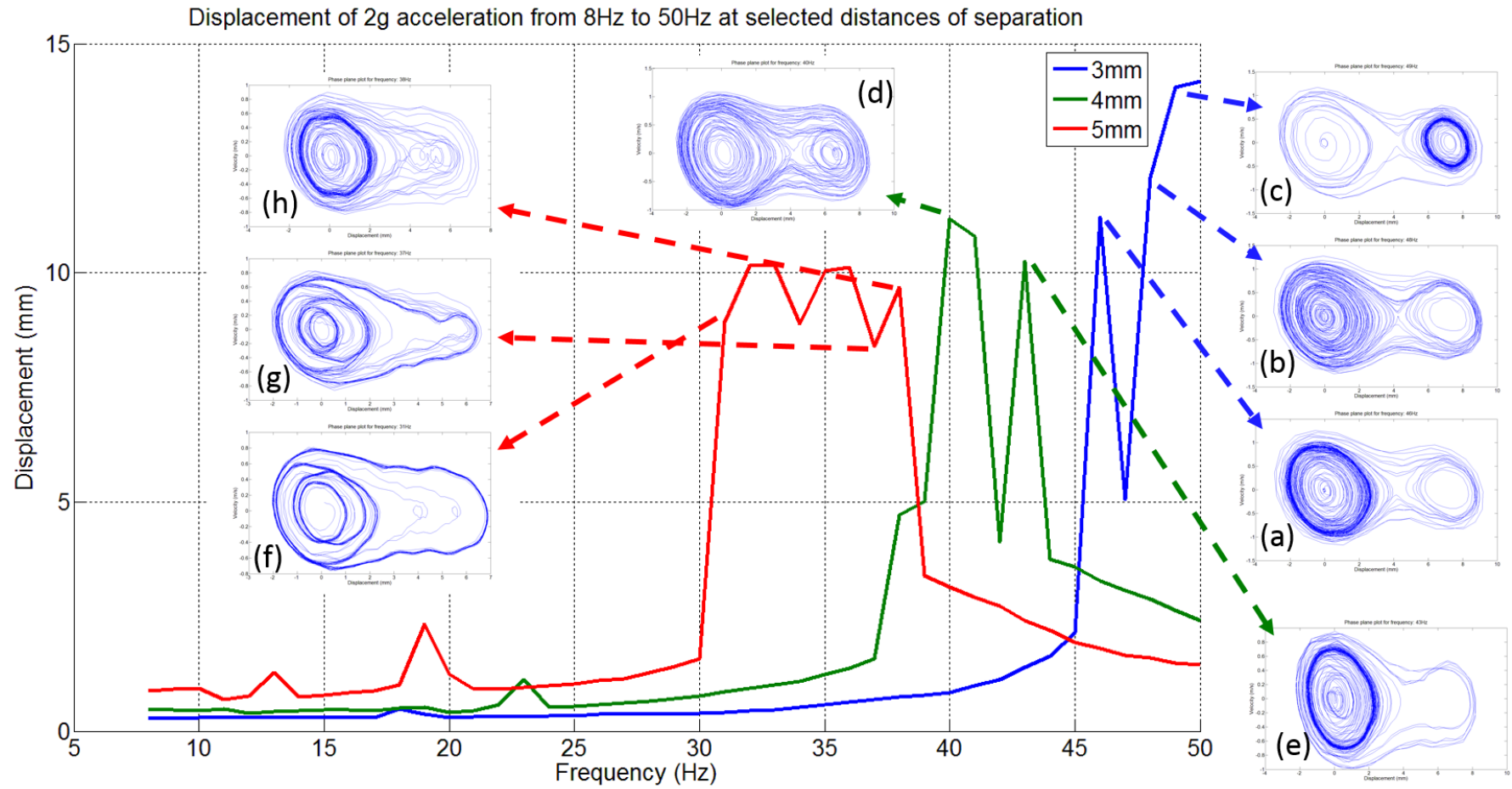


Figure 83: Phase plane plots from 3mm, 4mm and 5mm separation distance at 2g accelerations.

Frequency response showed in Figure 84 for 6mm and 7mm separation showed a different trend of outputs compared to Figure 83. Here the cantilever's frequency response is more varied, due to the change in the opposing magnetic force from the two magnets. (i), (j), (m) and (n) showed the cantilever executing a smaller oscillation before continuing towards a larger oscillation, similar to the 1g acceleration experiments where these behaviours were observed below the 20Hz frequency. (k) and (l) showed very similar behaviour to (f), (g) and (h) even though (l) showed the cantilever was producing varied displacements throughout the particular frequency of 36Hz.

(o) showed the cantilever producing stable displacements during resonant frequency of 25Hz at 7mm separation whilst (p) at 47Hz was also showing slightly similar behaviour but more chaotic with minor oscillations close to the starting location of the cantilever.

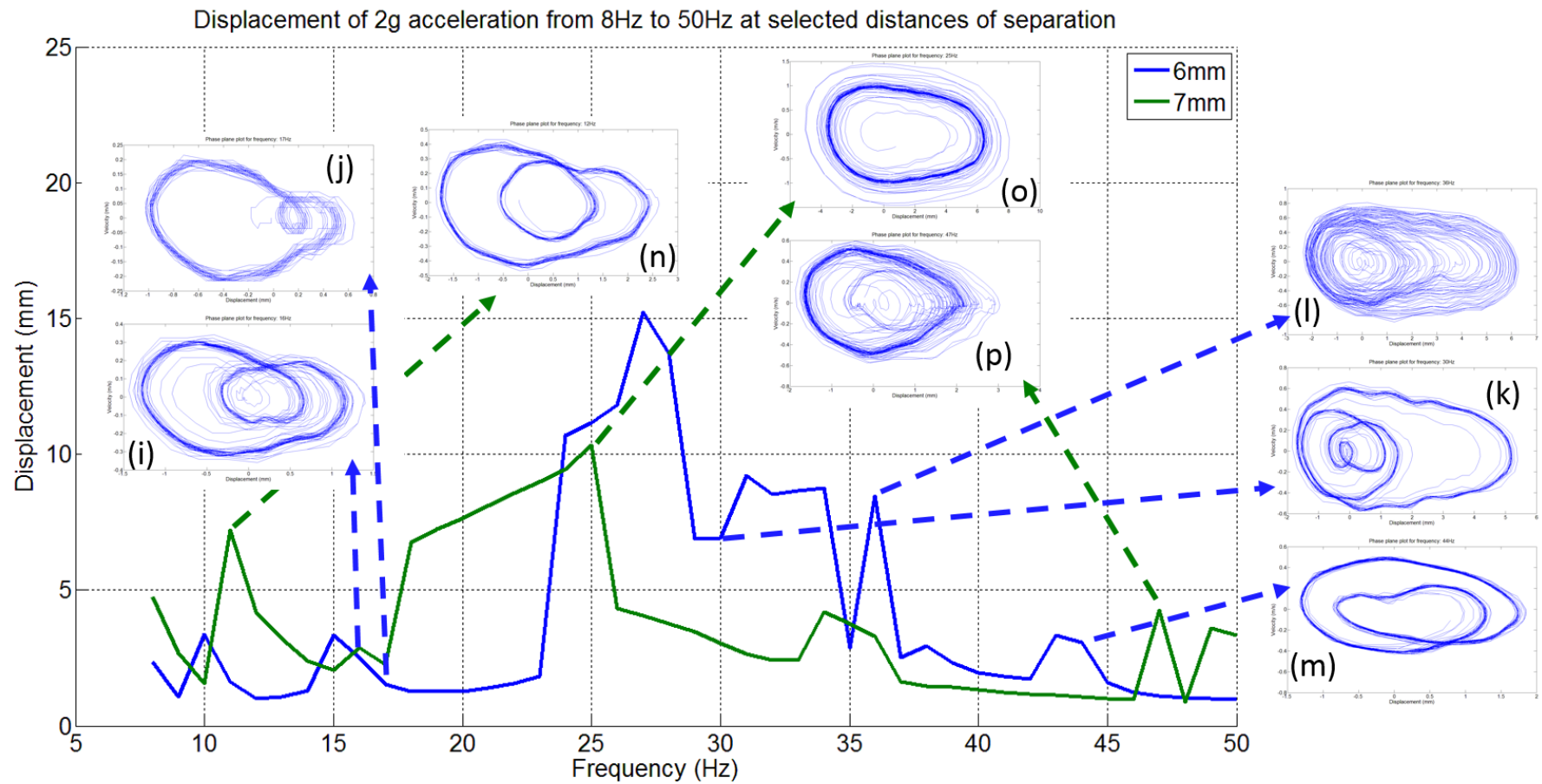


Figure 84: Phase plane plots from 6mm and 7mm separation distance at 2g accelerations.

Finally, Figure 85 showed the phase plane plots for the separation distances of 12mm and 18mm which are considered to be within the linear behaviour zone as the frequency responses for both separations resemble a linear set up. However, the behaviour of the cantilever at lower frequencies (<20Hz) show that the cantilever is behaving in a complex manner. (q), (s), (v) and (w) showed that the cantilever is alternating between a smaller oscillation and a larger oscillation except in (s) and (w)'s case, the larger oscillation appears within the positive region.

(r), (t) and (x) shows that the cantilever is oscillating with a complex chaotic behaviour especially in (t) as the cantilever is taking different amounts of time to achieve the same displacement from the positive region towards the negative region. Lastly, (u) and (y) show the resonant frequency behaviour of both high separation distances which the cantilever produced a high stabilised displacement. (y) produces the highest displacement throughout the whole experimental process of nearly 25mm displacement at 34Hz resonant frequency.

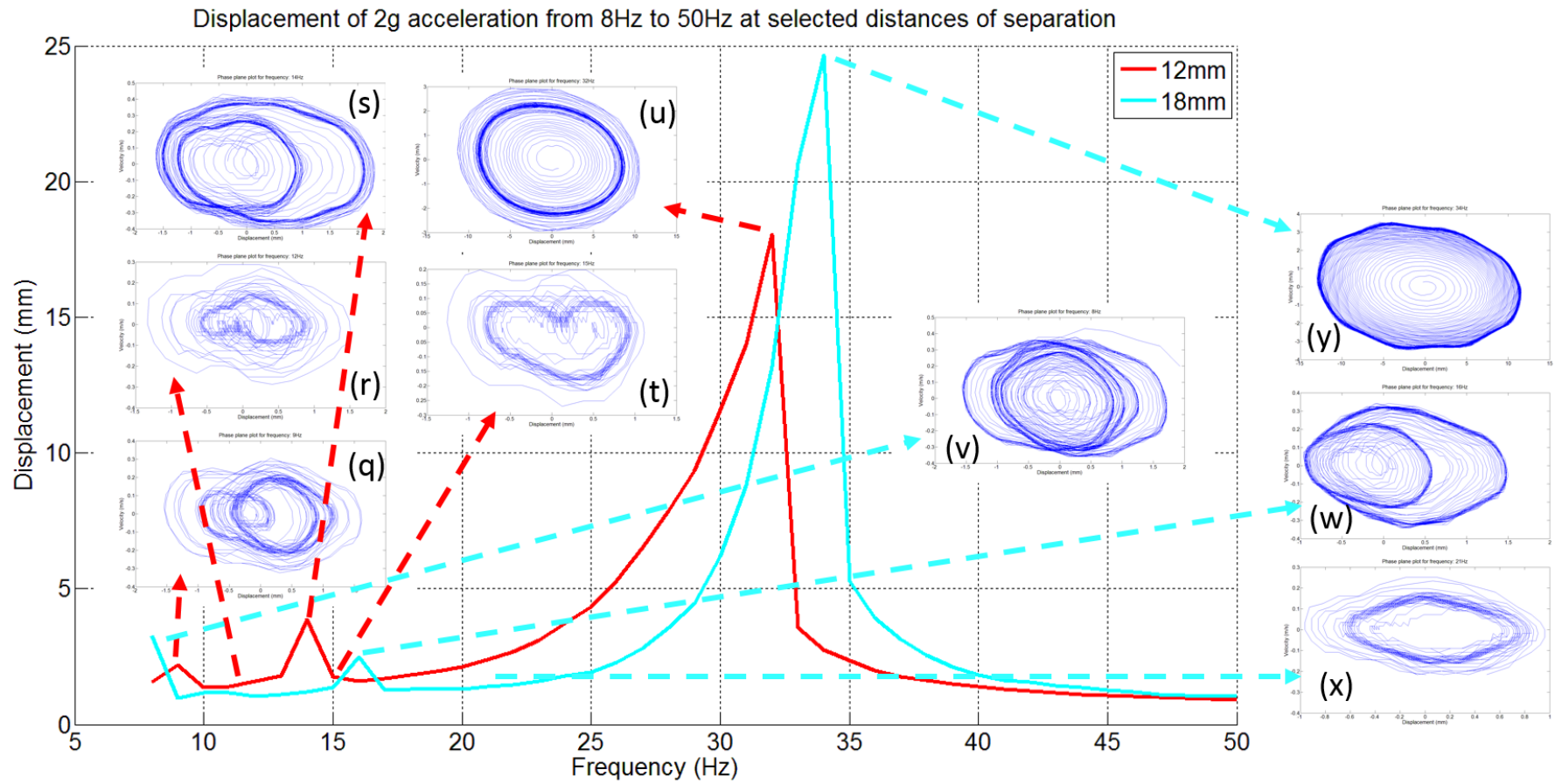


Figure 85: Phase plane plots from 12mm and 18mm separation distance at 2g accelerations.

5.4 Summary

This section provided a direct comparison of the experimental displacement measurements to the simulated displacement measurements. It clearly showed that the trend of the experimental displacement outputs is similar to the simulated outputs. It also showed that in the nonlinear region, the experimental bandwidth outputs are higher than the simulated results and the opposite can be said for the displacements obtained where the simulated results exceeded the experimentally recorded outputs. This shows that prototype is responding with outputs that were broadly in line with the trends shown during the simulations.

On the other hand, the phase plane plots from the experiments were distinctly different from the simulated phase plane plots. The experimental phase plane plots showed a lot more chaotic behaviour including nonlinear behaviour whereas the simulated phase plane plots showed more consistent behaviour. The reason for this difference is partly due to inaccuracies in the simulation model but also due to simulated model is acting under ideal conditions while the real system may be affected by external issues such as small build discrepancies. In chaotic systems, small disturbances and parameter changes can potentially result in markedly different behaviour.

Lastly, the next section will present and discuss the coils that are used to generate output voltage in the prototype system and the power generated from it.

6.0 Power Generation from the Experimental Cantilever System

Following Section 5.0, which presented experimental results from the prototype cantilever, showing the frequency response, displacements as well as the phase plane plots. This section presents and discusses about the power generated from the prototype system through a series of experiments that were conducted.

As the prototype energy harvester is designed as an electromagnetic harvester, a coil is placed in between the gap of the two opposing magnets of the prototype and the separation distance of the two magnets are able to be accurately controlled through the micrometer attached to the prototype.

The section will discuss about the coils that were designed and used on the prototype during the experiments before discussing the outputs obtained from the experiments.

6.1. Coils Used in the Prototype

This section discusses the design specifications of the coils that were used within the experiments in the prototype energy harvester.

To maximize the voltage output from the coils which are used within the prototype system, which has a moving magnet (cantilever magnet), a coil needs to be able to cover as much travel from the cantilever as possible of the magnet to “capture” the change in magnetic flux as described by Faraday’s Law of electromagnetic induction (Equation 2.13).

However, the small dimensions (6mm to 18mm) available in between the gap of the two opposing magnets pose problems towards the design of the coil as one of the main design criteria of the coils is to have as many turns as possible on the coil to maximize voltage generation. Using a copper wire of 0.15mm diameter, two coils were created. The first coil is made of cylindrical shape where the wire is wound onto a synthetic nylon core. The ends of the coil are made of electrical tape and are covered with non-conducting heat-shrink tubing to protect the wire from breaking. The coil is then attached to a vero-board to be attached to the prototype energy harvester. The second coil is constructed of a rectangular bar shape with the copper wire wound onto a rectangular Perspex bar of 3mm thickness. The ends of the coil are taped with masking

tape and the protruding wires are covered by heat-shrink tubing for protection. Table 15 presents the design specifications of the coils produced.

	Cylindrical Coil	Bar Coil
Number of turns (approx.)	450	255
Inner Diameter / Dimensions	1.35mm x 5.30mm width	16mm x 20mm x 3mm
Outer Diameter / Dimensions	5.50mm x 5.30mm width	16mm x 20mm x 5mm
Copper Wire Diameter	0.15mm	0.15mm

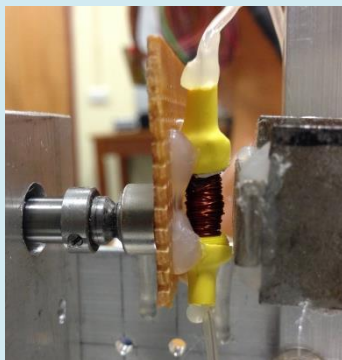
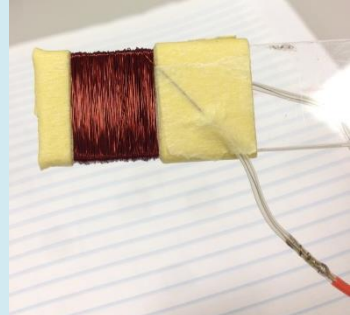



Table 15: Design specifications of the coils.

After construction of the coils and initial testing, it was found that the bar coil allows for a closer separation distance between the two opposing magnets. The lowest separation distance allowed by the cylindrical coil was at 9.5mm separation where the bar coil was able to allow smooth cantilever movements at 6mm separation distance. At 9.5mm separation distance, the two opposing magnets will not be close enough to have sufficient opposing magnetic force to produce nonlinear dynamics acting upon the prototype system. It was then decided that the bar coil will be main choice of coil to be coupled with the prototype energy harvester.

The experimental processes of the coils involve the coils to be placed in between the gap of the two opposing magnets. Attention was paid towards placing the coils as close as possible and in a central position towards the cantilever magnet (Figure 86) as it is moving and provides that change in magnetic flux. This produces the voltage outputs, which are measured from the coils. The coils are put through a similar experiment from Section 4.7 where the whole prototype system is put under 0.5g, 1g and 2g of acceleration through frequencies of 8Hz to 50Hz. The experimental process starts with the magnet separation distance at 6mm and finishing with 18mm. Outputs from the cylindrical coil is attached in Appendix C for reference.



Figure 86: Placement of the bar coil within the prototype during the experiments.

6.2. Location of Optimum Resistive Load for Power Generation for Prototype System

To obtain maximum power from the prototype system, an experiment was conducted to locate the resistive load that will provide the highest voltage output from the coil. Having the prototype system under test at resonant frequency of the cantilever at 18mm separation distance of the two magnets and with an acceleration of 2g, the prototype system produced a peak to peak voltage of 900mV with a resistive load of 2000Ω. The resistive load applied to the prototype was then changed systematically from 1Ω up to 2000Ω in search of a similar if not higher voltage output than what has been currently achieved. Figure 87 shows the output results of the experiment.

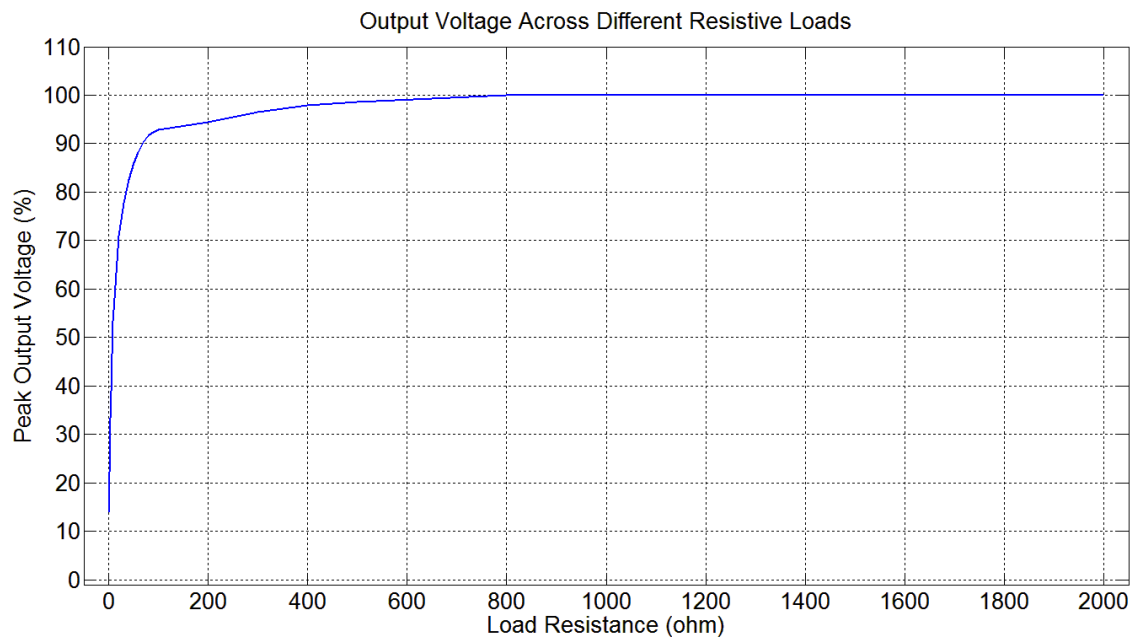


Figure 87: Resistive Load Calibration.

Through the experiment, it can be seen in Figure 87 that at only 800Ω, the outputs produced by the prototype is similar compared to the initial resistive load of 2000Ω. This has a major impact on the output power that is achievable from the prototype as the lower the resistive load at maximum output, the higher the power that the prototype system is producing (Equation 2.17).

However, this does show at 800Ω, the prototype produces maximum power. Using the same procedure, the RMS voltage output at resonant frequency at 18mm separation distance at 2g external acceleration is recorded. As the prototype system only has a resistive load connected to it, simplifying Equation 2.17 provides $P = \frac{V_{rms}^2}{R}$ which is to calculate the projected maximum power output curve with various resistive loads.

Figure 88 provides the projected output power curve that the prototype system will be able to produce under different resistive loads.

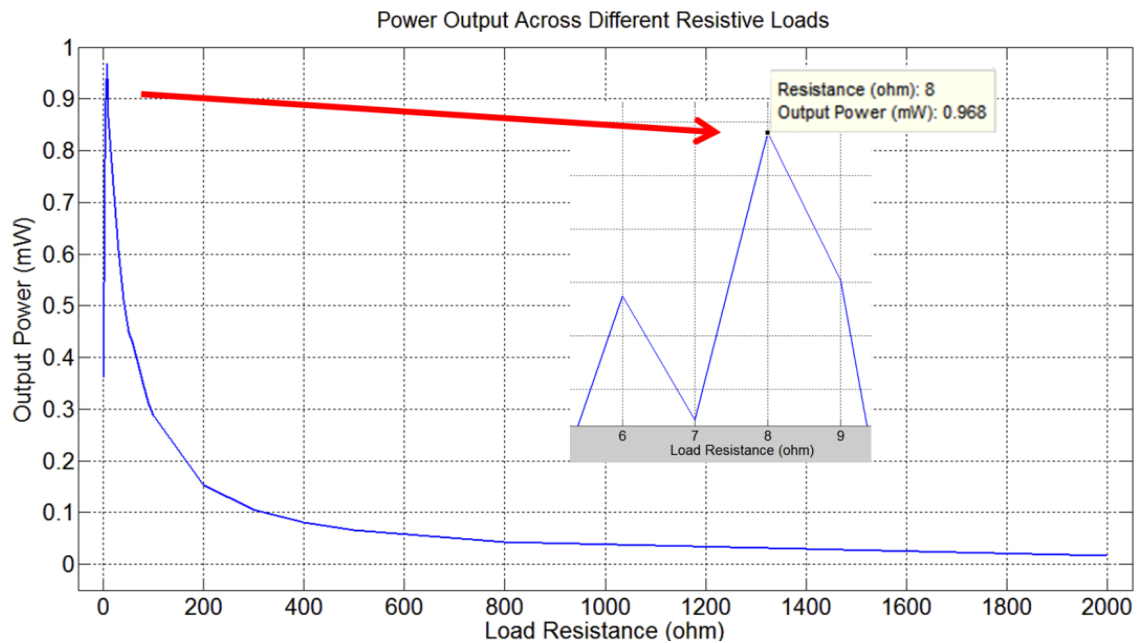


Figure 88: Power output curve across different resistive loads attached to the prototype system.

Figure 88 also shows 8Ω is the optimum resistive load to be attached to the prototype system. This shows that even though from the prototype is not producing maximum output at 8Ω load (at 8Ω load, the prototype only produces 50% peak output voltage compared to peak output voltage from 800Ω load (Figure 87)), the prototype is producing maximum power due to the resistive load being sufficiently small compared to 800Ω and 2000Ω .

Hence from this experiment, the load was set to a new value of 8Ω . And since the 2g acceleration group has the highest peak to peak voltage outputs, the previous experiment was rerun using a new resistive load value of 8Ω to determine if there are any changes to the produced peak to peak output voltage and resultant RMS output voltage.

6.3. Peak to Peak Voltage Output from the Bar Coil

The voltage outputs of the experiments from the bar coil are presented in this section. The results are split into different groups of accelerations where each figure shows the prototype under test at a specific acceleration at different separation distances under various frequencies. The Figure 89 presents the results obtained from the 0.5g acceleration followed by the 1g acceleration results in Figure 90 and lastly finishing with the results from the 2g acceleration shown in Figure 91. Discussion follows after the presentation of results in this subsection.

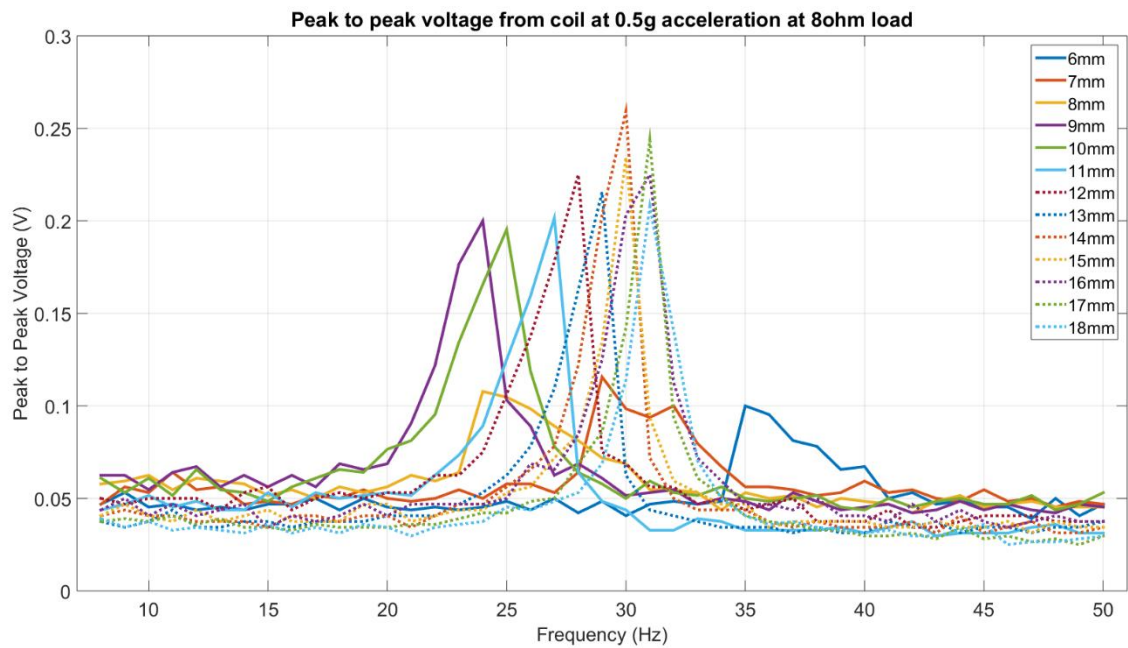


Figure 89: Peak to peak voltage output of the bar coil under 0.5g acceleration across various frequencies.

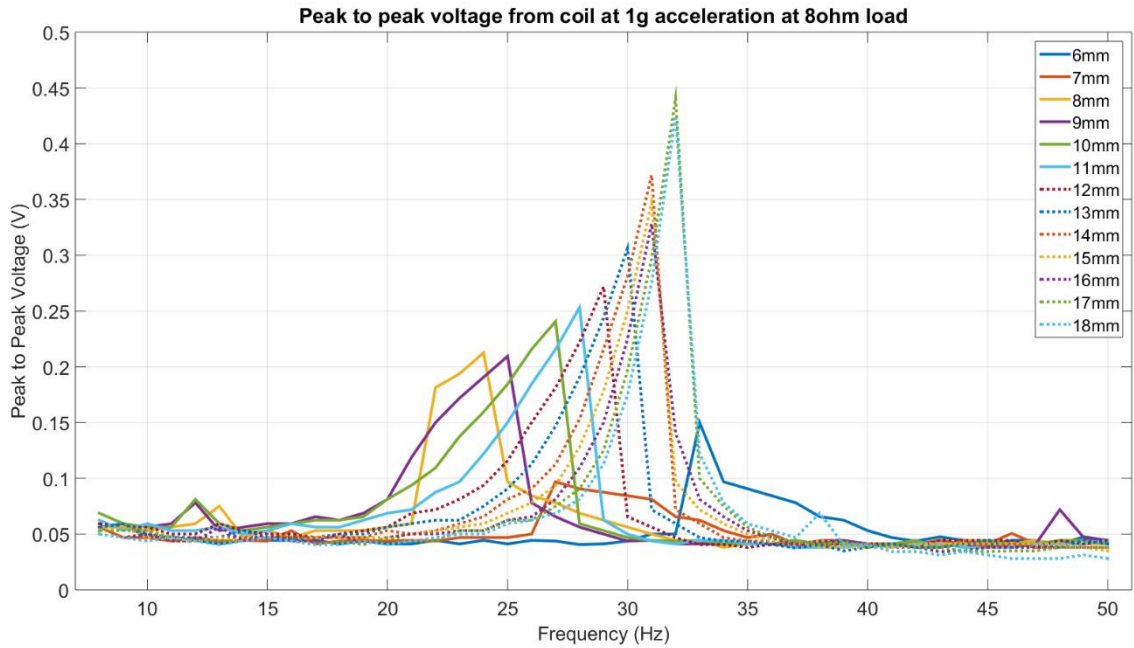


Figure 90: Peak to peak voltage output of the bar coil under 1g acceleration across various frequencies.

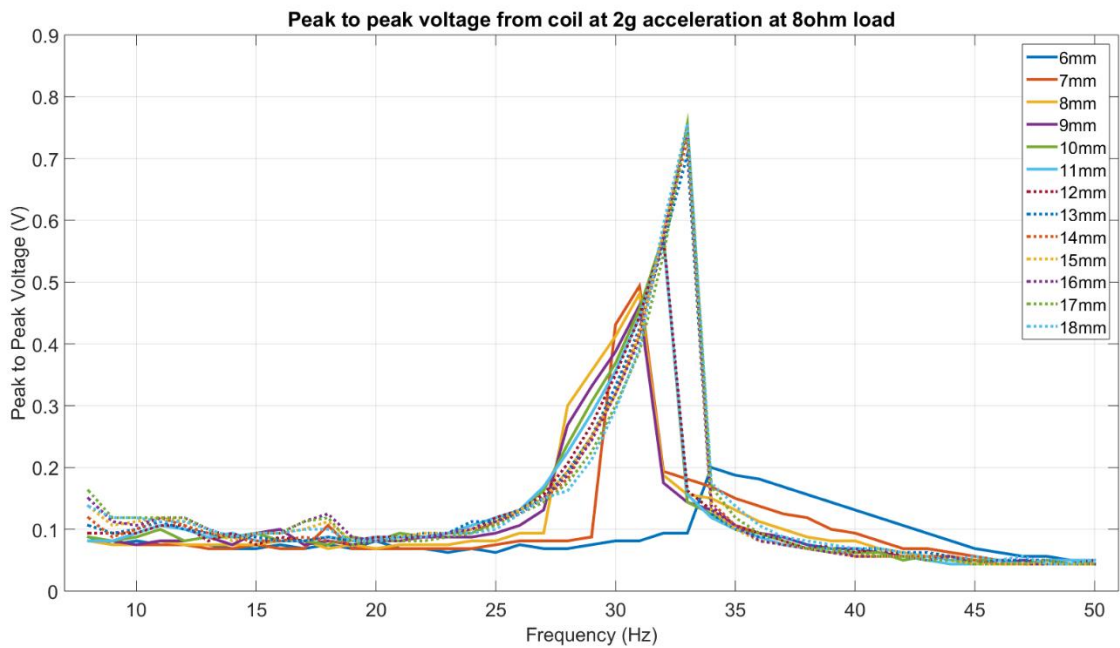


Figure 91: Peak to peak voltage output of the bar coil under 2g acceleration across various frequencies.

To help provide more clarity on the behaviour seen from the results obtained, the height of the coil when placed within the prototype is 16mm and the cantilever magnet's height is 10mm. By referring to Figure 92, assuming that the centre of the magnet with a diameter of half the height of the magnet (Red Ring) and has the strongest magnetic field. This essentially means that to maximize the surface area of the coil which

interacts with the magnetic field, the cantilever has to have a total displacement of around 10mm or higher. Also keeping in mind that a displacement too large would also reduce the optimum “contact area” or “sweetspot” as the magnetic field interacting with the coil are too far away and exits the coil surface area. This would cause the induced voltage from the coil to go in the opposite direction of the currently generated voltage. Thus it can be said that the prototype system has a coil “sweetspot” area that would accommodate the cantilever displacement of between 8mm to around 16mm or 18mm.

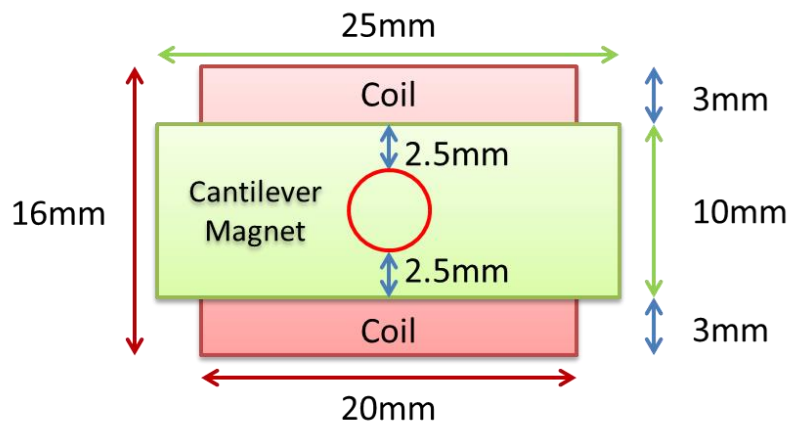


Figure 92: Dimensions of the coil and cantilever magnet and actual prototype.

This is clear that the output voltage that has been recorded is related to the displacements achieved by the cantilever. For example, the displacements achieved by the cantilever whilst the separation distance is 6mm at all accelerations was significantly lower than the 10mm displacement required to maximise the magnet and coil interaction.

Furthermore, as the raw output voltage from the coil is not exactly a proper sine wave for every single cycle of movement from the cantilever. RMS (root-mean-squared) voltage of the system has to be calculated to be able to present a more realistic representation of the output voltage from the coil and also to be able to calculate the power produced from the prototype.

6.4. RMS Output Voltage

To calculate the true power produced by the prototype system, RMS output voltages are needed. The resulting outputs of applying RMS calculations towards the

peak to peak voltage outputs measured from the coils are presented in Figure 93 to Figure 95.

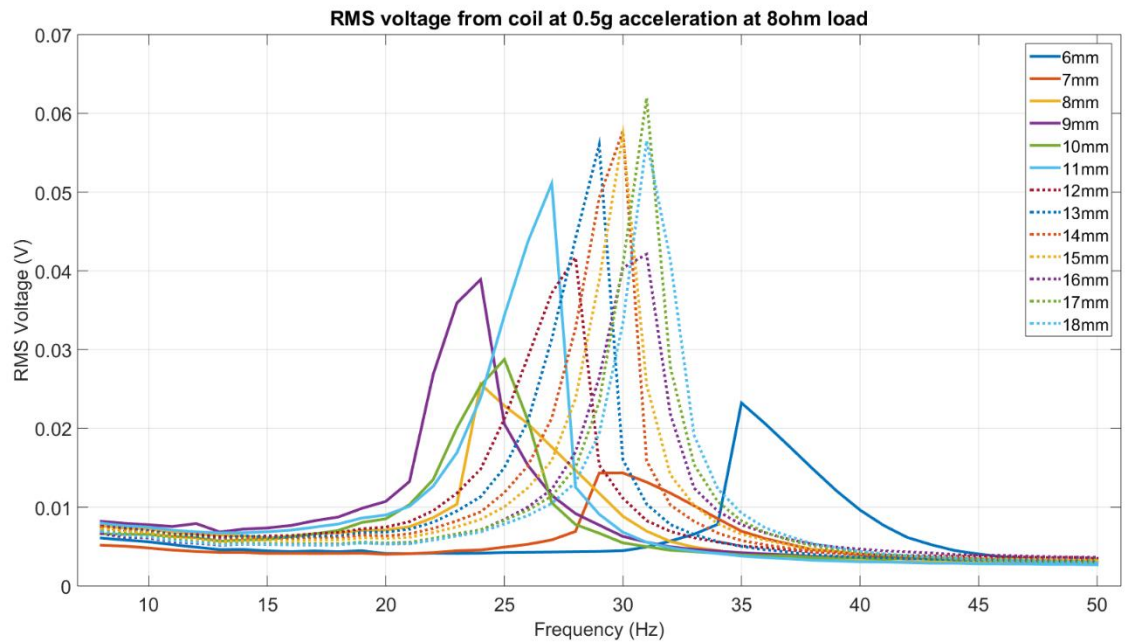


Figure 93: RMS voltage from all separation distances under 0.5g acceleration.

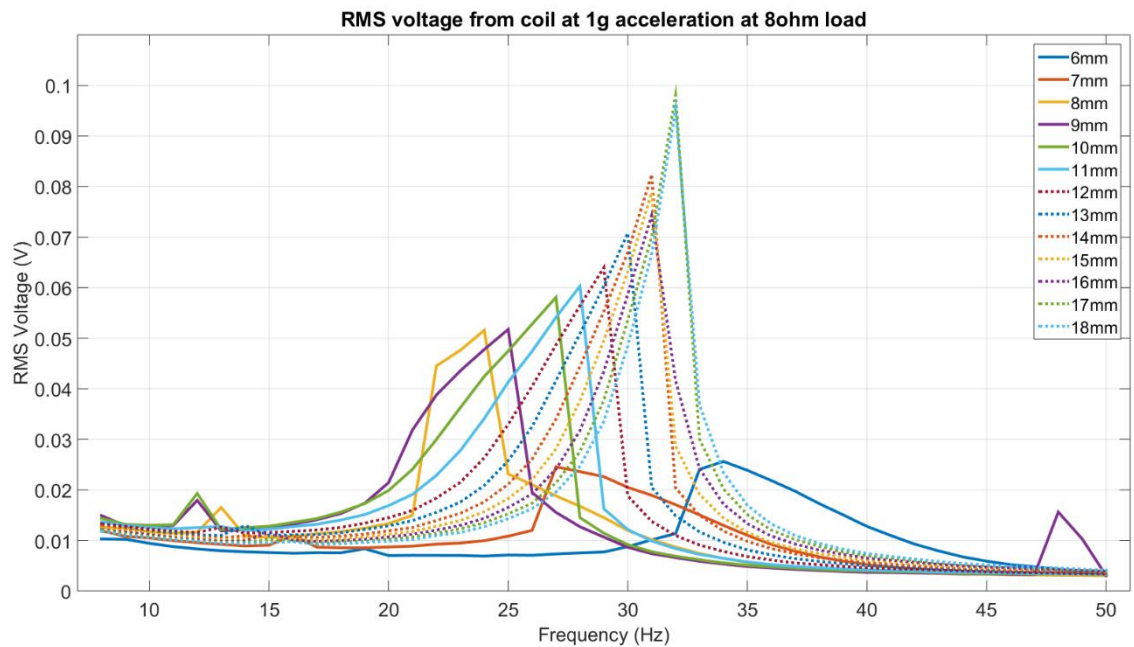


Figure 94: RMS voltage from all separation distances under 1g acceleration.

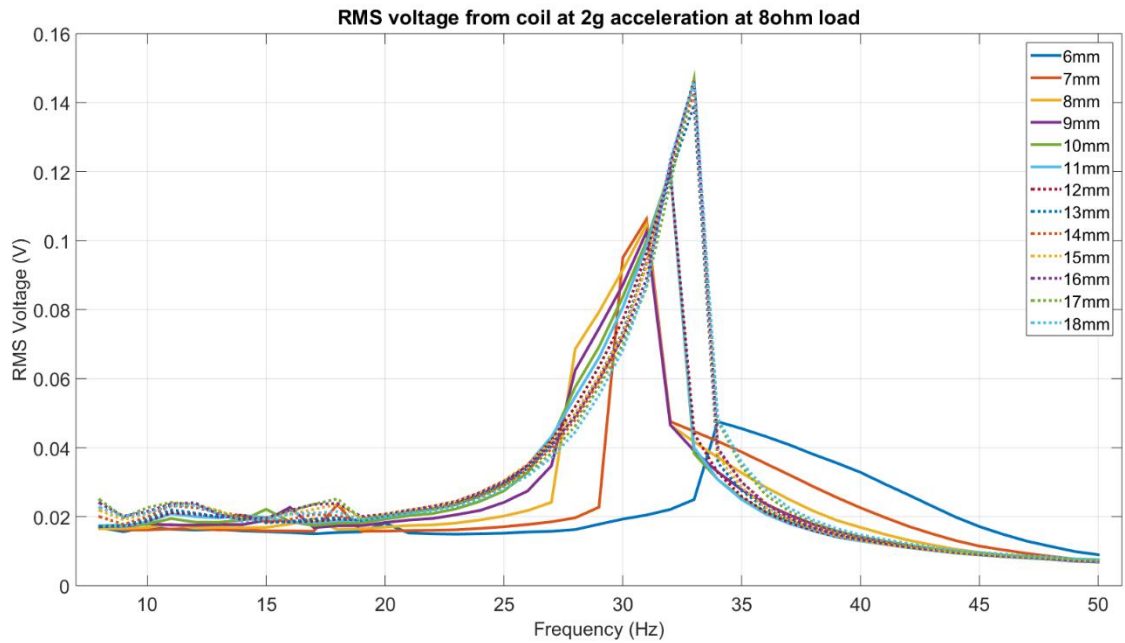


Figure 95: RMS voltage from all separation distances under 2g acceleration.

Whilst it is expected that the RMS output voltage from the 2g acceleration experiments would produce the highest values, the RMS output voltages from the experiments of both 0.5g and 1g acceleration did not exceed 0.1V. The highest RMS output voltage for the 0.5g acceleration was achieved by 17mm separation distance at a frequency of 31Hz at a value of 62mVrms whilst at 1g, the 17mm separation distance is also the highest output producing just below 0.1Vrms at a frequency of 32Hz.

Conversely, the lowest RMS output voltage for both 0.5g and 1g acceleration observed at 7mm separation distance without exceeding 0.03Vrms. However, at 2g acceleration, there was a higher increase in voltage output from all the separation distances and the 6mm separation distance did produce the lowest voltage output in that situation.

Another behaviour that replicated the behaviour seen from the displacement measurement experiments was the frequency of which the peak RMS voltages achieved. The increase in frequency across all the separation distances had peak RMS voltages measured coincided with the increase of the external acceleration applied. The voltages profile that are recorded are similar to the displacement profiles that were achieved in previous experiments.

Additionally, the change in resonance frequencies across different separation distances is due to the opposing forces of the two magnets attached on the prototype, which produces nonlinear dynamics reacting to the acceleration introduced to it.

However, obtaining the RMS output voltages for the prototype under these parameters is only one half of the required variables to be able to calculate the prototype's output power. The other half is to determine the resistive load that is applied on the prototype system. Having the correct resistive load will optimize the power output of the energy harvester.

6.5. Maximum Power and bandwidth from the Prototype

From Section 6.2, it was shown that 8Ω is the optimum resistive load to achieve maximum power from the prototype system. Calculation of the maximum power available from the prototype system requires the output voltages in terms of RMS voltages as the system is treated as an AC (Alternating Current) system.

The experiments from Section 6.3 and Section 6.4 are redone with the resistive load now set to 8Ω . Results are presented in Figure 96 to Figure 98 showing the data collected from the prototype at accelerations from 0.5g to 2g including bandwidth from prototype at Full Width Half Max (FWHM).

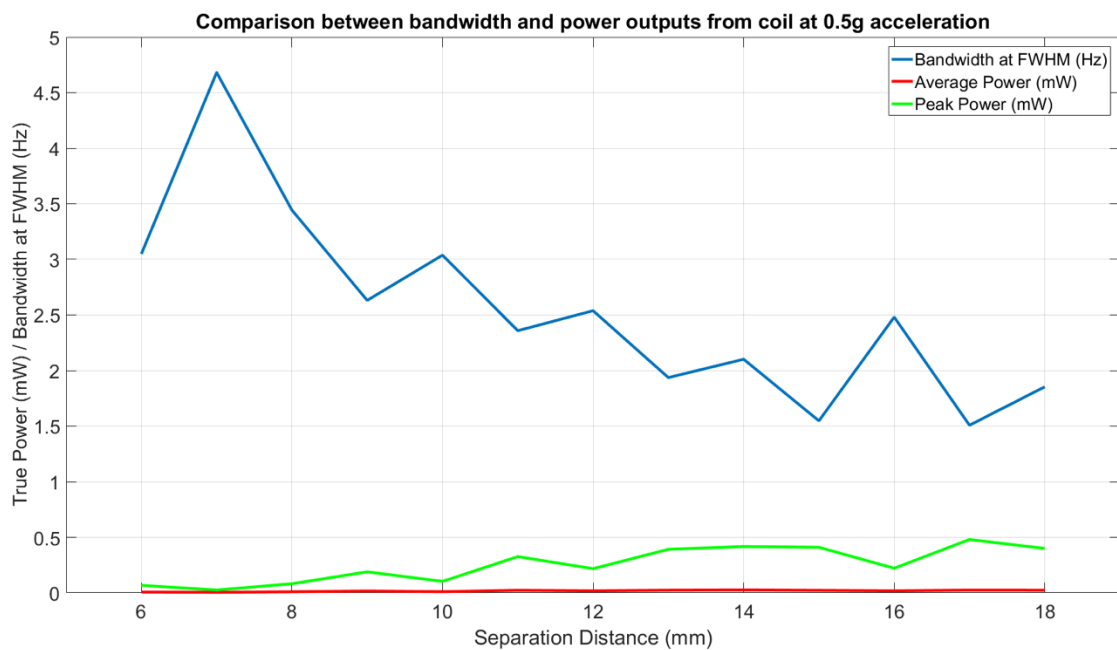


Figure 96: Power output and bandwidth comparison for prototype under 0.5g acceleration.

Figure 96 shows that the prototype under 0.5g acceleration at low separation distances, which the prototype exhibits nonlinear behaviour shows higher bandwidth for the power generated. Peak power from the prototype under 0.5g was generated when the separation distance of the two opposing magnets are at 17mm is 0.5mW, which is under the linear region. Bandwidth at the same time was also lowest at 1.5Hz at FWHM of 0.5mW power. Highest bandwidth was exhibited at 7mm separation distance where the bandwidth was more than three times higher compared to the peak power bandwidth at around 4.7Hz.

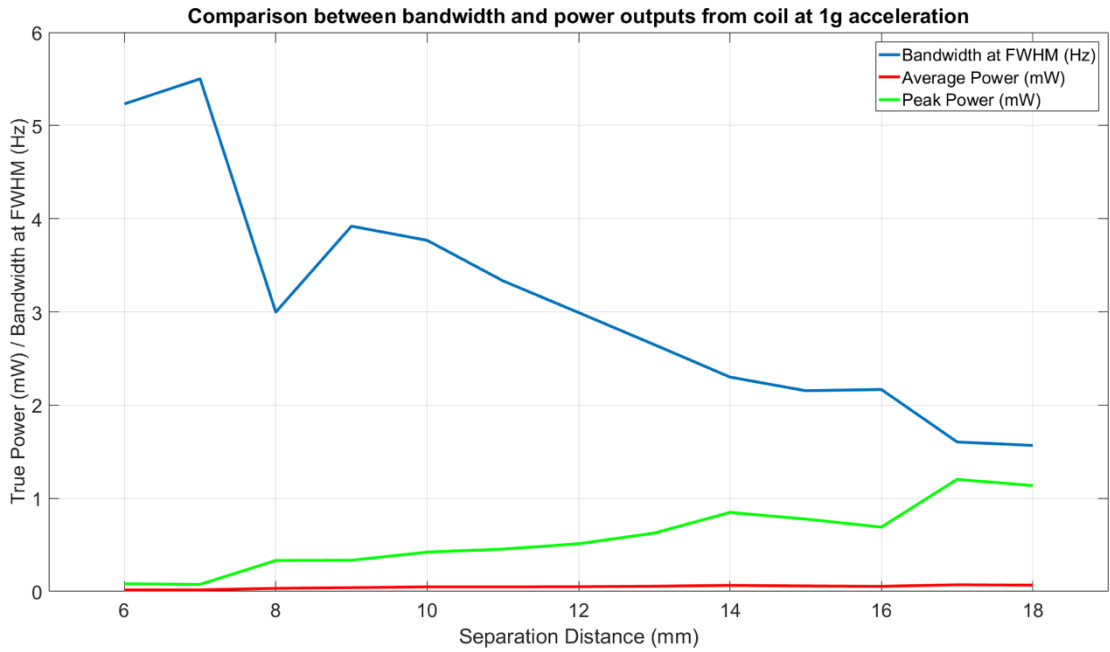


Figure 97: Power output and bandwidth comparison for prototype under 1g acceleration.

Figure 97 presents the power outputs in comparison to the bandwidth of the power output at FWHM where the highest power output managed to break the 1mW barrier. It is clear that the peak power of the prototype is highest when the cantilever is within the linear region where the separation distance of the two opposing magnets are high. This behaviour, in line with previous cantilever behaviour observed show that the cantilever has a low bandwidth when the cantilever separation distance is high / within the linear region. Conversely, the highest bandwidth was achieved at about 5.5Hz with a separation distance of 7mm albeit with the lowest power output of the whole 1g experiment.

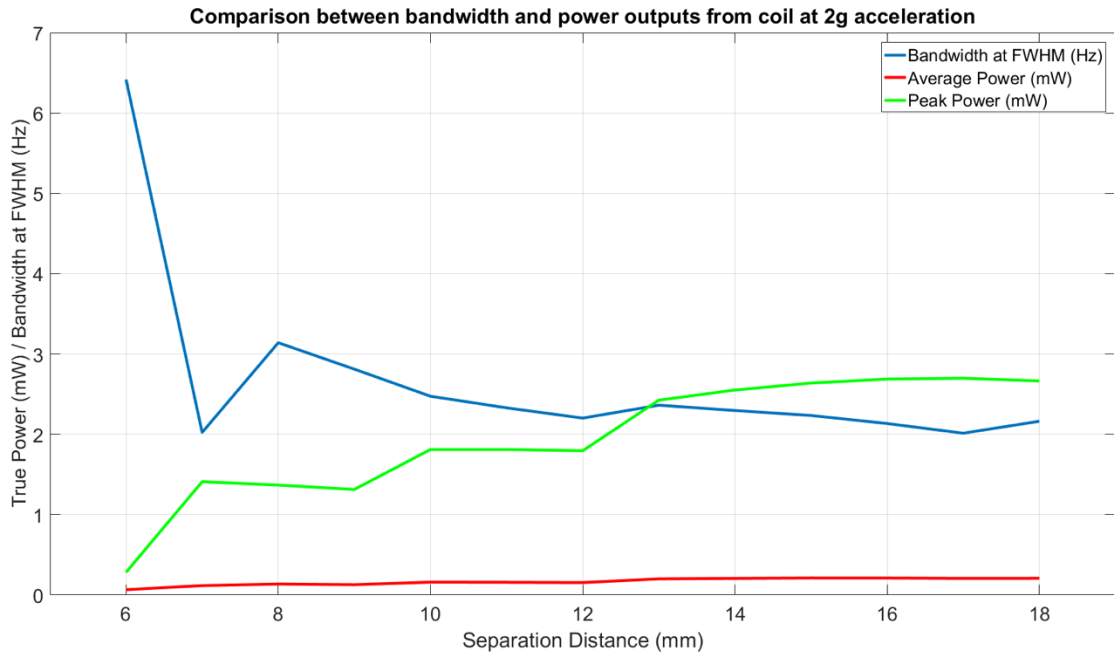


Figure 98: Power output and bandwidth comparison for prototype under 2g acceleration.

Figure 98 displays the data collected from the 2g acceleration experiment undertaken by the prototype. The prototype showed similar responses in comparison to the 1g acceleration experiment where the higher the separation distance, the higher the peak power and the inverse for bandwidth. The 2g acceleration prototype managed to achieve a peak power of close to 3mW with a bandwidth of over 2Hz across every single separation distance. Highest bandwidth was achieved by the 6mm separation distance where nonlinear behaviour was observed.

In summary, these power output behaviours are important as they can be tailored to suit certain requirements under certain conditions to provide a more efficient power harvesting medium. For example, an application which has a broader range of frequency and predominantly operating with a lower frequency can have the prototype to operate at the extreme nonlinear region of the prototype (6mm to 8mm) depending on the frequency of the application. If the application has a higher duty cycle with a higher frequency, then a higher separation distance should be used as it has a slightly higher resonant frequency compared to the lower separation distance. On the other hand, if an application has a small variation in frequency changes would be more suitable to have the prototype set to the highest separation distance to be able to generate maximum power for as much time as possible. Any applications that fall in between these two conditions can have the prototype set to a medium separation distance (12mm) where it

possesses the behaviour of a combination of both nonlinear and linear behaviours which would possibly be the most suitable for the required application.

6.6. Summary

This section presented the optimum power generation ability of the prototype when coupled with a coil and also an optimum resistive load. The power generation ability of the prototype was largely similar to the output trends observed in previous sections even though there were slight differences which will be further discussed in the following section.

Further discussions and conclusions of this section as well as the research as a whole will be presented in the next section.

7.0 Further Discussions, Conclusions and Future Work

This section summarizes the whole thesis and ties all the sections together, combining all the findings of the whole research process. The section ends with recommendations for future work.

7.1. Further Discussions Regarding Nonlinear Model and Prototype

This research has produced a working prototype of a nonlinear energy harvester using the electromagnetic method of transduction of converting vibrational accelerations into electrical energy. The novel idea of inserting a coil in the gap between the two opposing magnets used to produce nonlinear dynamics has also been implemented in the process. The results from both modelling simulations and the prototype shows that a higher bandwidth is achieved when the energy harvester is operating within the nonlinear region (low separation distances) compared to when the energy harvester was in the linear region (high separation distance). This behaviour agrees with the literature produced by other authors.

However, a comparison of the simulated results with the experimental results does not show like for like agreement which allows some discussions to be derived from it. For instance, it shows that the experimental outputs in the nonlinear region provide bandwidths which are higher than the simulated results. The two opposing magnets are the cause of the nonlinear dynamics which influence the behaviour of the cantilever. The lower the separation distance, the stronger the opposing forces of the magnets which results in the nonlinear dynamics.

This is believed to be due to a limitation of the dipole model which was used to calculate and predict the forces which are produced from the magnets within the prototype. The dipole model that was used breaks down at low distances and is unable to perfectly replicate the behaviour of the actual magnets. Also, this issue was further compounded by the use of different sized magnets. The dipole model was assumed to be propagating from a central point equally outwards. By having one of the magnets as a bar magnet resulted in a different form of propagation. This resulted in the completed simulation model underestimating the resulting forces on the nonlinear region and overestimating over on the linear region. However, the trend of results produced by both the model and the prototype conform to the literature produced by other authors hence the model provides a useful insight into the system behaviour.

In summary, the lower the separation distance, the higher the external accelerations needed to get the cantilever to move. However, at the right separation distance the nonlinear dynamics will boost the cantilever's displacement instead of holding it back which increases the rate of change of the magnetic field acting upon the coil which will result in a higher voltage output. It is observed at very low separation distances (ie: <5mm) requires external accelerations higher than 2g to consider to have an advantage to be used as the opposing forces are too strong otherwise and lesser accelerations are not able to flex the cantilever sufficiently.

Another interesting behaviour displayed by both the model and the experimental prototype was the change in resonance frequency of the cantilever while the system is operating within the nonlinear region. Both the model and prototype had a resonant frequency of 34Hz when operating in the linear regime. However, when the system was operated at low separation distances (nonlinear region), the resonant frequency of the system was reduced, especially at higher accelerations. A compilation of the resonant frequencies recorded from both the simulation model and the experimental prototype is presented in Figure 79.

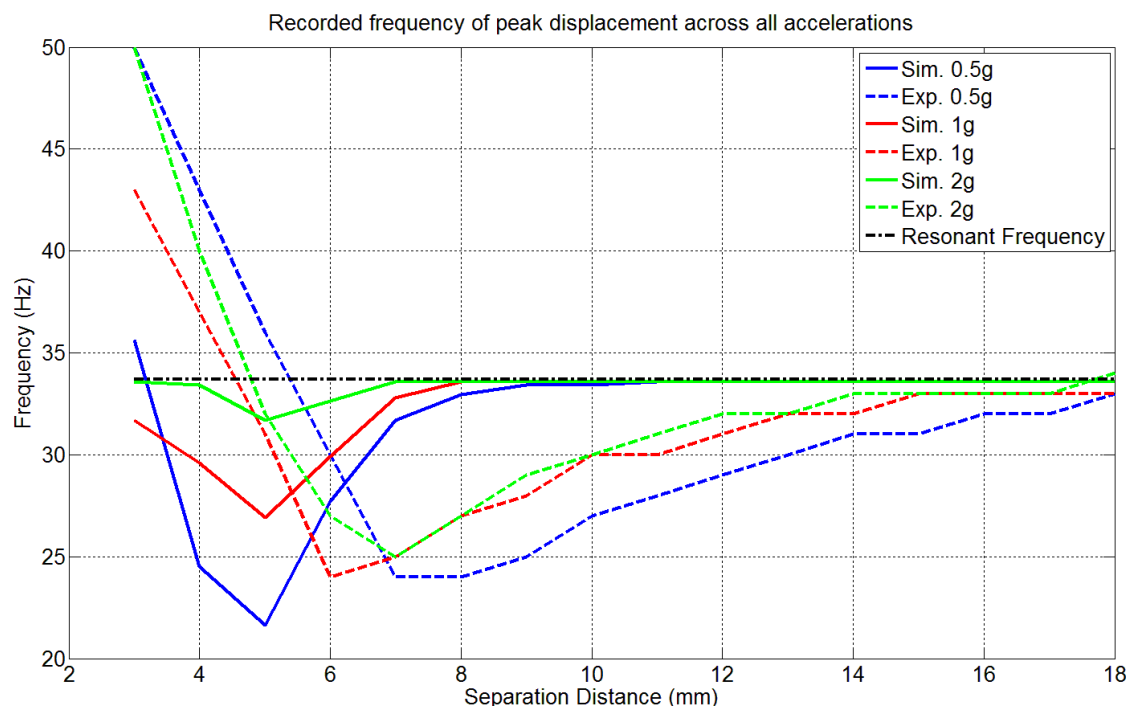


Figure 99: Copy of Figure 79.

This behaviour can be attributed to the nonlinear forces that were acting against the cantilever when the two opposing magnets were separated by a small distance. The lower separation distance results in a stronger opposing force acting against the

cantilever which in turn inhibits free movement of the cantilever unlike when the cantilever which operates in the linear region. The cantilever which operates within the linear region consistently shows resonant frequency which is very similar to the designed resonant frequency of the system. This shows free movement capability of the cantilever without external forces acting upon the cantilever.

This proves that this model and prototype has the ability to reduce a system's resonant frequency whilst operating within the nonlinear region at low separating distances of the two opposing magnets.

A look at the output voltages produced by the coil which is inserted in between the gap that was present between the two opposing magnets also presented some interesting results and behaviour. It was also noted that location of the optimum resistive load to be paired with the coil was extremely important as a lower resistive load would be able to produce a higher amount of power. 800Ω was found to be the lowest resistive load that enables the coil to produce the highest output voltages but 8Ω was the optimum resistive load for producing highest power. It was mentioned in Section 2.6 that the two opposing magnet configuration would be expected to produce a higher output voltage compared to a single magnet. The prototype showed the higher the cantilever displacement, which was during the cantilever's resonance frequency at any selected separation, the higher the voltage that was produced for the particular setting. Hence a similar trend of higher displacement/output, lower bandwidth was showed.

Moving on, the phase plane plots provided additional insight to the nonlinear cantilever behaviour. Even though the resolution of the experimental phase plane plots was limited by the sensitivity and frequency of the laser displacement sensor, it was still seen to be very chaotic for some of the phase plane plots. There was very clear nonlinear behaviour observed during the experimentation process.

Lastly, the power generated by the prototype from the coil peaked close to 3mW with an optimum resistive load of 8Ω . Power output of the coil again was influenced by the voltage generating ability of the whole prototype, which covers the coil itself as well as the magnetic field in touch with it. The higher the number of turns on the coil and the higher the rate of change of the magnetic field surrounding the coil, the higher the output voltage from the coil. Even though around 3mW was the prototype's peak power output, it was achieved by the 18mm separation which is within the linear region. The

areas which are strongly influenced by nonlinear dynamics (lower separation distances) produced similar power outputs around 1.5 to 2mW but carries higher bandwidth which enables a wider and lower operation frequency. This is especially useful when designing a system capable of operating within a wider window of operation.

In summary, even though the simulated model was not 100% accurate with its predicted results compared to the prototype, the trend of the results were very similar in which this model is sufficiently accurate to be considered for further modelling use.

7.2. Recommendations for Future Work

From the experience of the research, several suggestions for additional future work are recommended here:

- A more accurate model of the magnetic field will be needed to increase the accuracy of the simulation model as a whole as the current dipole model is limited. The choice of magnets' dimension is also important to the modelling process. Similar dimensions can be considered to aid the modelling process.
- The arrangements of both the magnets are also important in trying to increase voltage output from the coil. Currently within this research, only one magnet is used on one end (one on the cantilever and another on the micrometer). This created a nonlinear opposing force which is only significant for about 15mm displacement. To increase this distance, multiple magnets could be placed together to increase and enhance the opposing forces against both ends. This will also indirectly create a stronger magnetic field which will help produce higher voltage outputs from the coil used.
- As discussed in Section 6.1, the coil placement is as important as the makeup of the coil. Placing the coil within an area where the strongest magnetic field present will help increase power output of the prototype. However, placing the coil in the position which has the strongest magnetic field as well as the highest rate of change will be the best solution to this. Additionally, the coil could be wound with better conductive materials, smaller diameters, tighter and more compact so that as many turns are put onto the coil as possible with the smallest footprint possible. However, care must be taken to ensure that the wound coil has the surface area to completely cover the "sweetspot" of the magnetic

movement for maximum voltage generation. It is a compromise which has to be perfected to obtain the highest output from the prototype.

- Using a cantilever with a lower spring constant. However, obtaining a single whole cantilever with extremely low spring constant might prove to be difficult and costly. It is worth researching about creating a cantilever which is made up off two or more sections of different materials. Figure 100 shows the potential cantilever design which can be investigated. The red section is the longer stiffer section and the yellow section is the softer section.

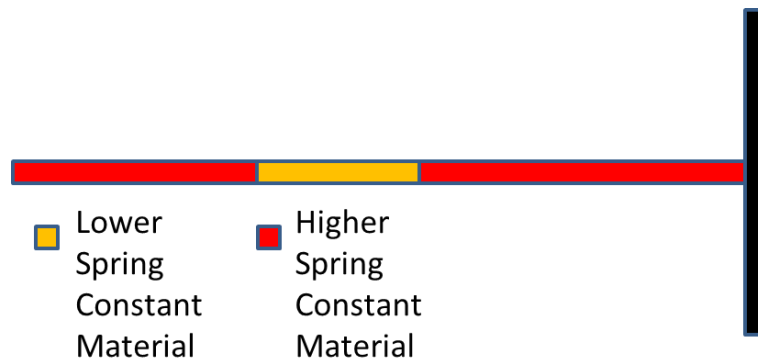


Figure 100: Potential cantilever design.

The idea behind this is to enable the cantilever to achieve higher rates of velocity and displacements which results in higher voltage output from the coil. The stiffer section keeps the cantilever in a neutral position when there are no external accelerations. The yellow provides the extra flex during operation to achieve the extra velocity in having a more flexible portion compared to the red section allowing “snap back” action (idea from badminton / tennis racket designs).

- The ability of the hardware to provide adequate accelerations across all frequencies to be tested. The shaker, power amplifier and the controlled voltage source has to be able to produce consistent accelerations across all ranges of accelerations. This is to improve consistency and quality of results.
- Reduction in size of the prototype is also essential if it is to exploit any commercial potential of this research. Converting this research into a commercial item requires slick packaging as well as a consistently easy to use platform which is reliable at all times. However, this is just purely an idea as the change in dimensions will alter all the dynamics of the system and create many problems.

8.0 References

- [1] M. Cooper, "Batteries not included," *New Scientist*, vol. 171 (2307), no. 24, 24 September 2001.
- [2] C. Kenneally, "Power from people breaks the gold of batteries and plugs," *New York Times*, p. Page G9, 3 August 2000.
- [3] P. D. Mitcheson, E. M. Yeatman, G. K. Rao, A. S. Holmes and T. C. Green, "Energy Harvesting From Human and Machine Motion for Wireless Electronic Devices," *Proceedings of the IEEE*, vol. 96, no. 9, pp. 1457-1486, September 2008.
- [4] S. Roundy, D. Steingart, L. Frechette, P. Wright and J. Rabaey, *Power Sources for Wireless Sensor Networks*, Berlin: Springer Berlin Heidelberg, 2004, pp. 1-17.
- [5] A. Bieberle-Hütter, D. Beckel, U. P. Muecke, J. L. M. Rupp, A. Infortuna and L. J. Gauckler, "Micro-Solid Oxide Fuel Cells as Battery Replacement," *Journal of Power Sources*, vol. 177, no. 1, pp. 123-130, 15 February 2008.
- [6] J. Rabaey, J. Ammer, J. d. Silva and D. Patel, "PicoRadio: Ad-hoc Wireless networking of Ubiquitous Low Energy Sensor/Monitor Nodes," in *VLSI, 2000. Proceedings. IEEE Computer Society Workshop, 27-28 April 2000*.
- [7] The Royal Academy of Engineering; nPower, "Wind Turbine Power Calculations," [Online]. Available: <http://www.raeng.org.uk/publications/other/23-wind-turbine>. [Accessed 25 March 2014].
- [8] B. L. Ooi, "Optimisation and Frequency Tuning Concepts for a Vibration Energy Harvester, PhD Thesis," The University of Hull, Hull, United Kingdom, 2010.
- [9] T. Starner and J. A. Paradiso, "Human Generated Power for Mobile Electronics," in *Low Power Electronics Design*, CRC Press, Fall 2004.
- [10] D. Morton, *Human Locomotion and Body Form*, Baltimore: The Williams &

Wilkins Co., 1952.

- [11] J. Comroe, *Physiology of Respiration*, 2nd Edition, Chicago: Year Book Medical Publishers, 1979.
- [12] A. Delnavaz and J. Voix, "Electromagnetic Micro-Power Generator for Energy Harvesting from Breathing," in *IECON 2012 - 38th Annual Conference on IEEE Industrial Electronics Society*, 25-28 Oct. 2012.
- [13] "Carnot Efficiency," [Online]. Available: http://www.engineeringtoolbox.com/carnot-efficiency-d_1047.html. [Accessed 23 August 2010].
- [14] O. Fischer and W. Braune, *The Human Gait*, Berlin: Springer-Verlag, 1895-1904; Reprinted 1987.
- [15] J. Gilbert, "In-Shoe Power Generation," School of Engineering, University of Hull, Hull, March 2000.
- [16] M. Shorten, "Energetics of running and running shoes," *Journal of Biomechanics*, vol. 26, no. 1, pp. 41-51, 1993.
- [17] The Energy Harvesting Network, "Energy Harvesting From Human Power - a roadmap to new research challenges," The Energy Harvesting Network, March 2011.
- [18] The Energy Harvesting - Special Interest Group, "Industry Needs Analysis - Potential opportunities for energy harvesting (Health and Medical section)," The Energy Harvesting - Special Interest Group, May 2013. [Online]. Available: <https://connect.innovateuk.org/documents/3176926/3726993/Industry%20Needs%20Analysis%20for%20Energy%20Harvesting%20final%20Sept%202013.pdf>. [Accessed 29 March 2014].
- [19] C. Yew and J. Gilbert, *Energy Harvesting and Human Movement (Poster)*, The Energy Harvesting Network Dissemination Event 2011 (London): The Energy Harvesting Network, 2011, <http://eh-network.org/events/dissemination2011/posters/Chun.pdf>.

- [20] K. Malasri and L. Wang, "Design and Implementation of a Secure Wireless Mote-Based Medical Sensor Network," *Sensors 2009*, vol. 9, p. page 6273 – 6297, 11 August 2009.
- [21] J. M. Gilbert and F. Balouchi, "Comparison of Energy Harvesting Systems for Wireless Sensor Networks," *International Journal of Automation and Computing*, vol. 05, no. 4, pp. 334-347, October 2008.
- [22] Microsemi, "Microsemi LX1802 Datasheet," Microsemi, [Online]. Available: <http://www.microsemi.com/existing-parts/parts/83938#docs-specs>. [Accessed 10 December 2013].
- [23] Microsemi, "Microsemi ZL70102 Wireless for Implantable Medical Sensors," Microsemi, [Online]. Available: <http://www.microsemi.com/products/ultra-low-power-wireless/implantable-medical-transceivers/zl70102#docs-amp-specs>. [Accessed 10 December 2013].
- [24] C. Williams and R. Yates, "Analysis of a micro-electric generator for microsystems," *Sensors and Actuators*, vol. A, no. 52, pp. 8-11, 1996.
- [25] S. J. Roundy, "Energy Scavenging for Wireless Sensor Nodes with a Focus on Vibration to Electricity Conversion (Thesis)," The University of California, Berkeley, 2003.
- [26] F. Cottone, *Nonlinear Piezoelectric Generators for Vibration Energy Harvesting*, Perugia, Italy: University of Perugia, PhD Thesis, 2007.
- [27] S. P. Beeby, R. N. Torah, M. J. Tudor, P. Glynn-Jones, T. O'Donnell, C. R. Saha and S. Roy, "A micro electromagnetic generator for vibration energy harvesting," *Journal of Microelectronics and Microengineering*, vol. 17, pp. 1257-1265, 2007.
- [28] H. Kim, Y. Tadasse and S. Priya, "Piezoelectric Energy Harvesting," in *Energy Harvesting Technologies*, New York, Springer, 2009, pp. 3-39.
- [29] L. Wang and F. G. Yuan, "Vibration energy harvesting by magnetostrictive material," *Smart Materials and Structures*, vol. 17, no. 4, 3 June 2008.

- [30] X. Dai, Y. Wen, P. Li, J. Yang and X. Jiang, "A Vibration Energy Harvester Using Magnetostrictive/Piezoelectric Composite Transducer," in *IEEE Sensors*, 25-28 Oct. 2009.
- [31] T. Ladont, J. Delamare, G. Lebedev, D. Zakharov, B. Viala, O. Cugat, O. Geoffroy, N. Galopin and L. Garbuio, "Magnetostrictive-Piezoelectric Composite Structure For Energy Harvesting," *Journal of Micromechanics and Microengineering*, vol. 22, no. 9, 24 August 2012.
- [32] W. Huang, K. Tzeng, M. Cheng and R. Huang, "Design and fabrication of a vibrational micro-generator for wearable MEMS," in *Proceedings of Eurosensors XVII*, Guimaraes, Portugal, 2003.
- [33] A. Pérez-Rodríguez, C. Serre, N. Fondevilla, C. Cereceda, J. Morante, J. Esteve and J. Montserrat, "Design of electromagnetic inertial generators for energy scavenging applications," in *Proceedings of Eurosensors XIX*, Barcelona, Spain, 2005.
- [34] C. Serre, A. Pérez-Rodríguez, N. Fondevilla, E. Martincic, S. Martí'nez, J. R. Morante, J. Montserrat and J. Esteve, "Design and implementation of mechanical resonators for optimized inertial electromagnetic microgenerators," *Microsys Technol*, vol. 14, pp. 653-658, 2008.
- [35] S. Beeby, M. Tudor, E. Koukharenko, N. White, T.O'Donnell, C. Saha, S. Kulkarni and S.Roy, "Micromachined silicon Generator for Harvesting Power from Vibrations," in *The 4th International Workshop on Micro and Nanotechnology for Power Generation and Energy Conversion Applications (PowerMEMS 2004)*, Kyoto, Japan, 28 Nov 2004.
- [36] I. Sari, T. Balkan and H. Kulah, "A wideband electromagnetic micro power generator for wireless microsystems," in *TRANSDUCERS 2007 - 2007 International Solid-State Sensors, Actuators and Microsystems Conference*, Lyon, 10-14 June 2007.
- [37] S. P. Beeby, M. J. Tudor and N. M. White, "Energy harvesting vibration sources for microsystems applications," *Measurement Science and Technology*, vol. 17, pp. 175-195, 2006.

- [38] D. P. Arnold, "Review of Microscale Magnetic Power Generation," *IEEE Transactions on Magnetics*, vol. 43, no. 11, pp. 3940-3951, 2007.
- [39] S. P. Beeby and T. O'Donnell, "Electromagnetic Energy Harvesting," in *Energy Harvesting Technologies*, New York, Springer, 2009, pp. 129-161.
- [40] M. El-Hami, P. Glynne-Jones, N.M.White, M. Hill, S. Beeby, E. James, A. Brown and J. Ross, "Design and fabrication of a new vibration-based electromechanical power generator," *Sensors and Actuators A: Physical*, vol. 92, no. 1-3, pp. 335-342, 2001.
- [41] P. Glynne-Jones, M. Tudor, S. Beeby and N. White, "An electromagnetic, vibration-powered generator for intelligent sensor systems," *Sensors and Actuators A: Physical*, vol. 110, no. 1-3, pp. 344-349, 2004.
- [42] A. Godfrey, R. Conway, D. Meagher and G. O'laighin, "Direct measurement of human movement by accelerometry," *Medical Engineering & Physics*, vol. 30, pp. 1364-1386, 2008.
- [43] F. Cottone, H. Vocca and L. Gammaitoni, "Nonlinear Energy Harvesting," *Physical Review Letters*, vol. 102, no. 8-27, 23rd February 2009.
- [44] S. Stanton, C. McGehee and B. Mann, "Nonlinear dynamics for broadband energy harvesting: Investigation of a bistable piezoelectric inertial generator," *Physica D*, vol. 239, pp. 640-653, 2010.
- [45] M. Ferrari, V. Ferrari, M. Guizzetti, B. Ando, S. Baglio and C. Trigona, "Improved Energy Harvesting from Wideband Vibrations by Nonlinear Piezoelectric Converters," *Procedia Chemistry*, vol. 1, pp. 1203-1206, 2009.
- [46] B. P. Mann and N. D. Sims, "Energy harvesting from the nonlinear oscillations of magnetic levitation," *Journal of Sound and Vibration*, vol. 319, pp. 515-530, 2009.
- [47] H. Huang, "Human Powered Inertial Energy Harvesters: The Effect of Orientation, Location and Activity on the Obtainable Electrical Power," University of Southampton, PhD Thesis, Southampton, United Kingdom, 2014.

- [48] “Animation Concepts,” [Online]. Available: <http://www.jimahoffman.com/Animation/Reference/Concepts.html>. [Accessed 14 January 2014].
- [49] Q. Meng, B. Li and H. Holstein, “Recognition of human periodic movements from unstructured information,” *Image and Vision Computing*, vol. 24, p. 795–809, 2006.
- [50] K. W. Yung, P. B. Landecker and D. D. Villani, “An Analytic Solution For The Force Between Two Magnetic Poles,” *Magnetic and Electrical Separation*, vol. 9, pp. 39-52, 1998.
- [51] T. Irvine, “Beams modelled as Single-Degree-Of-Freedom systems,” 12 November 2012. [Online]. Available: <http://www.vibrationdata.com/tutorials2/beam.pdf>. [Accessed 2 May 2014].
- [52] NT-MDT, “Effective mass and eigenfrequency of the cantilever,” [Online]. Available: <http://www.ntmdt.com/spm-basics/view/effective-mass-eigenfrequency-cantilever>.
- [53] University of California, Berkeley (Teaching Text), “Deflection of beams by integration (Chapter 8),” p. Page 399. [Accessed 2 June 2014]. <http://www.me.berkeley.edu/~lwlj/me128/BeamDeflection.pdf>
- [54] AdvancePipeliner, “AdvancePipeliner Beam Deflection Formulae,” [Online]. Available: http://www.advancepipeliner.com/Resources/Others/Beams/Beam_Deflection_Formulae.pdf. [Accessed 2 May 2014].
- [55] Handout, Carnegie Mellon University Course, “<https://www.andrew.cmu.edu/course/24-352/Handouts/logdecrement.pdf>,” [Online] [Accessed 14 January 2014].

Appendix A: Source Code Used For Importing Accelerometer Measurements into Matlab Workspace and Analysis

```
% This section of code reads the output of the accelerometer
% in binary format. It normalizes the measurements then converts
% the measurements from voltages into "g". Fast Fourier Transform
% (FFT) is applied to enable the accelerations be read in the
% frequency domain.
% This code can be applied to all movements recorded with the ADXL325

clear all;
[t,v1] = importAgilentBin ('leftfoot walking 1.bin',1);
[t,v2] = importAgilentBin ('leftfoot walking 1.bin',2);
[t,v3] = importAgilentBin ('leftfoot walking 1.bin',3);
% import the 3 axis data from the file saved by the accelerometer
% and splitting them into 3 variables.

figure; set(gca,'fontsize',20);
plot(t, (v1-1.56)/0.18908,t, (v2-1.62)/0.18908,'g',t,...
(v3-1.62)/0.18908,'r'),xlabel('Time [Seconds]','fontsize',20),...
ylabel('Acceleration [g]','fontsize',20),...
ylim([-4 3.0]), title('All Channels Sensor Output'), grid on,
legend('Channel X','Channel Y','Channel Z','Location','SouthEast');
% plots the figure after taking off the initial voltage offsets
% and converting the plots into "g" units.

a1=(v1-mean(v1))/0.18908; %normalize and convert to "g" units
y1=2*abs(fft(a1,1024)/1000); %FFT of the converted "g" units
f1=50*linspace(0,1,513); %frequency plot

a2=(v2-mean(v2))/0.18908;
y2=2*abs(fft(a2,1024)/1000);
f2=50*linspace(0,1,513);

a3=(v3-mean(v3))/0.18908;
y3=2*abs(fft(a3,1024)/1000);
f3=50*linspace(0,1,513);

A=y1.^2; %to obtain total accelerations from all 3 axis of the
B=y2.^2; %selected movement.
C=y3.^2;

Ttlacc= sqrt(A+B+C); %total acceleration

figure;set(gca,'fontsize',20);
stem(f1(1:100),Ttlacc(1:100),'m','linewidth',2),...
xlabel('Frequency [Hz]','fontsize',20),...
ylabel('Acceleration [g]','fontsize',20),...
xlim([-0.4 4.55]),ylim([-0.02 1.5]),...
title('Max Acceleration of all 3 Channels - Left Foot Walk'),
grid on ;
%plot total acceleration of all 3 axis' acceleration after FFT

figure;set(gca,'fontsize',20);
stem(f1(1:100),y1(1:100),'linewidth',2),...
xlabel('Frequency [Hz]','fontsize',20),...
ylabel('Acceleration [g]','fontsize',20),...
xlim([-0.4 4.55]),ylim([-0.02 0.2]),...
title('Channel X - Frequency Domain Values'), grid on ;
%plot channel X acceleration after FFT
```

```

figure;set(gca,'fontsize',20);
stem(f2(1:100),y2(1:100),'g','linewidth',2),...
xlabel('Frequency [Hz]','fontsize',20),...
ylabel('Acceleration [g]','fontsize',20),...
xlim([-0.4 4.55]),ylim([-0.02 0.2]),...
title('Channel Y - Frequency Domain Values'), grid on ;
%plot channel Y acceleration after FFT

figure;set(gca,'fontsize',20);
stem(f3(1:100),y3(1:100),'r','linewidth',2),...
xlabel('Frequency [Hz]','fontsize',20),...
ylabel('Acceleration [g]','fontsize',20),...
xlim([-0.4 4.55]),ylim([-0.02 0.2]),...
title('Channel Z - Frequency Domain Values'), grid on ;
%plot channel Z acceleration after FFT

```

Appendix B: Frequency Sweep of Calibrated Vibrator

```
%% Calibration Results

freq05=[8:1:50];
freq1=[8:1:50];
freq2=[8:1:50];

inputvolt2new=[1.45 1.14 0.93 0.78 0.66 0.57 0.5 0.44 0.4 0.36 0.34
0.31 0.292 0.28 0.265 0.255 0.25 ...
    0.247 0.247 0.247 0.25 0.255 0.26 0.265 0.27 0.275 0.282 0.29
0.297 0.305 0.315 0.325 0.335 ...
    0.345 0.355 0.365 0.37 0.38 0.39 0.4 0.415 0.42 0.435]; %for 2g
acceleration

inputvolt1new =[0.82 0.63 0.51 0.415 0.35 0.295 0.258 0.228 0.205
0.185 0.17 0.158 0.15 0.142 0.138 ...
    0.133 0.13 0.13 0.128 0.128 0.128 0.128 0.132 0.135 0.138 0.141
0.144 0.147 0.15 0.155 0.16 ...
    0.165 0.17 0.175 0.18 0.185 0.188 0.195 0.2 0.205 0.21 0.215
0.22];

inputvolt05new = [0.45 0.355 0.29 0.23 0.19 0.155 0.138 0.12 0.108 0.1
0.09 0.085 0.075 0.07 0.07 ...
    0.07 0.068 0.07 0.07 0.068 0.068 0.07 0.071 0.071 0.072 0.075
0.077 0.08 0.082 0.085 0.085 0.088 ...
    0.09 0.092 0.095 0.098 0.1 0.102 0.105 0.108 0.11 0.112 0.115];

min2g=min(inputvolt2new);%looking for minimum value from the measured
data
min05g=min(inputvolt05new);
min1g=min(inputvolt1new);

freqinterp= 8:0.1:50;
scaleinterp05=
interp1(freq05,inputvolt05new,freqinterp,'linear');%extending the
scale through interpolation
scaleinterp1= interp1(freq1,inputvolt1new,freqinterp,'linear');
scaleinterp2= interp1(freq2,inputvolt2new,freqinterp,'linear');
freqinterp= (round(freqinterp*10))/10;

multiplier05=scaleinterp05/min05g;%looking for the multiplier number
compared to the lowest input voltage
multiplier1=scaleinterp1/min1g;
multiplier2=scaleinterp2/min2g;

%% Load in PicoStatus values

PicoStatus;
%% Declare constants

global data;

data.TRUE = 1;
data.FALSE = 0;

% Identify type of generator on PicoScope
data.SIG_GEN_NONE = 0;
data.SIG_GEN_FUNCT_GEN = 1;
data.SIG_GEN_AWG = 2;
```

```

% External Threshold Range
data.EXT_RANGE = 5000; % milliVolts

% Signal Generator Constants

MIN_SIG_GEN_FREQ = 0.0;
MAX_SIG_GEN_FUNC_GEN_FREQ = 1000000.0; % A and B variants Function
Generator max 1MHz
MAX_SIG_GEN_AWG_FREQ = 20000000.0; % AWG max 20MHz

MIN_SIG_GEN_BUFFER_SIZE = 1;
MAX_SIG_GEN_BUFFER_SIZE = 8192;
PS3X06B_MAX_SIG_GEN_BUFFER_SIZE = 16384;

MIN_DWELL_COUNT = 10;

%% Device Connection

% Create device
ps3000a_obj = icdevice('ps3000a_IC_drv', '');

% Connect device
connect(ps3000a_obj);

% Provide access to enumerations and structures
[methodinfo, structs, enuminfo, ThunkLibName] = PS3000aMFile;

% pause(2); %wait for N seconds before starting frequency sweep
%% Show unit information

info_status = invoke(ps3000a_obj, 'GetUnitInfo',
ps3000a_obj.unithandle)

%% Obtain Maximum & Minimum values

max_val_status = invoke(ps3000a_obj, 'ps3000aMaximumValue');

fprintf('Max ADC value: %d\n', ps3000a_obj.maxValue);

while (1)
    %% Asking for input
    ch = '';
    fprintf('\nPlease select one from the following options: \nR - Repeat
Frequency Sweep\n');
    ch = input('X - Exit\n\nOption: ', 's');
    % Ensure upper case letter
    ch = upper(ch);

    %% Settings of the Sig Gen
    outputfreqsweep=8:1:50; %10-60 Hz for 0.5g, 15-60 Hz for 1g, 25-50 Hz
    for 2g

    switch (ch)
    case 'R'
        for d=outputfreqsweep
            fprintf('Frequency is: %dHz\n', d);

            n=find(freqinterp==d);%looking for the position of the multiplier
            number

```

```

vibratormultiplier05=multiplier05(1,n);%the multiplier number for the
selected acceleration for the selected frequency
vibratormultiplier1=multiplier1(1,n);
vibratormultiplier2=multiplier2(1,n);

pkToPk = vibratormultiplier2*2*min2g*1000000;; %SET THE ACCELERATION
VALUES

offsetVoltage = 0; %microVolts

waveformType = enuminfo.enPS3000AWaveType.PS3000A_SINE;
startFrequency = d; %number in Hz (10.0)
stopFrequency = d;
increment = 0;
dwellTime = 0;

sweepType = enuminfo.enPS3000ASweepType.PS3000A_UP;
operation = enuminfo.enPS3000AExtraOperations.PS3000A_ES_OFF; %
Applies to B variants only
shots = 0;
sweeps = 0;
triggerType = enuminfo.enPS3000ASigGenTrigType.PS3000A_SIGGEN_RISING;
triggerSource =
enuminfo.enPS3000ASigGenTrigSource.PS3000A_SIGGEN_NONE;
extInThreshold = int16(mv2adc(0, data.EXT_RANGE,
ps3000a_obj.maxValue));

sig_gen_built_in_status = invoke(ps3000a_obj,
'ps3000aSetSigGenBuiltIn', ...
    offsetVoltage, pkToPk, waveformType,
startFrequency, stopFrequency, increment, ...
    dwellTime, sweepType, operation, shots, sweeps,
triggerType, triggerSource, ...
    extInThreshold);

pause(3); %hold the frequency for how long in seconds

pkToPk = 0;
    waveformType =
enuminfo.enPS3000AWaveType.PS3000A_DC_VOLTAGE;
    increment = 0;
    dwellTime = 0;

    sig_gen_built_in_status = invoke(ps3000a_obj,
'ps3000aSetSigGenBuiltIn', ...
    offsetVoltage, pkToPk, waveformType,
startFrequency, stopFrequency, increment, ...
    dwellTime, sweepType, operation, shots, sweeps,
triggerType, triggerSource, ...
    extInThreshold);
    pause(1); %hold the frequency for how long in seconds

    end

case 'X'

    disp('Turning Signal generator off');

    pkToPk = 0;

```

```

        waveformType =
enuminfo.enPS3000AWaveType.PS3000A_DC_VOLTAGE;
        increment = 0;
        dwellTime = 0;

        sig_gen_built_in_status = invoke(ps3000a_obj,
'ps3000aSetSigGenBuiltIn', ...
        offsetVoltage, pkToPk, waveformType,
startFrequency, stopFrequency, increment, ...
        dwellTime, sweepType, operation, shots, sweeps,
triggerType, triggerSource, ...
        extInThreshold);

        %Exit
        break;
end
end

disconnect(ps3000a_obj);

```

Appendix C: Voltage Outputs from Cylindrical Coil

Results of the cylindrical coil from Section 6.1 which underwent the same experiment as the bar coil are attached here. The attached figures show the peak to peak voltage outputs of the cylindrical coil when the coil is put under 0.5g, 1g and 2g of accelerations at various frequencies at selected separation distances. The lowest separation distance allowing smooth cantilever movements achievable with the cylindrical coil was at 9.5mm hence the experiments were conducted with 9.5mm as the lowest separation distance of the magnets and continuing with 12mm and 18mm as the remaining separation distances. The coils are also connected to a resistive load of 2000Ω and the graphs are scaled to provide a comparison of the voltage achieved throughout all three accelerations.

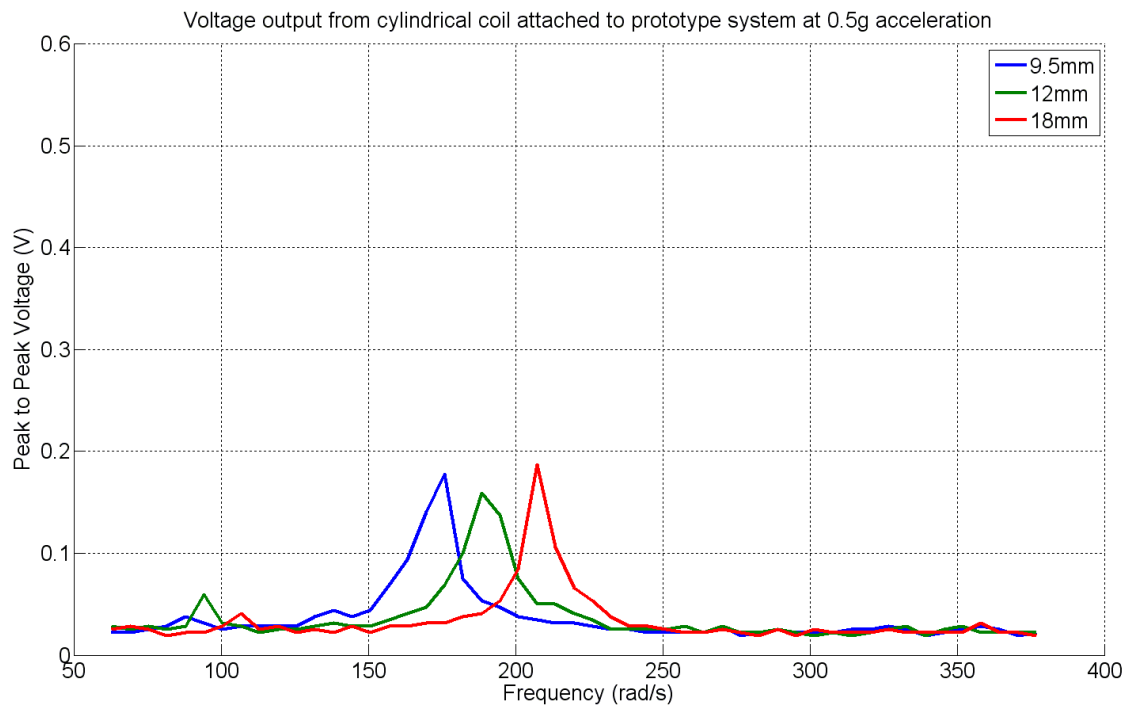


Figure 101: Voltage outputs of the cylindrical coil at 0.5g acceleration.

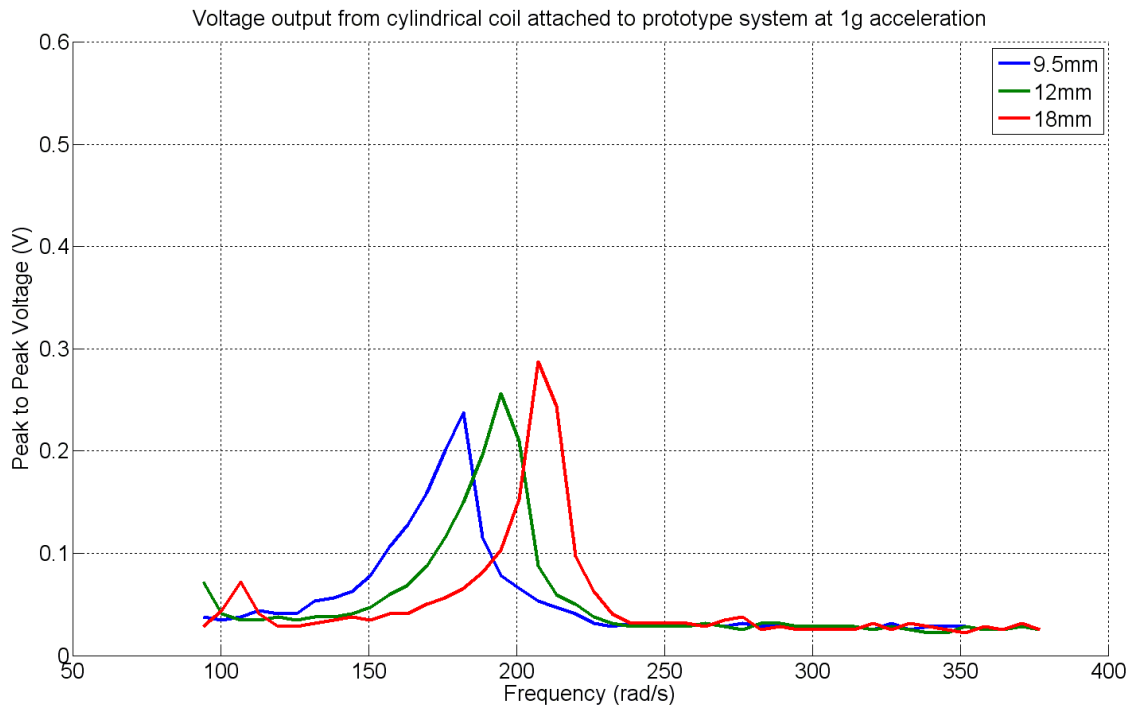


Figure 102: Voltage outputs of the cylindrical coil at 1g acceleration.

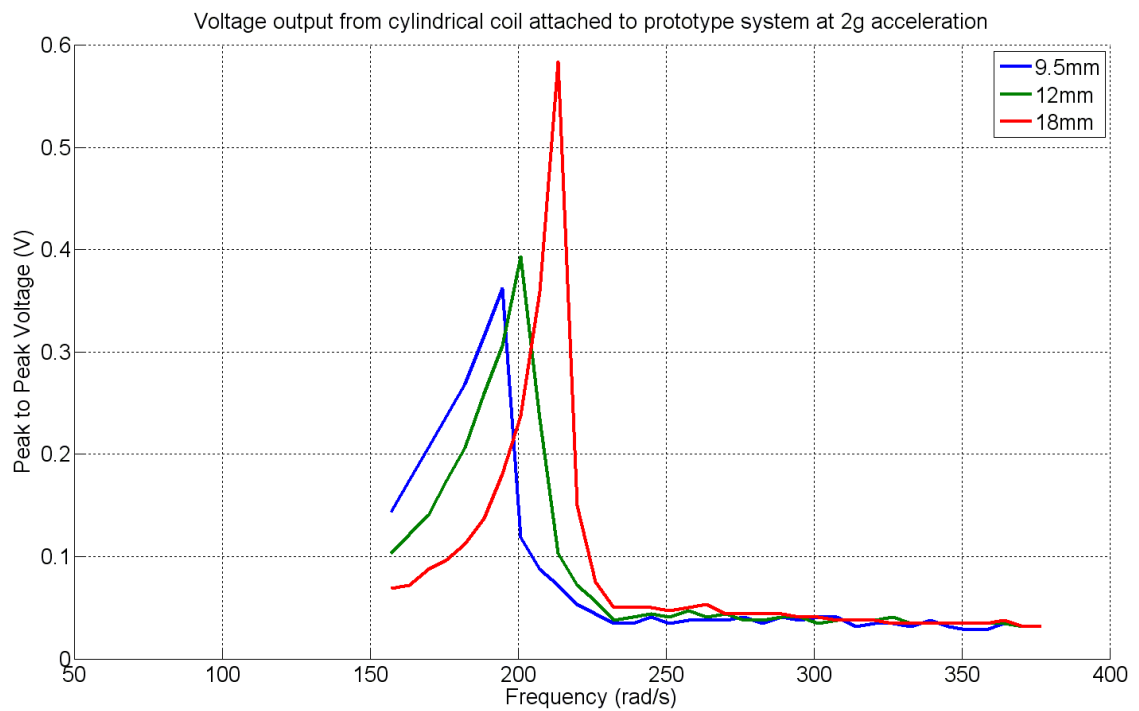


Figure 103: Voltage outputs of the cylindrical coil at 2g acceleration.

Appendix D: Source Code for Modelling Nonlinear Forces Generated by Dipoles

```

%This section of code calculates the forces created by the two
%dipoles which are facing against each other.
%dipoleForce function used from dipoleForce.m

%%%%%%%%%%%%%%%%%%%%%%%%%%%%%%%%%%%%%%%%%%%%%%%%%%%%%%%%%%%%%%%%%%%%%%%%
dipoleForce.m
%%%%%%%%%%%%%%%%%%%%%%%%%%%%%%%%%%%%%%%%%%%%%%%%%%%%%%%%%%%%%%%%%%%%%%%%
function F=dipoleForce(m1,m2,r);
mu0=pi*4e-7;
R=norm(r);
F=3*mu0/(4*pi*R^5)*(dot(m1,r)*m2+dot(m2,r)*m1+dot(m1,m2)*r-
5*dot(m1,r)*dot(m2,r)*r/(R^2));

%%%%%%%%%%%%%%%%%%%%%%%%%%%%%%%%%%%%%%%%%%%%%%%%%%%%%%%%%%%%%%%%%%%%%%%%

%close all;
figure;
m1=4.43e-2; % strength of magnet 1
m2=8.46e-2; % strength of magnet 2

M1=[0 m1 0]; % direction of magnet 1
M2=[0 -m2 0]; % direction of magnet 2
yy=-0.02:0.00001:0.02; % range of deflections (in meters)
dd=0.001:0.001:0.018; % range of separations (in meters)

FFY=[];
for d=dd
    FF=[];FX=[];FY=[]; MAXFY=[];
    for y=yy
        R=[d y 0]; % vector between magnets
        F=dipoleForce(M1,M2,R); % force vector
        FF=[FF norm(F)]; % total force
        FY=[FY F(2)]; % y component of force
        FX=[FX F(1)]; % x component of force
        MAXFY=[MAXFY max(FY)]; %locating maximum values
    end
    plot(yy*1000,FY,'linewidth',2);
    xlabel('Distance of deflection (mm)','fontsize',20);
    ylabel('Deflection forces between dipole (N)','fontsize',20);
    set(gca,'fontsize',20);
    legend(num2str((1000*dd')));
    title('Forces generated by magnets with varying separations
(mm)'...
        , 'fontsize',20)

    FFY=[FFY;FY];
    hold all;

end

```

Appendix E: Source Code for Frequency Response from Simulink model of Nonlinear Cantilever

```
%This section of code simulates the behaviour of the nonlinear  
%cantilever response using the Simulink model shown in Section 4
```

```
% close all;  
hold all;  
d1=[0.005 0.006 0.007 0.018]; %separation distance  
  
for d=d1;  
    ww=45:0.2:350; %frequency (rad/s)  
    A=[];  
    for w=ww  
        sim('NLcantilever'); %simulink model  
        A=[A std(y)]; %displacement use  
        A=[A std(ydot)]; %phase plane plot use  
    end  
    figure;  
    plot(ww,A,'linewidth',2);  
    xlabel('Frequency (rad/s)')  
    ylabel('Displacement (m)', 'fontsize',20);  
    xlabel('Frequency (rad/s)', 'fontsize',20);  
    set(gca, 'fontsize',20);  
    title(['Frequency Response for Distance of separation: '  
    num2str(d*1000) 'mm']);  
    axis([5 35 -0.00005 0.5]);  
  
end
```

Appendix F: Frequency Responses for All Separation Distances under All Accelerations from Simulation

0.5g Acceleration

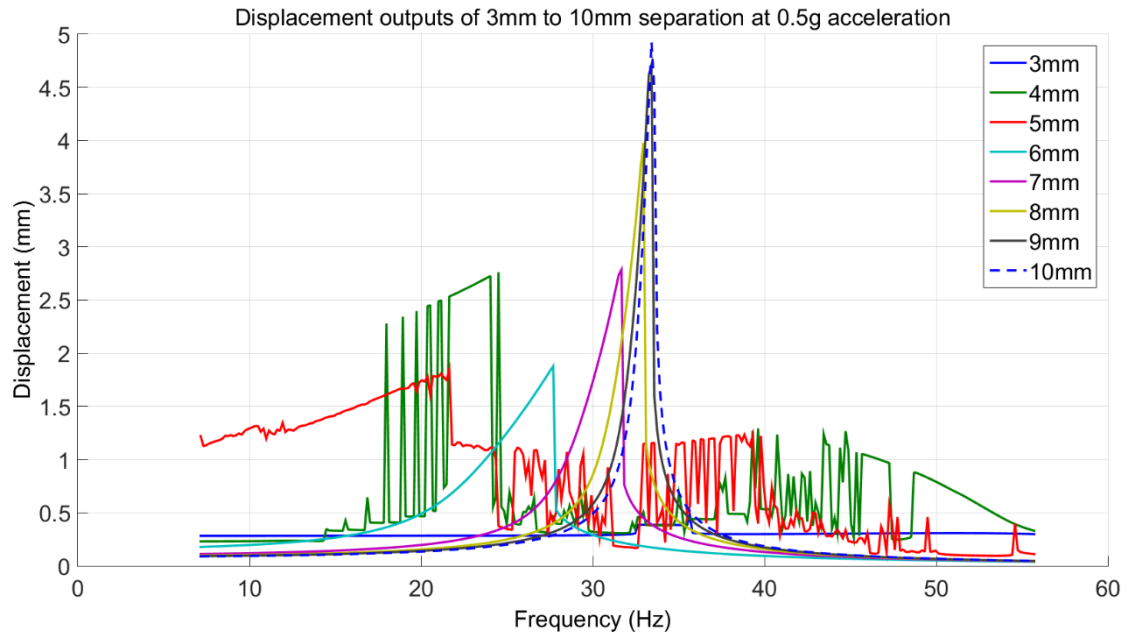


Figure 104: Frequency response of simulated cantilever at 0.5g acceleration from 3mm to 10mm separation.

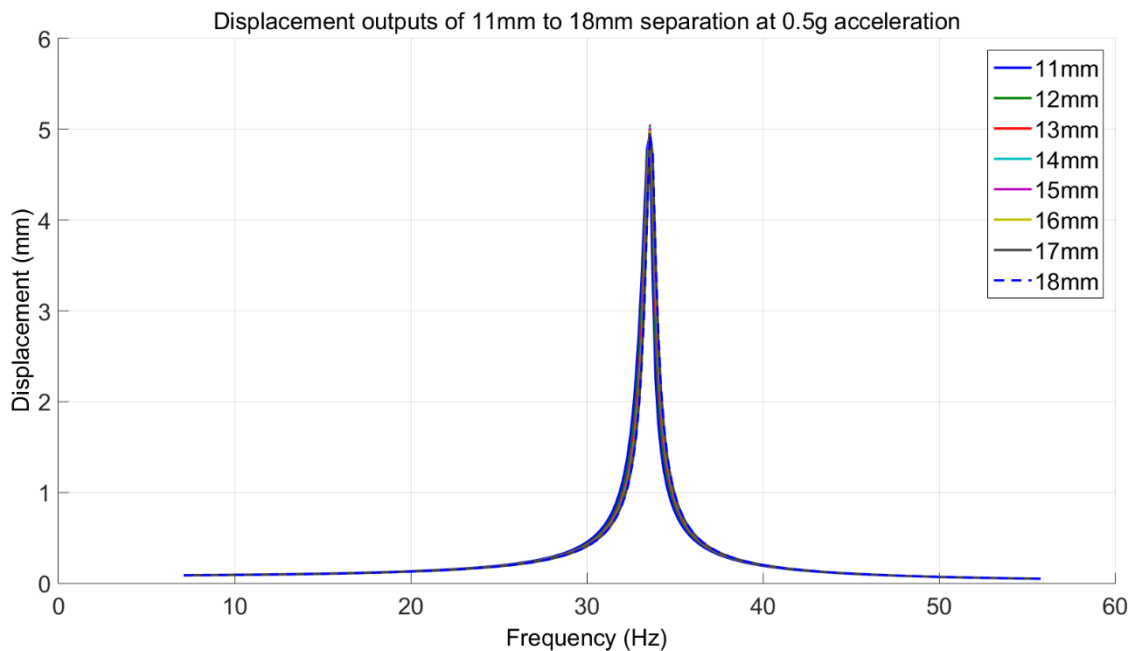


Figure 105: Frequency response of simulated cantilever at 0.5g acceleration from 11mm to 18mm separation.

1g Acceleration

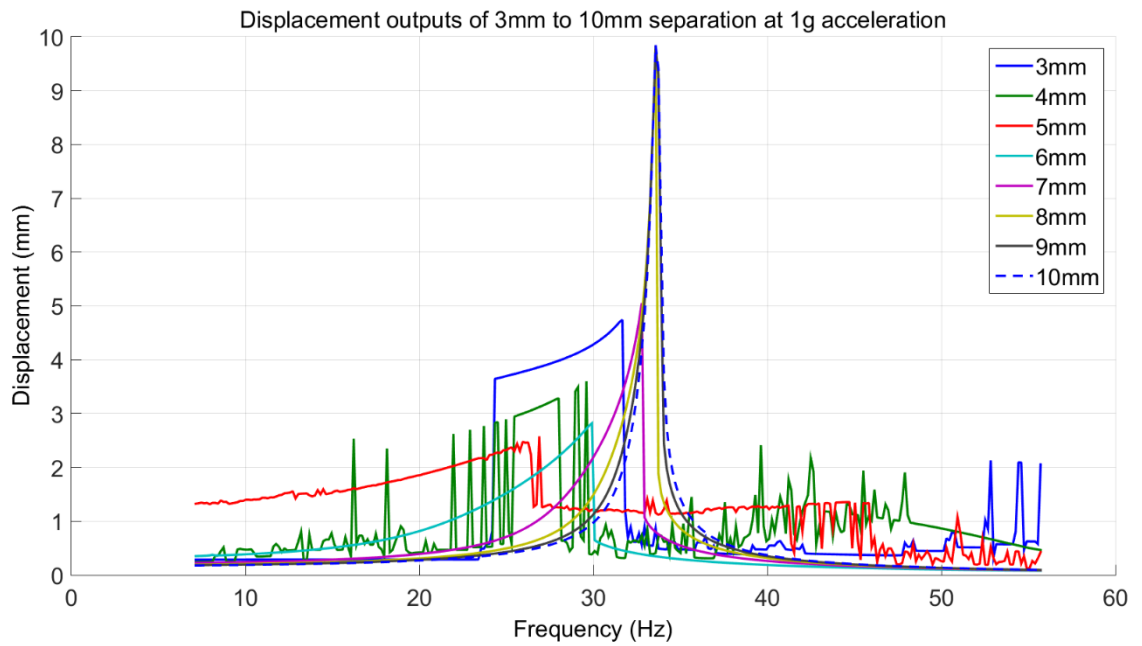


Figure 106: Frequency response of simulated cantilever at 1g acceleration from 3mm to 10mm separation.

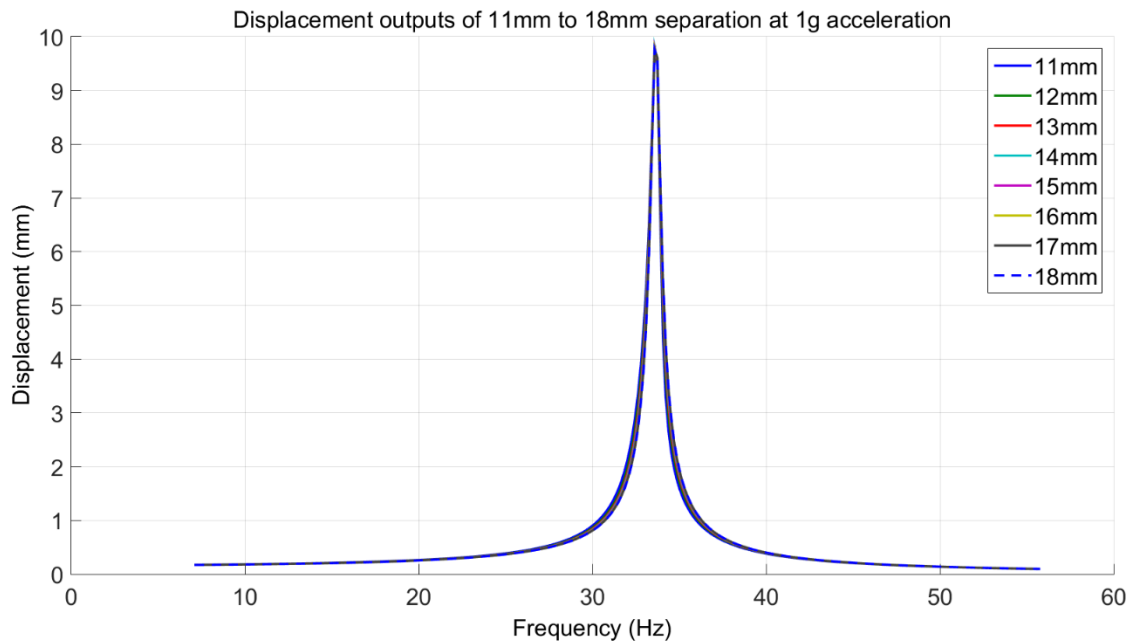


Figure 107: Frequency response of simulated cantilever at 1g acceleration from 11mm to 18mm separation.

2g Acceleration

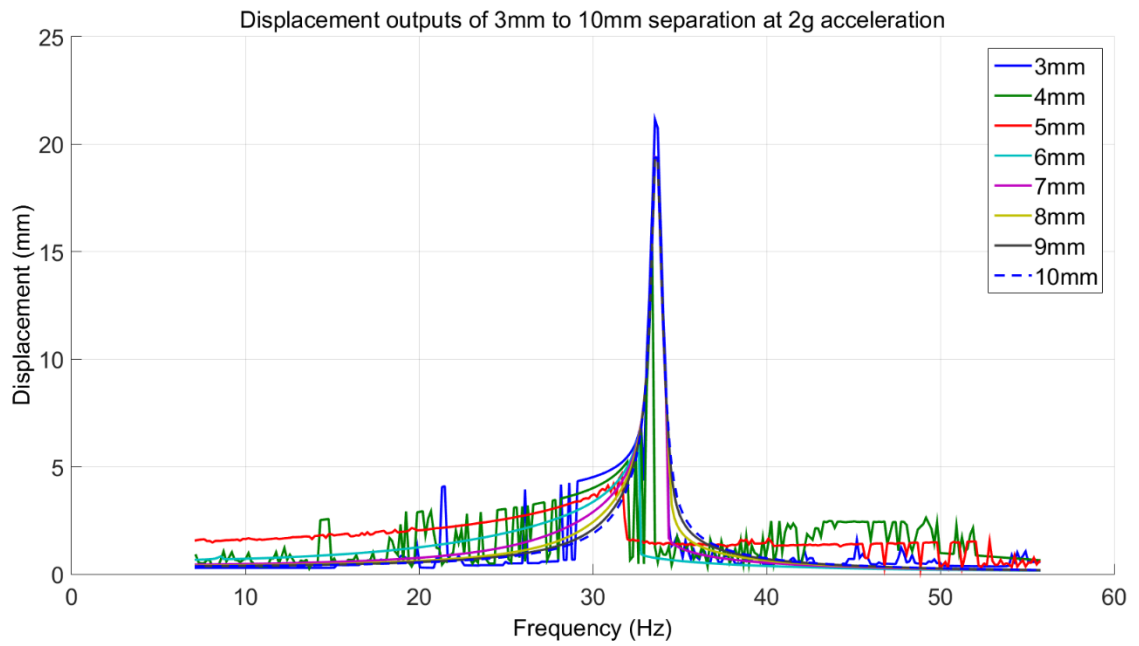


Figure 108: Frequency response of simulated cantilever at 2g acceleration from 3mm to 10mm separation.

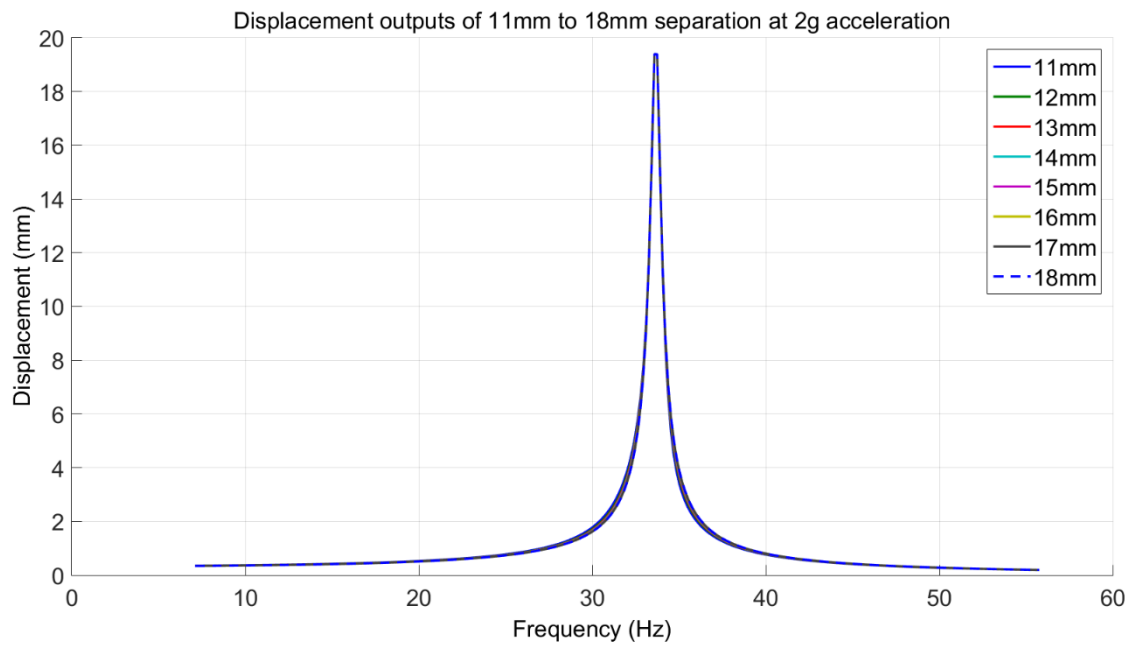


Figure 109: Frequency response of simulated cantilever at 2g acceleration from 11mm to 18mm separation.

Appendix G: Frequency Responses for All Separation Distances under All Accelerations from Experimental Prototype

0.5g Acceleration

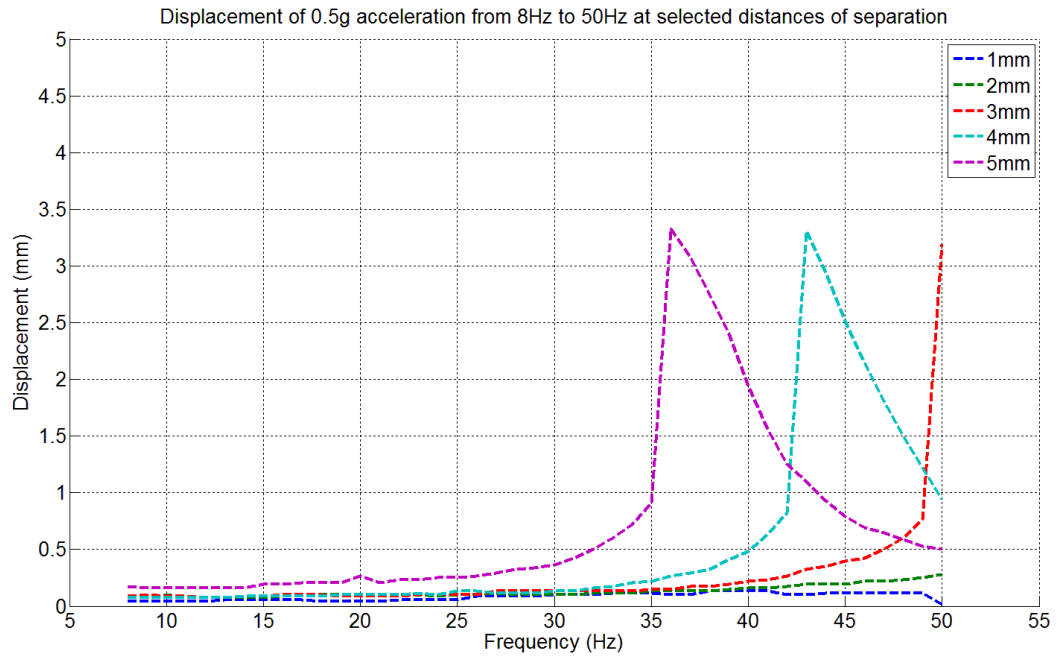


Figure 110: Frequency response of experimental prototype at 0.5g acceleration from 1mm to 5mm separation.

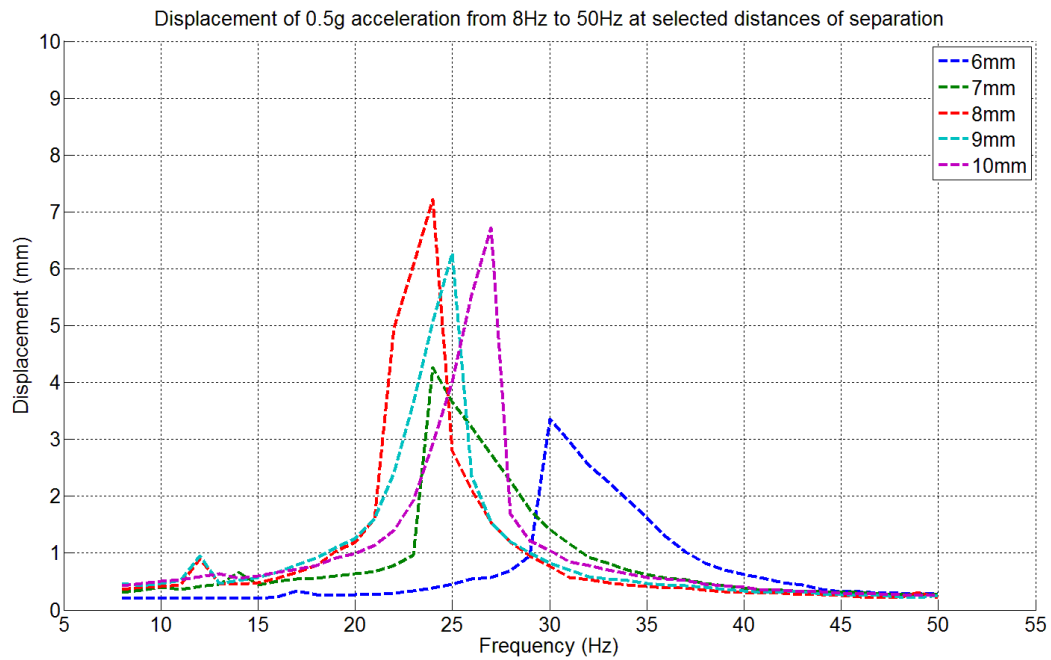


Figure 111: Frequency response of experimental prototype at 0.5g acceleration from 6mm to 10mm separation.

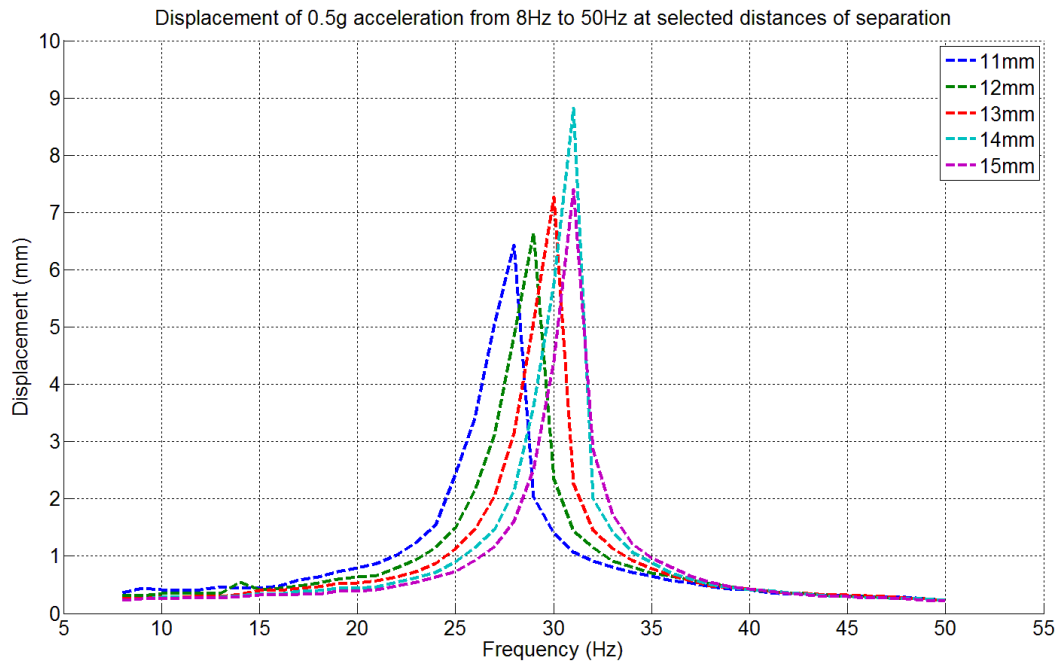


Figure 112: Frequency response of experimental prototype at 0.5g acceleration from 11mm to 15mm separation.

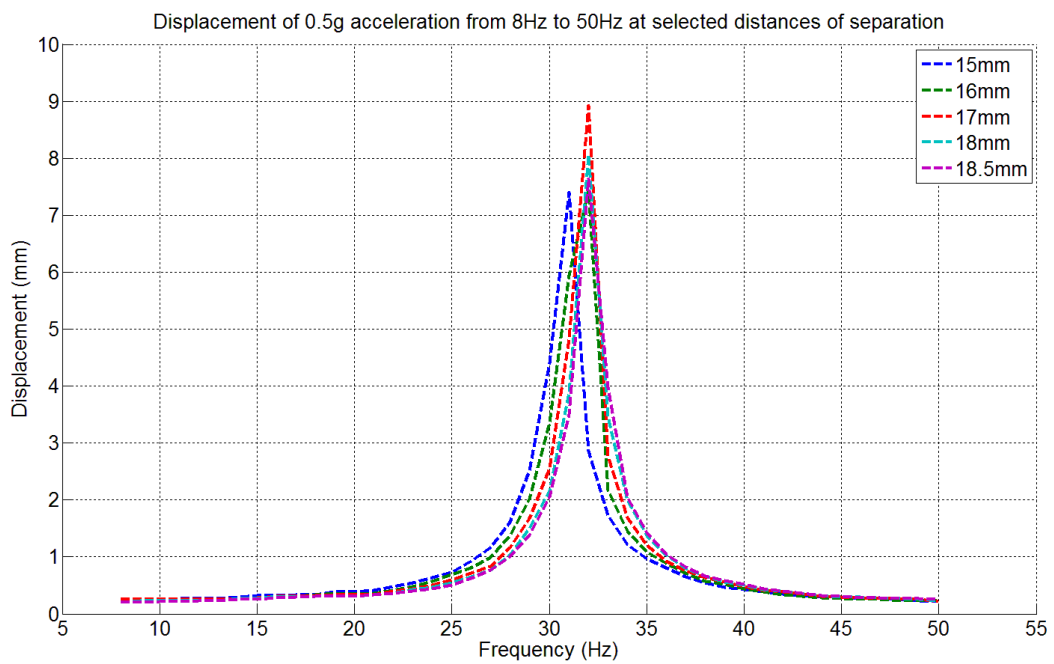


Figure 113: Frequency response of experimental prototype at 0.5g acceleration from 15mm to 18.5mm separation.

1g Acceleration

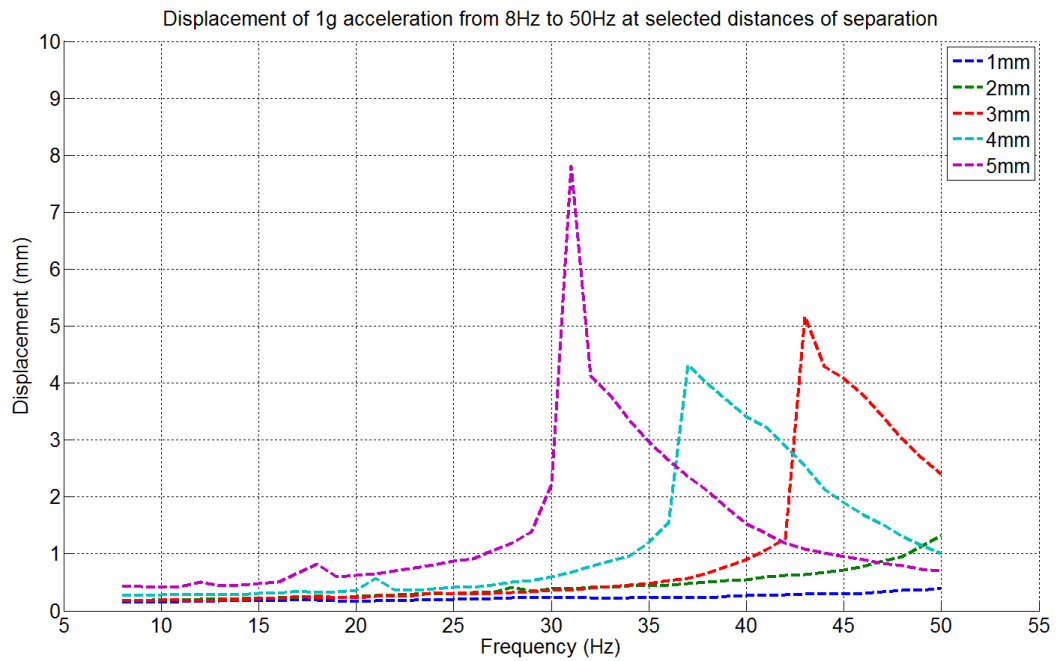


Figure 114: Frequency response of experimental prototype at 1g acceleration from 1mm to 5mm separation.

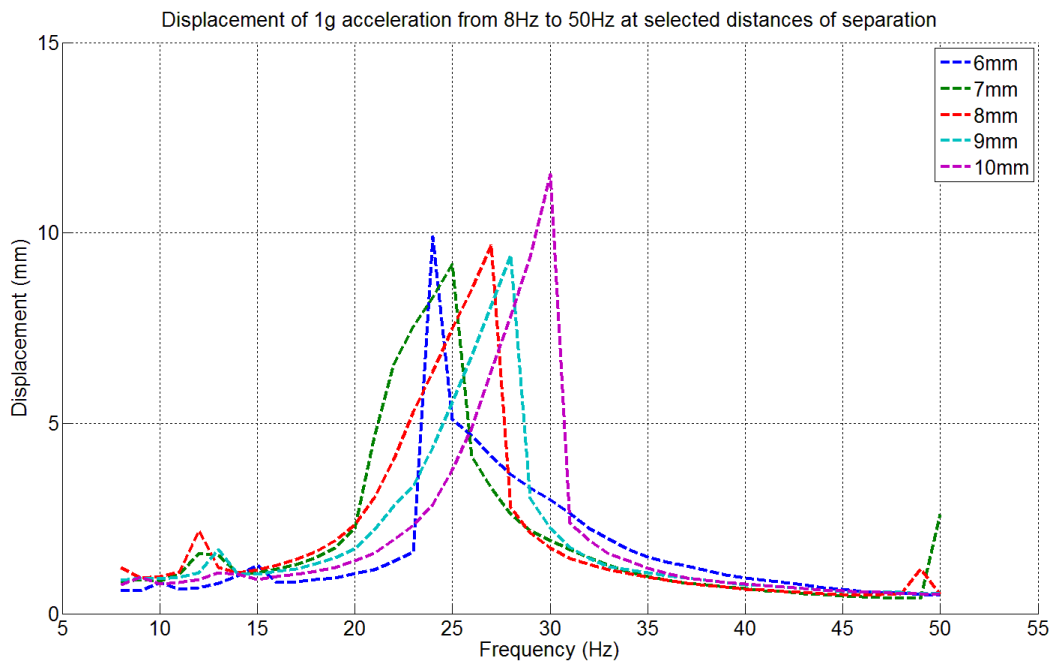


Figure 115: Frequency response of experimental prototype at 1g acceleration from 6mm to 10mm separation.

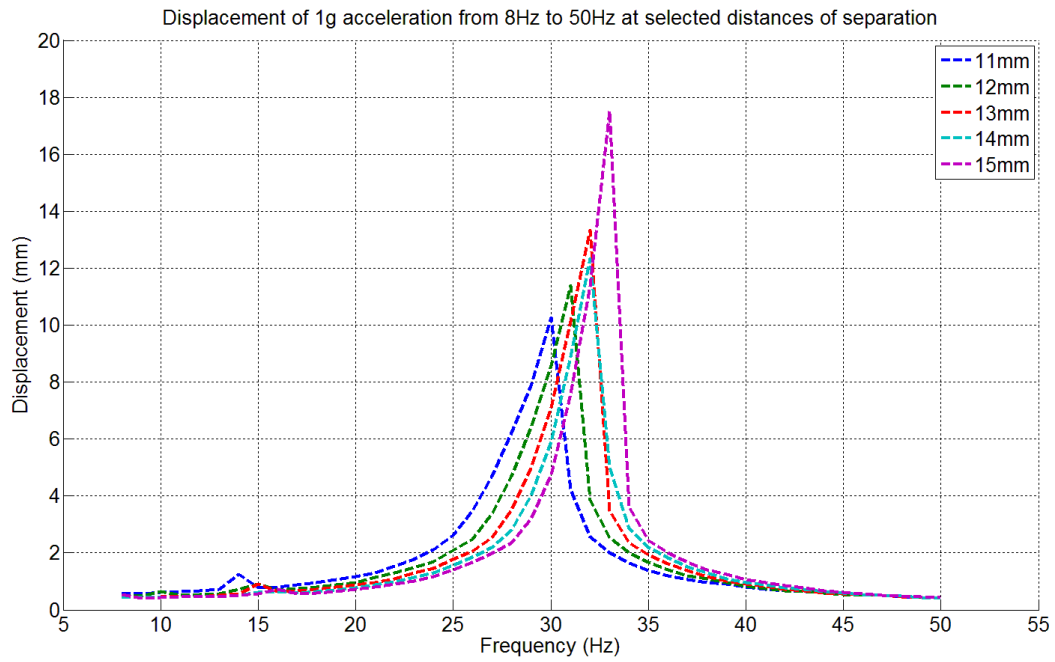


Figure 116: Frequency response of experimental prototype at 1g acceleration from 11mm to 15mm separation.

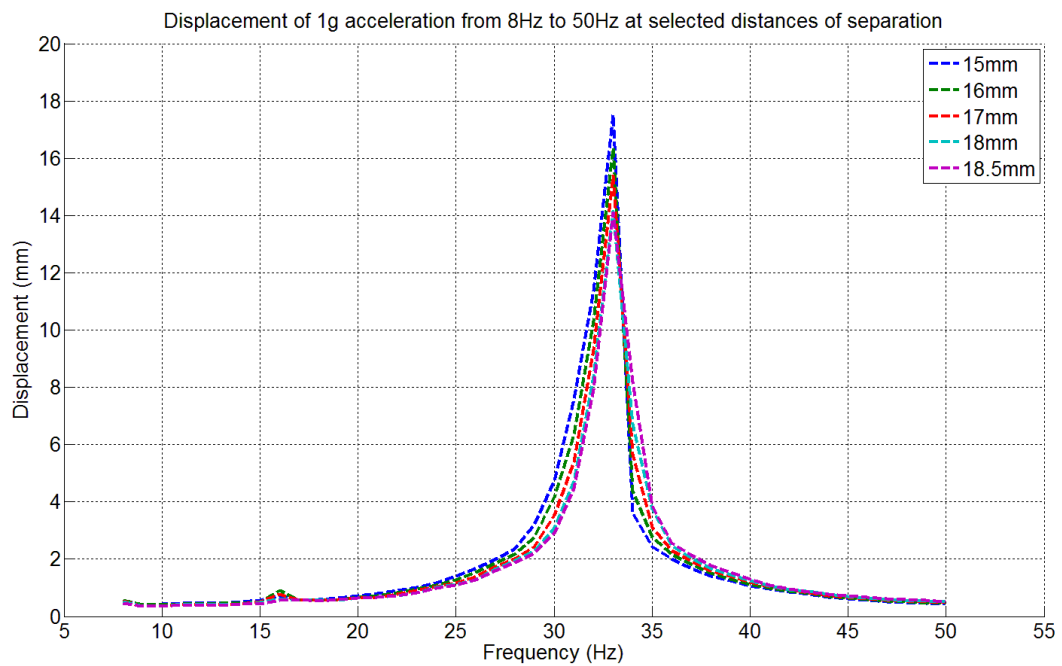


Figure 117: Frequency response of experimental prototype at 1g acceleration from 15mm to 18.5mm separation.

2g Acceleration

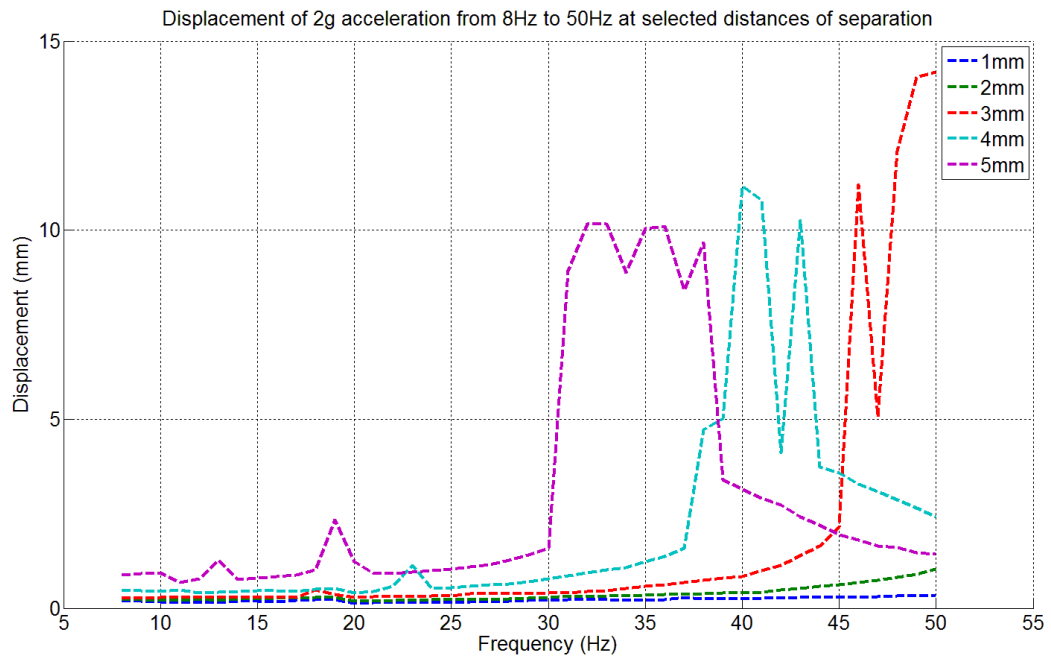


Figure 118: Frequency response of experimental prototype at 2g acceleration from 1mm to 5mm separation.

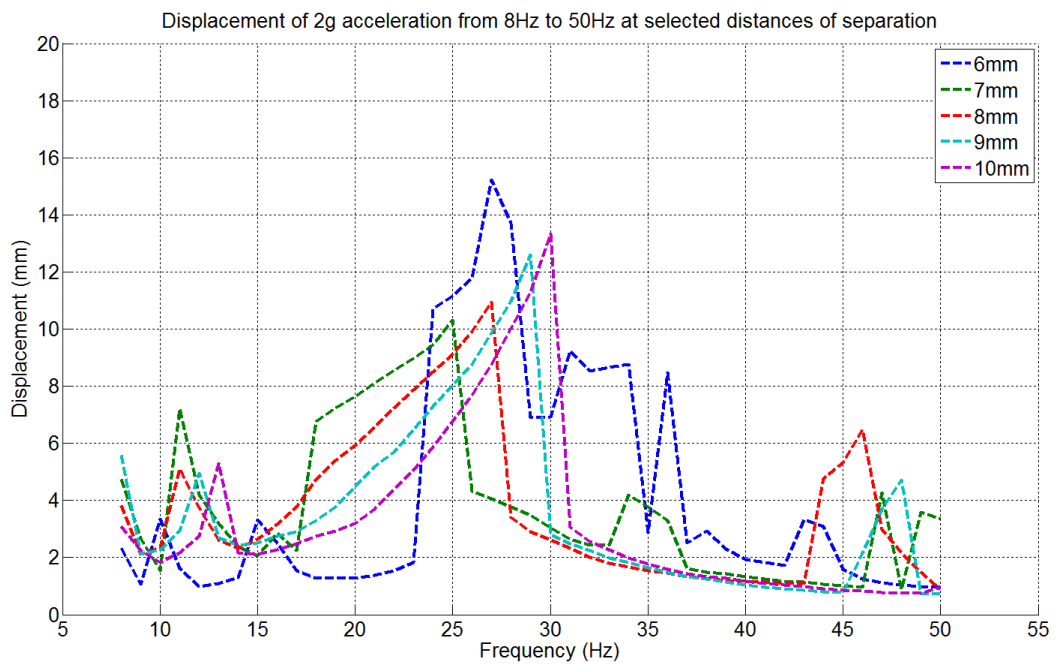


Figure 119: Frequency response of experimental prototype at 2g acceleration from 6mm to 10mm separation.

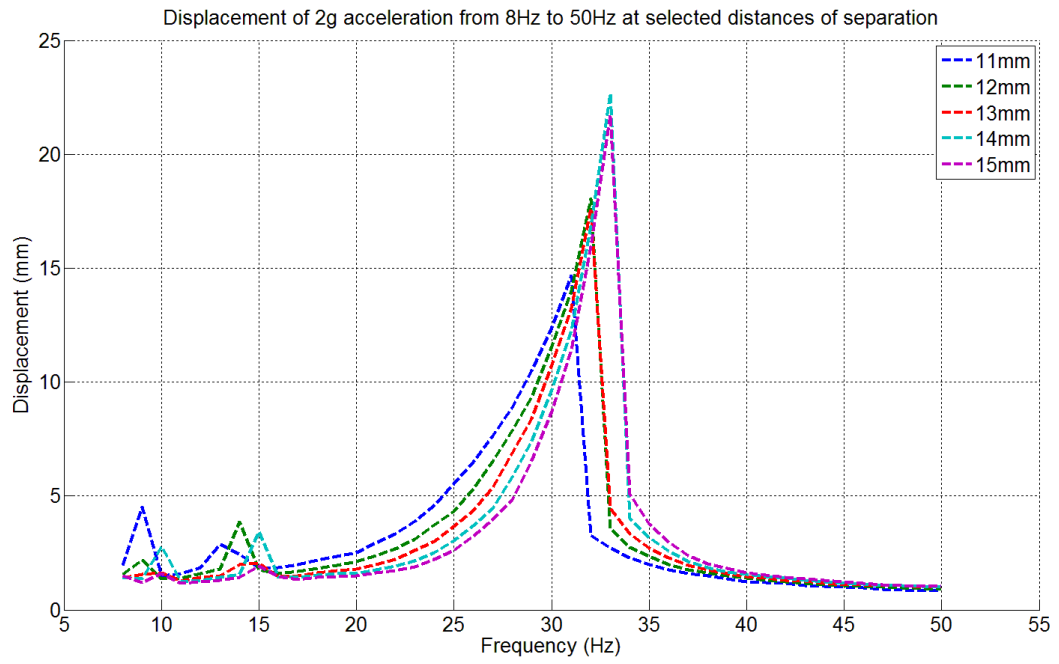


Figure 120: Frequency response of experimental prototype at 2g acceleration from 11mm to 15mm separation.

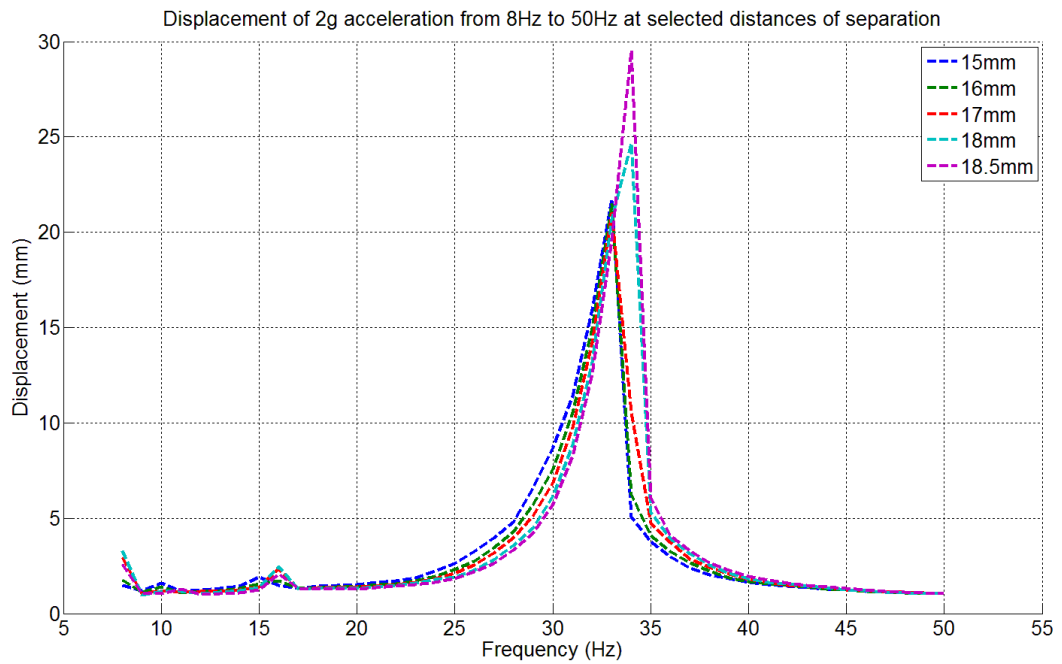


Figure 121: Frequency response of experimental prototype at 2g acceleration from 15mm to 18.5mm separation.

Appendix H: Additional Info on Human Movement Measurements

Sensor Location Acceleration Comparisons

This section presents the comparisons of accelerations recorded based on the sensor placement on the body during the experiment.

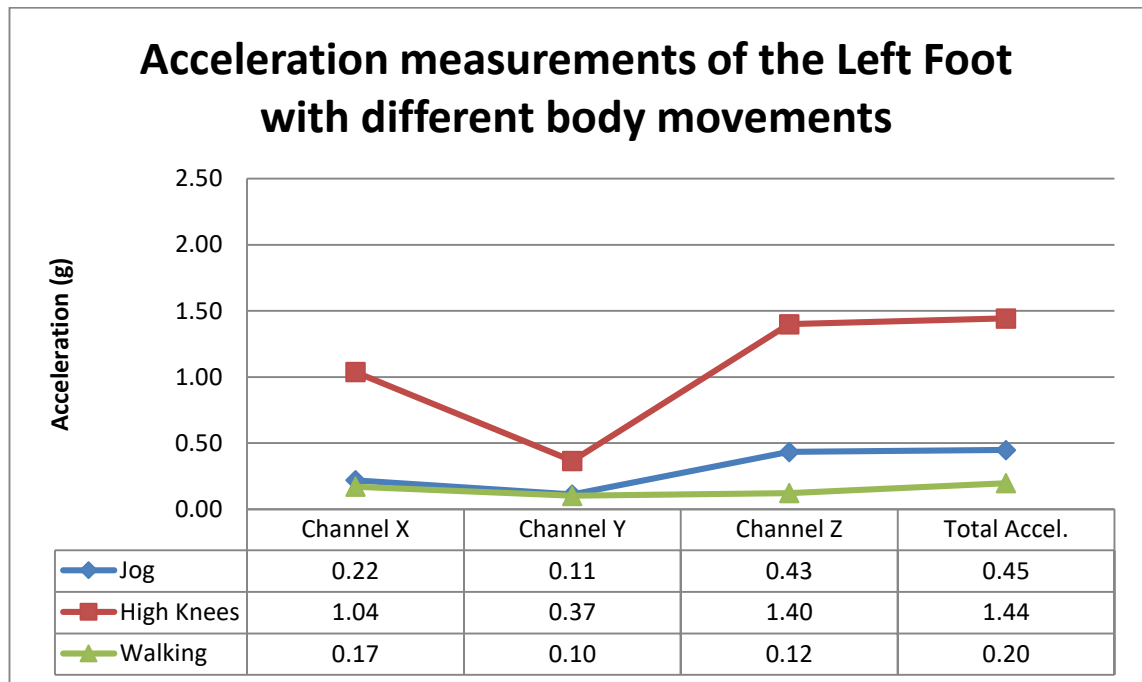


Figure 122: Acceleration Readings of Left Foot Sensor Placement.

Figure 122 further highlights the collection of data of the accelerations that was recorded through different movements on the left foot. It also highlights that the high knees movement produces the most acceleration for all 3 channels as well as the total acceleration value. Channel Z which is the vertical component of the acceleration measurements consistently shows the highest amount of acceleration throughout all 3 channels compared to the other 2 channels.

Channel X on the other hand which is the forwards – backwards component of the acceleration measurements was the second highest measured values on the jogging and high knees movement behind Channel Z. Whereas for the walking movement, Channel X recorded the highest value. This is due to the amount of ‘kick-out’ motion (Figure 123) during the movements performed.

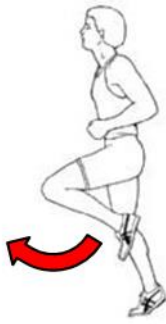


Figure 123: "kick out" motion used from the walking movement.

Channel Y represents the side-to-side component of the accelerometer measuring the accelerations of the foot. As these movements are generally moving in a straight forward direction, the measurements obtained are relatively small. For example if the movement was changed to doing side steps instead of walking, Channel Y would be expected to be at a much higher measurement than what is currently recorded. Consideration must also be given to people who walk with a slightly different gait where they walk with quite a pronounced gait with their foot swings outwards after the "toe lift-off" phase. This variation of walking movement would expect Channel Y's measurements to be slightly higher than a person who walks with a typical gait.

Lastly, the high knees and jogging movements produce a lot more forces compared to the walking movement over the horizontal measurement axis from the movements on the left foot.

Referring to Figure 124, the accelerometer orientation for the chest is now different when compared to how it was attached to the foot. Channel X is now the vertical component and Channel Y the horizontal component (side-to-side), finally Channel Z is the forwards – backwards component.

Notice that Channel X's measurements on Figure 125 are significantly higher when compared to other channels during the jogging and high knees movement. This is due to the much higher physical travel distance (displacement) as well as acceleration of the channel compared to other channels.

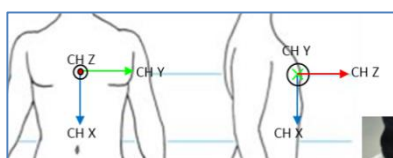


Figure 124: Orientation of the accelerometer placed on the chest.

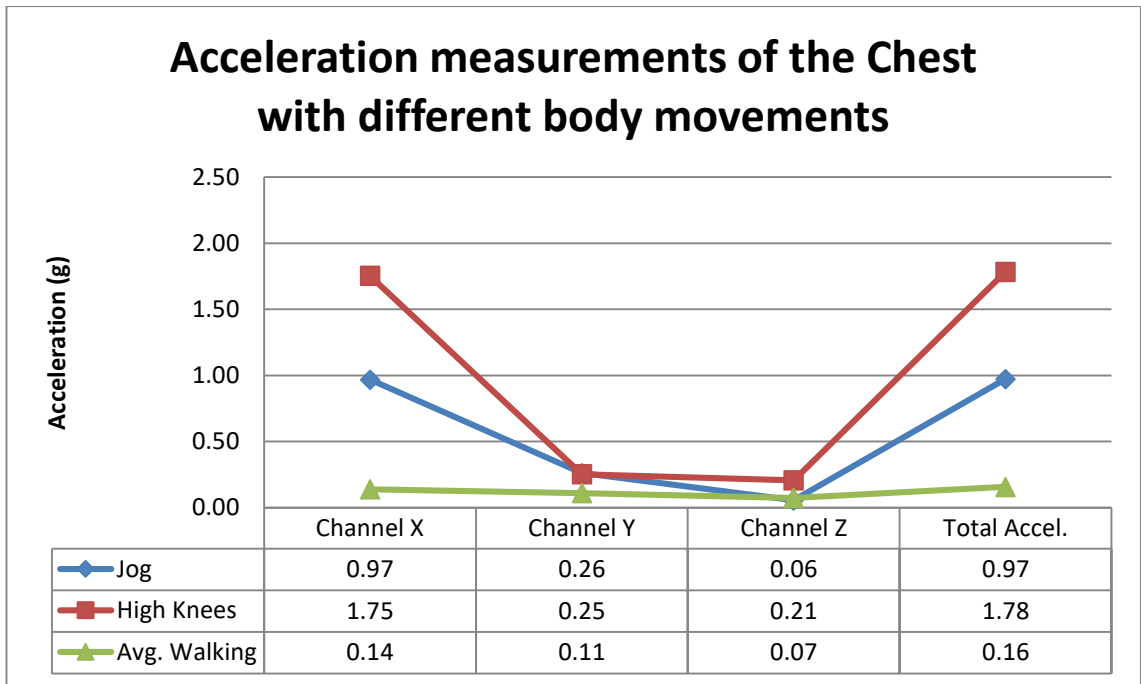


Figure 125: Acceleration Readings of Chest Sensor Placement.

A similar comparison is being made to the previous set of figures where Figure 126 now shows the orientation of the accelerometer that is attached to the hand of the subject. Channel Y now is the vertical component during the arm swing and Channel X is the forwards – backwards or outwards – inwards component. Channel Z now represents the horizontal component.

Figure 127 now shows that Channel Y has the highest measurements. This is expected due to the arm swinging in a more compact position closer to the chest during the jogging and high knees movements compared to the walking movement where the arms are loosely laid and swinging side by side. Conversely, if the arms were swung in a fashion where is it not as compact or close to the chest, a more similar measurement would be expect from both Channel X and Channel Y.

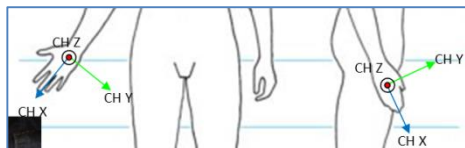


Figure 126: Orientation of the accelerometer placed on the hand.

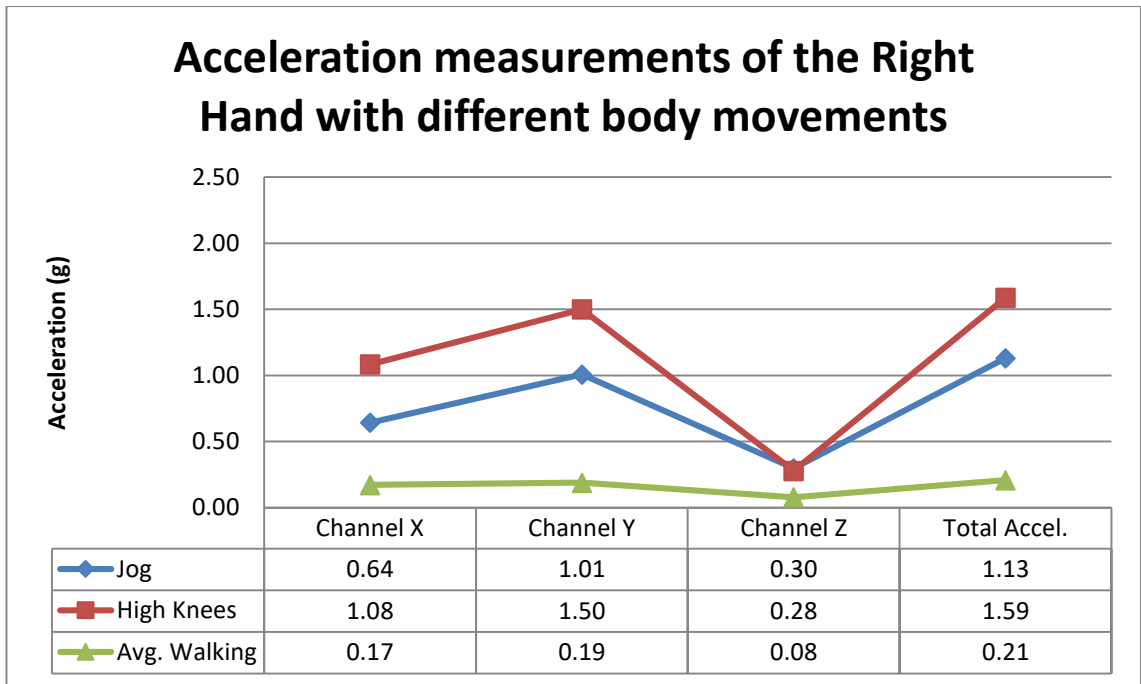


Figure 127: Acceleration Readings of Right Hand Sensor Placement.

Finally, the orientation of the accelerometer when placed at the ankle has Channel X on the vertical component but in a different direction compared when attached to the chest. Channel Y is the forwards – backwards component and finally Channel Z is the horizontal component.

As the vertical component, Channel X is expected to be the channel that has measured the highest accelerations. Accurately, Figure 129 shows that Channel X has the highest values of all 3 channels and with a trend of highest measured value, second and lowest measured value on Channel X, Channel Y and Channel Z respectively. Besides that, during the high knees movement, Channel X recorded a maximum acceleration of 2.06g acceleration which is highest of the whole experiment for a single axis/channel.

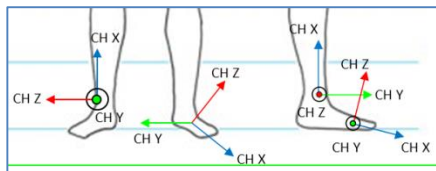


Figure 128: Orientation of the accelerometer when placed on the ankle.

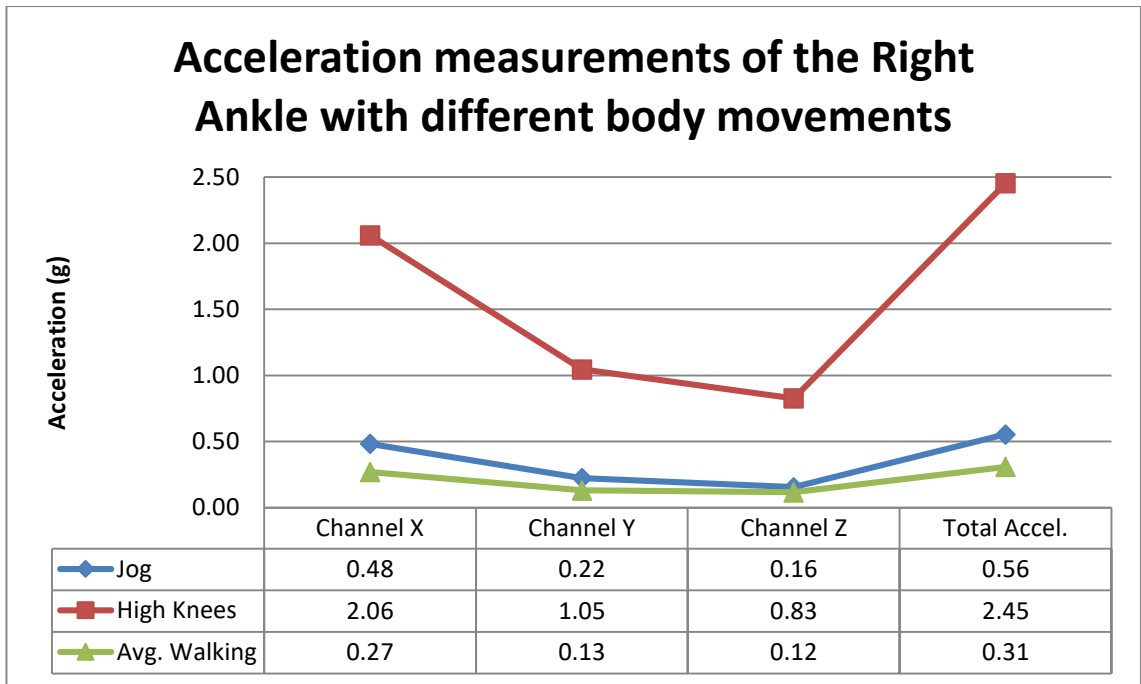


Figure 129: Acceleration Readings of Right Ankle Sensor Placement.

In summary, this experiment shows that the vertical component of the movements tested provides the highest acceleration with all four body locations' vertical component recording the highest outputs. The high knees movement also consistently shows the highest acceleration readings across all three different channels of the sensor. The jog movement also consistently recorded the second highest values and walk obtained the lowest values.

Additionally, the ankle is the best location overall in comparison to the other locations tested if a Single Degree of Freedom (SDOF) Energy Harvester is to be attached onto a test subject as it provides the highest recordings of accelerations.

Channel by Channel Acceleration Comparisons

This section looks at the channel by channel analysis of the recorded accelerations. Previously, the total acceleration measurements were obtained adding the squared values of all three acceleration measurements obtained before square rooting them to obtain the total acceleration values. The total acceleration values represent the total vector of all 3 channels of acceleration.

Figure 130 now presents the data in a different format which it highlights the individual channels of acceleration that is measured by each individual channel as well as the total acceleration value.

In this figure, there is a clear pattern that Channel Z has measured higher values for the jogging and the high knees movement. Channel X then comes in second highest with the acceleration measurements with Channel Y showing the least acceleration values. Channel Y represents the horizontal axis while looking from top down from the knees to the foot. This should again be noted that the values recorded here will differ from individual as everyone walks/run/jumps differently. One person may jump with a high value of leg supination or pronation whereas the other may jump with little or no supination or pronation. This will present a slightly different set of data in that situation.

Figure 130 also shows the potential of a single direction or degree of freedom energy harvester being tuned to the particular axis of acceleration to harvest or scavenge energy from. This would mean that Channel Z would be the perfect axis to be aligned to for an energy harvester to be attached to the left foot as the acceleration readings are the highest for the particular channel based on the 3 movement that have been tested.

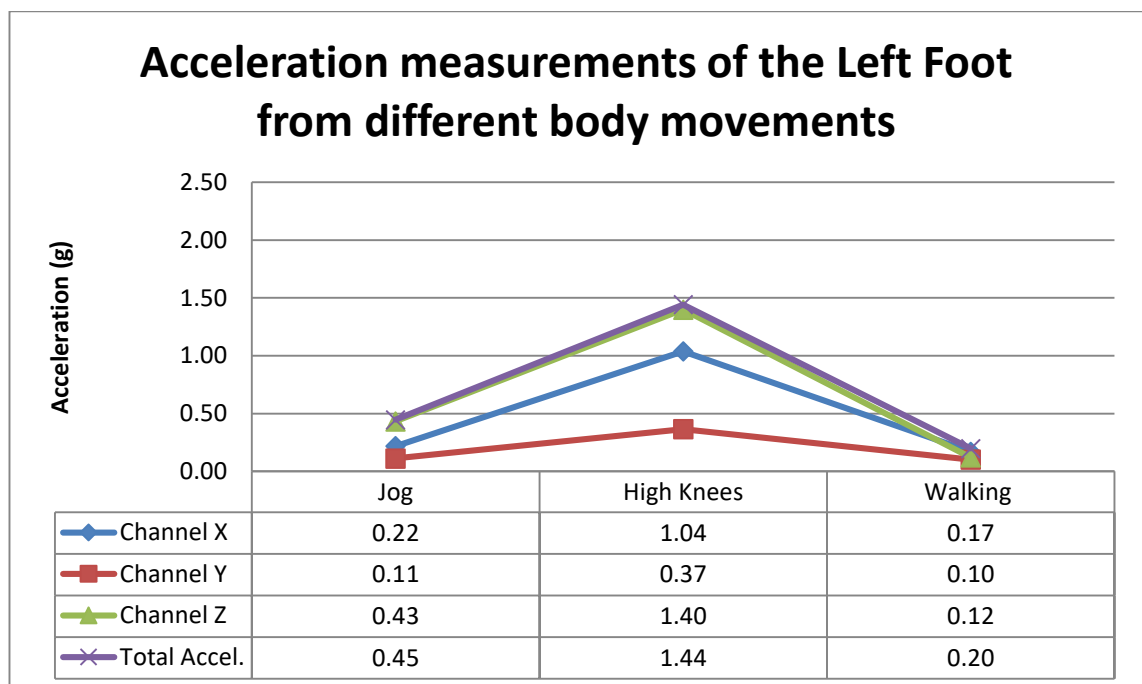


Figure 130: Acceleration readings based on channels for Left Foot movement.

Figure 131 shows an interesting phenomenon where the total acceleration is almost exactly the same as the measured values from Channel X. This also shows that if an energy harvester is to be tuned to a certain axis, it could be tuned to the axis of the vertical component, Channel X if it is going to be placed on the chest with similar movements to be done. This could potentially save a lot of time on trying to locate the best axis to tune the harvester to.

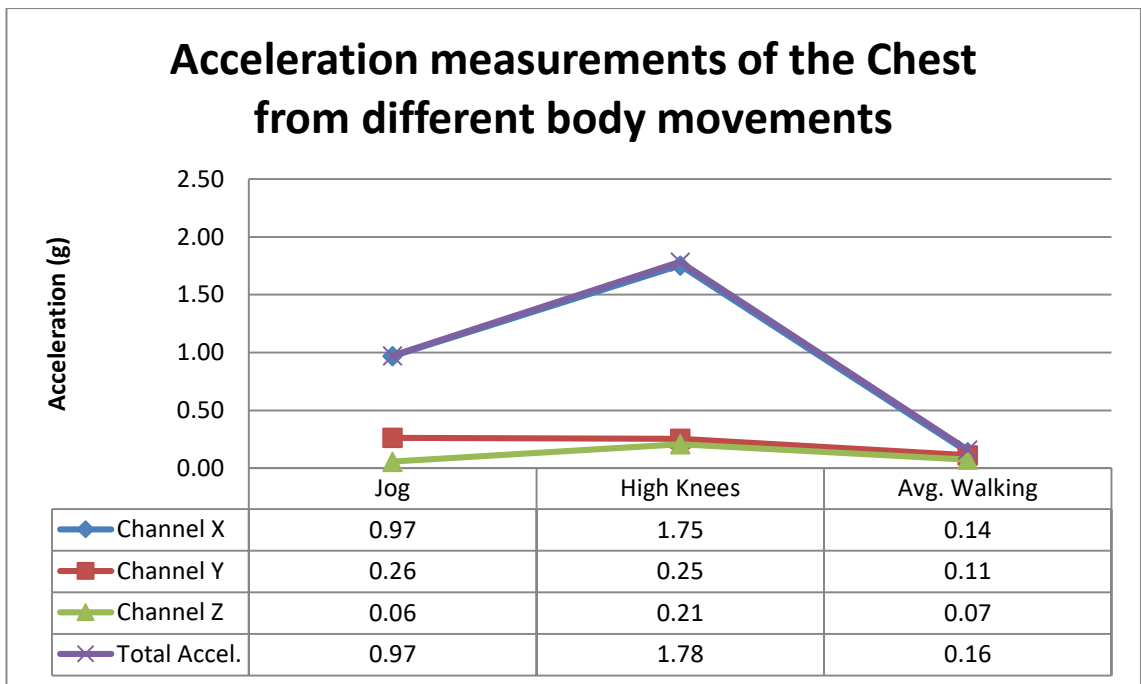


Figure 131: Acceleration readings based on channels for Chest movement.

A similar situation shown on Figure 132 where the total acceleration values are not much higher when compared to the highest measuring channel of acceleration, in this case Channel Y. This shows that a high portion of its acceleration is heavily loaded on one axis during these movements.

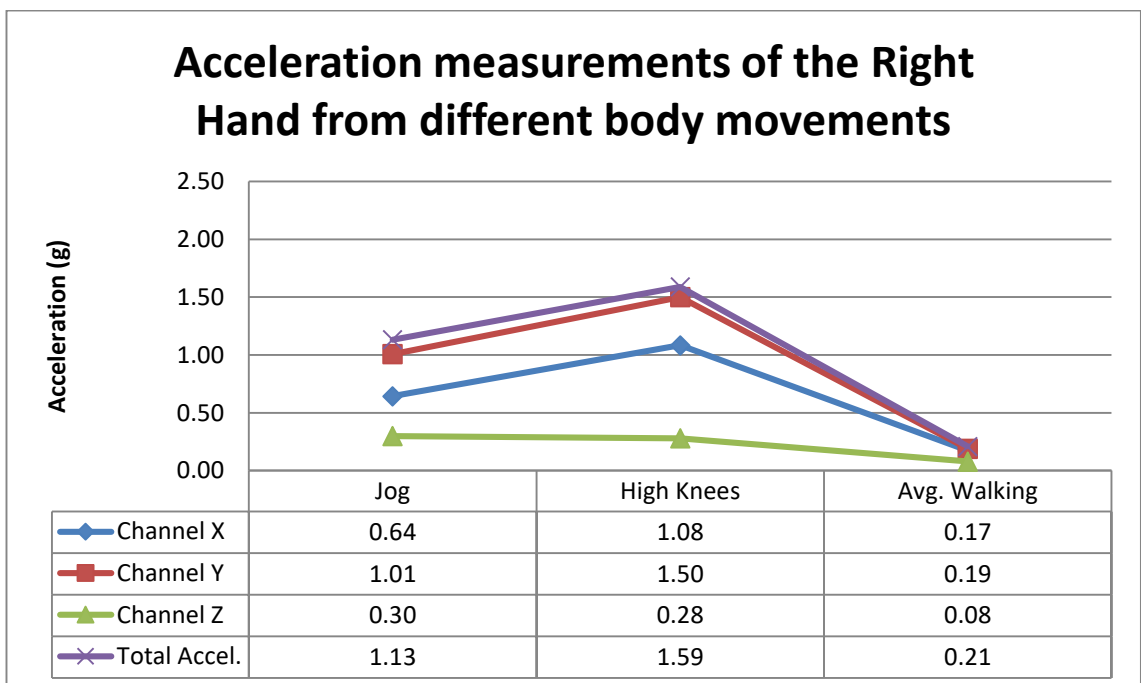


Figure 132: Acceleration readings based on channels for Right Hand movement.

The right ankle placement offers the highest acceleration measurement from the total acceleration values during the walking movement as well as the high knees

movement. Figure 133 shows this useful find as it is allowing the most acceleration to be harvested when doing a similar movement that was tested for example, the high knees or even the walking movement.

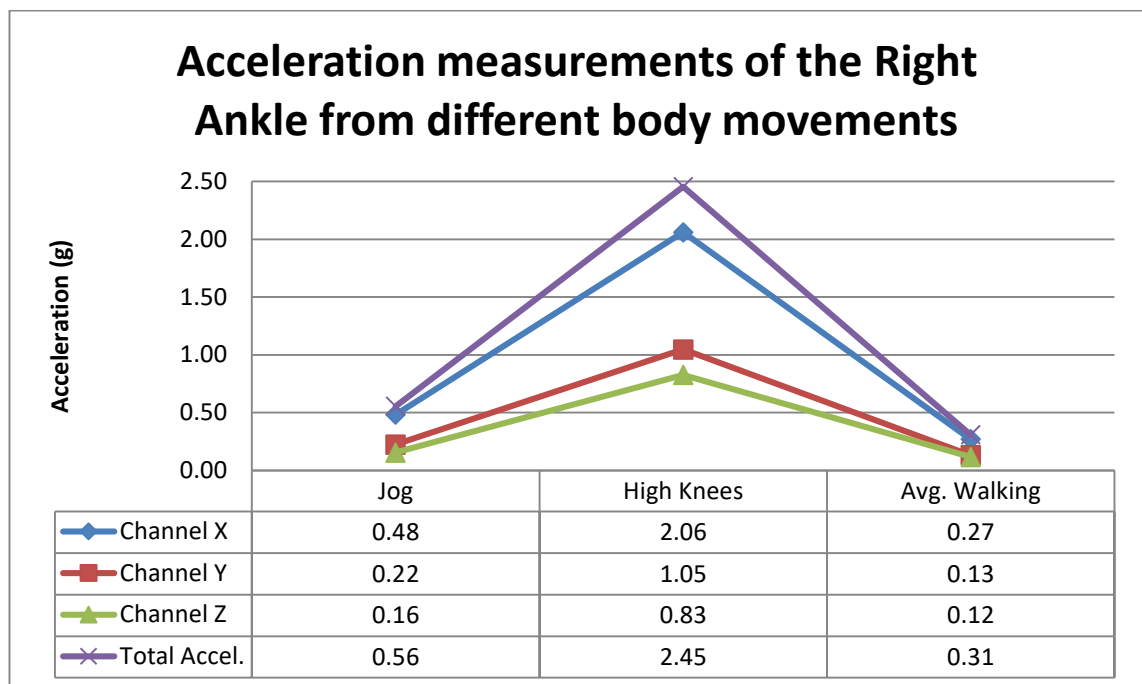


Figure 133: Acceleration readings based on channels for Right Ankle movement.

In summary, similar recommendations could be made for the Channel X of the chest placement, Channel Y of the right hand placement and again Channel X of the right ankle position of the sensor. These channels produced the highest accelerations during the measurement process. Thus if a single degree of freedom energy harvester was to be tuned to any axes to obtain maximum accelerations, these are the channels that it should be tuned to.

Movement by Movement Acceleration Comparisons

This subsection provides the acceleration values based on the movement that was tested and compares the values obtained with the different sensor placements that was used. Figure 134 shows the acceleration figures for the walking movement whereas Figure 135 presents the jogging movement data and finally Figure 136 displays the data collected from high knees.

During the walking phase, Figure 134 shows that there was an increase in acceleration measured from the top of the body going downwards. With the chest measurement receiving the least amount of acceleration while the ankle measuring the highest value.

The chest section receiving the lowest acceleration forces could be due to the vibration and acceleration forces from the walking movement has been damped and compensated by our muscles that are trying to keep us upright. It can also be assumed that if the sensor is place further upwards of the body for example the head section, the acceleration could also be even lower compared to the chest placement. In contrast, the foot measured the highest value of acceleration during the walking movement. This is due to the foot being the first limb to hit the floor during the walking movement. The vibration and acceleration forces reach the foot first before being sent upwards to other joints and body parts. But in line with previous explanation, the measured values may differ when the measurements are being done with another test subject as every person moves slightly differently and it can be different from one person to another.

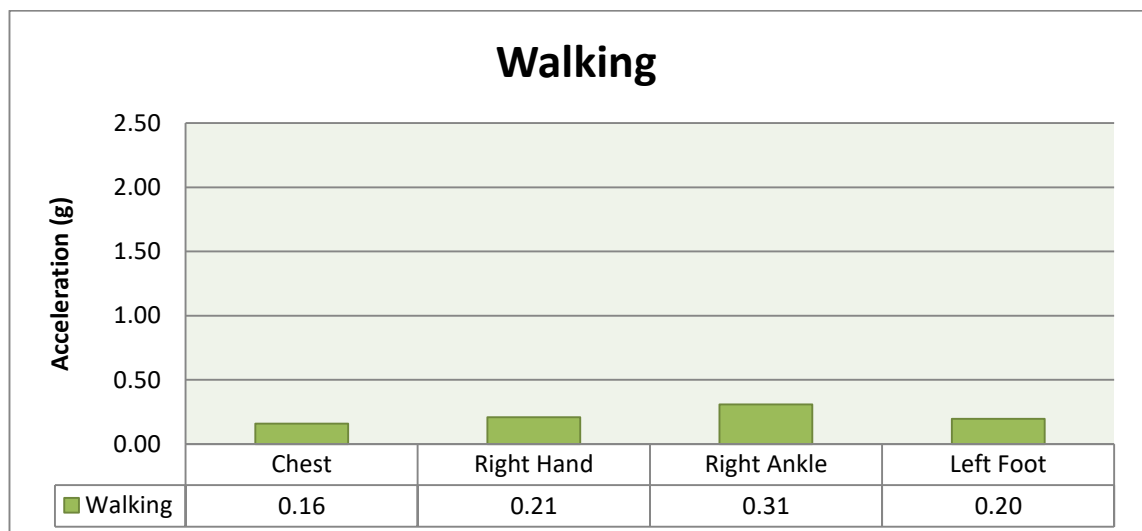


Figure 134: Side by side comparison of acceleration values from different placement of the sensor from walking movement.

Moving to the jogging movement phase, there is an interesting phenomenon where the chest and right hand acceleration values are higher compared to the acceleration values measured on the ankle and feet. This can be explained by for example, for a single jogging step, our hands swing in both directions, upwards and downwards in a single stroke/step. This means that there are 2 sets of almost equal

acceleration forces for one single step of the foot during the jogging movement acting on both the chest and also the hands. It should also be noted that the jogging movement was done as a ‘static jog’ as there was not enough room in the lab for a ‘proper’ jog. Similar explanations can also be applied to the acceleration data obtained for the chest measurement but as the chest does not sway as much as the hands, it is only the vertical component (Channel X) that will experience most of the acceleration forces. These tests could still be used as a gauge for people who are unable to move extensively or run very far, for example, hospital patients. They may be recommended some light exercises by the doctors or physiotherapists and static jog or high knees might be a good exercise to help them recover.

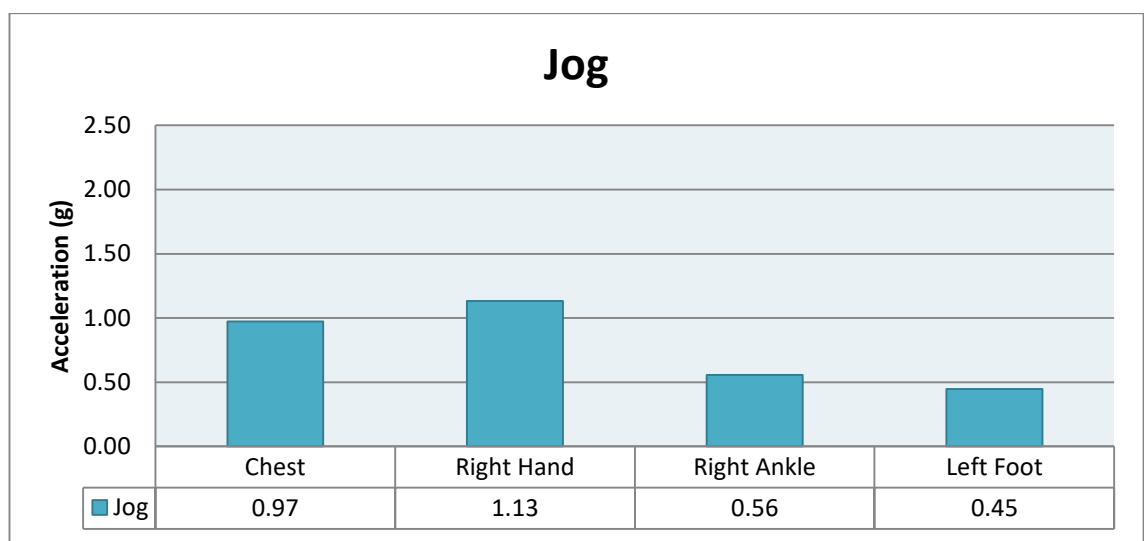


Figure 135: Side by side comparison of acceleration values from different placement of the sensor from jogging movement.

Finally the high knees movements’ shows that it puts our body through the most acceleration compared to all other movements. Also unsurprisingly, the ankle sensor placement recorded the highest acceleration readings. As this motion involves a lot of vertical movements of the legs, the vertical axis of the sensor (Channel X) recorded the highest value of the whole experiment at 2.06g acceleration. The measurement obtained from the ankle position was higher compared to the foot position could be due to the fact that the sensor was attached directly to the ankle. In the foot position, it was placed on top of the shoe. Thus the shoe that the test subject was wearing might have acted as a dampener to the acceleration forces that were acting on the foot. It was also in line with previous discussion that the chest and hand acceleration measurements obtained are slightly higher compared to the measurement from the feet as they produces 2 almost identical sets of acceleration with each single step of the foot.

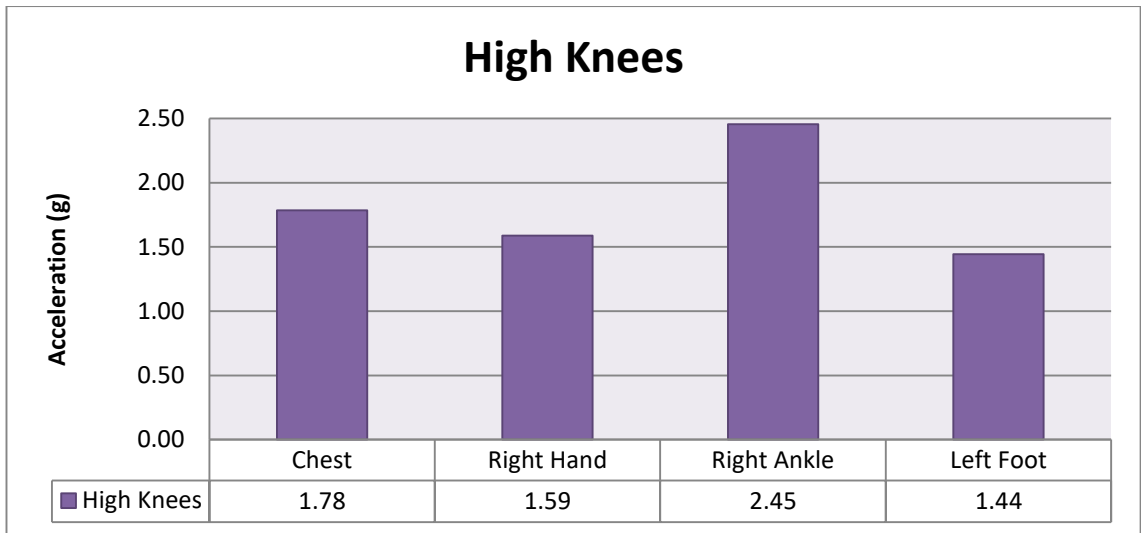


Figure 136: Side by side comparison of acceleration values from different placement of the sensor from high knees movement.